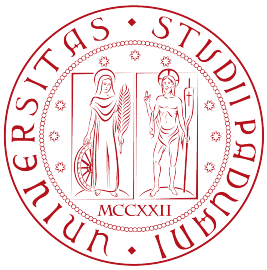

Università degli Studi di Padova

Department of Physics and Astronomy “Galileo Galilei”
Ph.D. course in Physics
Cycle XXXVI

FINAL DISSERTATION

Tensor Networks for Relativistic Hamiltonian Lattice Gauge Theory

Supervisor:
Prof. Simone Montangero

Candidate:
Marco Rigobello

Coordinator:
Prof. Giulio Monaco

Year of the final exam: 2024

We apply and implement numerical tensor network (TN) methods from quantum many-body physics to the simulation of high-energy physics. Relying on Hamiltonian lattice quantum field theory, we put forward a recipe for simulating the real-time dynamics of scattering events, and further develop the dressed site approach to lattice gauge theory (LGT). We focus on numerical applications to low-dimensional LGT problems, demonstrating the feasibility of their TN simulation. We devise a protocol for preparing asymptotic particle wave-packets for the lattice Schwinger model and characterize the entanglement generated during meson-meson collisions. In an effort towards generalizing this study to hadron-hadron collisions in quantum chromodynamics (QCD), we identify and characterize an SU(3) LGT of minimal complexity which reproduces some of QCD's distinctive features.

Acknoledgments: Written with the financial contribution of MIUR (through PRIN 2017), fondazione CARIPARO, the INFN project QUANTUM, the Horizon Europe (PASQuanS2) and Horizon 2020 (QuantERA, through the T-NISQ and QuantHEP projects) EU's research and innovation programs, the DFG project TWITTER, EU's NextGenerationEU project CN00000013 - Italian Research Center on HPC, Big Data and Quantum Computing, the Racah Institute of Physics of the Hebrew University of Jerusalem, and the Quantum Computing and Simulation Center of Padova University.

Contents

Introduction

With the exception of gravity [1], our current understanding of the fundamental laws of nature is elegantly encoded in the Standard Model of particle physics [2] — quantum field theory (QFT) and the paradigm of local gauge invariance constitute its skeleton [3]. This framework also has important applications in condensed matter physics [4–7], e.g., to the study of superconductivity [8, 9]. As a consequence, QFT has played a central role in physics for almost one century [10], leading to countless experimentally tested predictions: the quantum electrodynamics (QED) calculation of the anomalous magnetic moment of the electron with outstanding accuracy [11–14], the several precision tests of the theory of electroweak interactions [15–18], and the quark model interpretation of deep inelastic scattering, which established quantum chromodynamics (QCD) [19–24] as the description of the strong force, are just to name a few examples from particle physics. It is no coincidence that all the above results are rooted in perturbative expansions around well understood free theories [25]. Indeed, despite all the efforts put forward by the physics community over the last fifty years, we still lack non-perturbative control of any 1+3 dimensional interacting QFT [26]. Yet, because of its nature, the perturbative approach is viable only in weak coupling regimes. Even in that setting, defining a QFT through its perturbative expansion is problematic: the perturbative series is generally ill defined and plagued by divergencies that have to be cured order by order via regularization and renormalization procedures [26–28]. One might suspect that this unfortunate state of affairs precludes entirely the investigation of strongly interacting physics, such as low-energy emergent phenomena of QCD. Luckily, various techniques have been devised to overcome the aforementioned limitations, including renormalization group methods [29–31], the conformal bootstrap [32, 33], holography and duality conjectures [34] and lattice QFT [35]. The latter comes to the rescue reformulating the continuum field theory as a quantum many-body system with a finite number of degrees of freedom (d.o.f.), distributed on a regular space(time) grid [36]. At the conceptual level, this approach might furnish an alternative, non-perturbative way of defining QFTs [36] as continuum limits of lattice models, where ultraviolet and infrared divergencies are regulated by the very structure of spacetime. The lattice has opened the doors to numerical simulation [37] and lattice gauge theory (LGT) [38], introduced in the first Chapter, has been an immensely successful framework for extracting testable predictions outside the perturbative regime, such as the masses and decay rates of QCD hadrons [39–41]. Lattice simulations, however, still struggle with physically relevant scenarios, e.g. dense nuclear matter and dynamical problems [42]. To understand why, a closer look at the numerics is in order.

The numerical simulation of many-body systems, and thus of lattice QFT, is an extremely demanding task. Its complexity stems from the exponential growth of the Hilbert space dimension with the size of the system [43]. Most numerical investigations of lattice QFT are based on Monte-Carlo methods, which evaluate phase space integrals by means of stochastic sampling [44]. In order for the integral measure to be well behaved, Wick rotation to an imaginary time coordinate has to be performed beforehand [44, 45]. Results obtained in Euclidean space are then analytically continued back to physical observables in Minkowski space [44, 46]. This approach prevents direct numerical simulation of real-time evolution. Moreover, especially in systems involving fermions at finite chemical potential, the path-integral measure does not always loose its highly oscillatory nature even after Wick rotation. When this happens, cancellations between positive and negative contributions lead to an exponential growth of statistical errors on sampling averages with the system size, reestablishing the complexity of the many-body problem. This is the infamous Monte Carlo sign problem, known to be NP-hard to solve [47]. Although workarounds to mitigate the sign problem have been proposed [48–53], there is a strong demand for alternative, sign-problem free, non-perturbative techniques, capable of dealing natively with real-time dynamics and finite density scenarios [54]. Two candidates which have attracted enormous attention in the last two decades are quantum computation (QC) [55] and tensor networks (TN) [56]. The former idea revolves around using quantum hardware and the laws of quantum mechanics as a resource to processes information; while the latter are numerical techniques which evade the exponential growth of the Hilbert space by directly compressing the wavefunction. On the one hand, the way in which the two handle the exponential growth of the many-body Hilbert space is, in some sense, orthogonal: QC is based on the idea [57] of using a computational device whose computational power scales exponentially with the size of the device itself; while TN aim, and often succeed [58], at identifying an exponentially small portion of the Hilbert space relevant for the physical description of the system. On the other hand, applications of QC or TN to lattice QFT share a number of preliminary implementation steps, as both typically rely on the canonical formalism [59] and on constructing an explicit description the constituent degrees of freedom (d.o.f.) of the target many-body system. In QC, the latter are realized by other quantum d.o.f. belonging to a controllable synthetic quantum system [60], made, e.g., of trapped ions [61, 62], ultra-cold atoms in optical lattices [63, 64], or superconducting circuits [65]. Exploiting quantum phenomena such as interference and entanglement, these devices can potentially perform many-body calculations with resources that scale polynomially with the system size [66]. Most of QC falls into two broad classes, analog and digital [67]. Analog simulators are engineered to reproduce faithfully the constituents and the dynamics of the system of interest; while in digital QC the original d.o.f. are mapped to one or more qubits (or qudits [68]): general purpose 2-level (or d-level) quantum systems. In the circuit model [60, 69], the most widespread model of digital QC [70], calculations are then executed performing sequences of elementary operations, called quantum gates, on the qubits. Recent years have witnessed a surge in proposals and realizations of quantum simulations — many aimed specifically at LGT [71–81]. On par with QC, developing efficient classical numerical methods remains a primary research goal; for at

least two reasons: (i) classical simulation is vital for benchmarking quantum platforms [82], and (ii) present-day quantum technologies are not yet capable of reliably tackling large-scale LGT problems, as recent feasibility studies have shown [79, 83–85]. Quantum-inspired techniques, capable of reproducing closely both the theory of interest and the behaviour of a simulator, are therefore highly desirable. The state-of-the-art in this regard are tensor network state (TNS) methods [58, 86, 87], introduced in the second Chapter of this Thesis. TNS rely on the Hamiltonian formalism and on linear algebra to represent and manipulate many-body wavefunctions, which they efficiently compress by discarding the irrelevant information contained in the exact representation of the many-body Hilbert space [86]. There exist multiple families of TN state ansatze. Their effectiveness (and limitations) are rooted in profound results from quantum information theory regarding the entanglement content of physically relevant many-body states, with each ansatz being tailored to a specific pattern of correlations [88]. The first example of TNS ansatz, matrix product states (MPS), were originally introduced as analytical representations of certain states observed in quantum spin chains [89, 90]. Around the same time, the density matrix renormalization group (DMRG) [91], a landmark algorithm for studying the low-energy physics of quantum many-body systems, was formulated (with no reference to TN). It was soon realized that MPS constitute the natural variational class on which DMRG operates [92–95], marking the advent of numerical TN computations. Their domain of application quickly spread from spin systems [96], to a wide set of condensed matter physics, statistical mechanics, computational chemistry, and even machine learning problems [97–101]. With their application to LGT, a decade ago, TN methods started leaking into high-energy physics [75, 77, 102–112]. The goal of this Thesis is that of contributing to the TN simulation of high-energy physics. Focusing on low-dimensional LGT models inspired by sectors of the Standard Model, we study pilot problems which are difficult or impossible to address by means of other classical techniques.

The archetypal particle physics experiment is a scattering experiment [25]. First principles numerical simulations of scattering processes are essential for validating theoretical models against measurements carried out at particle colliders, e.g. the large hadron collider (LHC), possibly unveiling new physics. In the third Chapter of this Thesis, we report on proof-of-principle MPS simulations of high-energy physics collisions. After having characterized an ideal scattering process, we outline a general strategy to extract S-matrix elements from real-time lattice QFT. The critical step is the preparation of the asymptotic configurations. Once an initial state is given, however, real-time simulations can trace the whole scattering dynamics — not just the asymptotic information encoded in the S-matrix. Moreover, TN provide immediate access to the entanglement content of the system [86]. Leveraging on these two assets, we characterize the entanglement observed during meson-meson scatterings in (1+1)-dimensional QED, also known as massive Schwinger model [113–115]. Besides providing an ideal testbed for new numerical tools, the Schwinger model is interesting as a toy-model of QCD, of which it reproduces the mechanisms of chiral symmetry breaking, confinement, and mass generation [116–118]. QCD is the holy grail of lattice QFT [41]:

infrared slavery [119–121] means that its coupling increases with space separation and the theory becomes non-perturbative at low energies, making lattice QCD the only feasible approach to ab initio investigations of hadronic properties [122]. Two obvious differences between real-world QCD and the Schwinger model are spacetime dimensionality and the SU(3) versus U(1) gauge group. Both higher spacetime dimensions and non-Abelian gauge groups entail remarkable challenges for TN or QC. In starting the journey towards TN and quantum simulation of QCD, it is therefore reasonable to attack these two issues separately. The first TN simulation of a (1+3)-dimensional Abelian LGT appeared recently [123]. In the fourth and last Chapter of this Thesis we deal with the complementary task and study a (1+1)-dimensional truncated SU(3) LGT [124–127]. By means of MPS simulations, we show that the model admits a continuum limit, whose spectrum features particles reminiscent of QCD's hadrons. The implications are twofold: on the one hand, we prepare the ground for the TN simulation of hadron scatterings; on the other hand, we identify an SU(3) model of minimal complexity amenable to near-term QC.

Lying at intersection of classical and quantum approaches, the field of tensor network simulation of high-energy physics is undergoing rapid progress and is allowing a rich exchange of expertise between the quantum information, condensed matter, and high-energy physics communities. This thesis aims at contributing to this enterprise by tackling low-dimensional lattice gauge theory problems previously challenging by means of other classical techniques and, hopefully, moving the first steps towards the tensor network or quantum simulation of the building blocks of the universe.

1

Hamiltonian Lattice Gauge Theory

with finite resources

This Chapter aims at bridging between classical Lagrangian field theories in the continuum and their quantum Hamiltonian version on the lattice and thus, simultaneously, between the language of high-energy physics and that of many-body physics and quantum simulation. The general structure of relativistic field theories is briefly reviewed. Yang-Mills theory is introduced following a geometric construction that naturally translates to the lattice context. The Hamiltonian formulation of gauge theories is discussed, emphasizing how the consistency of the equations of motion gives rise to Gauss-law type constraints. A possible adaptation of canonical quantization to constrained systems, either in the continuum or on the lattice, is laid out. After having outlined the principles of Hamiltonian lattice quantum field theory, a discretization prescription is elaborated. We apply it to Yang-Mills theory, re-deriving the Kogut-Susskind Hamiltonian. Upon quantization, the operator algebras of its local matter and gauge constituents are realized explicitly and the truncation of the infinite dimensional gauge links is discussed. Finally we construct the dressed site: a strategy to enforce Gauss law by trading it for a set of simpler, Abelian constraints.

Attribution: The most original part of this Chapter is Section 1.4D, where the dressed site is developed. The idea is not new [105, 123, 128–130] but is here given a more systematic and general framing, as part of an ongoing project to automate its construction. Sections 1.1 and 1.2 are mostly adapted from Ref. [131], as partially is Section 1.4, which is also inspired by Refs. [76, 105, 132, 133].

1.1 Yang-Mills theory

Yang-Mills theories [134] are a class of relativistic field theories with local gauge invariance, which stand as the cornerstone of the Standard Model of particle physics [3] and provide a unified framework for the description of electroweak and strong interactions. In this Section, after having set the field theory notation, we review the classical Yang-Mills construction. We take a geometric approach that translates seamlessly to the lattice context. Finally, we review the Hamiltonian treatment of gauge theories, which provides the natural language for tensor network (and quantum) simulation. Throughout this Section, repeated indices are always contracted and natural units are employed.

1.1A Field theory notation

A common starting point for the construction of a relativistic quantum field theory is the Lagrangian description of some classical field theory. This approach makes it easy to fulfill symmetry requirements [135]. The degrees of freedom (d.o.f.) are functions of spacetime: the fields $\varphi = \{\varphi^n\}_{n=1}^N$ and their derivatives. By spacetime here it is meant the Minkowski $d = 1+D$ dimensional affine space equipped with the "mostly-minus" metric tensor $\eta_{\mu\nu}$,

$$\mathbb{R}^{1,D} = \{x^\mu = (x^0, x^i) = (t, \mathbf{x}) \,,\ i = 1, \dots, D\}, \qquad \eta = \mathrm{diag}(+, -\dots, -) \ . \tag{1.1}$$

Other than the physical case $D = 3$, hereafter the focus will be on $D = 1$. Under spacetime symmetries[1], namely Poincaré isometries $(\Lambda, a) \in \mathrm{O}(1, D) \ltimes \mathbb{R}^{1,D}$,

$$x^\mu \mapsto \Lambda^\mu{}_\nu x^\nu + a^\mu \ , \qquad \varphi^m(x) \mapsto \Omega(\Lambda)^m{}_n \, \varphi^n(\Lambda^{-1}(x - a)) \ , \tag{1.2}$$

where Ω is some representation of the Lorentz group $\mathrm{O}(1, D)$. Examples are, the trivial representation (scalar fields), the defining one (x^μ, vector fields), and the spinor one[2] (Dirac fields, reviewed below). Let G be the *compact*[3] group of internal (i.e., global pointwise) symmetries and V the representation in which the fields transform:

$$G \ni g : \ \varphi^m(x) \mapsto V(g)^m{}_n \, \varphi^n(x) \ . \tag{1.3}$$

In order to get, upon quantization (Section 1.2), a unitary theory with a finite number of fields, Ω and V must be finite-dimensional projective unitary representations [137].

The dynamics of the classical theory is specified by a variational principle as the stationary point $\delta S = 0$ of a *local* action functional

$$S(\varphi) = \int \mathrm{d}^d x \, \mathcal{L}(\varphi(x), \partial_\mu \varphi(x)) \ . \tag{1.4}$$

[1] In this Thesis we take parity and time reversal as valid spacetime symmetries.

[2] How spinors arise in $D = 1$ where there is no "spin" [136] is addressed, e.g. in Ref. [131, Appendix A].

[3] Compactness ensures the existence of finite-dimensional unitary representations.

The Lagrangian density $\mathcal{L}$ is real, has mass dimension[4] $\Delta(\mathcal{L}) = d$, and transforms as a scalar[5]. Invariance is ensured if all Lorentz and internal group indices are contracted through invariant tensors. If power-counting *renormalizability* [138] of the quantum theory is required[6], $\mathcal{L}$ must be a polynomial with coefficients of positive mass dimension. Finally, we canonically normalize the kinetic terms (quadratic part of the action) [138].

Free Dirac fermions. Dirac spinors in arbitrary spacetime dimensions d can be built from gamma matrices, namely matrices $(\gamma_\mu)^\alpha{}_\beta$ generating an irreducible representation of the Clifford algebra

$$\gamma_\mu\gamma_\nu + \gamma_\nu\gamma_\mu = 2\eta_{\mu\nu} \ . \tag{1.5}$$

Gamma matrices are $2^{\lfloor d/2 \rfloor} \times 2^{\lfloor d/2 \rfloor}$ dimensional, $\lfloor \cdot \rfloor$ denoting the integer part [139]. Now, $\sigma_{\rho\sigma} := (1/4)[\gamma_\rho, \gamma_\sigma]$ obey the Lorentz algebra and thus generate a representation Σ [25]. A multiplet ψ^α transforming with Σ is a Dirac spinor; the conjugate spinor $\overline{\psi}_\alpha := \psi^\dagger_\beta (\gamma_0)^\beta{}_\alpha$ is in the dual representation. Gamma matrices $(\gamma^\mu)^\alpha{}_\beta$ are invariant tensors with two spinor and one vector indices, thus allowing us to write down a kinetic Lagrangian[7] [25]:

$$\mathcal{L} = \overline{\psi}\left(i\partial\!\!\!/ - m\right)\psi \ , \tag{1.6}$$

where spinor indices have been omitted and $v\!\!\!/ = v^\mu\gamma_\mu$. No additional Lagrangian term compatible with our requirements can be built in $d > 2$. In $d = 2$, $\Delta(\psi) = (d-1)/2 = 1/2$, thus a four-fermion interaction is allowed by renormalizability — it appears, e.g., in the Thirring and Gross-Neveu models [118].

At the quantum level, ψ^α and $\overline{\psi}_\alpha$ become fermion fields, that is anticommuting operators[8]. Accordingly, for a consistent quantization procedure, the classical variables $\psi^\alpha(x)$ and $\overline{\psi}_\alpha(x)$ should be treated as Grassmann numbers. We define derivatives and complex conjugation by [143]:

$$\delta F(\psi, \overline{\psi}) = \delta\psi^\alpha \frac{\partial F}{\partial \psi^\alpha} + \delta\overline{\psi}_\alpha \frac{\partial F}{\partial \overline{\psi}_\alpha} \ , \qquad (FG)^* = G^* F^* \ . \tag{1.7}$$

---

[4] A functional of the fields Z has (classical) scaling dimension or mass dimension Δ if $Z \to \lambda^{-\Delta} Z$ under spacetime dilations $x \to \lambda x$. Obviously $\Delta(\partial/\partial x^\mu) = 1$ and $\Delta(\mathrm{d}x^\mu) = -1$. In natural units $\Delta(S) = 0$, whence $\Delta(\mathcal{L}) = -\Delta(\mathrm{d}^d x) = d$.

[5] That is, $(\Lambda, a, g)\colon \mathcal{L}(x) \equiv \mathcal{L}(\varphi(x), \partial_\mu\varphi(x)) \mapsto \mathcal{L}(\Lambda x + a)$.

[6] Renormalizability is not necessary if the theory is an effective theory, but the requirement is at the very least of historical importance, as it greatly constrained model-building freedom.

[7] If equations of motion are to be first order [140], this is the only possible quadratic Lagrangian. It is not real but its imaginary part is a total derivative (see the Grassmann number conventions below).

[8] The *spin-statistic* theorem [137, 141] states that, to preserve causality, fields carrying integer (half-integer) spin commute (anticommute) at space-like separated points, thus satisfying bosonic (fermionic) statistic. In $D = 1$ there is no spin, but the restricted Lorentz group has anyway integer and half-integer quantum number representations, which still correspond to commuting and anticommuting fields [131, 136, 142].

Hamiltonian formalism. Contrarily to the manifestly covariant Lagrangian approach, in the Hamiltonian formulation the time coordinate plays a privileged role and a choice of time direction has to be made. The degrees of freedom are then function of space only[9], namely the fields $\varphi = \{\varphi^n\}$ and their conjugate momenta $\pi = \{\pi_n\}$. To lighten the notation here the indices n, m also run over the position coordinate $\mathbf{x}$, unless the latter is spelled out explicitly. Their contraction involves summation over different fields as well as integration over space. The mapping from $(\varphi, \dot\varphi)$ space to phase space (φ, π) is the Legendre transform:

$$\pi_n = \delta L / \delta \dot\varphi^n \ , \tag{1.8}$$

where the Lagrangian L is the space integral of $\mathcal{L}$. The Hamiltonian is

$$H(\varphi, \pi) = \dot\varphi^n(\varphi, \pi)\, \pi_n - L(\varphi, \dot\varphi(\varphi, \pi)) \ . \tag{1.9}$$

Grouping the fields in commuting $\{\varphi^{n_e}\}$ and anticommuting $\{\varphi^{n_o}\}$ ones, the (super) Poisson bracket of two functionals $F(\varphi, \pi)$, $G(\varphi, \pi)$ is defined as [143]

$$\{F, G\} = \left[\frac{\delta F}{\delta \varphi^{n_e}} \frac{\delta G}{\delta \pi_{n_e}} - \frac{\delta F}{\delta \pi_{n_e}} \frac{\delta G}{\delta \varphi^{n_e}}\right] + \eta \left[\frac{\delta F}{\delta \varphi^{n_o}} \frac{\delta G}{\delta \pi_{n_o}} + \frac{\delta F}{\delta \pi_{n_o}} \frac{\delta G}{\delta \varphi^{n_o}}\right] \ ; \tag{1.10}$$

where $\eta = +1$ if F is commuting, -1 otherwise. The fundamental brackets read

$$\{\varphi^{m_e}, \pi_{n_e}\} = -\{\pi_{n_e}, \varphi^{m_e}\} = \delta^{m_e}{}_{n_e} \ , \qquad \{\varphi^{m_o}, \pi_{n_o}\} = +\{\pi_{n_o}, \varphi^{m_o}\} = -\delta^{m_o}{}_{n_o} \ . \tag{1.11}$$

As in the Lagrangian formalism, the dynamics descends from an action principle [143]

$$\delta S = \delta \int_{-\infty}^{+\infty} \mathrm{d}t \, [\dot\varphi^n \pi_n - H(\varphi, \pi)] = 0 \quad \Rightarrow \quad \dot F = \{F, H\} \ . \tag{1.12}$$

Symmetries and conservation laws. *Noether theorem* associates a conserved quantity to every infinitesimal transformation $\varphi \mapsto \varphi + \delta\varphi$ that leaves the action invariant. Suppose that the internal symmetry group G is a reductive[10] Lie group and let $\{T^a\}_{a=1}^{\dim G}$ be the generators of the V representation, $V(g) = \exp(\theta^a T^a)$ for g in a neighborhood of the identity and some $\theta^a \in \mathbb{R}$,

$$(T^a)^\dagger = -T^a \ , \qquad [T^a, T^b] = f^{abc} T^c \ , \tag{1.13}$$

where f^{abc} are the completely antisymmetric structure constants of the Lie algebra of G. The infinitesimal symmetry transformations of the fields read

$$\delta_\theta \varphi^m = \theta^a (T^a)^m{}_n \varphi^n \ , \qquad \theta^a \ll 1 \ . \tag{1.14}$$

---

[9] Their time dependence is fixed by time evolution.

[10] Reductiveness is here assumed to lighten the notation. The Lie algebra of a reductive Lie group is a direct sum of one-dimensional (Abelian) $\mathfrak{a}_j$ and simple (non-Abelian) $\mathfrak{h}_k$ factors $\mathfrak{g} = \mathfrak{a}_1 \oplus \cdots \oplus \mathfrak{a}_J \oplus \mathfrak{h}_1 \oplus \cdots \oplus \mathfrak{h}_K$.

Noether theorem provides as (independent) conserved currents and charges,

$$j^{a\,\mu} = (T^a)^m{}_n \varphi^n \frac{\partial \mathcal{L}}{\partial(\partial_\mu \varphi^m)} \ , \qquad Q^a(t) = \int \mathrm{d}^D\mathbf{x}\, j^{a\,0}(t,\mathbf{x}) \ . \tag{1.15}$$

On the solutions of the equations of motion,

$$\partial_\mu j^{a\,\mu} = 0 \ , \qquad \mathrm{d}Q^a/\mathrm{d}t = 0 \ . \tag{1.16}$$

In the Hamiltonian formalism, through the Poisson bracket, conserved charges form a representation of the symmetry algebra,

$$Q^a = \int \mathrm{d}\mathbf{x}\, (T^a)^m{}_n\, \varphi^n(\mathbf{x})\, \pi_m(\mathbf{x}) \ , \qquad \{Q^a, Q^b\} = f^{abc} Q^c \ . \tag{1.17}$$

Most importantly, the charges realize the internal symmetry transformations Eq. (1.14) as infinitesimal canonical transformations. Considering again a generic $F(\varphi,\pi)$

$$\delta_\theta F = \theta^a \{F, Q^a\} \ , \qquad \delta_\theta \varphi^m = \theta^a \{\varphi^m, Q^a\} = \theta^a (T^a)^m{}_n \varphi^n \ . \tag{1.18}$$

1.1B Gauge theories

A gauge theory is a redundant description of a physical system arising from an arbitrariness in the choice of some "frame of reference" in which the system configuration is specified. This redundancy, it turns out [137], is necessary for a local and Lorentz covariant formulation of an interacting quantum theory that includes massless particles of helicity ± 1, such as quantum electrodynamics. In the cases considered here, the arbitrariness corresponds to the freedom of performing *local gauge transformations* — namely, independent internal group[11] transformations at each spacetime point:

$$\varphi(x) \mapsto ({}^g\varphi)(x) = V(g(x))\, \varphi(x) \ , \qquad S(\varphi) = S({}^g\varphi) \ , \tag{1.19}$$

for smooth $g\colon \mathbb{R}^{1,D} \to G$ such that $g(x) \xrightarrow{|\mathbf{x}|\to\infty} 1_G$.

Geometrical viewpoint. Equation (1.19) can be interpreted stating that the image of φ at different spacetime points belongs to different copies of the G-representation space, with no canonical identification between them (fiber bundle [146]). When comparing field values at different points, e.g., in derivatives, such an identification has to be provided explicitly. This is usually done introducing the (differential) notion of covariant derivative which allows to define the (integral) notion of parallel transport. Here we proceed the other way round [25] and start from the parallel transport. This will provide useful insights on how to build a lattice Yang-Mills Hamiltonian.

[11] Here we assume G is a continuous Lie group; for finite groups see, e.g., [144, 145].

Let $\gamma\colon I \to \mathbb{R}^{1,D}$ be a smooth curve defined on an open interval $I \subset \mathbb{R}$. To each γ and $s,t \in I$ we associate a unitary matrix $U_\gamma(t,s)$ in the V representation of G, requiring

(i) the association to be smooth[12];
(ii) $U_\gamma(s,s) = 1_V$, the V representation space identity;
(iii) $U_\gamma(t,u)\,U_\gamma(u,s) = U_\gamma(t,s)$, in particular $U_\gamma(s,t) = U_\gamma^\dagger(t,s)$;
(iv) $U_\gamma(t,s) \mapsto V(g(\gamma(t)))\,U_\gamma(t,s)\,V^\dagger(g(\gamma(s)))$ under gauge transformations Eq. (1.19).

The *parallel transport* $U_\gamma(t,s)$ maps the representation space attached to $x = \gamma(s)$ to the one at $y = \gamma(t)$, in such a way that the difference

$$U_\gamma^\dagger(t,s)\,\varphi(y) - \varphi(x) \xmapsto{\text{Eq. (1.19) + (iv)}} V(g(x))\left[U_\gamma^\dagger(t,s)\,\varphi(y) - \varphi(x)\right] \tag{1.20}$$

makes sense and transforms covariantly (and independently of t) by construction[13]. When constructing local actions, we are interested in derivatives rather than finite differences[14]. A notion of covariant derivative along the curve γ, D_γ, is retrieved taking the $t \to s$ limit of Eq. (1.20):

$$D_\gamma\varphi(s) := \lim_{t\to s} \frac{U_\gamma^\dagger(t,s)\varphi(\gamma(t)) - \varphi(\gamma(s))}{t-s} = \frac{\mathrm{d}}{\mathrm{d}t} U_\gamma^\dagger(t,s)\varphi(\gamma(t))\Big|_{t=s} \,. \tag{1.21}$$

Recalling properties (i)–(ii), $U_\gamma(t,s)$ can be expanded for small $\epsilon = t - s$ in the generators T^a. Let us assume a γ dependence of the form

$$U_\gamma(t,s) = 1 + \epsilon\dot\gamma^\mu(0)\,A_\mu(x) + \mathcal{O}(\epsilon^2) \,, \quad A_\mu(x) = A_\mu^a(x)\,T^a \,, \quad A_\mu^a(x) \in \mathbb{R} \,, \tag{1.22}$$

where the *connection* 1-form A has been introduced. Setting $\eta = \dot\gamma(0)$, $x = \gamma(0)$,

$$D_\gamma\varphi(s) = \lim_{\epsilon\to 0} \frac{(1 - \epsilon\eta^\mu A_\mu)(\varphi + \epsilon\eta^\mu\partial_\mu\varphi)(x) - \varphi(x)}{\epsilon} = \eta^\mu(\partial_\mu - A_\mu)\varphi(x) \,, \tag{1.23}$$

which defines the *covariant derivative* of φ in x along η. Symbolically,

$$D = \partial - A \,, \qquad D \xmapsto{\text{Eq. (1.19)}} VDV^\dagger \,. \tag{1.24}$$

This adjoint transformation law is a consequence of Eqs. (1.19) and (1.20) and ensures that φ and $D\varphi$ belong to the same G representation. A global symmetry of the action is thus convert to a local one via *minimal substitution*

$$\partial \to D \,. \tag{1.25}$$

[12] This is better qualified deriving U_γ from the connection [146].

[13] It is anyway path dependent.

[14] At least in theories defined on a continuous spacetime. On the lattice this will change.

Equation (1.24) implies[15]

$$A \xmapsto{\text{Eq. (1.19)}} VAV^\dagger - V\partial V^\dagger \ ; \tag{1.26}$$

or, for infinitesimal transformations $V = \exp(\theta T^a)$ [138],

$$\delta_\theta A^a_\mu = D_\mu \theta^a = f^{abc}\theta^b A^c_\mu + \partial_\mu \theta^a \ . \tag{1.27}$$

Finally, the parallel transport can be expressed as a path-ordered[16] exponential [25]:

$$U_\gamma(t,0) = \mathcal{P}\exp\int_0^t \mathrm{d}s\ \dot\gamma^\mu(s)\, A_\mu(\gamma(s)) \ . \tag{1.28}$$

Pure Yang-Mills. The last step to obtain a proper gauge theory is to introduce a kinetic term for the connection components A^a_μ, thus promoting them to propagating d.o.f. termed *gauge fields* or *gauge bosons*. Recalling Eq. (1.24), a covariant term containing derivatives of the connection components is its *curvature* or *field strength*

$$F_{\mu\nu} = F_{[\mu\nu]} = -[D_\mu, D_\nu] = F^a_{\mu\nu}T^a \ , \quad F^a_{\mu\nu} = \partial_\mu A^a_\nu - \partial_\nu A^a_\mu - f^{abc}A^b_\mu A^c_\nu \ . \tag{1.29}$$

As a consequence of Eq. (1.24), the field strength also transforms in the adjoint

$$F_{\mu\nu} \xmapsto{\text{Eq. (1.19)}} VF_{\mu\nu}V^\dagger \ . \tag{1.30}$$

A valid kinetic term for gauge bosons should be local, Poincaré and internal group invariant, renormalizable (by our requirement) and quadratic (by definition). It is now evident that

$$\mathcal{L} \propto \operatorname{tr} F_{\mu\nu}F^{\mu\nu} \ , \tag{1.31}$$

provides such a term, together with cubic and quartic self-interactions whenever G is non-Abelian ($f^{abc} \neq 0$). Remarkably, gauge invariance forbids a gauge boson mass term $A^a_\mu A^{a\,\mu}$.

It is worth pursuing an alternative, easily discretized, derivation of Eq. (1.31). A gauge invariant scalar, the *Wilson loop* $W_\gamma = \operatorname{tr} U_\gamma$, is obtained taking the trace of the parallel transporter around a closed curve $\gamma = \partial\Sigma$ [35]. To construct a local action term, take Σ to be an infinitesimal square circuit (*plaquette*) with origin in x, spanned by the vectors $\epsilon\hat\alpha$

[15] Because of the inhomogeneous term, A is not a tensor under gauge transformations. Otherwise stated, it does not transform covariantly. It is nevertheless well defined, in the sense that the transformed connection is still algebra representation valued and its components A^a_μ are independent from the representation V chosen, as shown by the infinitesimal transformation (1.27).

[16] Path ordering $\mathcal{P}$ is needed when G is non-Abelian. The path ordered product of a one-parameter family of operators is here defined as the product of the operators ordered from right to left by increasing parameter. For functions, the ordering is done on the terms of the Taylor expansion.

and $\epsilon\hat{\beta}$ ($\hat{\alpha}^\mu = \delta^\mu_\alpha$, $\hat{\beta}^\mu = \delta^\mu_\beta$, $\epsilon \ll 1$). In Abelian U(1) case[17], via Stokes theorem:

$$U_{\partial\Sigma} = \exp \oint_\gamma A = \exp \int_\Sigma F = \exp\left(\epsilon^2 \sigma_1^\mu \sigma_2^\nu F_{\mu\nu}(x) + \mathcal{O}(\epsilon^3)\right) . \tag{1.32}$$

where the 2-form F is the field strength. The non-Abelian case is more involved [147] but for the infinitesimal circuit the result is analogous [25]. Taking the real part[18],

$$\mathrm{Re}\, W_{\alpha\beta}(x;\epsilon) := \mathrm{Re}\, W_{\partial\Sigma} = \mathrm{tr}\left[1_V + \frac{\epsilon^4}{2}\, \hat{\alpha}^\mu \hat{\alpha}^\rho \hat{\beta}^\nu \hat{\beta}^\sigma\, F^a_{\mu\nu} F^b_{\rho\sigma}(x)\, T^a T^b + \mathcal{O}(\epsilon^5)\right] \tag{1.33}$$

No intrinsic preferred directions are available and $\hat{\alpha}, \hat{\beta}$ ought to be replaced with an invariant tensor in the same Lorentz representation; the only[19] possibility is $\hat{\alpha}^\mu \hat{\alpha}^\rho \hat{\beta}^\nu \hat{\beta}^\sigma \to \eta^{\mu\rho}\eta^{\nu\sigma}$, amounting to $W_{\alpha\beta} \to \sum_{\alpha\beta} \eta^{\alpha\alpha}\eta^{\beta\beta} W_{\alpha\beta}$. Let us assume the representation V to be faithful, with generators normalized via [150]

$$\mathrm{tr}\, T^a T^b = -2g^2 \delta^{ab} . \tag{1.34}$$

The *pure Yang-Mills* (no matter fields) Lagrangian is

$$\mathcal{L} = \lim_{\epsilon\to 0} \frac{1}{4g^2\epsilon^4} \sum_{\alpha\beta} \eta^{\alpha\alpha}\eta^{\beta\beta}\, \mathrm{Re}\, W_{\alpha\beta}(\epsilon) = \frac{1}{8g^2}\, \mathrm{tr}\, F_{\mu\nu}F^{\mu\nu} = -\frac{1}{4} F^a_{\mu\nu} F^{a\,\mu\nu} ; \tag{1.35}$$

where we dropped an inconsequential (divergent) constant. The limit kills higher ϵ order terms whose coefficients have negative mass dimension[20]. As per Eq. (1.34), the coupling quantifying the strength of the interaction is hid in the algebra; it can be made explicit via

$$f^{abc} \to g f^{abc} , \quad T^a \to g T^a . \tag{1.36}$$

For now we refrain from performing this substitution and thus direct inspection reveals that algebra generators are, in general, dimensionful: $\Delta(f) = \Delta(T) = \Delta(g) = 2 - d/2$.

Equation (1.34) is justified if G is either one-dimensional Abelian or simple non-Abelian. In the general reductive case, we sum copies of Eq. (1.35), one for each algebra factor, each with its independent gauge boson fields A^a_μ and coupling g. This happens, e.g., for the Standard Model gauge group $\mathrm{SU}(3) \times \mathrm{SU}(2) \times \mathrm{U}(1)$.

---

[17] A and F are pure imaginary here, $(-i)$ being the (unique) generator of $G = \mathrm{U}(1)$.

[18] The $\mathcal{O}(\epsilon^3)$ terms in Eq. (1.32) (and its non-Abelian generalization) do not contribute up to $\mathcal{O}(\epsilon^6)$. To see this, recall that $U_{\partial\Sigma}$ is a matrix in the V representation of G. Then, order by order in ϵ, all the terms in the exponent in Eq. (1.32) are of the form $c^a T^a$ for some real c^a. In the first order expansion of the exponential they cancel with the contribution of the Hermitian conjugate.

[19] At least imposing parity or time-reversal invariance. Fixing an orientation of spacetime a topological θ-term can enter the action [148, 149].

[20] They are thus ruled out by renormalizability, but will play a role in the lattice theory.

Coupling to matter. We now want to couple Yang-Mills theory to Dirac fields. A theory of N free Dirac fermions $\{\psi^{\alpha,s}\}_{s=1}^{N}$, all with the same mass, has a global $\mathrm{U}(N)$ symmetry, with the fermions transforming in the defining representation, $V \in \mathrm{U}(N)$. Any continuous subgroups may be used to build a gauge theory. Let us consider the largest simple subgroup, $\mathrm{SU}(N)$. The minimal substitution in Eq. (1.25) provides

$$\mathcal{L} = -\frac{1}{4} F^a_{\mu\nu} F^{a\,\mu\nu} + \bar{\psi}(i\not{D} - m)\psi \ . \tag{1.37}$$

Expanding and isolating kinetic and interaction terms, $\mathcal{L} = \mathcal{L}_{\text{kin}} + \mathcal{L}_{\text{int}}$, yields

$$\mathcal{L}_{\text{kin}} = -\frac{1}{2}(\partial_\mu A^a_\nu - \partial_\nu A^a_\mu)\,\partial^\mu A^{a\,\nu} + \bar{\psi}_s(i\gamma^\mu \partial_\mu - m)\psi^s \tag{1.38}$$

$$\mathcal{L}_{\text{int}} = -i\bar{\psi}_r \gamma^\mu A^a_\mu (T^a)^r{}_s \psi^s + f^{abc}\partial_\mu A^a_\nu A^{b\,\mu} A^{c\,\nu} - \frac{1}{4} f^{abc} f^{ade} A^b_\mu A^c_\nu A^{d\,\mu} A^{e\,\nu} \ . \tag{1.39}$$

Noether theorem provides a particle number conserved current, associated with $\mathfrak{u}(1)$ transformations, as well as a conserved but not gauge invariant current for $\mathfrak{su}(N)$,

$$j^\mu_{\mathfrak{u}(1)} = \bar{\psi}_r \gamma^\mu \psi^r \ , \qquad j^{a\,\mu}_{\mathfrak{su}(N)} = i\bar{\psi}_r \gamma^\mu (T^a)^r{}_s \psi^s + f^{abc} A^b_\mu F^{c\,\mu\nu} \ . \tag{1.40}$$

The latter receives a contribution from the gluons, reflecting their self-interactions.

Some nomenclature: *electrodynamics* or *chromodynamics* with a single *electron* or *quark* flavor correspond to $N = 1$ and $N = 3$, respectively, in which case gauge bosons are called *photon* or *gluons*. Multiple flavours are accommodated introducing more than one Dirac multiplet, possibly having different masses. Multiple field species, transforming with different representations are also possible — in the $\mathrm{U}(1)$ case they correspond to different, *commensurate, charges*.

1.1C Constrained Hamiltonians

In the Hamiltonian formulation of a gauge theory, the canonical variables satisfy relations (*Gauss laws*) that constrain them to a submanifold of phase space[21]. Indeed, the solutions of the equations of motion of a gauge theory are not unique: they are determined only up to gauge transformations, implying that the Hessian

$$\frac{\delta^2 L}{\delta\dot{\varphi}^m\,\delta\dot{\varphi}^n} = \frac{\delta\pi_m}{\delta\dot{\varphi}^n} \ , \tag{1.41}$$

is not invertible[22] — which, on its turn, implies that neither is the Legendre transform. It is still possible to introduce an Hamiltonian which is well defined on this submanifold and

[21] Under some technical assumptions here omitted, see Ref. [143]

[22] Otherwise, Euler-Lagrange equations can be put in standard form and thus the existence and uniqueness theorems applies to their solutions.

freely extensible elsewhere [143, 151, 152]. The core ideas of the constrained Hamiltonian formalism [151, 152] are now sketched. We assume that all fields are Grassmann even, the extension to the Grassmann odd case is a matter of keeping track of the correct signs.

The initial ingredients are the Hamiltonian $H(\varphi,\pi)$ and some (*primary*) constraints

$$\kappa^{u_1}(\varphi,\pi)=0\ , \qquad u_1=1,\dots,U_1\ . \tag{1.42}$$

These can be enforced in the action principle using the method of Lagrange multipliers, introducing auxiliary variables (functions) $\lambda_{u_1}(t,\mathbf{x})$,

$$\delta S=\delta\int_{-\infty}^{+\infty}\mathrm{d}t\left[\dot\varphi^n\pi_n-H(\varphi,\pi)-\lambda_{u_1}\kappa^{u_1}(\varphi,\pi)\right]=0\ , \tag{1.43}$$

where the implicit integration over repeated indices has been extended con the constraints. Canonical and auxiliary variables are implicitly evaluated along a trajectory $t\to(\varphi,\pi,\lambda)(t)$, an abuse of notation that will be reiterated in the following. The time evolution along such trajectories is then

$$\dot F=\{F,H+\lambda_{u_1}\kappa^{u_1}\}\ . \tag{1.44}$$

Consistency algorithm. We now show that, in order for the primary constraints to be preserved by the time evolution, a new set of constraints as well as some restrictions on the Lagrange multipliers might have to be enforced. We have the initial value problem:

$$\kappa^{u_1}(\varphi,\pi)=0\ , \qquad \dot\kappa^{u_1}(\varphi,\pi)=\{\kappa^{u_1},H\}+\lambda_{u_1'}\{\kappa^{u_1},\kappa^{u_1'}\}=0\ . \tag{1.45}$$

Each of the right equations results either in a restriction on the auxiliary variables or, when the λ dependence cancels, in a (possibly new, *secondary*) constraint. The same equation is then imposed on the U_2 newly obtained constraints and so on, until no new independent condition is generated. In the end we are left with an enlarged set of constraints κ^u and a system of linear equations for the auxiliary variables $\{\lambda_{u_1}\}$. The former, here assumed to be all independent, identify the *constraint surface*

$$\Sigma=\{(\varphi,\pi)\ :\ \kappa^u(\varphi,\pi)=0\,,\ u=1,\dots,U=U_1+U_2+\dots\}\ ; \tag{1.46}$$

the latter reads ("$\approx$" denotes equality on Σ)

$$\{\kappa^u,H\}+\lambda_{u_1}\{\kappa^u,\kappa^{u_1}\}\approx 0 \qquad \forall\ u=1,\dots,U\ , \tag{1.47}$$

Plugging a solution $\lambda_{u_1}=A_{u_1}$ in the action principle provides a refined time evolution generated by

$$H'=H+A_{u_1}\kappa^{u_1} \tag{1.48}$$

which automatically preserves the constraints, all is left to do is to choose valid initial conditions $(\varphi,\pi)\in\Sigma$.

Gauge invariance. This refined time evolution has the noteworthy advantage of isolating and making manifest the eventual "ambiguity" in the dynamics of the system. Indeed A_{u_1} (and thus H') is only determined up to solutions $\{B^v{}_{u_1}\}_{v=1}^V$ of the homogeneous system associated with Eq. (1.47). Let $\eta^v = B^v{}_{u_1}\kappa^{u_1}$. For initial configurations $(\varphi,\pi) \in \Sigma$, the dynamics of the modified action principle in Eq. (1.43) is equivalent to that generated by the *total Hamiltonian*

$$H_T = H' + \lambda_v \eta^v \ . \tag{1.49}$$

where λ_v are completely arbitrary: two Hamiltonian flows that differ only by the choice of $\lambda_v = \lambda_v(t,\mathbf{x})$ are *gauge equivalent*. The relation between constraints and gauge invariance suggests that it might be difficult or impossible to completely remove the constraints by solving them explicitly. Nevertheless, not all constraints reflect a gauge freedom and while gauge symmetries imply the existence of constraints, the reverse is not true[23]. An $F(\varphi,\pi)$ such that $\{\kappa^u, F\} \not\approx 0$ for some u cannot generate a valid canonical transformation because this would violate the constraints. In Dirac's terminology [152] it is said to be *second-class*, as opposed to *first-class*[24]. Second-class constraints do not generate gauge transformations; they are just relations between the canonical variables which can be solved restricting phase space to their zero locus Σ^*, which inherits a symplectic structure from the original phase space. Conversely, *first-class* constraints can generate gauge transformations. They may still be converted to second-class ones by imposing gauge-fixing conditions, but this is not always convenient or even doable (due to Gribov obstructions [143, 153]).

Dirac bracket. The symplectic structure of Σ^* is given by a modified bracket $\{\,\cdot\,,\,\cdot\,\}^*$, called *Dirac bracket* [152]. Let $\{\chi^w\}_{w=1}^W$ be the second-class constraints,

$$\{F,G\}^* = \{F,G\} - \{F,\chi^w\}[\Omega^{-1}]_{ww'}\{\chi^{w'},G\} \ , \quad \Omega^{ww'} = \{\chi^w,\chi^{w'}\} \ . \tag{1.50}$$

It has all the properties of the Poisson bracket and reduces to it on first-class functionals but it vanishes if F or G are second-class constraints, so its restriction to $\Sigma^* = \{\chi^w(\varphi,\pi)=0\}$ is well defined [143].

Free Dirac fermions. As a first example of the above machinery, consider the Lagrangian in Eq. (1.6). The conjugate momenta to the matter fields ψ, $\psi^\dagger$ are

$$\pi = \frac{\partial\mathcal{L}}{\partial(\partial_0\psi)} = -i\psi^\dagger \ , \qquad \pi^\dagger = \frac{\partial\mathcal{L}}{\partial(\partial_0\psi^\dagger)} = 0 \ ; \tag{1.51}$$

[23] It may happen that Eq. (1.47) completely fixes the auxiliary variables.

[24] H', H_T and η^v are first-class by construction.

Recalling $\overline{\psi} = \psi^\dagger \gamma^0$ and $(\gamma^0)^2 = 1$ the Hamiltonian is[25]

$$H = \int \mathrm{d}\mathbf{x} \left[\dot{\psi}(-i\psi^\dagger) - \psi^\dagger \gamma^0 \left(i\gamma^\mu \partial_\mu - m \right) \psi \right] = \int \mathrm{d}\mathbf{x}\, \overline{\psi} \left(-i\gamma^i \partial_i + m \right) \psi \tag{1.52}$$

Equation Eq. (1.51) provides two primary second-class constraints,

$$\kappa^1 = \pi + i\psi^\dagger = 0 \ , \qquad \kappa^2 = \pi^\dagger = 0 \ ; \tag{1.53}$$

$$\{\kappa^1(\mathbf{x}), \kappa^2(\mathbf{y})\} = \{i\psi^\dagger(\mathbf{x}), \pi^\dagger(\mathbf{y})\} = -i\delta(\mathbf{x}-\mathbf{y}) \ . \tag{1.54}$$

The consistency algorithm just fixes the Lagrange multipliers. We thus have an example of a constrained but not gauge invariant theory; π and $\pi^\dagger$ can be safely eliminated solving $\kappa^{1,2}$ and introducing

$$\{\psi(\mathbf{x}), \psi^\dagger(\mathbf{y})\}^* = -i\delta(\mathbf{x}-\mathbf{y}) \ . \tag{1.55}$$

Pure Yang-Mills. We now turn to the pure Yang-Mills theory, described by Eq. (1.35). Due to the space-time splitting, in the Hamiltonian formalism it is convenient to parametrize the field strength by (chromo)electric and (chromo)magnetic fields (in $D > 1$):

$$F^a_{0i} = E^a_i \ , \quad F^a_{ij} = B^a_{ij} \ . \tag{1.56}$$

For the reminder of this Section, $(X^{ab\dots}_{ij\dots})^2$ represents $\sum_{i<j<\dots,\, ab\dots} (X^{ab\dots}_{ij\dots})^2$ and repeated spatial $i, j \dots$ indices are summed over independently from their upper or lower position.

The conjugate momenta of the gluons A^a_μ read

$$\Pi^{a\mu} = \frac{\partial \mathcal{L}}{\partial(\partial_0 A^a_\mu)} = -\frac{1}{2} F^{b\,\rho\sigma} \frac{\partial F^b_{\rho\sigma}}{\partial(\partial_0 A^a_\mu)} = -F^{a\,0\mu} = \delta^\mu_i E^a_i \ ; \tag{1.57}$$

providing a family of primary constraints

$$\kappa^{1a} = \Pi^{a0} \approx 0 \ . \tag{1.58}$$

Invertibility of the Legendre transform is lost because $\dot{A}^a_0$ is not specified by the canonical coordinates A^a_μ and $\Pi^{a\mu}$; but the Hamiltonian is still unambiguously defined on Σ:

$$H = \int \mathrm{d}\mathbf{x} \left[\dot{A}^a_\mu \Pi^{a\mu} - \mathcal{L} \right] = \int \mathrm{d}\mathbf{x} \left[\dot{A}^a_i E^a_i - \frac{(E^a_i)^2 - (B^a_{ij})^2}{2} \right] \ . \tag{1.59}$$

Integrating by parts (assuming appropriate behavior at spatial infinity) we have

$$\dot{A}^a_i E^a_i = \left[F^a_{0i} + \partial_i A^a_0 + f^{abc} A^b_0 A^c_i \right] E^a_i = (E^a_i)^2 - A^a_0 (D_i E^a_i) \ , \tag{1.60}$$

[25] Space dependence of the integrands is omitted when this does not creates confusion.

where in the last step the fact that E_i^a transforms in the group adjoint was used. Thus,

$$H = \int \mathrm{d}\mathbf{x} \left[\frac{1}{2}(E_i^a)^2 + \frac{1}{2}(B_{ij}^a)^2 - A_0^a (D_i E_i^a) \right] \ . \tag{1.61}$$

Consistency of $\kappa^{1a} \approx 0$ then implies[26]

$$\dot{\kappa}^{1a}(t,\mathbf{x}) = \{\Pi^{a0}(\mathbf{x}), H\}_t + \int \mathrm{d}\mathbf{y}\, \lambda_1^b(t,\mathbf{y})\, \{\Pi^{a0}(\mathbf{x}), \Pi^{b0}(\mathbf{y})\}_t = D_i E_i^a(t,\mathbf{x}) \approx 0 \ ; \tag{1.62}$$

thus giving *Gauss Law* as a secondary constraint:

$$\kappa^{2a} = \mathcal{G}^a = D_i E_i^a \approx 0 \ . \tag{1.63}$$

It can be shown that the consistency algorithm stops here, namely that no new independent conditions are obtained imposing $\dot{\kappa}^{2a} \approx 0$ [154, 155]. Moreover, the $\mathcal{G}^a$ satisfy the algebra

$$\{\mathcal{G}^a(\mathbf{x}), \mathcal{G}^b(\mathbf{y})\} = f^{abc}\, \mathcal{G}^c(\mathbf{x})\, \delta(\mathbf{x}-\mathbf{y}) \approx 0 \ . \tag{1.64}$$

Obviously we also have

$$\{\kappa^{1a}, \kappa^{2b}\} = \{\Pi^{a0}, D_i E_i^b\} = 0 \ , \tag{1.65}$$

therefore all constraints are first-class and the auxiliary functions λ_1^a are free. This has the immediate consequence that the solution $A_0^a(t,\mathbf{x})$ is an arbitrary function:

$$\dot{A}_0^a(t,\mathbf{x}) = \{A_0^a(\mathbf{x}), H\}_t + \int \mathrm{d}\mathbf{y}\, \lambda_1^b(t,\mathbf{y})\, \{A_0^a(\mathbf{x}), \Pi^{b0}(\mathbf{y})\}_t = \lambda_1^a(t,\mathbf{x}) \ . \tag{1.66}$$

We can use it to express λ_1^a. Summarizing all the above, the total Hamiltonian is

$$H_T = H + \int \mathrm{d}\mathbf{x}\, \lambda_1^a \kappa^{1a} = \int \mathrm{d}\mathbf{x} \left[\frac{1}{2}(E_i^a)^2 + \frac{1}{2}(B_{ij}^a)^2 - A_0^a\, (D_i E_i^a) + \dot{A}_0^a \Pi^{a0} \right] \ . \tag{1.67}$$

Hamiltonian flows that differ by the choice $A_0^a(t,\mathbf{x})$ are gauge equivalent and we can almost[27] read off the generator of gauge transformations from H_T. Calling $\theta^a(t,\mathbf{x})$ the A_0^a parametrizing the transformation,

$$\int \mathrm{d}\mathbf{x} \left[-\theta^a(t)\, (D_i E_i^a) + \dot{\theta}^a(t)\, \Pi^{a0} \right] = \int \mathrm{d}\mathbf{x} \left[(D_i \theta^a(t))\, E_i^a + \dot{\theta}^a(t)\, \Pi^{a0} \right] \ , \tag{1.68}$$

where we moved the covariant derivative as in Eq. (1.60).

[26] $\{\,\cdot\,,\,\cdot\,\}_t$ is the Poisson bracket evaluated along the solutions of the equations of motion, at time t.

[27] The generator given below is incomplete, it does not give the correct transformation laws of the arbitrary variables A_0^a. While it can be completed by a standard procedure [154] to $(D_\mu \theta)^a \Pi^{\mu a}$, we do not need this result because we will completely remove A_0^a by gauge-fixing.

Temporal gauge. For our purposes, it is convenient to work in the *temporal gauge* $A_0^a \approx 0$. Since

$$\{A_0^a(\mathbf{x}), \Pi^{b0}(\mathbf{y})\} = \delta^{ab}\delta(\mathbf{x}-\mathbf{y}) \ , \tag{1.69}$$

the gauge-fixing converts Π^{a0} and A_0^a into second-class constraints and, by Eq. (1.66), its consistency fixes λ_1^a:

$$\dot{A}_0^a(t,\mathbf{x}) = \lambda_1^a(t,\mathbf{x}) \approx 0 \quad \Rightarrow \quad \lambda_1^a = 0 \quad \Rightarrow \quad A_0^a(t,\mathbf{x}) = A_0^a(\mathbf{x}) \ . \tag{1.70}$$

Then the last term of the total Hamiltonian Eq. (1.67) is removed and the residual gauge transformations are time-independent; they are generated by the first-class $\mathcal{G}^a$:

$$-\int \mathrm{d}\mathbf{x}\, \theta^a \left(D_i E_i^a\right) = +\int \mathrm{d}\mathbf{x}\, \left(D_i\theta^a\right) E_i^a \ , \qquad \theta^a(t,\mathbf{x}) = \theta^a(\mathbf{x}) \ . \tag{1.71}$$

A direct computation reveals that Eq. (1.27) for A_i^a and the adjoint E_i^a transformation are recovered [131]

$$\delta_\theta A_i^a = D_i\theta^a \ , \qquad \delta_\theta E_i^a = f^{abc}\theta^b E_i^c \ . \tag{1.72}$$

Introducing $\{A_0^a, \Pi^{a0}\}^* = 0$ we can restrict phase space, removing A_0^a and Π^{a0}. All other fundamental Dirac brackets coincide with Poisson ones. Finally,

$$H(A_i^a, \partial_i A_j^a, \Pi^{ai}) = \int \mathrm{d}\mathbf{x}\, \frac{(E_i^a)^2 + (B_{ij}^a)^2}{2} = \int \mathrm{d}\mathbf{x}\, \frac{(\Pi^{ai})^2 + (\partial_i A_j^a - \partial_j A_i^a)^2}{2} \ . \tag{1.73}$$

Notice how the electric energy density is the sum of squares of the conjugate momenta to the "position" coordinates A_i^a, and may thus be interpreted as the algebra *Laplacian*[28].

Electrodynamics and Chromodynamics. The matter coupled Yang-Mills theory is obtained combining the two previous ones. Here we just state some results, working directly in the temporal gauge (see, e.g., Ref. [26]). The Hamiltonian is the sum of Eq. (1.52) (eventually generalized to many flavours) and Eq. (1.73), plus the potential accounting for the interaction between fermions and gauge fields:

$$\begin{aligned} H &= \int \mathrm{d}\mathbf{x}\, \left[\frac{1}{2}(E_i^a)^2 + \frac{1}{2}(B_{ij}^a)^2 + \overline{\psi}_r \left(-i\gamma^i\partial_i + m\right)\psi^r + i\overline{\psi}_r\gamma^i A_i^a (T^a)^r{}_s \psi^s\right] \\ &= \int \mathrm{d}\mathbf{x}\, \left[\frac{1}{2}(E_i^a)^2 + \frac{1}{2}(B_{ij}^a)^2 + \overline{\psi} \left(-i\gamma^i D_i + m\right)\psi\right] \ . \end{aligned} \tag{1.74}$$

Observe that, in temporal gauge, the minimal coupling of Eq. (1.25) (here involving space derivatives only) gives precisely the interaction term between gauge and matter fields.

[28] $E_i^a = \Pi^{ai}$ is associated with a differential operator through its Hamiltonian vector field, $\{\cdot, \Pi^{ai}\} = \delta/\delta A_i^a$.

As expected, matter fields give an additional contribution to Gauss law:

$$\mathcal{G}^a = D_i E^a_i - i\bar{\psi}_r \gamma^0 (T^a)^r{}_s \psi^s = \partial_i E^a_i - j^{a\,0} \approx 0 \; ; \tag{1.75}$$

where $j^{a\,0}$ is the Noether current in Eq. (1.40). Smeared with a time-independent parameter $\theta^a(\mathbf{x})$, $\mathcal{G}^a$ are still the generators of local gauge transformations. If θ^a are taken also space-independent, global transformations are recovered: integrating by parts,

$$-\int \mathrm{d}\mathbf{x}\, \theta^a \mathcal{G}^a(\mathbf{x}) = \int \mathrm{d}\mathbf{x}\, \theta^a j^{a\,0} = \theta^a Q^a \; . \tag{1.76}$$

1.2 Canonical quantization

Canonical quantization "maps" a classical Hamiltonian theory $H(\varphi, \pi)$ in a quantum one promoting the canonical fields φ^n, π_n and their functionals $F(\varphi, \pi)$ to field operators $\hat{\varphi}^n$, $\hat{\pi}_n$, $\hat{F}(\varphi, \pi) = F(\hat{\varphi}, \hat{\pi})$. Namely operator valued functions[29] of space acting on some Hilbert space $\mathscr{H}$. The field operators are constructed to obey [156]

$$[\hat{F}, \hat{G}]_\pm = i\, \widehat{\{F, G\}} \; , \qquad \hat{F}^\dagger = \widehat{(F^*)} \; ; \tag{1.77}$$

where the graded commutator $[\hat{F}, \hat{G}]_\pm$ is equal to $\hat{F}\hat{G} - \hat{G}\hat{F}$ unless F and G are both Grassmann odd, in which case the anticommutator $\hat{F}\hat{G} + \hat{G}\hat{F}$ is used [143]. By Eqs. (1.11) and (1.77), conjugate canonical field operators $\hat{\varphi}, \hat{\pi}$ obey the *canonical commutation* (or *anticommutation*) *relations*

$$[\hat{\varphi}^m(\mathbf{x}), \hat{\pi}_n(\mathbf{y})]_\pm = \mp i \delta^m{}_n \delta(\mathbf{x} - \mathbf{y})\, \hat{\mathbf{I}} \; . \tag{1.78}$$

By Eqs. (1.12) and (1.77), in the Heisenberg picture, time evolution is specified by

$$\frac{\mathrm{d}}{\mathrm{d}t} \hat{F} = i\, [\hat{H}, \hat{F}]_- \; . \tag{1.79}$$

Alternatively, working in the Schrödinger picture, field operators are time independent while the state $|\Psi(t)\rangle$ evolves according to the *Schrödinger equation*

$$i \frac{\mathrm{d}}{\mathrm{d}t} |\Psi(t)\rangle = \hat{H} |\Psi(t)\rangle \; . \tag{1.80}$$

Let us stress the obvious: formally, all the above applies unchanged to quantum mechanical (QM) systems, quantum many-body (QMB) systems with many (3 to countable infinity) d.o.f. or quantum field theories (QFT) in the continuum.

[29] Technically, distributions.

Ordering of operators. The given quantization prescription leaves some ambiguity [157]: $\varphi\pi = \pi\varphi$ classically, but not in the quantum theory, due to Eq. (1.78) — making the recipe $\hat{F}(\varphi,\pi) = F(\hat{\varphi},\hat{\pi})$ ambiguous, unless an ordering prescription for the operators is identified [158]; an example will be given in Section 3.2.

Quantum symmetries. We denote $\hat{\mathscr{U}}(\Lambda,a)$ and $\hat{\mathscr{V}}_x(g)$ the representatives of the Poincaré and internal groups on $\mathscr{H}$, respectively. Equations (1.2) and (1.3) become [137]:

$$\hat{\mathscr{U}}(\Lambda,a)\,\hat{\varphi}^m(x)\,\hat{\mathscr{U}}^\dagger(\Lambda,a) = \Omega(\Lambda^{-1})^m{}_n\,\hat{\varphi}^n(\Lambda^{-1}(x-a))\;, \tag{1.81a}$$

$$\hat{\mathscr{V}}(g)\,\hat{\varphi}^m(x)\,\hat{\mathscr{V}}^\dagger(g) = V(g)^m{}_n\,\hat{\varphi}^n(x)\;. \tag{1.81b}$$

If the internal symmetry group G is continuos, a representation of the symmetry algebra is now realized on $\mathscr{H}$ by the charge operators $\hat{Q}^a$ and the commutator[30],

$$[\hat{Q}^a,\hat{Q}^b]_- = if^{abc}\hat{Q}^c\;, \qquad \delta_\theta\hat{F} = i\theta^a[\hat{Q}^a,\hat{F}]_- \quad \text{or} \quad \delta_\theta|\Psi\rangle = i\theta^a\hat{Q}^a|\Psi\rangle\;. \tag{1.82}$$

Moreover, the conservation of the charges $\hat{Q}^a$ reads $[H,Q]_- = 0$.

1.2A Quantization of gauge theories

The constraints that appear in Hamiltonian of gauge theories require particular care during quantization and the prescription given above has to be integrated with further conditions. In the phase space of the classical theory, only configurations obeying the constraints are physical. A similar condition holds for the Hilbert space of the quantum theory. However, it is important to distinguish between first-class and second-class constraints.

In Section 1.1C second-class constraints have been solved: they correspond to null operators in the quantum theory obtained using the Dirac bracket in Eq. (1.77) [143]. First-class constraints have been recognized as generators of gauge transformations. A possibility is to fix the gauge and convert them to second-class constraints. This is the approach adopted in Section 3.3 to remove the gauge redundancy of one-dimensional lattice electrodynamics. However, solving Gauss laws at the operator level always results in a non-local operator algebra [159], it is thus often convenient not to impose their vanishing in the operatorial sense [26]. Still, physics is expected to be invariant under gauge transformation. Therefore, we impose the (weaker) condition [143, 152] that only the gauge-invariant states annihilated by first-class constraints are physical and identify the *physical subspace*:

$$\mathscr{H}_{\text{phys}} = \{|\Psi_{\text{phys}}\rangle : \hat{\mathcal{G}}|\Psi_{\text{phys}}\rangle = 0\} \subset \mathscr{H}\;, \tag{1.83}$$

where $\hat{\mathcal{G}}$ denotes symbolically the set of all first-class constraint operators. A third way of dealing with Gauss law is discussed in Section 1.4D.

[30] Here we assume that all the charges are bosonic, i.e. Grassmann even at the classical level.

An attempt at the quantization of the photon. Even in the simplest scenario, the quantization of pure electromagnetism, the prescription just presented encounters a difficulty. This emerges when we try to impose the physical condition on the states

$$\hat{\mathcal{G}}|\Psi_{\text{phys}}\rangle = \partial_i \hat{\Pi}^i |\Psi_{\text{phys}}\rangle = 0 \ . \tag{1.84}$$

Then,

$$\langle\Psi_{\text{phys}}| \left[\hat{O}, \partial_j \hat{\Pi}^j\right] |\Psi_{\text{phys}}\rangle = 0 \qquad \forall\, \hat{O} \tag{1.85}$$

a result that clashes with the canonical commutation relations [160], giving

$$\langle\Psi_{\text{phys}}| \left[\hat{A}_i^a(\mathbf{x}), \partial_j \hat{\Pi}^j(\mathbf{y})\right] |\Psi_{\text{phys}}\rangle = -i\frac{\partial}{\partial x^i}\delta(\mathbf{x}-\mathbf{y})\langle\Psi_{\text{phys}}|\Psi_{\text{phys}}\rangle \ . \tag{1.86}$$

It has been suggested [161] to circumvent the problem assuming that the states satisfying Gauss law are not normalizable. Yet, among these states there must be the vacuum $|\Omega\rangle$. As pointed out in Ref. [26], an unormalizable vacuum may lead to inconsistencies from the perspective of a rigorous non-perturbative quantization. We do not discuss this problem any further because it is beyond the scope of this Thesis and, interestingly, will disappear when we formulate the theory on the lattice.

From now on, we typically write O in place of $\hat{O}$ and drop the $\pm$ in the graded commutator.

1.3 Lattice as a regulator

Applying the canonical quantization prescription to a classical Hamiltonian is not enough to completely define a QFT. The theory obtained in this way produces divergent results that must be cured by also specifying a *regularization* prescription. A possible strategy is to start from a theory with a finite number of d.o.f. defined on a lattice, a discrete and finite space(time), and then *define* the QFT as the *continuum* and *thermodynamic limits* of this finite theory — this is the paradigm of lattice QFT. The lattice provides both an ultraviolet (UV) cutoff, due to the finite spacing between lattice points, and an infrared (IR) cutoff, because of the finite extent of the lattice. The continuum and thermodynamic limits consist in sending the lattice spacing to zero and its volume to infinity. In doing so, a *renormalization* procedure is necessary to ensure that physical quantities remain finite in the limits. For a renormalizable theory this amounts to letting the model's parameters, also called *bare parameters*, run — i.e. acquire a cutoff dependence [162]. In the following we will use the expression continuum limit to refer to both the above limits, however, the two do not always commute [44, 163].

There are many technical and conceptual reasons to study lattice QFT [44]. The lattice regularization is genuinely *non-perturbative* [44]. Additionally, prior to taking the continuum limit, the theory is really a *many-body quantum mechanical system.* Avoiding the problem of dealing directly with an infinite number of d.o.f. has important advantages: far-reaching

statements can be made quite rigorous and the finiteness of the problem makes it accessible to numerical simulation on the computer. Clearly, some difficulties are just postponed to the delicate task of taking the continuum limit. Whether the exact results mentioned above continue to hold in this limit is generally not clear for interacting theories and positive answers are often based on circumstantial evidence [44]. The continuum limit can not be performed numerically (a computer always has finite resources) and ad hoc techniques have been developed for its extrapolation, most notably *finite-size scaling* analysis [164, 165] and the *Lüscher formalism* [166, 167].

Depending on personal taste, the lack of a rigorous continuum limit might not be perceived as too severe. Without dwelling too much on topics that go beyond the scope of this Thesis and partially pertain to philosophy of science [168], if the universe is assumed to be finite and quantum gravity appears at some ultraviolet scale, any theory on flat Minkowski spacetime is to be considered an effective field theory, only relevant over a finite distance and up to a finite energy. Consequently, a finite and discrete theory might actually even be a better approximation of nature than its continuum counterpart [44].

Hamiltonian approach. Lattice theories are most commonly quantized in Euclidean[31] spacetime using the *path-integral* formalism and numerically simulated via *Monte Carlo* — a formula which has yielded unparalleled insights on the phenomenology of quantum chromodynamics [41], but still suffers from numerical sign problems in physically relevant scenarios[32]. Here we take a different but promising path [112, 169]: canonical quantization and tensor network simulation (see Chapter 2). Importantly, the latter is *immune to sign problems* [56], Wick rotation is superfluous, and *real-time* dynamical simulation is possible. Because Hamiltonian fields are functions of space, not spacetime, it is only $\mathbb{R}^D$ space that has to be truncated and discretized while time is kept in continuous[33] [170]. This selects a privileged time direction, thus spoiling manifest Lorentz boost invariance, which was nevertheless already broken by the lattice. On the other hand, the Hamiltonian approach is particularly well suited to compute ground states, properties of bound states, and phase diagrams, which are sometimes hard to extract from the path-integral formulation [170]. Finally, the canonical formulation is also the "natural" one for quantum simulation [55].

Lattice and reciprocal lattice. We consider cubic lattices with spacing a and linear size $L = Na$,

$$\Lambda := a\{1, 2, \dots, N\}^D \; ; \tag{1.87}$$

Analytic derivations are often carried out in *periodic boundary conditions*, $\Lambda \cong a(\mathbb{Z}_N)^D$. Continuous spacetime symmetries cannot be implemented on the lattice but are recovered

[31] Wick rotation [45] to imaginary time is used to cure the oscillating phase of the path-integral measure, $\mathcal{D}\varphi e^{iS(\varphi)}$, and ensure convergence [44].

[32] See the discussion in the Introduction of this Thesis and the references therein.

[33] In numerical simulations time is often discretized anyway but this is not in the definition of the theory.

in the continuum limit [36]: space rotations are broken down to the finite rotation group of the D-hypercube, while only translations by multiples of the lattice step a are available (for periodic boundaries), their group being Λ itself. There are still conserved charges associated with these symmetries, such as momentum, but they take discrete values [44].

The lattice UV and IR regulators are a and $1/L$, respectively. Morally[34], the continuum theory is defined removing them ($a, 1/L \to 0$) after a renormalization procedure. The role of a and L as cutoffs is even clearer in momentum space, where (discrete) Fourier transforms of spatial functions are defined. Assuming even N for ease of notation, the reciprocal lattice is [171]

$$\Lambda^* := \frac{2\pi}{L}\left\{-\frac{N}{2}, -\frac{N}{2}+1, \dots, \frac{N}{2}-1\right\}^D \simeq \frac{2\pi}{L}(\mathbb{Z}_N)^D \ . \tag{1.88}$$

Accordingly, the frequency spectrum of a function defined on Λ cannot contain modes of wavelength shorter than a or longer than L. Λ^* is the discrete subset of the Brillouin zone of solid state physics on which Fourier transforms of L-periodic functions are supported. For $L \to \infty$ the full Brillouin zone $\mathbb{T}^D \simeq [-\pi/a, +\pi/a[^D$ is recovered [172].

Discretization prescritpion. Loosely speaking, limiting procedures ($\epsilon \to 0$) appearing in analytic operations (e.g., Riemann integration and differentiation) have to be reverted on the lattice and incorporated in the continuum limit (setting $\epsilon \sim a$). The above recipe is not uniquely determined but different implementations must yield the same $a \to 0$ limit. Yet, some choices may display better continuum-limit convergence than others, thus allowing to work with smaller lattices, reducing the computational cost of numerical simulations. The precise quantification of discretization errors is the content of Symanzik's improvement program [173–176]. Improved actions have become a standard tool in Euclidean lattice QFT and have significantly contributed to its success [41]. Although the program is now making its way also into Hamiltonian simulation [177–180], here we adopt the simplest choice and replace integrals and derivatives by Riemann sums and central derivatives:

$$\begin{aligned} \int \mathrm{d}^D x\, \phi(x) \ &\to\ a^D \sum_{x\in\Lambda} \phi_x \ , \qquad \partial_j \phi(x) \ \to\ \frac{1}{2a}[\phi_{x+a\hat{j}} - \phi_{x-a\hat{j}}] \ , \\ \delta(x-y) \ &\to\ a^{-D}\delta_{xy} \ , \qquad \frac{\delta}{\delta\varphi(x)} \ \to\ a^{-D}\frac{\partial}{\partial\varphi_x} \ . \end{aligned} \tag{1.89}$$

Analogous substitutions apply in momentum space with Λ, x, a replaced by $\Lambda^*, k, 2\pi/L$.

Lattice units. In lattice field theory, the spacing a provides a convenient length scale. All bare parameters and operators can be made dimensionless rescaling them by appropriate powers of a, dictated by their classical scaling dimension Δ (see Footnote 4):

$$Z = a^{-\Delta(Z)} Z_{\text{latt}} \ . \tag{1.90}$$

[34] Apart from commutativity issues, L and a are dimensionful parameters (more on this below).

In Chapters 3 and 4, where *lattice units* are consistently adopted, we will omit the "latt" subscript and Eq. (1.90) practically amounts to setting $a = 1$ in all expressions. Lattice units are particularly convenient for numerical simulations because only dimensionless numbers can be stored in a computer.

Continuum limit. Let ξ be a physical length scale of the theory — e.g., the inverse of a physical mass M (Hamiltonian gap). The continuum limit reads $L/\xi \to \infty$, $a/\xi \to 0$, i.e., the lattice size (spacing) becomes much larger (smaller) than any physical length scale. In lattice units, the limit reads $N, \xi_{\text{latt}} \to \infty$, corresponding to a *second-order phase transition* of the lattice model [181, 182]. Of course, this does not imply that the continuum theory is critical, namely that correlation lengths diverge and physical masses vanish. Rather, in order for the physical length ξ to stay finite its value measured in lattice units $\xi_{\text{latt}} = \xi/a$ has to diverge when the spacing shrinks. In this sense, the perspective is different from the one of solid state physics, where the crystal is real and the physical correlation length diverges [181]. Nevertheless, in order to locate (an prove the existence of) the continuum limit of a lattice model, a critical point of the model has to be identified. In lattice units, the spacing is hidden in the rescaled lattice bare parameters. A first clue on the continuum limit location is obtained keeping the dimensionful bare parameters Z fixed and scaling Z_{latt} according to Eq. (1.90). This classical approximation, however, ignores the running of the bare parameters due to quantum effects[35] (renormalization). A more refined approach is to let the parameters flow along *lines of constant physics* [44].

1.4 Kogut-Susskind Hamiltonian

The plan for this Section is to reformulate continuum Yang-Mills theories on the lattice and, afterwards, quantize them. Some peculiarities emerge for both matter (fermion doubling) and gauge fields (compact formulation). In dealing with them, we will reproduce a lattice Hamiltonian originally proposed in 1975 by Kogut and Susskind [184–186], which has become the starting point for many Hamiltonian studies of Abelian and non-Abelian relativistic gauge theories.

1.4A Matter Fields

The discretization of fermionic fields requires particular care. The most striking consequence of a naïve discretization is the *doubling problem* [172, 187]: a proliferation of propagating degrees of freedom on the lattice. A possible solution are *staggered fermions* [184–186], introduced below and adopted throughout the remainder of the Thesis.

[35] For instance, in (1+3)D QCD the coupling g is dimensionless but asymptotic freedom [119, 120] means that the continuum limit is at $g \to 0$ (negative beta function) [183].

Doubling problem. Momentarily resorting to the path-integral formulation on an infinite spacetime $a\mathbb{Z}^d$ and applying the spacetime equivalent of the discretization prescription from the previous Section to the action of free Dirac fermions in Eq. (1.6) gives

$$S = \int \mathrm{d}x\, \bar{\psi} \left[i\not{\partial} - m \right] \psi \;\to\; a^{2d} \sum_{xy} \bar{\psi}_x \Gamma^x{}_y \psi^y \;, \qquad \Gamma^x{}_y = i\not{\partial}^x{}_y - \frac{m}{a^d} \delta^x{}_y \;. \tag{1.91}$$

Here spinor indices are left implicit and

$$(\partial_\mu)^x{}_y := \frac{1}{2a^{1+d}} \left[\delta^{x+a\hat{\mu}}{}_y - \delta^{x-a\hat{\mu}}{}_y \right] \tag{1.92}$$

is the central derivative. In momentum space,

$$a^{2d} \sum_{xy} e^{-i(px+qy)} (\partial_\mu)^x{}_y = \frac{e^{-iap_\mu} - e^{+iap_\mu}}{2a}\, a^d \sum_x e^{-i(p+q)x} = \frac{-i \sin(ap_\mu)}{a} (2\pi)^d \delta(ap + aq) \;.$$

Therefore

$$\Gamma(k) = \gamma^\mu \frac{1}{a} \sin(ak_\mu) - m \;; \tag{1.93}$$

and the propagator reads

$$\Gamma^{-1}(k) = \frac{\gamma^\mu \tilde{k}_\mu + m}{\tilde{k}^2 - m^2} \;, \qquad \tilde{k}_\mu = \frac{1}{a} \sin(ak_\mu) \;. \tag{1.94}$$

Its denominator is invariant under $k_\mu \to k_\mu + \Delta_\mu$ with $\Delta_\mu \in \{0, \pi/a\}^d$. Hence, our lattice version of a continuum theory with one fermion has a propagator with 2^d poles and just as many propagating fermion species. Even if an initial state composed by excitations in a single Dirac cone only is prepared, as soon as some interaction is included the additional fermions can be produced just as easily as the original ones [188]. The problem clearly does not fade away in the continuum limit $a \to 0$, nor it is a peculiarity of our discretization prescription, but rather a consequence of the first derivative nature of fermionic actions (there is no doubling problem for bosons). The doubling is symptomatic of a general result, the Nielsen-Ninomiya no-go theorem [188–192], which forbids chiral lattice fermions (absence of axial anomaly [193–195] on the lattice [196, 197]). Note that, if only space is discretized, the doublers are 2^D.

Staggered fermions. We turn to one of the possible (partial) solution of the doubling problem: staggered fermions. The staggered formulation stems from a procedure of spin-diagonalization [172, 187] of the action: at each lattice site, a unitary transformation of the spinor allows to put the action in a diagonal and degenerate form with respect to the $2^{d/2}$ spinor components (even d is assumed here). Finally, the contribution of only one component is kept. In this way some doublers are removed, however $2^{d/2} - 1$ of them persist. In 1+1 dimensions, with only space discretized, the "staggerization" completely

removes the doublers. For Dirac Hamiltonian in Eq. (1.52) one gets [184–186]:

$$H = a^D \sum_{x,i} \frac{i}{2a} \psi_x^\dagger \, \psi_{x+a\hat{\imath}} + \text{H.c.} + a^D \sum_x (-1)^{\|x/a\|_1} \, m \, \psi_x^\dagger \psi_x \,, \tag{1.95}$$

where $\|\cdot\|_1$ is the 1-norm and the staggered fermion ψ_x is a complex Grassmann number corresponding to a single component of the original Dirac spinor on each lattice site[36]. Equation (1.55) implies

$$\{\psi_y, \psi_z^\dagger\}^* = -i a^{-D} \delta_{yz} \ . \tag{1.96}$$

Equations (1.95) and (1.96) define the the Kogut-Susskind discretization of a mass m free relativistic Dirac field. The generalization to a multiplet is straightforward: the Hamiltonian is just a sum of Eq. (1.95) type terms and different field components anticommute.

Quantization and Jordan-Wigner representation. We may now take ψ_x and $\psi_x^\dagger$ to be quantum operators. Canonical quantization applies straightforwardly and results in the canonical anticommutation relations

$$[\psi_y, \psi_z^\dagger] = a^{-D} \delta_{yz} \ , \qquad [\psi_y, \psi_z] = 0 \ , \qquad [\psi_y^\dagger, \psi_z^\dagger] = 0 \ . \tag{1.97}$$

To find an irreducible representation of this algebra observe that, on a given site,

$$[a^D \psi_x^\dagger \psi_x, \psi_x^\dagger] = \psi_x^\dagger \ , \qquad (\psi_x)^2 = 0 \ , \qquad (a^D \psi_x^\dagger \psi_x)^2 = a^D \psi_x^\dagger \psi_x \ . \tag{1.98}$$

The first identifies $\psi_x^\dagger$ as a raising operator for the non-negative definite *occupation number* operator $N_x = a^D \psi_x^\dagger \psi_x$; the others show that there are two occupation levels: $|0\rangle$ and $|1\rangle$. Hence $\mathscr{H}_{\text{site}} \cong \mathbb{C}^2$ and, for a one-site lattice, in the $\{|1\rangle, |0\rangle\}$ basis, a representation of Eq. (1.97) is in terms of spin-1/2 raising and lowering matrices: $a^{D/2} \psi_x = \sigma^-$. Extending to multiple sites, anticommutation between fermionic operators acting on different sites can be achieved, e.g., adopting the *Jordan-Wigner* representation [198]

$$a^{D/2} \psi_x = \Big[\bigotimes_{y<x} (-1)^N \Big] \otimes \sigma^- \otimes \Big[\bigotimes_{z>x} \mathbf{I} \Big] \,, \tag{1.99}$$

where an ordering relation among lattice sites x has been introduced. For a multiplet $\psi_{x,r}$, the internal index r is involved as well. Notice that, in the 1D version of the (quantized) staggered fermion Hamiltonian, the $(-1)^N$ strings cancel out for open boundary conditions. For periodic boundaries, observing that $\sigma^+ = -(-1)^N \sigma^+$ we have [199]

$$a^D \psi_L^\dagger \psi_1 = (-1)^{\sum_{x<L} N_x} \sigma_L^+ \sigma_1^- = -(-1)^{\sum_x N_x} \sigma_L^+ \sigma_1^- \ . \tag{1.100}$$

Kronecker products with local identities are here left implicit, and so will be from now on.

[36] In 1D, the upper and lower component on even and odd lattice sites respectively.

Symmetries. As its continuum counterpart, the staggered fermion Hamiltonian has a global U(1) symmetry for $\psi_x \to e^{i\theta}\psi_x$, generated by the particle number charge $Q = a\sum_x N_x$ (up to ordering issues). For the general case of a multiplet, in the notations of Section 1.1,

$$Q^a = a^D \sum_x \rho^a_x \,, \qquad \rho^a_x = i \sum_{rs} \psi^\dagger_{xr} T^a_{rs} \psi_{xs} \,. \tag{1.101}$$

The charge densities ρ^a_x obeys a continuity equation in the lattice sense [131]. In the thermodynamic limit or for periodic boundaries the theory is also translation invariant. Due to the staggered sign in front of the mass term, however, valid translations $x \to x + \Delta x$ are only those for which $\|\Delta x\|_1$ is an even multiple of the lattice spacing a.

1.4B Gauge fields

Lattice gauge theories (LGT) originate, analogously to the continuum case, imposing the invariance under internal group transformations specified independently at each lattice site. In principle there could also be a time dependence but temporal gauge is here assumed. The same geometric picture presented in the continuum applies. To compare fields at different lattice sites, gauge d.o.f. are introduced. However, since sites are finitely separated, we have to compensate finite rather than infinitesimal transformations. The (algebra valued) connection is thus replaced with (compact, group valued) *comparators* $U_{xi} \equiv U(x, x + a\hat{i})$: matrices in the V representation. This is the so called *compact* formulation of LGT [44]. Comparators can be thought of as a parallel transport along a straight path connecting neighbouring sites, they naturally live on oriented lattice links and transform as

$$U(x, x + a\hat{i}) \mapsto V(g(x))\, U(x, x + a\hat{i})\, V^\dagger(g(x + a\hat{i})) \tag{1.102}$$

(notations and assumptions of Section 1.1B). When G is a Lie group, we make contact with the continuum associating to each link a connection A^a_{xi}, such that:

$$U_{xi} = e^{aA^a_{xi}T^a} \;; \tag{1.103}$$

however, the fundamental d.o.f. is now U_{xi}. Comparators are periodic in A^a_{xi}, which are thus now "angular" variables (they become again "flat" directions in the $a \to 0$ limit) [35]. In analogy to the continuum, their conjugate angular momenta, generating group rotations, may then be identified with the electric fields. For non-Abelian groups, however, we must distinguish between left and right group actions [132, 200]. Indeed, if we naïvely apply our discretization prescription and insist on defining E^a_{xi} via

$$\{A^a_{xi}, E^b_{yj}\} = a^{-D}\delta_{xy}\delta_{ij}\delta^{ab} \quad \Leftrightarrow \quad \{\,\cdot\,, E^b_{yj}\} = a^{-D}\frac{\partial}{\partial A^b_{yj}} \;; \tag{1.104}$$

we run into the problem that, on a given link (x,i), left implicit, the fundamental bracket

$$a^D\{U,E^b\} = \frac{\partial \exp(aA^aT^a)}{\partial A^b} \tag{1.105}$$

does not have a closed form in the non-Abelian case. We instead define,

$$a^D\{U_{yj},L^b_{yj}\} = aT^bU_{yj}\ , \qquad a^D\{U_{yj},R^b_{(y+j)j}\} = -aU_{yj}T^b\ . \tag{1.106}$$

We stress that L^b_{yj} and $R^b_{(y+j)j}$ are associated to the left and right end of the same link: $(y,y+j)$. Brackets between variables associated with different links always vanish. The labeling convention for $R^b_{(y+j)j}$ is convenient because, by Eq. (1.102), right rotations of the comparator are associated to gauge transformations at $y+j$. Plugging the small-a expansion of the comparator $U_{xi}\approx 1+aA^a_{xi}T^a$ in the above we find [131],

$$E^b_{yj} = L^b_{yj} + \mathcal{O}(a) = -R^b_{(y+j)j} + \mathcal{O}(a)\ . \tag{1.107}$$

Obviously, the equalities are exact in the Abelian case. Generators of group rotations realize the symmetry algebra: from their definition, by Jacobi identity, on a given link [131, 132]

$$a^D\{L^a,L^b\} = af^{abc}L^c\ , \qquad a^D\{R^a,R^b\} = af^{abc}R^c\ , \qquad a^D\{L^a,R^b\} = 0\ . \tag{1.108}$$

Their sum of squares is the Laplacian in group space, namely quadratic *Casimir* [145],

$$\mathcal{C}_2 = \sum\nolimits_a (L^a)^2 = \sum\nolimits_a (R^a)^2\ ; \tag{1.109}$$

which commutes with all the generators [76]: $\{\mathcal{C}_2,L^b\} = \{\mathcal{C}_2,R^b\} = 0$. For finite groups there are no generators of infinitesimal transformations but a (non-unique) appropriate discretization of the Laplacian can be still identified [144].

Pure lattice Yang-Mills Hamiltonian. With the ingredients introduced above we can map continuum Yang-Mills theories to their lattice counterpart. Without matter, gauge invariants are Casimirs, built out of L^a_{xi} or R^a_{xi}, and Wilson loops, obtained concatenating comparators along any closed lattice path. These are all valid Hamiltonian terms [145]. In order to reproduce the continuum theory, we restrict to those arising from the discretization prescription applied to the continuum pure Yang-Mills Hamiltonian in Eq. (1.73), namely

$$H = \int \mathrm{d}\mathbf{x}\ \left[\frac{1}{2}\sum_{i,a}(E^a_i)^2 + \frac{1}{2}\sum_{i<j,a}(B^a_{ij})^2\right]\ . \tag{1.110}$$

Recalling Eq. (1.35) and the discussion that precedes, up to an constant,

$$\sum_a (B^a_{ij})^2 = \sum_a (F^a_{ij})^2 = -\lim_{\epsilon\to 0}\frac{1}{g^2\epsilon^4}\,\mathrm{Re}\,W_{ij}(\epsilon)\ ; \tag{1.111}$$

reverting the limit ($\epsilon = a$), this becomes a *plaquette* term:

$$\mathrm{Re}\, W_{ij}(x;a) = \frac{1}{2}\,\mathrm{tr}\, P_{x;ij} = \frac{1}{2}\,\mathrm{tr}\left(U_{x,j}\, U_{x+a\hat{j},i}\, U^\dagger_{x+a\hat{i},j}\, U^\dagger_{x,i}\right) + \text{H.c.}\ . \tag{1.112}$$

At finite spacing, plaquettes introduces infinite additional tree-level terms that start from next-to-leading order in a and correspond to non-renormalizable or, in Wilson's language, irrelevant, self-interactions of the gauge boson [44]. The electric energy density was already identified with

$$\frac{1}{2}\mathcal{C}_2 = -\frac{1}{4g^2}\,\mathrm{tr}\, L^2_{xi}\ , \qquad L_{xi} = L^a_{xi} T^a\ . \tag{1.113}$$

Thus [184, 200],

$$H = -\frac{a^D}{4g^2}\sum_x \mathrm{tr}\left[\sum_i L^2_{xi} + \frac{1}{a^4}\sum_{i<j} P_{x;ij}\right]\ . \tag{1.114}$$

Coupling to matter. We now couple the gauge theory to a multiplet of staggered fermion matter fields transforming in the representation V. Representation indices are left implicit. The lattice minimal coupling consists in the insertion of a comparator in the hopping term of the staggered fermion Hamiltonian (1.95):

$$\psi^\dagger_x\, \psi_{x+a\hat{i}} \ \to\ \psi^\dagger_x\, U_{xi}\, \psi_{x+a\hat{i}}\ . \tag{1.115}$$

This substitution makes the hopping term gauge invariant by construction and reproduces the covariant derivative term of the continuum Hamiltonian in Eq. (1.74). Indeed,

$$a^D \sum_{x,i} \frac{i}{2a}\psi^\dagger_x\, U_{xi}\, \psi_{x+a\hat{i}} + \text{H.c.} = i a^D \sum_{x,i} \psi_x \frac{U(x, x+a\hat{i})\, \psi_{x+a\hat{i}} - U(x, x-a\hat{i})\, \psi_{x-a\hat{i}}}{2a}\ . \tag{1.116}$$

Comparing with Eq. (1.21), the finite difference is recognized as a central covariant derivative. In the temporal gauge, the minimal substitution does not interfere with the staggering procedure and thus the correct (classical) continuum limit is obtained.

Kogut-Susskind Hamiltonian Combining the pure lattice Yang-Mills and the minimally coupled free staggered Hamiltonians, the *Kogut-Susskind* Hamiltonian is obtained [184–186]. We now report it, for later convenience, implementing a few useful rescalings. Firstly, we canonically normalize algebra generators via Eq. (1.36), that is $f^{abc} \to g f^{abc}$, $T^a \to g T^a$. This, however leads to coupling dependence of the brackets in Eqs. (1.106) and (1.108). We reabsorb it in the chromoelectric fields: $E^a_{xi} \to g E^a_{xi}$, and the analogous for L^a_{xi} and R^a_{xi}. Finally, having already checked that (at the classical level) the continuum limit is correctly reproduced, we switch to lattice units. Dimensional analysis shows that the dimensionless couplings and operators are introduced via:

$$am \to m\ , \quad a^{(3-D)/2} g \to g\ , \quad aH \to H\ , \quad a^{D/2}\psi \to \psi\ , \quad a^{D-1} E \to E\ . \tag{1.117}$$

Leaving representation indices implicit, as usual, the Kogut-Susskind lattice discretization of the temporal-gauge Yang-Mills Hamiltonian reads $H = \sum_x h_x$, with

$$h_x = \sum_i \left[\frac{i}{2} \psi_x^\dagger U_{xi} \psi_{x+\hat{\imath}} + \text{H.c.} \right] + (-1)^{\|x\|_1} m \psi_x^\dagger \psi_x - \frac{1}{4} \operatorname{tr} \left[g^2 \sum_i L_{xi}^2 + \frac{1}{g^2} \sum_{i<j} P_{x;ij} \right] . \quad (1.118)$$

It involves a staggered fermion matter field multiplets, $\psi_{x,r}$ and $\psi_{x,r}^\dagger$, sitting on lattice sites; as well as gauge comparators $U_{xi,rs}$ and chromoelectric fields $g L_{xi}^a$, living on lattice links. The rescalings in Eq. (1.117) show that, at tree-level, the dimensionless m and g parameters flow towards zero in the continuum limit when[37] $D < 3$, while the ratio g^2/m^{3-D} is fixed and can be used to quantify the strength of the interaction [201]. Finally, note that in $D=1$ there is no magnetic field and, correspondingly, no plaquette term.

We now quantize the theory: we construct the gauge link operator algebra in two dual bases (magnetic and electric), show that it is infinite dimensional, and discuss truncation approaches. Finally, we define the physical Hilbert space of the model and present a general strategy for enforcing the lattice version of the Gauss Law constraint.

Link Hilbert space. As shown by Eq. (1.27), connection components are representation independent (in technical jargon, A_μ^a is Lie algebra valued). Similarly, the configuration of a gauge link cannot depend on the representation V: in the end, we must be able to parallel transport fields in arbitrary representations. Therefore, the classical link configurations are in one-to-one correspondence with the group elements $g \in G$. At the quantum level, the link Hilbert space is spanned by (improper) "position" eigenstates $|g\rangle$, $\langle g|h\rangle = \delta(g-h)$ [133, 188]. Accordingly, $\mathscr{H}_{\text{link}}$ is the group algebra $\mathbb{C}[G]$ for a finite group, or the space of square-integrable functions on G, $L^2(G)$, for a continuous group [144].

Gauge algebra. By its very definition, the matrix elements of the comparator operator do depend on the representation V. Compatibility with Eq. (1.102) mandates [133],

$$U|g\rangle = V(g)|g\rangle \, . \quad (1.119)$$

Notice that, since V is unitary, so is U: $U^\dagger U = U U^\dagger = \mathbf{I}$, provided Hermitian conjugation also acts on the representation indices. For a faithful representation V, the comparator U may be regarded as the "position" operator on $L^2(G)$. Its conjugate "angular momenta", generating left and right rotations, read [133]

$$L^b = -i \frac{\mathrm{d} \mathscr{L}(e^{\epsilon \tau^b})}{\mathrm{d}\epsilon} \bigg|_{\epsilon=0} , \qquad R^b = -i \frac{\mathrm{d} \mathscr{R}(e^{\epsilon \tau^b})}{\mathrm{d}\epsilon} \bigg|_{\epsilon=0} ; \quad (1.120)$$

[37] Including quantum corrections, for non-Abelian theories this is true also in $D = 3$. See Footnote 35.

where $\tau^a \in \mathfrak{g}$ is a group generator and $\mathscr{L}$ and $\mathscr{R}$ are finite rotation operators

$$\mathscr{L}(h)|g\rangle = |hg\rangle \ , \qquad \mathscr{R}(h)|g\rangle = |gh^{-1}\rangle \ . \tag{1.121}$$

Acting on a test wavefunction $\Psi(g)$ shows that these obey the fundamental commutators,

$$[U, L^b] = iT^b U \ , \qquad [U, R^b] = -iUT^b \ , \tag{1.122}$$

provided by canonical quantization of Eq. (1.106). The same applies to the gauge algebra. Gauge operators on different links commute, thus the representation extends trivially to the whole lattice.

Gauge invariance, Gauss law & physical Hilbert space. The total Hilbert space of the model is the tensor product of all the matter site and gauge link local Hilbert spaces. The physical Hilbert space $\mathscr{H}_{\rm phys}$ is the subspace of gauge invariant states obeying the lattice Gauss law vertex constraint [105, 132, 143]:

$$\mathscr{V}_x(g) \prod_i \mathscr{L}_{xi}(g)\mathscr{R}_{xi}(g)|\Psi_{\rm phys}\rangle = |\Psi_{\rm phys}\rangle \quad \forall\, g \in G \ ; \tag{1.123}$$

or, in terms of the generators of infinitesimal transformations (if G is continuous):

$$\mathcal{G}^a_x|\Psi_{\rm phys}\rangle = 0 \quad \forall\, x, a \ , \qquad \mathcal{G}^a_x = \sum_i L^a_{xi} + \sum_i R^a_{xi} - \rho^a_x \ . \tag{1.124}$$

$\mathcal{G}^a_x$ generates time-independent local gauge transformations via $\exp(-i\sum_x \theta^a_x \mathcal{G}^a_x)$, as can be easily verified from the fundamental commutators. Together with the Hamiltonian and the operator algebra, the physical state condition shall be taken as part of the definition of the quantum theory [26]. For the Kogut-Susskind model, the matter contribution ρ^a_x is given by Eq. (1.101). Reinstantiating the lattice spacing (and recalling $L^a_{xi} \sim -R^a_{(x+i)i} \sim E^a_{xi}$), $\mathcal{G}^a_x$ is found to reproduce its continuum counterpart in Eq. (1.75) for $a \to 0$.

Gauss law has manifold physical consequences, largely independent of the specific gauge model considered: from the evasion of the Goldstone theorem, to the superselection of Gauss charges, and the violation of the cluster property by charge-carrying fields [26]. In particular, due the linear rise of the Coulomb potential, (1+1)-dimensional gauge theories typically exhibit a confining force, isolated charges correspond to states of infinite energy [118], and stable asymptotic states are charge-neutral bound states [114, 116, 118].

1.4C Link truncation

For a continuos group G, the gauge link Hilbert space constructed in the previous Section, $\mathscr{H}_{\rm link} = L^2(G)$, is clearly infinite dimensional. If gauge fields are to be explicitly represented, a truncation is in order. Gauge truncation is a subject of intense cross-fertilization, where schemes put forward in the context of quantum simulation have found thriving applications

in tensor network algorithms; these encompass: (i) quantum link models (QLMs) [202–204], (ii) q-deformation of the gauge algebras [125, 205–207], (iii) discrete subgroup approximations, i.e. truncation in the magnetic or group basis [208–210], and its dual, (iv) projection onto low-dimensional irreducible representations (irreps) of the gauge group i.e. truncation in the electric or irrep basis [132]; finally, proposals that combine the electric and magnetic bases have also recently emerged [211]. Each of the above has its own advantages. Key properties which help classify truncation approaches are: (a) preservation of the gauge algebra, (b) unitarity of the comparator, (c) existence of a (smooth) and efficient untruncated limit, and (d) ability to accurately reproduce the continuum physics even at finite truncation. In the quantum-link model approach, D-theory mandates that the untruncated theory is obtained by dimensional reduction from one extra (compact) space dimension [204, 212], which can be computationally costly for tensor networks. Discrete subgroups and q-deformation break the algebra by construction; the former has an intrinsic "resolution" limit dictated by the largest discrete subgroup of G while q-deformation provides a controllable untruncated limit [206]. Here we focus on irrep truncation, which spoils the unitarity of comparators and is not physically motivated in the continuum regime [79], but preserves exact gauge invariance and has a tunable and, importantly, provably accurate untruncated limit [213].

Irrep basis. According to the Peter-Weyl theorem [214], for a compact Lie group[38] G,

$$L^2(G) = \bigoplus_j \mathscr{H}_j^* \otimes \mathscr{H}_j \; ; \tag{1.125}$$

where the sum is over all unitary irreps of G, $\mathscr{H}_j$ is the representation space of irrep $\mathbf{j}$, and $\mathscr{H}_j^*$ is its dual, transforming with the conjugate irrep $\mathbf{j}^*$. In the light of this decomposition, a basis for $\mathscr{H}_{\text{link}}$ is provided by $|jmn\rangle$, where m and n index basis states in $\mathbf{j}$ and its dual, respectively[39]. The change from the irrep basis $|jmn\rangle$ to the group basis $|g\rangle$ reads [215]

$$\langle g|jmn\rangle = \sqrt{\frac{d_j}{|G|}}\, \mathbf{j}_{mn}(g) \; ; \tag{1.126}$$

where $d_j = \dim \mathbf{j}$ and $|G|$ is the volume of G, as given by the Haar measure $\mathrm{d}g$. This change of basis is a generalization of the Fourier transformation, and reduces to it in the Abelian case, where all representations are one-dimensional and thus m, n indices can be dropped. For instance, for U(1), $\mathbf{j}(e^{i\theta}) = e^{ij\theta}$ with $|G| = |S^1| = 2\pi$. The great orthogonality theorem ensures the irrep basis is orthonormal [216]:

$$\int \mathrm{d}g\; \mathbf{j}^*_{mn}(g)\, \mathbf{j}'_{m'n'}(g) = \frac{|G|}{d_j} \delta_{jj'}\delta_{nn'}\delta_{mm'} \; . \tag{1.127}$$

The notation $\mathbf{j}^*_{mn}$ is not ambiguous because, for unitary irreps, $\mathbf{j}^*(g) = [\mathbf{j}(g)]^*$.

[38] Most results given below hold, mutatis mutandis, also for finite groups [144].

[39] The set of values m and n indices can take clearly depends on j.

The comparator U is diagonal in the group basis:

$$U = \int \mathrm{d}g \, |g\rangle V(g) \langle g| \, . \tag{1.128}$$

In the new basis its matrix elements are obtained inserting completeness relations:

$$\langle jmn| U_{MN} \, |j'm'n'\rangle = \frac{\sqrt{d_{j'} d_j}}{|G|} \int \mathrm{d}g \; \mathbf{j}^*_{mn}(g) \, V_{MN}(g) \, \mathbf{j}'_{m'n'}(g) \, . \tag{1.129}$$

Orthogonality implies that two representations in the integrand, say V and $\mathbf{j}'$, have to fuse into the conjugate of third one, i.e. $\mathbf{j}$. It is not restrictive to assume $V = \mathbf{J}$ is also an irrep. Then, the solution can be given in terms of Clebsch-Gordan coefficients [132]:

$$\langle jmn| U_{MN} \, |j'm'n'\rangle = \sqrt{\frac{d_{j'}}{d_j}} \sum_\alpha \Big[C^{jm\alpha}_{JMj'm'} \Big]^* C^{jn\alpha}_{JNj'n'} \; ; \tag{1.130}$$

where α is the outer multiplicity index. This results shows that the comparator acts as irrep composition (tensor product) in the irrep basis. Assuming $\mathbf{J}$ is faithful, any irrep can be written as linear combinations of $\mathbf{J}^{\otimes p} \otimes \mathbf{J}^{* \otimes q}$ for some $p, q \in \mathbb{N}_0$ [217] and thus the link space is generated acting with U_{MN} and $U^\dagger_{MN}$ on the trivial irrep state $|000\rangle$.

Left and right group rotations,

$$\mathscr{L}(h) = \int \mathrm{d}g \, |hg\rangle\langle g| \, , \qquad \mathscr{R}(h) = \int \mathrm{d}g \, |g\rangle\langle gh| \, , \tag{1.131}$$

become block diagonal and act nontrivially only in the left or right factor of $L^2(G)$:

$$\langle jmn| \mathscr{L}(h) \mathscr{R}(h') \, |j'm'n'\rangle = \frac{\sqrt{d_j d_{j'}}}{|G|} \int \mathrm{d}g \, \mathbf{j}^*_{mn}(hg) \, \mathbf{j}'_{m'n'}(gh') = \delta_{jj'} \, \mathbf{j}^*_{mm'}(h) \, \mathbf{j}_{nn'}(h') \, . \tag{1.132}$$

Compactly [144],

$$\mathscr{L}(h) \mathscr{R}(h') = \bigoplus_j \mathbf{j}^*(h) \otimes \mathbf{j}(h') \, . \tag{1.133}$$

Setting $h = e^{\epsilon \tau^a}$ and $h' = 1_G$ (or vice versa) and taking an ϵ-derivative,

$$\langle jmn| L^a \, |j'm'n'\rangle = \delta_{jj'} (iT^a_{j^*})_{mm'} \delta_{nn'} \, , \tag{1.134a}$$

$$\langle jmn| R^a \, |j'm'n'\rangle = \delta_{jj'} \delta_{mm'} (iT^a_j)_{nn'} \, . \tag{1.134b}$$

The Casimir operator in Eq. (1.109) follows. It is diagonal and block-degenerate [132]:

$$\langle jmn| \mathcal{C}_2 \, |j'm'n'\rangle = \mathcal{C}_2(j) \, \delta_{jj'} \delta_{mm'} \delta_{nn'} \tag{1.135}$$

G	U(1)	SU(2)	SU(3)
$\{j\}$	$\mathbb{Z}$	$\mathbb{N}/2$	$\{(p,q)\} \in \mathbb{N}_0^2$
d_j	1	$2j+1$	$(1/2)(p+1)(q+1)(p+q+2)$
$\mathcal{C}_2(j)$	j^2	$j(j+1)$	$(4/3)(p^2+q^2+3p+3q+pq)$

Table 1.1: Examples of irrep dimensions and quadratic Casimirs [218].

where $\mathcal{C}_2(j) = \mathcal{C}_2(j^*) \geq 0$ is the quadratic Casimir of irrep $\mathbf{j}$:

$$\sum_a T_j^a T_j^a = -\mathcal{C}_2(j)\mathbf{I}_{d_j} \,. \tag{1.136}$$

Three well known examples are reported in Table 1.1.

Truncation. The series expansion of Kogut-Susskind Hamiltonian in the coupling reads

$$H = g^2 H_E + g^{-2} H_B + \mathcal{O}(1) \,. \tag{1.137}$$

Here $\mathcal{O}(1)$ collects the matter and gauge-matter interaction terms, while H_E and H_B are the electric ("kinetic") and magnetic ("potential") energy terms. Symbolically,

$$H_E = \frac{1}{2}\sum_{-} \mathcal{C}_2 \,, \qquad H_B = -\frac{1}{2}\sum_{\square} \mathrm{Re}\,\mathrm{tr}\, UUU^\dagger U^\dagger \,; \tag{1.138}$$

(the sums are over lattice edges and plaquettes). As just shown, H_E and H_B are diagonal respectively in the irrep (a.k.a. "momentum" or electric) and group ("position" or magnetic) bases, which are related by non-Abelian Fourier transform [133].

At strong lattice coupling, where the electric energy dominates, link configurations with high Casimir eigenvalue are energetically suppressed and may be legitimately discarded, keeping only link irreps j such that $\mathcal{C}_2(j) \leq \Lambda$, for some cutoff Λ. In particular, the $g \to \infty$ ground state is the product state with all the links in the singlet irrep: $|\Omega_E\rangle = \bigotimes_- |000\rangle$, $\mathcal{C}_2(0) = 0$. Conversely, at weak lattice coupling, magnetic energy dominates and virtually all irreps become relevant. Indeed, a $g \to 0$ ground state is such that[40] $UUU^\dagger U^\dagger |\Omega_B\rangle = \mathbf{I}|\Omega_B\rangle$ on every plaquette; an example being the state with all links in the neutral group element configuration $|\Omega_B\rangle = \bigotimes_- |1_G\rangle$ [133]. Via non-Abelian Fourier transform:

$$|000\rangle = \frac{1}{|G|}\int \mathrm{d}g\, |g\rangle \,, \qquad |1_G\rangle = \sum_{jmm} \sqrt{\frac{d_j}{|G|}}\, |jmm\rangle \,. \tag{1.139}$$

[40] The eigenvalues of a unitary matrix are phases and the real part is maximum when all are equal to 1.

Unfortunately, the continuum limit is typically precisely at $g \to 0$ (recall Eq. 1.117). Thus, when approaching it, the irrep truncation must be relaxed [219]. A meaningful extrapolation to the untruncated theory should be possible with a finite number of irreps [220].

In the irrep basis, the restriction of link operators to the truncated space is straightforward. However, all comparator matrix elements intertwining with discarded irreps have to be set to zero, spoiling its unitarity. On the other hand, since each irrep space is separately closed under group rotations $\mathscr{L}$ and $\mathscr{R}$, gauge transformations can still be implemented and the gauge invariance of the Hamiltonian is preserved exactly.

1.4D Dressed site formalism

In a gauge theory, physical quantities are strictly gauge invariant. In numerical simulations it is desirable to exploit this fact to lower the dimensionality of the computational space by *discarding unphysical states*. At the same time, for our purposes, it is imperative to *preserve the local structure* of the global computational Hilbert space, namely its realization as a tensor product space, upon which tensor network techniques rely. It is in general not obvious how to enforce Gauss law in a "local" fashion because gauge transformations at neighbouring sites involve non-disjoint sets of local degrees of freedom (they share a link). Ingenious strategies to remove entirely either the matter or the gauge fields have been put forward. However, in their current formulation, these do not work for multi-flavor LGTs, such as the 2-flavor SU(3) model studied in Chapter 4 [220, 221].

Our approach to enforce Gauss law consists of three steps, now outlined and detailed in the following. In the first step we draw inspiration from Peter-Weyl theorem to decompose each link in a pair of *rishons*: new d.o.f. each residing on one end of the link and accounting for the respective gauge transformations. Next, we restrict to valid link states whose rishons are in mutually conjugate irreps, by putting a local Abelian symmetry constraint on each link. In the third and last step, a composite site is forged fusing together a matter site and its attached semilinks. Gauge invariance mandates that these are collectively in a *singlet* state and Gauss law is thus recast as an internal constraint on the composite site. We solve it, identifying the *dressed site* local computational basis. Overall, the procedure trades the (generally non-Abelian) Gauss law vertex constraint, which involves one matter site and its $2D$ attached gauge links, for a simpler *Abelian* selection rule on each pair of neighboring dressed sites [105].

It is worth mentioning that the dressed site construction is not restricted to Kogut-Susskind theory or, more generally LGT, but rather applies to any problem involving local constraints. Recently, a protocol that relies on a dressed site encoding to convert a fermionic many-body system into a bosonic one has been proposed [222]. We now detail the derivation of the dressed site for a LGT with arbitrary matter content and a simple (finite, or compact Lie) gauge group. A generalization to non-simple gauge groups [223] will briefly hinted in Chapter 4.

Link splitting & link symmetries. A link Hilbert space can be decomposed into the tensor product of two semilink spaces by exchanging the order of the direct sum and the tensor product in the (truncated) Peter-Weyl decomposition. The embedding reads

$$\begin{gathered}\bigoplus_j \Big[\mathscr{H}_j^* \otimes \mathscr{H}_j\Big] = \mathscr{H}_{\text{link}} \;\hookrightarrow\; \mathscr{H}_{\text{L}} \otimes \mathscr{H}_{\text{R}} = \Big[\bigoplus_j \mathscr{H}_j^*\Big] \otimes \Big[\bigoplus_j \mathscr{H}_j\Big] \\ |jmn\rangle \mapsto |jm\rangle \otimes |jn\rangle\end{gathered} \tag{1.140}$$

where all direct sums are over the (finite) set of G-irreps kept after the link truncation. With this operation, however, mixed terms corresponding to semilinks occupying non-conjugate irreps are generated. We can get rid of them by projection, introducing

$$\Pi = \sum_j \pi_j \otimes \pi_j \;, \tag{1.141}$$

where π_j projects on the j-th subspace of a semilink — or, equivalently, by a local Abelian[41] link symmetry constraint, as follows: (i) introduce independent generators Φ on each link, (ii) assigning conjugate charges to the j-th factor of $\mathscr{H}_{\text{L}}$ and $\mathscr{H}_{\text{R}}$:

$$\Phi|jm\rangle \otimes |kn\rangle = (\phi_j - \phi_k)|jm\rangle \otimes |kn\rangle \;, \tag{1.142}$$

and (iii) work in the sector where all link charges equal to zero. Finally,

$$\mathscr{H}_{\text{link}} \cong \text{range}\,\Pi = \ker \Phi \;. \tag{1.143}$$

The embedding in Eq. (1.140) lifts straightforwardly to chromoelectric operators:

$$L^a = \bigoplus_j \Big[iT^a_{j^*} \otimes \mathbf{I}\Big] \mapsto \Big[\bigoplus_j iT^a_{j^*}\Big] \otimes \mathbf{I} \;, \qquad R^a = \bigoplus_j \Big[\mathbf{I} \otimes iT^a_j\Big] \mapsto \mathbf{I} \otimes \Big[\bigoplus_j iT^a_j\Big] \;; \tag{1.144}$$

and, by extension, the Casimir $\mathcal{C}_2$. All are naturally realized as operators acting to a single (left or right) semilink. As usual, for G finite, L^a and R^a shall be replaced with generators of finite rotations, $\mathscr{L}$ and $\mathscr{R}$. An analogous result applies. Conversely, by Eq. (1.130), the comparator decomposes as a linear combination of tensor products of rishon operators ζ:

$$U_{MN} \;\mapsto\; \Pi\Big[\sum_\alpha {\zeta_M^{(\alpha)}}^\dagger \otimes \zeta_N^{(\alpha)}\Big] \;, \quad \langle jm|\zeta_M^{(\alpha)}|j'm'\rangle = \sqrt[4]{\frac{d_{j'}}{d_j}} C^{jm\alpha}_{JMj'm'} \;. \tag{1.145}$$

Note that the extension of link operators to the enlarged link space $\mathscr{H}_{\text{L}} \otimes \mathscr{H}_{\text{R}}$ is not unique; their action on range$(1 - \Pi)$ is arbitrary.

[41] Link symmetries can be either U(1) or $\mathbb{Z}_P$, where P is the number of pairs of conjugate nontrivial irreps kept. Here we assume the former is chosen.

Gauss law as an onsite constraint. As just shown, after the links are split, L^a_{xi} and R^a_{xi} act nontrivially on a single semilink and Gauss vertex operators $\mathcal{G}^a_x$ and $\mathcal{G}^b_y$ have disjoint support whenever $x \neq y$. The support of each consists in one site and its $2D$ attached semilinks. Fusing them together, the composite site is forged and Gauss law becomes an onsite constraint. We solve it, identifying the gauge invariant subspace: the dressed site,

$$\mathscr{H}_{\text{dressed}} \cong \bigcap_{a=1}^{\dim G} \ker \mathcal{G}^a \subset \mathscr{H}_{\text{site}} \otimes \mathscr{H}_{\text{L}}^{\otimes D} \otimes \mathscr{H}_{\text{R}}^{\otimes D} \ . \tag{1.146}$$

A local-G singlet basis for $\mathscr{H}_{\text{dressed}}$ is found via iterated Clebsch-Gordan decompositions, together with its expansion in terms of the original "physical" site and semilink bases.

Singlets are conveniently computed first decomposing the Hilbert space of each d.o.f. in a direct sum of G-irreps. For semilinks the decomposition is built-in the definition of $\mathscr{H}_{\text{L,R}}$; thus in practice only the matter site requires further work. For a fermion multiplet $\{\psi_r\}_{r=1}^{\dim V}$ transforming with the representation V, the site Hilbert space is the exterior algebra $\bigwedge(\mathscr{H}_V)$. If V is irreducible, denoting $|r_1, \dots, r_N\rangle$ the N-particle Fock state obtained consecutively occupying modes $r_1, \dots, r_N$, nested Clebsch-Gordan series give

$$\langle j\alpha m | r_1, \dots, r_N\rangle = \mathcal{A}\, C^{j_{12} m_{12} \alpha_1}_{V r_1 V r_2} C^{j_{123} m_{123} \alpha_2}_{j_{12} m_{12} V r_3} \cdots C^{j m \alpha_{N-1}}_{j_{1\dots N-1} m_{1\dots N-1} V r_N} \ . \tag{1.147}$$

Here $\mathcal{A}$ denotes antisymmetrization over the r_i indices; indices α_i keep track of the multiplicity in a elementary tensor product; and $\alpha = (\alpha_1, \dots, \alpha_{N-1})$ accounts for the overall degeneracy of irrep j. Generalizing to a reducible representation ($V = \bigoplus_k V_k$, e.g. multiple flavours) requires additional decompositions and follows from the identity $\bigwedge(\bigoplus_k \mathscr{H}_{V_k}) \cong \bigotimes_k \bigwedge(\mathscr{H}_{V_k})$. Analogous results apply to bosons, with antisymmetrization replaced by symmetrization. However, the symmetric algebra $S(\mathscr{H}_V)$ is infinite dimensional and thus has to be truncated.

2

Tensor Networks

wavefunction compression and manipulation

The many-body problem is formulated, highlighting the consequences of entanglement on the classical simulability of quantum many-body systems and stressing the urge for numerical techniques that circumvent the exponential growth of the Hilbert space. Area laws for the entanglement of local lattice models are stated and justified, motivating the introduction of tensor networks as valid candidate techniques meeting said demand. We explain what tensor networks are, and why they furnish a good description of quantum many-body systems. A few selected topics are given prominent attention: energy minimization and time evolution; all are extensively relied upon throughout this Thesis. Finally, the extension to continuum systems is discussed. An ansatz capable of dealing directly with an infinite number of degrees of freedom is presented, stressing the difficulties arising in the relativistic context and numerically investigating its ability to capture the divergent entanglement content of field theories.

Attribution: Sections 2.4C to 2.4E constitute the Chapter's main original contribution and report on unpublished work on continuous tensor networks carried out in collaboration with Prof. E. Zohar and T. Shachar from the Hebrew University of Jerusalem. In Section 2.1, the pedagogical introduction to the many-body problem follows closely Ref. [131], while the discussion on local lattice models is inspired by Refs. [58, 86, 88]. In Section 2.2, the framing of tensor network techniques is influenced by Refs. [86, 87, 224], matrix product states and algorithms are again derived from Ref. [131], together with [87, 225]. The presentation of the tensor renormalization group algorithm in Section 2.3 is a review of Refs. [97, 226]; its application to the 2D classical Ising model follows in part Ref. [227] and the numerics consists in an independent re-implementation reproducing known results [228, 229]. Section 2.4 introduces continuous tensor network methods as defined in Ref. [230].

2.1 Motivation: the many-body problem

The quantum many-body problem — namely, the study of several interacting quantum d.o.f., called *constituents* — is encountered in a multitude of scientific settings. Condensed matter physics, quantum chemistry, atomic and nuclear physics being just a few prominent examples [43, 231]. Among them, and of obvious relevance for this Thesis, are also Hamiltonian lattice gauge theories, encountered in low- and high-energy physics [170] and introduced Chapter 1. Finally, with the advent of quantum simulation platforms, many-body systems can also be prepared in laboratory with an unprecedented degree of control, e.g. using cold atoms in optical lattices.

The Hilbert space is far too large. The total Hilbert space of an N-body system is the tensor product of N single-body or *local* Hilbert spaces,

$$\mathscr{H} = \bigotimes_{j=1}^{N} \mathscr{H}_j \ . \tag{2.1}$$

The single-body constituents of the system can be any quantum degree of freedom. In the lattice QFT case, they will encode the local state of a field, and their index j will run over the lattice sites and/or links. Chosen a *local basis* $\{|\sigma_j\rangle\}_{\sigma_j=1}^{\dim \mathscr{H}_j}$ for each $\mathscr{H}_j$ space, a state $|\Psi\rangle \in \mathscr{H}$ can be represented by an order-N complex tensor *wavefunction* $\Psi_{\sigma_1 \dots \sigma_N}$ via

$$|\Psi\rangle = \sum_{\sigma_1 \dots \sigma_N} \Psi_{\sigma_1 \dots \sigma_N} |\sigma_1\rangle \otimes \cdots \otimes |\sigma_N\rangle \ . \tag{2.2}$$

Let us assume for simplicity that all the local Hilbert spaces have dimension $d \equiv \dim \mathscr{H}_j$. Then $\dim \mathscr{H} = d^N$ independent complex coefficients have to be specified in order to specify the state $|\Psi\rangle$. This exponential growth of the Hilbert space with the system size makes many-body problems extremely challenging to attack numerically [86]. For instance, storing explicitly all the $\Psi_{\sigma_1 \dots \sigma_N}$ coefficients for some of the systems studied in this Thesis would require some 10^{230} bytes, a staggering number compared to the $\mathcal{O}(10^{15})$ byte random access memories available in current day most powerful supercomputers [232].

Mean field and beyond. Key in overcoming the above obstacle is realizing that not all the states in the Hilbert space $\mathscr{H}$ have the same physical relevance. Usually the description of physical phenomena involves only an exponentially small portion of the exponentially large Hilbert space $\mathscr{H}$ [86]. Crucial for the investigation of many-body systems is thus the development of formalisms and numerical methods that target directly the relevant portion of $\mathscr{H}$. As an example, at the basis of *mean field* theory is the assumption that a good approximate description of a many-body system can be accomplished considering only *separable* states, namely states that factorize as

$$|\Psi\rangle = |\Psi_1\rangle \otimes \cdots \otimes |\Psi_N\rangle \ ; \tag{2.3}$$

namely, neglecting the correlations between the components of the system. In this way, each of the $|\Psi_j\rangle$ is specified separately and only Nd parameters are needed to represent the overall state of the system. The complexity of the problem has thus been reduced from exponential to linear in the system size. However, the mean field ansatz is an uncontrolled and not always justified approximation. To show how it can be improved, consider a bipartition of the system in two complementary subsystems A and B, $\mathscr{H} = \mathscr{H}_\mathrm{A} \otimes \mathscr{H}_\mathrm{B}$. Up to an eventual reshuffling of the constituents, we can take $\mathrm{A} = \{j\}_{j=1}^{|\mathrm{A}|}$ ($|\cdot|$ denoting set cardinality). Then, for any normalized state, *Schmidt decomposition* gives

$$|\Psi\rangle = \sum_{\varsigma=1}^{\chi} \lambda_\varsigma |\Psi_\varsigma^\mathrm{A}\rangle \otimes |\Psi_\varsigma^\mathrm{B}\rangle \tag{2.4a}$$

with

$$\chi \leq \min(\dim \mathscr{H}_\mathrm{A}, \dim \mathscr{H}_\mathrm{B}) \ , \qquad \lambda_1 \geq \lambda_2 \geq \dots \lambda_\chi > 0 \ , \qquad \sum \lambda_\varsigma^2 = 1 \ . \tag{2.4b}$$

Here λ_ς are the *Schmidt coefficients*, the vectors $|\Psi_\varsigma^{\mathrm{A,B}}\rangle \in \mathscr{H}_{\mathrm{A,B}}$ are *orthonormal* and their number χ is the *Schmidt rank* of $|\Psi\rangle$ for the bipartition AB. In practice, the decomposition in Eq. (2.4) is computed by reshaping the wavefunction as a matrix and performing a (compact) *singular value decomposition* (SVD):

$$\Psi_{\{\sigma_j\}_{j\in\mathrm{A}}\{\sigma_j\}_{j\in\mathrm{B}}} \cong \Psi_{\alpha\beta} = \sum_{\varsigma\varsigma'}^{\chi} A_{\alpha\varsigma} \Lambda_{\varsigma\varsigma'} B^\dagger_{\varsigma'\beta} \ ; \tag{2.5}$$

with $\chi = \mathrm{rank}\{\Psi_{\alpha\beta}\}$; A, B semi-unitary, $A^\dagger A = B^\dagger B = \mathbf{I}_\chi$; and Λ positive definite diagonal, $\Lambda_{\varsigma\varsigma} = \lambda_\varsigma$ (non-zero *singular values*, sorted in descending order). The matrices A and B map Schmidt "bases" to the computational ones:

$$A_{\alpha\varsigma} = \langle \alpha | \Psi_\varsigma^\mathrm{A} \rangle \ , \quad B_{\beta\varsigma} = \langle \beta | \Psi_\varsigma^\mathrm{B} \rangle \ . \tag{2.6}$$

Often, for non-random states and in particular for states describing physical configurations, there is a strong hierarchy in the singular values. We can exploit this fact to discard the smallest ones and reduce the dimensionality of the matrices in Eqs. (2.4) and (2.5). Denoting with $\tilde{\chi}$ the number of singular values kept, the approximation, called *truncated Schmidt decomposition*, reads

$$|\Psi\rangle \approx |\tilde{\Psi}\rangle = \frac{1}{\mathcal{N}} \sum_{\varsigma=1}^{\tilde{\chi}} \lambda_\varsigma \, |\Psi_\varsigma^\mathrm{A}\rangle \otimes |\Psi_\varsigma^\mathrm{B}\rangle \ , \qquad \mathcal{N} = \sqrt{\textstyle\sum_{\varsigma=1}^{\tilde{\chi}} \lambda_\varsigma^2} \ ; \tag{2.7}$$

where $\mathcal{N}$ enforces the normalization of the state. The approximation is optimal, in the sense that, for fixed rank $\tilde{\chi}$, it minimizes the 2-norm $\epsilon = \|\Psi - \tilde{\Psi}\|$ [233–235]. For a two-body system, varying ϵ or $\tilde{\chi}$, Eq. (2.7) interpolates between the mean field ($\tilde{\chi} = 1$) and exact representations in a controlled way [87].

Entanglement entropy. The effectiveness of the compression in Eq. (2.7) depends heavily on how rapidly the singular values decrease. If the Schmidt rank is one for all possible bipartitions, $|\Psi\rangle$ is separable and the mean field representation is exact. Generally this is not the case and $|\Psi\rangle$ is said to be an *entangled* state. To quantify the achievable compression we need a measure of entanglement. Namely, a measure of how far from the separable case $|\Psi\rangle$ is and how much the configurations of the subsystems A and B are correlated, for arbitrary bipartitions. On its turn, this requires us to be able to specify the configurations of the subsystems.

Consider again the decomposition in Eq. (2.4): unless $|\Psi\rangle$ is separable, we cannot associate well-defined wavefunctions, $|\Psi^{\mathrm{A}}\rangle$ and $|\Psi^{\mathrm{B}}\rangle$, to the subsystems. Indeed, the wavefunction is not the most general description of the state of a quantum system. When we want to stress this, we refer to states that admit a wavefunction representation, e.g., $|\Psi\rangle$, as *pure states*. In *open systems* interacting with an environment, such as the subsystems A and B, the state generally consists of a statistical mixture of pure states $\{|\Psi_n\rangle\}_n$, each associated with a classical probability or population p_n. We refer to these configurations as *mixed states*. A mixed state is described in terms of a *density matrix* or *density operator* ρ [236],

$$\rho = \sum_n p_n |\Psi_n\rangle\langle\Psi_n| \ , \qquad \sum_n p_n = 1 \ . \tag{2.8}$$

The density matrix is Hermitian, positive semidefinite, has unit trace, and satisfies

$$\mathrm{tr}(\rho^2) \leq 1 \ . \tag{2.9}$$

The inequality is saturated if and only if ρ represents a pure state $|\Psi\rangle$, in which case it is the projector $|\Psi\rangle\langle\Psi|$. Plugging in the Schmidt decomposition from Eq. (2.4),

$$\rho = |\Psi\rangle\langle\Psi| = \sum_{\varsigma\varsigma'} \left[|\Psi^{\mathrm{A}}_\varsigma\rangle \otimes |\Psi^{\mathrm{B}}_\varsigma\rangle\right] \lambda_\varsigma \lambda_{\varsigma'} \left[\langle\Psi^{\mathrm{A}}_{\varsigma'}| \otimes \langle\Psi^{\mathrm{B}}_{\varsigma'}|\right] \ . \tag{2.10}$$

The *reduced density matrix* ρ_{A} for the subsystem A is simply the partial trace of ρ over the subsystem B. Using the orthonormality of Schmidt vectors,

$$\rho_{\mathrm{A}} = \mathrm{tr}_{\mathrm{B}}\, \rho = \sum_\beta \langle\beta|\rho|\beta\rangle = \sum_\varsigma |\Psi^{\mathrm{A}}_\varsigma\rangle \lambda^2_\varsigma \langle\Psi^{\mathrm{A}}_\varsigma| \ ; \tag{2.11}$$

whence the squared singular values are interpreted as populations. Analogously for ρ_{B}.

Given a density matrix ρ, its *Von Neumann entropy* is the scalar

$$S(\rho) = -\,\mathrm{tr}(\rho \log \rho) \ . \tag{2.12}$$

Notice it vanishes for pure states. As we now motivate, the *entanglement entropy* [237],

$$S(\rho_{\mathrm{A}}) = S(\rho_{\mathrm{B}}) = -\sum_\varsigma \lambda^2_\varsigma \log \lambda^2_\varsigma \ , \tag{2.13}$$

provides a good entanglement measure for any given bipartition of a pure state. Assuming $|\mathrm{A}| \leq |\mathrm{B}|$ and, as usual, all local dimensions to be the same,

$$0 \leq S(\rho_\mathrm{A}) \leq |\mathrm{A}| \log d \ . \tag{2.14}$$

$S(\rho_\mathrm{A})$ vanishes if $|\Psi\rangle$ is separable and takes the maximum value when all the $\dim \mathscr{H}_\mathrm{A} = d^{|\mathrm{A}|}$ singular values are equal (maximally entangled subsystems, incompressible decomposition). As a consequence, S provides a good estimate of how difficult it is to compress $|\Psi\rangle$ or, otherwise stated, how much information the state contains. For a "typical" (i.e., random[1]) state, the extensive scaling $S(\rho_\mathrm{A}) \sim |\mathrm{A}|$ is saturated. On the other hand, many quantum states appearing in nature are much less entangled [58], in a sense that we now make precise.

2.1A Local quantum lattice models

A *local quantum lattice model* is a many-body system whose degrees of freedom live on a lattice $\Lambda \subset \mathbb{R}^D$, and whose Hamiltonian H is a sum of compactly supported terms[2]. Quantum lattice models are ubiquitous in physics. In condensed matter physics they are used to grasp emergent properties of strongly correlated materials in terms of microscopic constituents with short-ranged interactions. Similarly, high-energy physicists have a long-standing tradition of employing lattice models, especially local ones, to regulate the ultraviolet divergencies arising in quantum field theories. The ground state or vacuum $|\Omega\rangle$ of such systems — namely the lowest energy eigenstate of the Hamiltonian, which for simplicity we assume to be non-degenerate — is of paramount importance as it captures the low-enough temperature equilibrium physics [58]. Locality of the interactions has well-known implications on the amount of correlations present in the ground state. We further define the *spectral gap* Δ as the energy difference between the vacuum and the first excited state [238]. If the gap closes $\Delta \to 0$ in the thermodynamic limit $|\Lambda| = N \to \infty$, the system is said to be in a *gapless* or *critical* phase, otherwise it is said to be *gapped* [58].

Clustering of correlations. If the model is gapped, the connected contribution to vacuum correlation functions decays exponentially with space separation: given two observables $O_\mathrm{A}, O_\mathrm{B}$ supported on some compact patches $\mathrm{A}, \mathrm{B} \subset \Lambda$, we have [58, 238]

$$|\langle O_\mathrm{A} O_\mathrm{B}\rangle - \langle O_\mathrm{A}\rangle\langle O_\mathrm{B}\rangle| \lesssim e^{-|y-z|(\mathrm{A},\mathrm{B})/\xi} \|O_\mathrm{A}\| \|O_\mathrm{B}\| \ , \tag{2.15}$$

where $\langle O\rangle = \langle\Omega|O|\Omega\rangle$ denotes the vacuum expectation value of O and $\|O\|$ is the operator norm of O (its largest singular value). The characteristic length scale on which correlations survive, called *correlation length* is dictated by the gap: $\xi \sim \Delta^{-1}$. In a gapless phase the length scale disappears, $\xi \to \infty$, and vacuum correlators decay algebraically [58].

[1] As defined through the Haar measure of the unitaries acting on $\mathscr{H}$.

[2] Thus involving finitely many bodies each.

Entanglement area laws. It is reasonable to expect fast decaying correlations to imply, on their turn, bounds on the entanglement content of the vacuum [88]. Especially in gapped phases, where correlations become negligible beyond a system-size independent length scale ξ, it is natural to conjecture that any region A is intertwined with the rest of the system only through the degrees of freedom in proximity of its boundary ∂A. On a regular lattice, their number scales like the size $|\partial \mathrm{A}|$ of the boundary rather than $|\mathrm{A}|$. The conjecture thus replaces a volume law bound on the entanglement entropy with a (much stricter, for large enough A) area law one [58, 239]:

$$S_{\mathrm{A}} \lesssim |\partial \mathrm{A}| \ . \tag{2.16}$$

Equation (2.16) has been proven for free gapped models in any dimension [58], as well as for generic 1D gapped chains [240, 241], where $|\partial \mathrm{A}| = \mathcal{O}(1)$ for any interval A and thus S is bounded by a constant [88]. For (general in $D = 1$, free in any D) gapless models, there are logarithmic corrections and vacua are slightly more entangled, with $S \lesssim |\partial \mathrm{A}| \log |\mathrm{A}|$ [88, 242–244]. Surprisingly, this logarithmic violation is absent for $D > 1$ free bosons, which satisfy an area law even when critical [88].

The Hilbert space is a delusion. For states fulfilling Eq. (2.16), the number of non-negligible Schmidt coefficients associated with any bipartition will generally scale with the linear size L of the smaller subsystem as $d^{L^{D-1}}$. Albeit still exponential for $D > 1$, this is exponentially smaller that the volume law bound d^{L^D}, suggesting a drastic reduction in the number of parameters required to represent these states, which therefore occupy a tiny "corner" of the gigantic Hilbert space [86]. In fact, as we discuss in the next Section, one can do even better and represent area law states with polynomial resources, with far-reaching consequences on the classical simulability of this class of states which, we remind, encompasses the ground states of many natural Hamiltonians [58, 86]. It is not only area law states that occupy an exponentially small "corner" of the Hilbert space, however. The same holds true for all efficiently preparable quantum states [58]. Specifically, the manifold that can be reached by evolving a many-body state for a time polynomial in N with a local Hamiltonian is also exponentially small, while the vast majority of $\mathscr{H}$ is reachable only after a time $t \sim e^N$, meaning practically unreachable [86]. This fascinating realization led some authors to dub the Hilbert space a "convenient illusion" [245].

2.2 Tensor network methods

Tensor networks are an important class of analytical and numerical techniques that allow to solve many-body problems efficiently [246, 247]. As just discussed, many-body computations involve huge tensors; tensor network methods allow to break these huge tensors into smaller ones, while accommodating as much *information* as possible with the available resources. Originally conceived in the context of quantum spin chains [90, 96], TN quickly spread to a diverse set of problems in condensed matter physics, statistical physics [97], quantum chemistry [99], and recently even machine learning [100, 101]. Of particular relevance for this

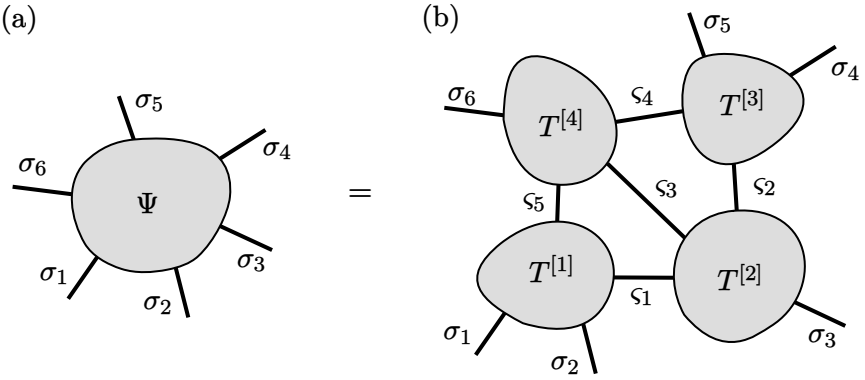

Figure 2.1: (a) A "large" tensor with $N = 6$ indices (legs) σ_j, like the wavefunction of a six-body system. (b) A possible TN decomposition in terms of smaller order-4 tensors T connected by virtual indices ς_k — explicitly contracting them yields back the original tensor. Figure from Ref. [224] (notation adapted).

Thesis, is their application to lattice gauge theories [75, 77, 248]. With it, approximatively a decade ago [104–107, 110, 249–252], TN started leaking into high-energy physics domain [79, 80, 111, 112].

Tensor networks. A *tensor network* (TN) is a collection of tensors and contraction rules. Just like an ordinary complex tensor, a TN returns a $\mathbb{C}$-number[3] for each assignment of all the uncontracted tensor indices. There exists a particularly convenient *diagrammatic notation* for TN [87, 253, 254], sketched in Fig. 2.1. A TN diagram is a sort of "graph" in which a node (or vertex) corresponds to a tensor and the edges attached to it represent its indices (also called legs). Contrarily to ordinary graphs, in a TN diagram open edges attached to a single node are allowed but isolated nodes with no edge attached are not[4]. Dangling edges, enumerated by j, are free tensor indices σ_j (external legs); while those connecting two nodes denote lazily contracted indices ς_k (internal, auxiliary or virtual legs). With a slight abuse of notation, we sometimes confuse an index ι with the set of values it can take $\{\iota\}$; accordingly, $|\iota|$ denotes its dimension. The maximum dimension of all internal indices, $\chi = \max_k |\varsigma_k|$, is called bond dimension of the network. We use the letter T to denote the TN tensors (more specific labels will be introduced below) and adopt the convention that tensors are identified not only by their name but also by their indices. In this Section we always assume that repeated indices are implicitly contracted. The advantage of a graphical notation should already be obvious from above discussion.

[3] Clearly real TN can be constructed in an identical fashion, allowing for a lower computational and memory footprint of numerical routines when a convenient basis in which the Hamiltonian is a real matrix is known, such as in the presence of time reversal symmetries [224].

[4] This last constraint can be lifted. We introduce it mostly for internal consistency with what follows. Regardless, having an edge k with $|\varsigma_k| = 1$ (see below) is the same as not having an edge at all.

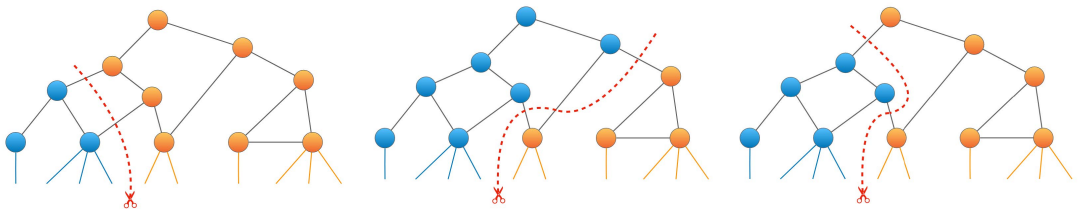

Figure 2.2: Three different bipartitions (blue/orange) of a TNS, corresponding to the same bipartition of the physical system. The dashed line shows the cut, crossing three possible sets $\{\not{k}\}$ of virtual legs. Figure from Ref. [255].

Tensor network states. A *tensor network state* (TNS) is a representation of a quantum many-body state by means of a TN where each dangling edge spans over the states $|\sigma_j\rangle$ of a local quantum degree of freedom j; $|j| = N$ and $|\sigma_j| = \dim \mathscr{H}_j \equiv d$. The number of tensors in the network will scale with the system size N. On the other hand, necessary conditions for a TNS to provide an efficient computational model are: (i) the degree of vertices (order of the corresponding tensors) does not increase with N; and (ii) the bond dimension χ scales at most as $\mathrm{poly}(N)$. When these are verified, the TNS description involves a polynomial number of parameters and thus provides an efficient representation. As we now discuss, when and why the above requirements can be fulfilled is dictated by the amount of entanglement present in the system.

The entanglement entropy that the TNS can accommodate is subject to rigorous bounds. To see this, consider once again a bipartition of the system. As shown in Fig. 2.2, the physical bipartition induces a family of possible network bipartitions, each obtained by cutting a set $\{\not{k}\}$ of virtual legs. For each of these, the wavefunction can be written

$$\Psi_{\alpha\beta} \cong \Psi_{\{\sigma_j\}_{j\in \mathrm{A}}\{\sigma_j\}_{j\in \mathrm{B}}} = A_{\{\varsigma_{\not{k}}\}\{\sigma_j\}_{j\in \mathrm{A}}} B_{\{\varsigma_{\not{k}}\}\{\sigma_j\}_{j\in \mathrm{B}}} \ , \tag{2.17}$$

where the tensors A and B result from separately contracting the two subnetworks (blue and orange tensors in Figure, respectively). After proper reshaping this is just a product of two matrices, contracted through the index $\varsigma \cong \{\not{k}\}$. Thus, besides the volume law from Eq. (2.14), an additional upper bound on the Schmidt rank for the decomposition is

$$\operatorname{rank} \Psi_{\alpha\beta} = \operatorname{rank}(A_{\alpha\varsigma} B_{\beta\varsigma}) \leq |\varsigma| = \prod_{\not{k}} |\varsigma_{\not{k}}| \ . \tag{2.18}$$

Combining the bounds given by all possible cuts, i.e. network bipartitions, gives[5]

$$S \leq \min \left[\sum_{\not{k}} \log |\varsigma_{\not{k}}| \right] \leq \log \chi \cdot \min |\not{k}| \ ; \tag{2.19}$$

[5] Clearly, the second inequality is saturated if all the virtual indices in the network have dimension χ.

where $|\not{k}|$ is the number of edges cut and the minimization are over all possible cuts $\{\not{k}\}$, i.e. TN bipartitions. Loosely speaking, Eq. (2.19) says that TNS encode efficiently — i.e., with low bond dimension and vertex degree — precisely *weakly entangled states*. In fact, ultimately, the amount and the structure of entanglement is the only factor limiting TNS methods. Unsurprisingly, Eq. (2.19) implies that a TNS with $\chi = 1$ is always separable, while any state is expected to admit a TNS representation with $\chi \sim \exp(N)$. Hence, by tuning the bond dimension, TNS *interpolate in a controlled way between the mean field ansatz and the exact representation.*

Equation (2.19) also suggests that TNS should be especially effective at targeting local lattice models, where a great deal of interesting physics is captured precisely by states which obey strong entanglement bounds. Given a lattice model, it is not too hard to devise a TNS with fixed, uniform χ ad yet accommodating area law entanglement by construction: tensor are distributed on lattice sites and contracted with their neighbours installing one virtual leg on every lattice link; finally one additional (physical) leg is attached to each tensor. For this network topology, a unique cut with $|\not{k}| \sim |\partial \mathrm{A}|$ is associated with every physical bipartition. The construction above is called *projected entangled pair state* (PEPS) [247, 256] and in principle it works in every space dimension D — however, the higher D is, the higher the vertex degree will be. Furthermore, while PEPS do encode area law states in every dimension with $\mathrm{poly}(N)$ resources, numerically manipulating PEPS and accessing the information they contain efficiently is less straightforward in $D > 1$. In $D = 1$ a dedicated set of highly optimized algorithms has been devised and the situation is radically different, earning the ansatz a special name[6]: *matrix product state* (MPS) [89, 90, 92–94, 257, 258]. PEPS and MPS are just 1.5 paradigmatic examples of TNS ansatze, many others have been conceived, often accompanied by specialized algorithms, each tailored to a distinct pattern of correlations — namely, entanglement geometry [86].

2.2A Matrix product state methods

Matrix product states are arguably the most successful TNS ansatz for one-dimensional (closed, gapped) many-body quantum systems [95]. Together with DMRG and TEBD, two simple yet powerful algorithms introduced below, they are the workhorse of the numerical study of strongly correlated one-dimensional systems [58]. The simulations presented in this Thesis rely on the *Tensor Network Python* (`TeNPy`) library [225] implementation of these algorithms. Here we present their working principles, mostly disregarding optimization details and other technicalities.

[6] To be historically accurate, MPS were discovered long before PEPS (as theoretical tools, rather than numerical).

Matrix product states. A *matrix product state* (MPS) or *tensor train* [89, 90, 257, 258] is a TNS encoding the wavefunction of a chain with a linear cost in N [58], as

$$|\Psi\rangle = T^{\sigma_1}_{\varsigma_0\varsigma_1} T^{\sigma_2}_{\varsigma_1\varsigma_2} \cdots T^{\sigma_{N-1}}_{\varsigma_{N-2}\varsigma_{N-1}} T^{\sigma_N}_{\varsigma_{N-1}\varsigma_N} |\sigma_1\sigma_2\ldots\sigma_{N-1}\sigma_N\rangle \ ; \tag{2.20}$$

where we moved the physical indices σ_j up to better distinguish them from virtual ones ς_j. For open boundary conditions, the indices ς_0, ς_N are introduced just to uniformize the MPS layout are trivial ($\varsigma_0 \equiv \varsigma_N \equiv 1$). Contrarily, on a ring with periodic boundaries it is natural to identify $\varsigma_0 \cong \varsigma_L$ and treat it as a proper virtual index[7]. An MPS with uniform bond dimension χ naturally realizes the one-dimensional area law: for every bipartition $S \leq \log\chi$ [86]. For each $\{\sigma_j\}_j$ assignment, evaluating the corresponding wavefunction component $\Psi_{\sigma_1\ldots\sigma_N}$ amounts to taking a product of matrices, hence the name. Because of this matrix product structure, MPS virtual indices are sometimes omitted in the following.

A constructive derivation of the MPS ansatz is obtained starting from the exact wavefunction and iteratively reshuffling tensor indices and performing Schmidt decompositions. The procedure goes as follows: start from $\Psi_{\sigma_1\ldots\sigma_N}$ in Eq. (2.2);

(i) identify $\sigma_1 \cong \alpha$ and $\sigma_2\ldots\sigma_N \cong \beta$;
(ii) perform the SVD in Eq. (2.5) (eventually truncating it);
(iii) adsorb the singular values on the right, defining $\Psi_{\varsigma_1\beta} = (\Lambda B)_{\varsigma_1\beta}$;
(iv) split back $\beta \cong \sigma_2\ldots\sigma_N$.

The procedure is then repeated for $\Psi_{\varsigma_1\sigma_2\ldots\sigma_N}$, this time fusing $\varsigma_1\sigma_2 \cong \alpha$ and $\sigma_3\ldots\sigma_N \cong \beta$. Proceeding iteratively until Ψ has a single physical leg, one gets [75, 86]

$$\Psi_{\sigma_1\ldots\sigma_N} = A^{\sigma_1}_{\varsigma_1} A^{\sigma_2}_{\varsigma_1\varsigma_2} \cdots A^{\sigma_{N-1}}_{\varsigma_{N-2}\varsigma_{N-1}} \Psi^{\sigma_N}_{\varsigma_{N-1}} \ , \tag{2.21}$$

where physical indices have been moved up as usual. A few comments are due: Firstly, following the above recipe, any $|\Psi\rangle \in \mathscr{H}$ can be represented *exactly* as an MPS. Otherwise stated, the manifold spanned by MPS is dense in the Hilbert space [86]. At the same time, carefully keeping track of the shape of $\Psi_{\alpha\beta}$ at every iteration shows that, unless truncated, the bond dimension will generally increase exponentially with each iteration, until the middle of the chain is reached: $|\varsigma_k| = d^{\min(k,\,N-k)}$, implying $\chi \sim \exp(N)$. This is expected: representing *any* $|\Psi\rangle \in \mathscr{H}$ requires all the exponentially-many wavefunction coefficients. Indeed, the above construction of an MPS out of an order-N tensor is only a formal procedure. In practice, TN are typically employed in the study of systems whose exact wavefunction cannot even be stored. Accordingly, TN algorithms assume the existence of a faithful TN representation of the state of interest with sufficiently low bond dimension. The circumstances under which this is a good assumption have already been discussed at length. Finally, notice also that the tensors in Eq. (2.21) satisfy by construction the

[7] At least formally. As far as numerics is concerned, this choice yields a loopy TN, thus its advantages and disadvantages should be analyzed on a case-by-case basis.

isometric condition

$$A^{*\sigma_1}_{\varsigma_1'} A^{\sigma_1}_{\varsigma_1} = \delta_{\varsigma_1\varsigma_1'} \ , \qquad A^{*\sigma_j}_{\varsigma_{j-1}\varsigma_j'} A^{\sigma_j}_{\varsigma_{j-1}\varsigma_j} = \delta_{\varsigma_j\varsigma_j'} \quad \forall j < N \ . \tag{2.22}$$

It is always possible to enforce this or similar isometric conditions on the MPS in Eq. (2.20) exploiting the invariance of the network under the local invertible transformations

$$T^{\sigma_j} \to T^{\sigma_j} Y^{-1} \ , \qquad T^{\sigma_{j+1}} \to Y T^{\sigma_{j+1}} \ ; \tag{2.23}$$

with Y an invertible $|\varsigma_j| \times |\varsigma_j|$ matrix acting on the right (left) virtual leg of T_{σ_j} ($T_{\sigma_{j+1}}$). Chosen a site j, via a sequence of such transformations it is possible to impose [87, 225]

$$\begin{aligned} \left[T^{\dagger\sigma_{j-1}} \dots T^{\dagger\sigma_1}\right] \otimes \left[T^{\sigma_1} \dots T^{\sigma_{j-1}}\right] &= \mathbf{I}_{|\varsigma_{j-1}|} \ , \\ \left[T^{\dagger\sigma_N} \dots T^{\dagger\sigma_{j+1}}\right] \otimes \left[T^{\sigma_{j+1}} \dots T^{\sigma_N}\right] &= \mathbf{I}_{|\varsigma_j|} \ ; \end{aligned} \tag{2.24}$$

known as *mixed canonical form* of the MPS [225]. Equation (2.24) reduces the evaluation of the norm of the MPS to the complete contraction of $T^{\varsigma_{j-1}\varsigma_j}_{\sigma_j}$ with its conjugate — an $\mathcal{O}(1)$ operation in the system size. Similarly for expectation values of local operators with support on the site j. Finally, the *isometry center* j can be moved quite efficiently [95].

Matrix Product Operator. Another ansatz emerging naturally in MPS computations is the *matrix product operator* (MPO) [259]. It is used to represent many-body operators as

$$O = W^{\sigma_1\tau_1}_{\varsigma_0\varsigma_1} W^{\sigma_2\tau_2}_{\varsigma_1\varsigma_2} \cdots W^{\sigma_N\tau_N}_{\varsigma_{N-1}\varsigma_N} |\sigma_1\sigma_2\dots\sigma_N\rangle\langle\tau_1\tau_2\dots\tau_N| \ . \tag{2.25}$$

At notational level, the main difference with the MPS ansatz is that each tensor has a pair of physical indices (ingoing and outgoing). As for the MPS, trivial boundary virtual legs are introduced for convenience. Remarkably, Hamiltonians with short ranged interactions can be represented exactly as an MPO with small bond dimension [225]. MPO are also used to represent density matrices of mixed states [58].

Variational energy minimization. Many properties of a quantum mechanical system can be understood studying it low-energy eigenstates. The MPS representation of these states can be computed with an efficient, *deterministic, variational* algorithm: the *density matrix renormalization group* (DMRG) algorithm [91, 260, 261]. This renormalization group (RG) method was originally put forward to remedy the shortcomings of previous real-space RG approaches, especially in relation to their failure for the 1D particle-in-a-box problem [91, 262, 263]. It was later realized that the recently introduced MPS constitute the natural *variational class* on which DMRG operates [92–95]. In its MPS formulation, DMRG relies on an MPO representation of the Hamiltonian to recasts the global energy optimization problem as a sequence of *local* optimizations — each replacing one MPS tensor with the solution of a local eigenvalue problem for some *effective Hamiltonian*, as depicted in Fig. 2.3.

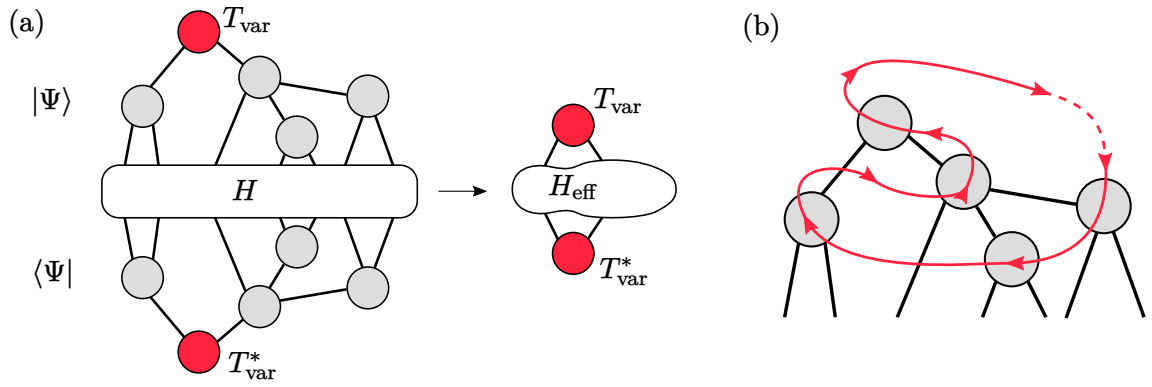

Figure 2.3: Basic idea of the variational ground state search: (a) In order to reduce the complexity of the minimization problem, only the parameters of one tensor T_{var} (red) are taken as variational while all other tensors are taken as fixed. The variational tensor forms the *optimization center*, while the fixed tensors form an *environment*. The latter can be efficiently contracted with the Hamiltonian H, leading to a reduced *effective* Hamiltonian H_{eff}. (b) By solving the reduced optimization problem sequentially (for varying locations of the optimization center), the energy expectation value is gradually reduced. This iterative minimization is commonly called *sweeping*. Figure and caption from Ref. [224] (notation adapted).

The optimization problem for the ground state is encoded by the Lagrangian function [87]

$$\mathscr{L}(\{T^{\sigma_j}_{\varsigma_{j-1}\varsigma_j}, T^{*\,\sigma_j}_{\varsigma_{j-1}\varsigma_j}\}) = \langle\Psi|H|\Psi\rangle - \lambda\Big[\langle\Psi|\Psi\rangle - 1\Big] \,, \tag{2.26}$$

where $|\Psi\rangle$ is the MPS and the variables with respect to which we optimize are its tensors, as well as the Lagrange multiplier λ, enforcing the normalization of the state. Stationarity of $\mathscr{L}$ with respect to $T^{*\,\varsigma_{j-1}\varsigma_j}_{\sigma_j}$ provides

$$(H_{\text{eff}})^{\sigma_j\tau_j}_{\varsigma_{j-1}\varsigma_j\varsigma'_j\varsigma'_{j+1}} T^{\tau_j}_{\varsigma'_j\varsigma'_{j+1}} - \lambda T^{\sigma_j}_{\varsigma_{j-1}\varsigma_j} = 0 \,, \tag{2.27}$$

where we assumed the mixed canonical form of Eq. (2.24) to simplify the derivative of $\langle\Psi|\Psi\rangle$ [87, 95], while H_{eff} is the effective Hamiltonian for the j-th tensor, obtained contracting the Hamiltonian MPO with all other MPS tensors and their conjugates. Ideally, all variational parameters should be simultaneously optimized — including the ones entering H_{eff}. In practice this is not efficient or even viable [86]. Instead, we start from some initial guess or random MPS and take as variational parameters the entries of a single tensor at time, while keeping the other tensors fixed. In Eq. (2.27) we treat H_{eff} as a constant and vary only $T_{\text{var}} = T^{\sigma_j}_{\varsigma_{j-1}\varsigma_j}$. Fusing $\sigma_j\varsigma_j\varsigma_{j+1} \cong \iota$ and $\tau_j\varsigma'_j\varsigma'_{j+1} \cong \iota'$, Eq. (2.27) becomes an ordinary eigenvalue problem and can be solved via standard algorithms (e.g., Lanczos). The new

ground MPS guess is then obtained replacing $T^{\sigma_j}_{\varsigma_{j-1}\varsigma_j}$ with the lowest energy eigenstate; the corresponding eigenvalue λ_0 gives the current ground state energy estimate. The update of $T^{\sigma_j}_{\varsigma_{j-1}\varsigma_j}$ changes the effective problem for the other tensors. The algorithm *sweeps* over the network iteratively, performing local optimizations until desired convergence in λ_0 or some other observable is reached.

A few comments are due: Presented above is the 1-site implementation of DMRG for MPS. As Fig. 2.3 suggests, the algorithm can be applied to other TNS ansatze as well [86], such as PEPS [247] and TTN [264–267]. There is also a 2-site variant of DMRG, which optimizes two neighbouring tensors at a time. At the end of the update, the optimized 2-site tensor has to be split back via (truncated) SVD to recover the original MPS structure. Although slightly more computationally costly, the 2-site update scheme allows for an adaptive growth of the bond dimension by truncating the SVD to the chosen precision[8] [225]. Larger site blocks can be used but the advantages are limited and the exponential complexity of the global optimization is eventually re-established. Finally, once a ground MPS $|\Omega\rangle$ has been found, the first excited state can be computed adding a term $\lambda'\langle\Omega|\Psi\rangle$ to the Lagrangian in Eq. (2.26) to enforce orthogonality of the new solution to the ground state. Proceeding iteratively a few low-energy eigenstates can be determined [87].

Trotterized time evolution. Predicting the dynamics of a closed quantum system requires solving the *Schrödinger equation*,

$$i\frac{\mathrm{d}}{\mathrm{d}t}|\Psi(t)\rangle = H|\Psi(t)\rangle \ . \tag{2.28}$$

Given a nearest-neighbour[9] Hamiltonian and an initial MPS $|\Psi(0)\rangle$, an approximate MPS representation of $|\Psi(t)\rangle$ can be computed using the *time evolving block decimation* (TEBD) numerical algorithm [246, 268]. Solving Eq. (2.28) in principles requires exponentiating the huge matrix $-itH$. At the core of TEBD is the simple observation that, once Hamiltonian terms acting on even and odd bonds are isolated, their respective exponentials factorize *exactly* because each is a sum of commuting operators.

Let

$$H = H_{\mathrm{E}} + H_{\mathrm{O}} \ , \qquad H_{\mathrm{E}} = \sum_{j \text{ even}} H_{[j,j+1]} \ , \qquad H_{\mathrm{O}} = \sum_{j \text{ odd}} H_{[j,j+1]} \ , \tag{2.29}$$

with $H_{[j,j+1]}$ acting non-trivially only on sites $j, j+1$. Then,

$$e^{H_{\mathrm{E}}} = \prod_{j \text{ even}} e^{H_{[j,j+1]}} \ , \qquad e^{H_{\mathrm{O}}} = \prod_{j \text{ odd}} e^{H_{[j,j+1]}} \ . \tag{2.30}$$

[8] Notice that the mixed canonical form, namely the orthonormality of the left and right Schmidt bases, is essential to ensure a meaningful truncation [225].

[9] In the presence of slightly longer range interactions a nearest-neighbour Hamiltonian can be recovered by fusing groups of neighbouring sites in a single, bigger, local Hilbert space.

The small matrices $H_{[j,j+1]}$ can be easily exponentiated numerically. Relying on a Suzuki-Trotter decomposition [269], the interval $[0,t]$ is then divided in small steps of duration ϵ and each evolution step is decomposed as (there exist higher order variants as well)

$$e^{-i\epsilon H} = e^{-i\epsilon H_{\mathrm{E}}/2} e^{-i\epsilon H_{\mathrm{O}}} e^{-i\epsilon H_{\mathrm{E}}/2} + \mathcal{O}(\epsilon^3) \ . \tag{2.31}$$

Plugging in Eq. (2.30) and contracting each term with the MPS yields the evolved state after t/ϵ steps. Without going into the implementation details (see e.g. [225]), notice that acting with $e^{\epsilon H_{[j,j+1]}}$ on $T^{\sigma_j}_{\varsigma_{j-1}\varsigma_j} T^{\sigma_{j+1}}_{\varsigma_j\varsigma_{j+1}}$ merges the two MPS tensors in a single, bigger tensor. The MPS form is recovered applying an SVD and truncating[10] to the desired precision after each update. Generally the update increases the entanglement entropy (and thus $|\varsigma_j|$) at the bond between sites j and $j+1$.

The error sources of the algorithm are the truncation of the singular values, controlled by $|\varsigma_j|$, and the Trotterization, controlled by ϵ. The former is once again dictated by the amount of entanglement generated during the evolution; as for the latter, a Suzuki-Trotter decomposition of order M introduces an error $\mathcal{O}(t\epsilon^M)$ on the final state $|\Psi(t)\rangle$ [225].

2.3 An application to statistical mechanics

Even before being introduced as representations of quantum many-body states, TN had been used in statistical physics to represent partition functions of classical lattice models [270], an example being the vertex model [271]. Up to now, the presentation has been focused on TNS techniques because we are mostly interested in the Hamiltonian approach to lattice field theory, where canonical quantization yields precisely a many-body quantum system. However, in the widely adopted Euclidean path-integral formulation of lattice QFT, one essentially deals with a statistical system in equilibrium [44]. We now briefly show how TN can be a useful resource also in this setting, introducing the tensor renormalization group algorithm and providing a simple application example to the 2D classical Ising model.

Tensor network models. A *tensor network model* [97] is a classical statistical mechanics model whose partition function can be represented by a fully contracted TN. Classical lattice models with a finite local configuration space and nearest-neighbours interactions belong to this class [97, 270]. The relevance of TN models comes from the existence of an efficient algorithm for the (typically numerical) evaluation of Eq. (2.32), discussed in the next paragraph.

In order to recast a nearest-neighbour statistical lattice model as a TN model, introduce a partition of the lattice in a grid of square subdomains[11]. For each square, define a "restricted

[10] The unitarity of the transformation ensures that it can be performed in a way that preserves the canonical form of the MPS (up to truncation error) [225].

[11] Other grid geometries can be considered as well [97].

partition function" Ψ_{abcd} which depends on the configurations of the degrees of freedom on its sides, indexed by a, b, c and d. This is obtained summing the Boltzmann weights associated to lattice sites and bonds within the square over all the configurations of the bulk degrees of freedom. The partition function of the model is then obtained multiplying the Ψ of all the squares and summing over all possible boundary configurations:

$$Z = \sum_{abcd\ldots} \Psi_{abcd}\Psi'_{aefg}\Psi''_{bhij}\Psi'''_{cklm}\cdots \ ; \tag{2.32}$$

which is precisely the form expected for a TN model. Note that, unlike in quantum systems, the local tensors of a TN model are readily determined inspecting the Hamiltonian [270]. The TN in Eq. (2.32) can be represented as a square grid with the nodes (tensors) located at the center of each square of the original lattice partitioning. In the following, we assume that the model is uniform, therefore every node corresponds to the same tensor Ψ_{abcd} whose indices run from 1 to χ.

Tensor renormalization group. The *tensor renormalization group* (TRG) algorithm [97] is a strategy for approximating a fully contracted network of tensors iteratively, by coarse graining [226]. In the context of TN models, TRG is a real space renormalization prescription. A TRG iteration consists of two local operations — updates of the network involving subsets of neighbouring tensors — namely: (i) an approximate factorization and (ii) an exact contraction. Focusing on square geometries and grouping the network nodes in two alternating sublattices, A and B, these operations read [229]:

$$\Psi_{abcd} \xrightarrow{\text{(i, on A)}} \sum_{\varsigma=1}^{\chi} \Phi^{(1)}_{\varsigma ab}\Phi^{(3)}_{\varsigma cd} \ , \qquad \Psi_{abcd} \xrightarrow{\text{(i, on B)}} \sum_{\varsigma=1}^{\chi} \Phi^{(2)}_{\varsigma bc}\Phi^{(4)}_{\varsigma da} \ ; \tag{2.33}$$

followed by

$$\sum_{ijkl=1}^{\chi} \Phi^{(1)}_{ail}\Phi^{(2)}_{bji}\Phi^{(3)}_{ckj}\Phi^{(4)}_{dlk} \xrightarrow{\text{(ii)}} \Psi'_{abcd} \ . \tag{2.34}$$

After one iteration step, a new network of Ψ' tensors with half as many nodes as the original one is obtained. Although the decimation halves the number of "microscopic degrees of freedom", the macroscopic size of the system is not affected.

The Φ tensors introduced in the first step are computed performing an SVD and distributing the singular values evenly on the unitaries. For the SVD, the Ψ and Φ tensors are reinterpreted as matrices by appropriately grouping their indices; e.g. as $\Psi_{ab,cd}$ and $\Phi^{(i)}_{\varsigma,ab}$ on subsystem A. In principle the index ς should be χ^2 dimensional. Yet, this would result in χ^2 dimensional indices for Ψ', which means that the complexity of the above operations increases exponentially with each TRG iteration. To prevent this, only the χ largest singular values are kept during the SVD [97]. A straightforward inspection reveals that, with this truncation, the cost of each TRG operations is $\mathcal{O}(\chi^6)$.

Motivation: the signature of entanglement in statistical systems. As just shown, TRG can be formulated without any reference to the lattice model or the partitioning procedure introduced in constructing TN models. Nonetheless, as we now discuss, the justification for the truncation discussed above relies precisely on the assumption that the network to be evaluated arises from a non-critical statistical mechanics model [97]. In terms of the lattice partitioning, TRG operations correspond to the following splitting and gluing:

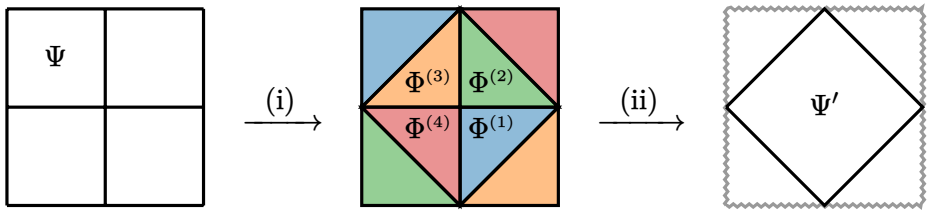

. (2.35)

Each square in the leftmost term represents a Ψ tensor. Blue, green, yellow and red triangles in the center term corresponds to $\Phi^{(i)}$, $i = 1, 2, 3, 4$. The two squares (squiggly paths are identified by PBC) in the rightmost term are Ψ' tensors. After a coarse graining iteration, the number of boundary degrees of freedom of each square increases by a factor of $\sqrt{2}$. The rank of the tensor Ψ as defined in Eq. (2.34) should in principle increase accordingly. To understand why the naïve scaling does not apply, we exploit the duality between 2D classical and (imaginary-time) 1D quantum models [97, 272]. We interpret Ψ_{abcd} as the wave function of a 1D quantum system living on the boundary of the square. The imaginary-time evolution generated by its Hamiltonian H corresponds to the coarse-graining procedure, relating a square of smaller size to a larger one [97] Then, for large enough squares, the Ψ tensor approaches the ground state of H, up to exponentially small corrections. The factorization step of TRG is just a bipartition of the quantum system and, if H is gapped, the justification for truncating the SVD is provided by the entanglement area law in Eq. (2.16).

If the original 2D classical model is critical, then the associated 1D quantum system is gapless [97]. The absence of a length scale makes gapless ground state more correlated. Given a subsystem of size L described by a reduced density matrix ρ, for L large enough

$$S = -\operatorname{tr} \rho \log \rho \sim \log L \tag{2.36}$$

(logarithmic violation of the entanglement area law) [244]. This implies that an increasing number of Schmidt states are relevant during the TRG factorization step, and the truncation in is no longer justified. Consequently, in principle, TRG should break down at criticality. Nevertheless, the above observations concern asymptotic behaviours and in practice it is often possible to study systems close to criticality by simply choosing χ large enough [97].

The TRG flow converges to a fixed point tensor Ψ^*. In the light of the previous observations, Ψ^* corresponds to the ground state of the 1D quantum system on the square in the thermodynamic limit. A more rigorous argument is given in [97].

2D classical Ising model. An implementation of TRG for the 2D square lattice classical isotropic Ising model is now discussed. The Ising model constitutes an ideal testbed for new numerical techniques, as numerical results can be benchmarked against an exact solution [273]. The partition function of the model reads

$$Z = \sum_{\{s_x\}} \exp\Big(K \sum_{x \text{—} y} s_x s_y\Big) \ , \tag{2.37}$$

where the sum in the exponent is over lattice bonds ${}_{x}\text{—}_{y}$, $s_x \in \{0,1\}$ is the spin configuration at site x, and $K = \beta J$ with β the inverse temperature and J the model coupling. Equivalently, organizing the Hamiltonian terms by plaquettes ${}^{w}_{x}\square^{z}_{y}$ instead of bonds

$$Z = \sum_{\{s_x\}} \prod_{{}^{w}_{x}\square^{z}_{y}} \exp\left(K \frac{s_x s_y + s_y s_z + s_z s_w + s_w s_x}{2}\right) . \tag{2.38}$$

This expression can be rewritten solely in terms of domain wall variables $w_{xy} = s_x s_y$ (with x, y nearest neighbours). To replace the trace over spin configurations in with a trace over domain wall configurations we write

$$Z = \sum_{\{s_x\}} \sum_{\{w_{xy}\}} \prod_{x \text{—} y} \delta(w_{xy} - s_x s_y) \prod_{{}^{w}_{x}\square^{z}_{y}} \exp\left(K \frac{w_{xy} + w_{yz} + w_{zw} + w_{wx}}{2}\right) \tag{2.39}$$

and observe that[12] [229]

$$\sum_{\{w_{xy}\}} \sum_{\{s_x\}} \prod_{x \text{—} y} \delta(w_{xy} - s_x s_y) \prod_{{}^{w}_{x}\square^{z}_{y}} = \sum_{\{w_{xy}\}} \prod_{{}^{w}_{x}\square^{z}_{y}} \frac{1 + w_{xy} w_{yz} w_{zw} w_{wx}}{2} \ . \tag{2.40}$$

Let us define a tensor

$$T_{abcd} = \frac{1 + (-1)^{abcd}}{2} \exp\left(\frac{(-1)^a + (-1)^b + (-1)^c + (-1)^d}{2}\right) \tag{2.41}$$

living on a plaquette, whose indices $a, b, c, d \in \{0,1\}$ are associated to the lattice bonds of the plaquette. By the above discussion, the TN model representation of Z reads

$$Z = \prod_{\square} T^K \ , \tag{2.42}$$

where every lattice bond is associated with a (contracted[13]) index.

[12] There are a couple of subtleties involved in this step: the mapping $\{s_x\} \to \{w_{xy}\}$ (i) is not injective (it is clearly 2-to-1) (ii) it is not surjective (not all the domain wall configurations are physical [227]).

[13] Every bond is shared by a pair of neighbouring plaquettes, thus the associated index appears in two T tensors.

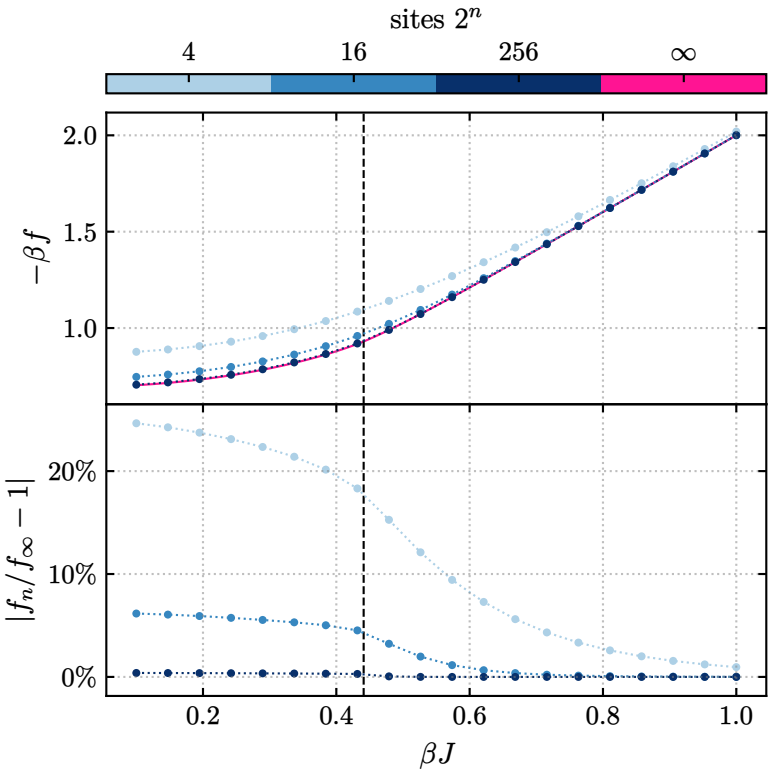

Figure 2.4: *Top:* free energy densities ($-\beta f$) for the 2D Ising model as a function of $K = \beta J$, for different number of lattice sites. *Bottom:* relative deviation of the finite size estimates ($\chi = 12$) from the exact thermodynamic limit value in Eq. (2.43). The vertical dashed line corresponds to $\beta J = K_c$.

The Ising model free energy per site f is computed numerically for different values of K. The results obtained for $n = 2, 4, 8$ TRG iterations with $\chi = 12$ are shown in Fig. 2.4, together with the thermodynamic limit exact result [273, 274]

$$-\beta f_\infty = \log(2\cosh(2K)) + \frac{1}{2\pi}\int_0^\pi \mathrm{d}\theta \log\left(\frac{1+\sqrt{1-\kappa^2\sin^2\theta}}{2}\right), \tag{2.43}$$

where $\kappa = 2\sinh(2K)\cosh^{-2}(2K)$.

As Fig. 2.4 show, the numerical results are in good agreement with the exact ones for $n > 2$. The dominant deviation comes from finite size effects (number of TRG iterations). Truncation effects are subleading: for $n = 8$ iterations the relative deviations between $\chi = 3$ and $\chi = 12$ results is at most 0.5%. As expected and as shown by Fig. 2.5, truncation effects get more dramatic near the critical point $\beta J = K_c \approx 0.441$ [229].

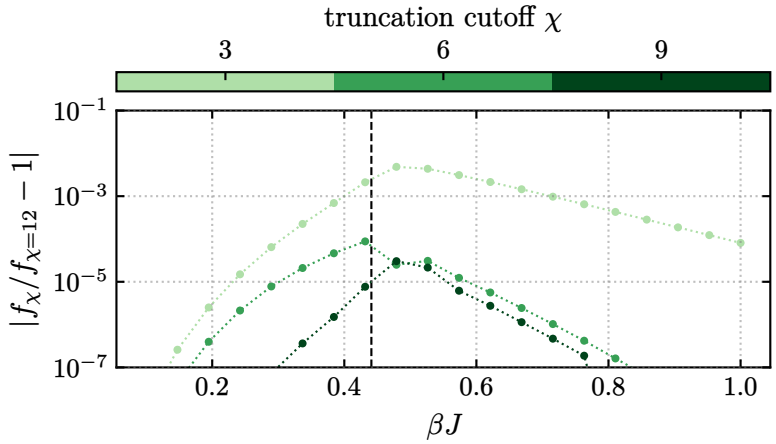

Figure 2.5: Convergence of the TRG ($n = 8$) free energies with χ. Specifically: absolute relative deviation of the $\chi = 3, 6, 9$ results from the $\chi = 12$ one. Notice the spikes at the critical point.

2.4 Working directly in the continuum

Previous Sections were entirely devoted to systems with a finite set of constituents, i.e. with discrete j. Given its versatility as a non-perturbative variational class, extending the TNS construction to quantum degrees of freedom living in a continuous space ($j \to x$) is not only an intriguing prospect, but also one particularly relevant for the scope of this Thesis, which ultimately aims at developing tools to study continuum (relativistic) QFT. This avenue was first explored with the introduction of continuous matrix product states (CMPS) [275] and then generalized to higher dimensions with the introduction of generic continuous TNS (CTNS) [276], which were later shown to emerge as the continuum limit of PEPS [230].

Additional difficulties arise when the variational principle is applied to relativistic fields [277, 278], as these are typically plagued by ultraviolet (UV) divergencies. As a result, the optimization will adjust the variational parameters of the CTNS toward fitting shorter and shorter distances, which dominate the energy density, paradoxically degrading the accuracy at physical length scales [278].

In this Section we review the CPEPS construction, focusing on Gaussian CPEPS (GCPEPS) — a subset of CPEPS allowing for straightforward analytical manipulation [230]. After having set the notation, we first identify the *parent Hamiltonian* of an arbitrary GCPEPS, namely the Hamiltonian having the GCPEPS as its (exact) ground state (Section 2.4A). Then we proceed in the opposite direction, and sketch two strategies to obtain the CPEPS approximation of the vacuum of a given QFT (Sections 2.4B and 2.4C). We highlight the mechanism leading to failure in relativistic contexts, discuss possible countermeasures, and we introduce a metric to asses the quality of the approximation (Section 2.4D). Finally, we benchmark the ability of GCPEPS to capture the (divergent) entanglement entropy of a free relativistic QFT (Section 2.4E).

CPEPS. Let $\varphi = \varphi_0$ be a (real[14], scalar) field on $\mathbb{R}^D$, with conjugate momentum $\pi = \pi_0$. A CPEPS [230] (equivalently, CTNS [276]) with χ *auxiliary* or *virtual* fields $\{\varphi_\alpha\}_{\alpha=1}^{\chi}$ is a state $|\Psi_W\rangle$ admitting the following path-integral representation[15]:

$$|\Psi_W\rangle = \int \mathcal{D}\{\varphi_\alpha\}_{\alpha=0}^{\chi}\, e^{-W(\{\varphi_\alpha\})}|\varphi_0\rangle \ . \tag{2.44}$$

Here $|\varphi_0\rangle$ is a field configuration eigenstate — i.e. an eigenfunctional of the field operator, $\hat{\varphi}(x)|\varphi_0\rangle = \varphi_0(x)|\varphi_0\rangle$ — and W is a local functional of all the fields[16]. We furthermore require W to be invariant under space rotations and translations. Finally, unless otherwise stated, we also assume W is first-derivative-order. It has been shown in [230] that Eq. (2.44) is the continuum limit of an ordinary PEPS with bond dimension χ. In this sense the number of auxiliary fields represents the continuum analogous of the bond dimension.

A recurrence relation. Integrating out the virtual fields one by one, starting from φ_χ, yields a sequence $\{W^{(M)}\}_M$ of functionals of the first $M+1$ fields $\Phi_M = \{\varphi_\alpha\}_{\alpha=0}^{M}$, implicitly defined by

$$W^{(\chi)} = W \ , \qquad \int \mathcal{D}\Phi_\chi\, e^{-W^{(\chi)}(\Phi_\chi)}|\varphi_0\rangle = \int \mathcal{D}\Phi_{\chi-1}\, e^{-W^{(\chi-1)}(\Phi_{\chi-1})}|\varphi_0\rangle = \dots \ . \tag{2.45}$$

Generally $W^{(M)}$ will not be local for $M < \chi$.

Gaussian CPEPS. Equation (2.44) yields a Gaussian state when W is quadratic, as seen immediately by integrating out virtual fields (Section 2.4A). In this case, translation invariance makes it particularly convenient to work in momentum space. A general first-derivative-order Gaussian CPEPS with all the desired properties is obtained setting[17]

$$W = \frac{1}{2}\int \mathrm{d}^D x \left[X_{\alpha\beta}\varphi_\alpha\varphi_\beta + Y_{\alpha\beta}\partial_j\varphi_\alpha\partial_j\varphi_\beta\right] = \frac{1}{2}\int \frac{\mathrm{d}^D k}{(2\pi)^D} W_{\alpha\beta}(k)\bar{\varphi}_\alpha\varphi_\beta \ , \tag{2.46}$$

where $X_{\alpha\beta}$, $Y_{\alpha\beta}$ are some constant symmetric matrices, $W_{\alpha\beta}(k) = X_{\alpha\beta} + k^2 Y_{\alpha\beta}$ and summation over repeated indices is implicit. $W_{\alpha\beta} = W_{\beta\alpha}$ and $W_{\alpha\beta}(-k) = W_{\alpha\beta}(k)$. Fields and their Fourier transforms are denoted in the same way, with their x or k argument omitted for brevity. They can be discerned from the integration measure.

[14] Reality is not restrictive as a complex field can always be decomposed in a real doublet.

[15] The Dirac ket $|\Psi\rangle = \int \mathcal{D}\varphi\, \Psi(\varphi)|\varphi\rangle$ is equivalent to the Schrödinger wavefunctional $\Psi : \varphi \mapsto \langle\varphi|\Psi\rangle$.

[16] Namely, $W(\{\varphi_\alpha\}) = \int \mathrm{d}^D x\, w(\{\varphi_\alpha(x)\}, \{\partial_j\varphi_\alpha(x)\}, \{\partial_j\partial_{j'}\varphi_\alpha(x)\}, \dots)$ for some function w of the fields $\{\varphi_\alpha\}_{\alpha=0}^{\chi}$ and a finite number of their derivatives.

[17] Recall that, for a real field, $\bar{\varphi}(k) = \varphi(-k)$ is not an independent degree of freedom.

2.4A Parent Hamiltonians

Gaussian CPEPS are ground states of quadratic models with dispersion relations that are *rational functions* of k^2. One way to see this is to compute explicitly the wavefunction by *contracting* the CTNS or, in other words, by integrating out the virtual fields $\{\varphi_\alpha\}_{\alpha=1}^{\chi}$. To this aim we isolate the physical field φ_0 in Eq. (2.46), recasting W as

$$\begin{aligned} W = \frac{1}{2}\int \frac{\mathrm{d}^D p}{(2\pi)^D}\frac{\mathrm{d}^D q}{(2\pi)^D} \sum_{\alpha\beta=1}^{\chi} \varphi_\alpha(p)(2\pi)^D\delta(p+q)W_{\alpha\beta}(p)\varphi_\beta(q) + \\ + \int \frac{\mathrm{d}^D k}{(2\pi)^D} \sum_{\alpha=1}^{\chi} \varphi_0(-k)W_{0\alpha}(k)\varphi_\alpha(k) + \frac{1}{2}\int \frac{\mathrm{d}^D k}{(2\pi)^D}\, \varphi_0(-k)W_{00}(k)\varphi_0(k)\ . \end{aligned} \tag{2.47}$$

The last term is not involved in the integration; as for the first two, we identify

$$\mathbf{s} \leftrightarrow \{\varphi_\alpha(k)\}_{\alpha>0,k}\,, \quad \mathbf{b} \leftrightarrow \{W_{\alpha 0}(k)\bar{\varphi}_0(k)\}_{\alpha>0,k}\,, \quad \mathbf{A}^{\pm 1} \leftrightarrow \{(2\pi)^D\delta(p+q)\mathbf{W}^{\pm 1}(p)\}_{pq}\,; \tag{2.48}$$

where $\mathbf{W}(k) = \mathbf{X} + \mathbf{Y}k^2$ is the $\alpha\beta > 0$ block of $W_{\alpha\beta}$, and $kpq \in \mathbb{R}^D$ — and recall that, for a positive definite, real, symmetric, $N \times N$ matrix A, we have the Gaussian integral

$$\begin{aligned} \int \mathrm{d}^N\mathbf{s}\, e^{-\left[\frac{1}{2}\mathbf{s}^{\mathrm{T}}\mathbf{A}\mathbf{s} \pm \mathbf{b}^{\mathrm{T}}\mathbf{s}\right]} &= \int \mathrm{d}^N\mathbf{s}\, e^{-\frac{1}{2}\left[\left[\mathbf{s}^{\mathrm{T}} \pm \mathbf{b}^{\mathrm{T}}\mathbf{A}^{-1}\right]\mathbf{A}\left[\mathbf{s} \pm \mathbf{A}^{-1}\mathbf{b}\right] - \mathbf{b}^{\mathrm{T}}\mathbf{A}^{-1}\mathbf{b}\right]} \\ &= \sqrt{\det 2\pi\mathbf{A}^{-1}}\, e^{+\frac{1}{2}\mathbf{b}^{\mathrm{T}}\mathbf{A}^{-1}\mathbf{b}}\ . \end{aligned} \tag{2.49}$$

The determinant in Eq. (2.49) is independent of $\mathbf{b}$ (i.e., φ_0) and can thus be adsorbed in the state normalization. In the end [230],

$$\Psi_W(\varphi) = \exp\left(-\frac{1}{2}\int \frac{\mathrm{d}^D k}{(2\pi)^D}\, \omega_\chi(k)\bar{\varphi}\varphi\right) \tag{2.50a}$$

with

$$\omega_\chi = W_{00} - \sum_{\alpha\beta=1}^{\chi} W_{0\alpha}[\mathbf{W}^{-1}]_{\alpha\beta}W_{\beta 0}\ ; \tag{2.50b}$$

resembling a Schrieffer-Wolff transformation [279]. The parent Hamiltonian of $|\Psi_W\rangle$ — i.e., the Hamiltonian having $|\Psi_W\rangle$ as its ground state — defines a free QFT with dispersion relation $\omega_\chi(k)$ [230]. It follows that the class of GCPEPS can represent exactly vacua of free QFTs with dispersions of the form Eq. (2.50b) — namely rational functions of k^2 with degree less or equal to $\chi + 1$ over χ. This is seen immediately rewriting $\mathbf{W}^{-1}$ in terms of the adjugate matrix $\operatorname{adj}\mathbf{W}$:

$$[\mathbf{W}^{-1}(k)]_{\alpha\beta} = \frac{\operatorname{adj}(\mathbf{X} + \mathbf{Y}k^2)_{\alpha\beta}}{\det(\mathbf{X} + \mathbf{Y}k^2)}\ . \tag{2.51}$$

Tridiagonal case. The case of a tridiagonal $W_{\alpha\beta} = u_\alpha \delta_{\alpha\beta} + v_\alpha \delta_{\alpha\alpha\pm1}$ is important both because it appears in physically relevant scenarios (see Section 2.4C), and because general results about the inverse $\mathbf{W}^{-1}$ can be found in literature [280–282]. Alternatively, a more explicit computation of $\omega_\chi(k)$ can be carried out integrating out virtual layers one by one, as per Eq. (2.45). In such case, all $W^{(M)}$ in Eq. (2.45) have the form[18] ($v_0 = 0$)

$$W^{(M)}(\Phi_M) = \frac{1}{2} \sum_{\alpha=0}^{M} \int \frac{\mathrm{d}^D k}{(2\pi)^D} \left[u_\alpha^{(M)}(k) \bar{\varphi}_\alpha \varphi_\alpha + v_\alpha(k) [\bar{\varphi}_{\alpha-1} \varphi_\alpha + \bar{\varphi}_\alpha \varphi_{\alpha-1}] \right] . \tag{2.52}$$

The integrating-out procedure induces a flow in the space of structure constants $u_\alpha^{(M)}$:

$$u_{M-1}^{(M-1)} = u_{M-1}^{(M)} - \frac{v_M^2}{u_M^{(M)}} , \qquad u_\alpha^{(M-1)} = u_\alpha^{(M)} \quad \forall \alpha < M-1 , \tag{2.53}$$

providing a (finite, generalized) continued fraction representation of the "fixed-point"

$$\omega_\chi(k) = u_0^{(0)} = u_0 - \cfrac{v_1^2}{u_1 - \cfrac{v_2^2}{\ddots \; - \cfrac{v_\chi^2}{u_\chi}}} , \qquad u_\alpha = u_\alpha^{(\chi)} . \tag{2.54}$$

2.4B Vacuum via rational approximants

We just characterized the parent Hamiltonian of a generic GCPEPS. The converse problem is arguably even more common. We thus now discuss how to find a, possibly approximate, (G)CPEPS representation of the vacuum Ω of a given QFT. Suppose the QFT's dispersion relation ω is known (exactly, e.g. for free models, or approximately [283]). Then a GCPEPS approximation of Ω with χ virtual fields can be obtained in two steps:

(i) identify a rational approximant ω_χ of ω of degree $\chi + 1$ over χ, e.g. via continued fractions or Padé approximants [230];

(ii) invert Eq. (2.50b), namely find the (possibly non unique) $W_{\alpha\beta}$ satisfying Eq. (2.50b).

If a continued fraction approximation is employed, the second step amounts to reading off the tridiagonal GCPEPS coefficients from Eq. (2.54). If the target dispersion relation is already a rational function of k^2, an exact GCPEPS representation of Ω with finite χ exists. Clearly this is only a subset of all possible free QFTs. Among the excluded models are paradigmatic examples, such as the Klein-Gordon field theory, which is characterized by $\omega(k) = \sqrt{m^2 + k^2}$, where m is the field mass, i.e. the inverse of the correlation length ξ.

[18] $W^{(\chi)} = W$ matches Eq. (2.52) by hypothesis and Gaussian integration preserves such structure.

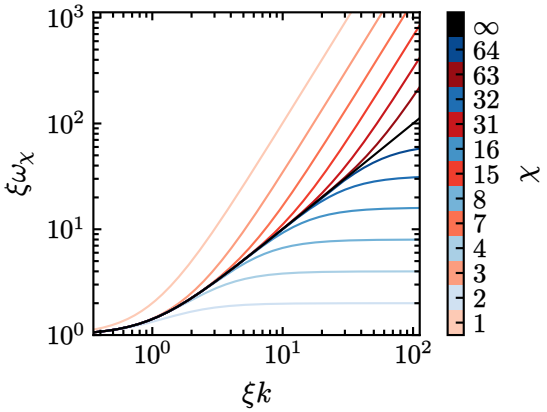

Figure 2.6: CPEPS approximants $\omega_\chi(k)$ of the Klein-Gordon dispersion relation $\omega(k)$ for different number χ of auxiliary fields ($\omega_\infty \equiv \omega$, black line).

Klein-Gordon. The Klein-Gordon (KG) field is the prototypical example of a relativistic QFT. It provides the ideal testbed for studying the consequences of approximating relativistic dispersions by means of a rational function of k^2, as dictated by Eq. (2.50b). The construction of a continued fraction converging to the KG dispersion relation — i.e., of a possible tridiagonal GCPEPS approximation of the KG vacuum — is detailed in [230]. For our purposes it is acceptable to work in one dimensional space, where the momentum vector k has a single component and there exist no space rotations. Then, assuming $m > 0$, a valid choice is also

$$\{u_\alpha\}_{\alpha=0}^{\chi} = \{m, 2m, 2m, \ldots\} \,, \qquad v_\alpha = ik \,; \tag{2.55}$$

which yields the continued fraction expansion centered in $k = 0$ and generated via recursion by the identity

$$\sqrt{m^2 + k^2} = m + \frac{k^2}{m + \sqrt{m^2 + k^2}} \,. \tag{2.56}$$

Figure 2.6 compares the exact dispersion relation $\omega_\infty = \omega$ (black line) with its finite χ approximant $\omega_\chi(k)$ obtained plugging Eq. (2.55) into Eq. (2.54). As expected, the approximation improves for larger χ, however the convergence is not uniform [230]. Qualitatively different behaviors arise for even χ (blue lines, converging from below) and odd χ (red, from above). Indeed, proceeding by induction it easy to see that

$$\omega_\chi(k) \underset{k\to\infty}{\sim} \begin{cases} k & \text{for } \chi = \infty \\ k^2/(m\chi) & \text{for } \chi \text{ odd} \\ m\chi & \text{for } \chi \text{ even} \end{cases} \,. \tag{2.57}$$

Ultimately, an infinite number of high-frequency modes are misrepresented by the GCPEPS for any finite χ [277], reflecting the fact that a rational function of k^2 can never reproduce the relativistic asymptotic behaviour $\omega(k) \sim k$. An interesting workaround is proposed

in [284], by modifying the state ansatz. It should be noted, however, that the approach seems somewhat rooted in a "free theory + interaction" splitting of the Hamiltonian and, most importantly, it relies on the exact solution of the free part to identify new non-local elementary position-space degrees of freedom (essentially Wannier functions).

Cutoff dependence. As previously discussed, no rational function of k^2 can reproduce relativistic dispersions for large momenta, in the continuum. However, as suggested in [230] one could introduce a UV regulator (cutoff) and let the parameters of the rational approximation flow with it. While this "renormalization group" strategy should allow for an improvement of the scaling towards the continuum limit, an explicit cutoff dependence makes some sort of regularization unavoidable, arguably partially defeating the purpose of introducing continuous tensor network states in the first place [277, 284]. Nonetheless, CMPS have been successfully combined with an explicit cutoff before [285, 286] and the strategy devised in [230] is nevertheless worthy of attention.

2.4C Vacuum via imaginary time evolution

For a gapped model, an approximate CPEPS description of the vacuum can be in principle obtained also without any knowledge about the dispersion relation, via imaginary time evolution. As we now show, in this case, the role of virtual fields can be interpreted as that of sampling the possible field configuration at past time slices.

The ground state $|\Omega\rangle$ of a gapped Hamiltonian $\hat{H}$ can be written as:

$$|\Omega\rangle \sim e^{-\tau \hat{H}} |\Psi_0\rangle \quad \text{for} \quad \tau \to \infty \,, \tag{2.58}$$

where $|\Psi_0\rangle$ is any state with non-vanishing overlap with $|\Omega\rangle$. Splitting the imaginary time interval $[-\tau, 0]$ in χ small segments of duration ϵ (Trotter step), let[19]

$$|\Omega_\chi\rangle = e^{-\chi\epsilon\hat{H}}|\Psi_0\rangle = \int \mathcal{D}\{\varphi_\alpha\}_{\alpha=0}^{\chi} |\varphi_0\rangle\langle\varphi_0|e^{-\epsilon\hat{H}}|\varphi_1\rangle\langle\varphi_1|\cdots e^{-\epsilon\hat{H}}|\varphi_\chi\rangle\langle\varphi_\chi|\Psi_0\rangle \tag{2.59}$$

Suppose the Hamiltonian decomposes[20] as $\hat{H} = H(\hat{\pi}, \hat{\varphi}) = T(\hat{\pi}) + V(\hat{\varphi})$. Since $\epsilon \ll 1$,

$$\begin{aligned} Z_\epsilon(\varphi_{\alpha-1}, \varphi_\alpha) := \langle\varphi_{\alpha-1}|e^{-\epsilon\hat{H}}|\varphi_\alpha\rangle &\approx \int \mathcal{D}\pi \langle\varphi_{\alpha-1}|\pi\rangle\langle\pi|e^{-\epsilon T(\hat{\pi})}e^{-\epsilon V(\hat{\varphi})}|\varphi_\alpha\rangle \\ &= \int \mathcal{D}\pi \, \exp\Big(i\pi\cdot[\varphi_{\alpha-1} - \varphi_\alpha] - \epsilon H(\pi, \varphi_\alpha)\Big) \,; \end{aligned} \tag{2.60}$$

where "$\cdot$" implies integration over space[21]. Taking the $\epsilon\chi \to \infty$ and $\epsilon \to 0$ limits[22], the

[19] $\epsilon\chi$ and ϵ play the role of IR and UV regulators, respectively.

[20] The result holds for any Weyl ordered Hamiltonian [25].

[21] Scalar product in $L^2(\mathbb{R}^D)$.

[22] Recall $\epsilon\sum_{\alpha=1}^{\chi} \to \int \mathrm{d}t$, $[\varphi_{\alpha-1} - \varphi_\alpha]/\epsilon \to \dot{\varphi_\alpha}(-\alpha\epsilon)$.

usual path-integral representation of the QFT vacuum functional is obtained:

$$\Omega(\varphi_0) \propto \int_{\varphi(t=0)\equiv\varphi_0} \mathcal{D}\pi\mathcal{D}\varphi \lim_{T\to-\infty} \langle\varphi(T)|\Psi_0\rangle \exp\int_{-\infty}^{0} \mathrm{d}t \left[i\pi(t)\cdot\dot{\varphi}(t) - H(\pi(t),\varphi(t))\right] \ , \tag{2.61}$$

where the path-integrands are now functions of both space and imaginary time t. For finite ϵ and χ, $|\Omega_\chi\rangle$ provides a CPEPS approximation of the vacuum with

$$W = -\log\prod_{\alpha=1}^{\chi} Z_\epsilon(\varphi_{\alpha-1},\varphi_\alpha) - \log\langle\varphi_\chi|\Psi_0\rangle \ . \tag{2.62}$$

The CPEPS auxiliary fields are snapshots of past imaginary times and W only intertwines fields from subsequent time steps.

Recurrence relation. For $|\Omega_\chi\rangle$, the recurrence relation Eq. (2.45) can be interpreted as a sequence of imaginary time approximations of the vacuum functional:

$$\Omega_0(\varphi) = \langle\varphi|\Psi_0\rangle \ , \qquad \Omega_M(\varphi) = \int \mathcal{D}\tilde{\varphi}\ Z_\epsilon(\varphi,\tilde{\varphi})\ \Omega_{M-1}(\tilde{\varphi}) \ . \tag{2.63}$$

At least at the formal manipulation level, it is convenient to set $|\Psi_0\rangle = \int\mathcal{D}\varphi|\varphi\rangle$. Then, $\Omega_0 = 1$ and the overlaps in Eqs. (2.59), (2.61) and (2.62) disappear. The practical usefulness of Eq. (2.63) remains limited: quadratic models aside, solving the path-integral is highly nontrivial.

Quadratic Hamiltonian. If the Hamiltonian is quadratic in π, the path-integrals over π can be carried out substituting the integrand with its value at the stationary point[23] $\pi = \pi_{\mathrm{cl}}$ [137]. For $T(\pi) = \int\mathrm{d}^D x\,\pi^2/2$,

$$\pi_{\mathrm{cl}} = \frac{\delta H}{\delta\pi}(\pi_{\mathrm{cl}},\varphi_\alpha) = i\frac{\varphi_{\alpha-1}-\varphi_\alpha}{\epsilon} \xrightarrow[\epsilon\to0]{} i\dot{\varphi}(-\alpha\epsilon) \ , \tag{2.64}$$

and the exponent in Eq. (2.60) becomes simply

$$-\log Z_\epsilon(\varphi_{\alpha-1},\varphi_\alpha) = \epsilon H\left(\frac{\varphi_{\alpha-1}-\varphi_\alpha}{\epsilon},\varphi_\alpha\right) = \frac{\epsilon}{2}\int\mathrm{d}^D x\left[\frac{\varphi_{\alpha-1}-\varphi_\alpha}{\epsilon}\right]^2 + \epsilon V(\varphi_\alpha) \tag{2.65}$$

For a free field with dispersion relation $\omega(k)$, in momentum space,

$$V(\varphi) = \frac{1}{2}\int\frac{\mathrm{d}^D k}{(2\pi)^D}\ \omega^2(k)\bar{\varphi}\varphi \ . \tag{2.66}$$

[23] Up to a possibly divergent multiplicative constant which can be reabsorbed in the normalization.

Then, recalling Eq. (2.62), and using

$$\sum_{\alpha=1}^{\chi}\int \mathrm{d}^D x \left[\varphi_{\alpha-1} \pm \varphi_\alpha\right]^2 = \int \frac{\mathrm{d}^D k}{(2\pi)^D} \sum_{\alpha=1}^{\chi} [\overline{\varphi}_{\alpha-1} \pm \overline{\varphi}_\alpha][\varphi_{\alpha-1} \pm \varphi_\alpha]$$
$$= \int \frac{\mathrm{d}^D k}{(2\pi)^D} \left[\overline{\varphi}_0\varphi_0 + 2\sum_{\alpha=1}^{\chi-1} \overline{\varphi}_\alpha\varphi_\alpha + \overline{\varphi}_\chi\varphi_\chi \pm \sum_{\alpha=1}^{\chi}\left[\overline{\varphi}_{\alpha-1}\varphi_\alpha + \overline{\varphi}_\alpha\varphi_{\alpha-1}\right]\right] \tag{2.67a}$$

and

$$\int \frac{\mathrm{d}^D k}{(2\pi)^D}\left[\overline{\varphi}_{\alpha-1}\varphi_\alpha + \overline{\varphi}_\alpha\varphi_{\alpha-1}\right] = 2\int \frac{\mathrm{d}^D k}{(2\pi)^D}\overline{\varphi}_{\alpha-1}\varphi_\alpha \ ; \tag{2.67b}$$

we get

$$W = \frac{1}{2}\int \frac{\mathrm{d}^D k}{(2\pi)^D}\left[\left[\frac{2}{\epsilon} + \epsilon\omega^2(k)\right]\sum_{\alpha=1}^{\chi}\overline{\varphi}_\alpha\varphi_\alpha + \frac{1}{\epsilon}\overline{\varphi}_0\varphi_0 - \frac{1}{\epsilon}\overline{\varphi}_\chi\varphi_\chi - \frac{2}{\epsilon}\sum_{\alpha=1}^{\chi}\overline{\varphi}_{\alpha-1}\varphi_\alpha\right] . \tag{2.68}$$

We could also evaluate the potential V in $[\varphi_\alpha + \varphi_{\alpha-1}]/2$, then

$$W = \frac{1}{2}\int \frac{\mathrm{d}^D k}{(2\pi)^D}\left[u(k)\left[\overline{\varphi}_0\varphi_0 + \overline{\varphi}_\chi\varphi_\chi + 2\sum_{\alpha=1}^{\chi-1}\overline{\varphi}_\alpha\varphi_\alpha\right] - 2v(k)\sum_{\alpha=1}^{\chi}\overline{\varphi}_{\alpha-1}\varphi_\alpha\right] , \tag{2.69a}$$

with

$$u, v = \frac{1}{\epsilon} \pm \frac{\epsilon\omega^2}{4} \ . \tag{2.69b}$$

Equations (2.68), (2.69) and similarly obtained variations differ only by $\mathcal{O}(\epsilon)$ terms and are thus equivalent in the $\epsilon \to 0$ limit but some may still exhibit better convergence than others (analogously to improved actions in lattice field theory).

Because imaginary time evolution only intertwines virtual fields at subsequent time steps, the resulting GCPEPS are always tridiagonal, and Eqs. (2.52) to (2.54) apply. Moreover, due to time translation invariance, their coefficients are uniform (namely, α independent) in the bulk of the time interval $1 < \alpha < \chi$; and

$$\{u_\alpha\}_{\alpha=0}^{\chi} = \{u + \mathcal{O}(\epsilon), 2u, 2u, \ldots, u_\chi\} \ , \qquad v_\alpha = v \ . \tag{2.70}$$

The u_χ term is irrelevant in the $\chi \to \infty$ limit, therefore the continued fraction approximation of a square root is once again recovered, up to $\mathcal{O}(\epsilon)$ artifacts:

$$\lim_{\chi\to\infty} \omega_\chi(k) = \sqrt{u^2 - v^2} + \mathcal{O}(\epsilon) \ . \tag{2.71}$$

This applies to both Eqs. (2.68) and (2.69) — to leading order in ϵ and exactly, respectively.

Therefore, in the $\chi \to \infty$ and $\epsilon \to 0$ limits, the exact dispersion relation ω is recovered[24]:

$$\text{Eq. (2.68)}: \quad \lim_{\chi\to\infty} \omega_\chi(k) = \left[\epsilon^{-1}\sqrt{\left[1+\tfrac{\epsilon^2\omega^2}{2}\right]^2 - 1} + \mathcal{O}(\epsilon)\right] = \omega + \mathcal{O}(\epsilon) \ , \tag{2.72a}$$

$$\text{Eq. (2.69)}: \quad \lim_{\chi\to\infty} \omega_\chi(k) = \epsilon^{-1}\sqrt{\left[1+\tfrac{\epsilon^2\omega^2}{4}\right]^2 - \left[1-\tfrac{\epsilon^2\omega^2}{4}\right]^2} = \omega \ . \tag{2.72b}$$

Generally ω is not a finite polynomial of k, translating in arbitrarily high derivative terms in position-space and manifesting the non-local nature of vacuum wavefunctionals, such as that from the Klein-Gordon case discussed above. A counterexample is provided by (massive deformations of) Lifshitz models.

Lifshitz models. Lifshitz models describe non-relativistic scale invariant systems which exhibit anisotropic scaling between space and time, also known as Lifshitz scaling:

$$t \to \lambda^z t \ , \quad x \to \lambda x \ , \quad \lambda > 0 \ . \tag{2.73}$$

Quoting [287], "*Lifshitz theories with (even) positive integer z possess the remarkable feature that their ground state wavefunctional takes a local form*". For the free Lifshitz field, Eq. (2.73) mandates $\omega(k) = \gamma|k|^z$, where $\gamma > 0$ is a dimensionless parameter [288]. For even z, the absolute value can be dropped, leaving a finite-derivative-order local ground state wavefunctional. Lifshitz scale invariance implies the absence of a gap and thus prevents the convergence of imaginary time evolution, however massive deformations preserving the finite-polynomial nature of $\omega(k)$ have been considered in literature for $z = 2$ [287], corresponding to $\omega(k) = m^2 + \gamma k^2$.

There is an important (yet expected) lesson to be learnt: imaginary time evolution is not guaranteed to give the optimal CPEPS representation of a vacuum wavefunctional with the given number of auxiliary fields. Indeed, we just identified a class of ground states which are local wavefunctionals, admitting an exact representation as a CPEPS with $\chi = 0$ auxiliary fields. Yet, imaginary time evolution gives an approximate CPEPS representation of them for any finite χ and only converges to the exact result for $\chi = \infty$, as per Eq. (2.72).

2.4D Fidelity

Fidelity — namely the absolute square of the overlap of a quantum state with a given target state — is a key metric in assessing the quality of state preparation. It thus lends itself naturally also to estimating the convergence of previous ground state preparation protocols. A formal expression for the fidelity F of two CPEPS follows directly from Eq. (2.44). Integrating out all auxiliary fields, it simply becomes the overlap between two wavefunctionals.

[24] $\omega(k) > 0 \ \forall k$ is assumed.

Let $\Psi_A(\varphi) = e^{-A(\varphi)}$ and analogously for Ψ_B. Assuming A and B are real,

$$F = \frac{|\langle\Psi_A|\Psi_B\rangle|^2}{\langle\Psi_A|\Psi_A\rangle\langle\Psi_B|\Psi_B\rangle} = \left[\int \mathcal{D}\varphi\, e^{-2A(\varphi)}\right]^{-1} \left[\int \mathcal{D}\varphi\, e^{-2B(\varphi)}\right]^{-1} \left[\int \mathcal{D}\varphi\, e^{-(A+B)(\varphi)}\right]^2 . \tag{2.74}$$

Generic path-integrals are involved; A and B are generally not even be local if they are obtained by integrating out, as in Eq. (2.45). When A and B are small perturbations of quadratic functionals, perturbative expansion is viable. Alternatively, for each integral in Eq. (2.74), saddlepoint approximation yields

$$\begin{aligned}\int \mathcal{D}\varphi\, e^{-W(\varphi)} &= e^{-W_{\mathrm{cl}}} \int \mathcal{D}\varphi\, e^{-\int \mathrm{d}^D x \int \mathrm{d}^D y\ \frac{1}{2}[\varphi(x)-\varphi_{\mathrm{cl}}(x)]W''_{\mathrm{cl}}(xy)[\varphi(y)-\varphi_{\mathrm{cl}}(y)]+\dots} \\ &= e^{-W_{\mathrm{cl}}} \left[\det \frac{W''_{\mathrm{cl}}}{2}\right]^{-\frac{1}{2}} + \mathcal{O}(\hbar) \\ &= \exp\left(-W_{\mathrm{cl}} - \frac{1}{2}\operatorname{tr}\log\frac{W''_{\mathrm{cl}}}{2}\right) + \mathcal{O}(\hbar)\ , \end{aligned} \tag{2.75}$$

where W_{cl}, W''_{cl} are W and its second φ-derivative, evaluated at the minimum point φ_{cl} of W. In the second to last step we performed the change of variable $\varphi \to \varphi + \varphi_{\mathrm{cl}}$, neglected higher $\hbar$-order terms $(\dots)$, and carried out Gaussian integration. Plugging in Eq. (2.74),

$$\log F = -2[C_{\mathrm{cl}} - A_{\mathrm{cl}} - B_{\mathrm{cl}}] + \operatorname{tr}\log\frac{2\sqrt{A''_{\mathrm{cl}}B''_{\mathrm{cl}}}}{C''_{\mathrm{cl}}} + \mathcal{O}(\hbar) = \operatorname{tr}\log\frac{2\sqrt{A''_{\mathrm{cl}}B''_{\mathrm{cl}}}}{A''_{\mathrm{cl}} + B''_{\mathrm{cl}}} + \mathcal{O}(\hbar)\ . \tag{2.76}$$

In the last step we assumed A and B share the same minimum point.

The above derivation is non-perturbative (the expansion is in $\hbar$, not in some coupling). Nevertheless, obtaining A, B, or their minimum often requires perturbative calculations. Of course, in the Gaussian CPEPS case all the above is exact. A'' is constant (in φ) and, working in k-space, proportional to the dispersion relation

$$A''(pq) \equiv A''_{\mathrm{cl}}(pq) = (2\pi)^D \delta(q-p)\omega_A(p) \tag{2.77}$$

(same for B). Unsurprisingly, in this case the F becomes a measure of the functional distance between the dispersion relations ω_A and $\omega_B(k)$:

$$\log F = \operatorname{vol}\Sigma \int \frac{\mathrm{d}^D k}{(2\pi)^D} \log\frac{2\sqrt{\omega_A(k)\omega_B(k)}}{\omega_A(k)+\omega_B(k)}\ . \tag{2.78}$$

In deriving Eq. (2.78) we observed that, for any function f,

$$\operatorname{tr} f(A'',B'') = (2\pi)^D\delta(0)\int\frac{\mathrm{d}^D k}{(2\pi)^D} f(\omega_A(k),\omega_B(k)) = \operatorname{vol}\Sigma\int\frac{\mathrm{d}^D k}{(2\pi)^D} f(\omega_A(k),\omega_B(k))\ ; \tag{2.79}$$

where in the last step $\delta(0)$ was regularized by moving to a finite volume space Σ. The resulting $\mathrm{vol}\,\Sigma$ prefactor in Eq. (2.78) shows that the fidelity decays exponentially with the system size, a manifestation of Anderson's orthogonality catastrophe [230, 289]. To recover an IR finite quantity in the infinite volume limit it is convenient to introduce the fidelity per unit volume $\mathcal{F} = \lim_{\mathrm{vol}\,\Sigma\to\infty} F^{1/\,\mathrm{vol}\,\Sigma}$.

2.4E Entanglement content

The amount of entanglement which ordinary TNS (ones involving a finite number degrees of freedom) can capture is usually bounded by some function of the bond dimension χ. For instance, $S \sim |\partial \mathrm{A}| \log \chi$ for a subregion A of a MPS or 2D PEPS [58]. Devising similar bounds for CTNS is an ambitious goal. Indeed, it is not even clear wether a connection between the maximum entanglement that can be stored in a CTNS and the number of auxiliary fields χ exists at all. Furthermore, entanglement entropy is known to be a UV divergent quantity in QFT, where every (finite) patch of space hosts an infinite number of degrees of freedom [290]. It follows that, in answering the above questions, it is crucial to identify finite (or, better universal [291]) entanglement quantifiers. On a more positive note, general results obtained for free theories are typically expected to hold for interacting ones as well [291]. A relevant excerpt from Ref. [291] reads:

> *[...] In d spatial dimensions we should have for any QFT*
>
> $$S(V) = g_{d-1}[\partial V]\,\epsilon^{-(d-1)} + ... + g_1[\partial V]\,\epsilon^{-1} + g_0[\partial V]\,\log(\epsilon) + S_0(V)\,, \quad (2.80)$$
>
> *where $S_0(V)$ is a finite part, ϵ is a short distance cutoff, and the g_i are local and extensive functions on the boundary ∂V, which are homogeneous of degree i. [...]. This area law is a consequence of the large number of degrees of freedom at high energies present in the QFT which induce entanglement across the boundary ∂V. [...]*
>
> *These terms proportional to g_i for $i > 0$ are not physical within QFT since they are not related to quantities well defined in the continuum. On the contrary, the coefficient g_0 of the log term is expected to be universal (in this review we use the word universal in the sense of independence of the regularization prescription or of the microscopic model used to obtain the continuum QFT at distances large with respect to the cutoff). [...]*

Universal quantities related to the entropy are the mutual information $I(\mathrm{A},\mathrm{B})$ between non-intersecting regions and, in one spatial dimension, the entropic c-function $c(r)$ [291]:

$$I(\mathrm{A},\mathrm{B}) = S(\mathrm{A}) + S(\mathrm{B}) - S(\mathrm{A}\cup\mathrm{B})\,, \qquad c(r) = r\frac{dS(r)}{dr}\,. \quad (2.81)$$

We study the entanglement properties of the GCPEPS representation of the ground state of a free relativistic real scalar field. The theory was chosen because exact results on its

vacuum entanglement are easily found in literature, e.g. [242, 243]. We attack the problem numerically, by introducing a lattice regularization and following the real-time approach for a free real lattice boson in [291, Sec. 2.2.1]. According to [291], the vacuum reduced density matrix ρ_{A} (and thus its Von Neumann entropy) of a subsystem A can be expressed solely in terms of the 2-point functions of degrees of freedom situated inside A:

$$\mathbf{X} = \Big\{\langle\varphi_x\varphi_y\rangle\Big\}_{xy\in\mathrm{A}} \ , \qquad \mathbf{P} = \Big\{\langle\pi_x\pi_y\rangle\Big\}_{xy\in\mathrm{A}} \ . \tag{2.82}$$

In particular, the entanglement entropy of the associated bipartition reads

$$S = \mathrm{tr}\left((\mathbf{C}+1/2)\log(\mathbf{C}+1/2) - (\mathbf{C}-1/2)\log(\mathbf{C}-1/2)\right) \ , \qquad \mathbf{C} = \sqrt{\mathbf{X}\mathbf{P}} \ . \tag{2.83}$$

For a quadratic model,

$$\mathbf{X}_{xy} := \langle\varphi_x\varphi_y\rangle = \frac{1}{2}(\mathbf{O}^{-1/2})_{xy} \ , \quad \mathbf{P}_{xy} := \langle\pi_x\pi_y\rangle = \frac{1}{2}(\mathbf{O}^{+1/2})_{xy} \ , \quad \langle\varphi_x\pi_y\rangle = \frac{i}{2}\delta_{xy} \ ; \tag{2.84}$$

where $\mathbf{O}$ is the Fourier transform[25] of $\omega^2(k)$:

$$\sum_k \omega^2(k)\varphi_k^2 = \sum_{xy}\varphi_x\left[\sum_k \omega^2(k)e^{ik[x-y]}\right]\varphi_y =: \sum_{xy}\varphi_x\mathbf{O}_{xy}\varphi_y \ . \tag{2.85}$$

It follows that ρ_{A} and S are completely specified by the dispersion relation ω (and A).

We already know from Section 2.4A that (at finite χ) Gaussian CPEPS fail at reproducing $\omega(k)$ asymptotically. For this reason we do not expect the GCPEPS Klein-Gordon vacuum to capture the correct continuum limit scaling of S from Eq. (2.80). In what follows we verify this claim numerically. Since all the terms in Eq. (2.80) specific of $d > 1$ are unphysical (cutoff dependent), a first meaningful answer can be given already in one spatial dimension.

Working on a periodic lattice of length L and spacing a, we study the Klein-Gordon vacuum given by Eqs. (2.54) and (2.55). The dispersion relation is modified by lattice artifacts[26] according to [44]

$$k \to \tilde{k} = \frac{2}{a}\sin\frac{ak}{2} \ , \qquad \tilde{k} \approx k \quad \text{when} \quad ak \ll 1 \ . \tag{2.86}$$

Figure 2.7 shows the entanglement entropy S from Eq. (2.83) for a bipartition of the ring, as a function of the chord length ℓ of either one of the two intervals A, namely

$$\ell(\mathrm{A}) = \frac{L}{\pi}\sin\frac{\pi|\mathrm{A}|}{L} \ , \qquad \ell(\bar{\mathrm{A}}) = \ell(\mathrm{A}) \ , \qquad \ell \approx |\mathrm{A}| \quad \text{when} \quad |\mathrm{A}| \ll L \ ; \tag{2.87}$$

[25] The Fourier normalization convention is irrelevant in the above equations. On the other hand, orthonormality is required if spectral decomposition is used to evaluate the square root of O and its reciprocal directly in Fourier space (as done in the numerical code).

[26] We neglect finite volume corrections.

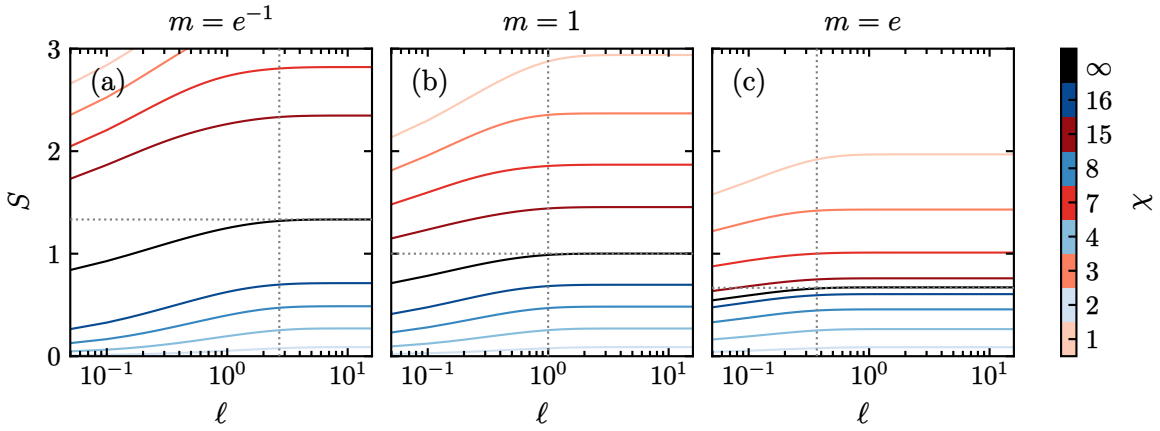

Figure 2.7: Bipartition entanglement entropy S from Eq. (2.83) of the GCPEPS approximation of the Klein-Gordon vacuum, as given by Eqs. (2.54) and (2.55). Subsystems of different chord lengths ℓ and various numbers χ of auxiliary fields are shown. Regulators: $a = 1/e^3$ (UV), $L = 50$ (IR). The horizontal dashed line is the area law entanglement bound from Eq. (2.88); the vertical dashed line marks the chord length associated with the correlation length, $\ell(\xi) \approx \xi = 1/m$.

where $\bar{\mathrm{A}}$ is the complement of A, $|\bar{\mathrm{A}}| = L - |\mathrm{A}|$. In periodic boundary conditions, for the exact vacuum one expects [243].

$$S(\ell) \sim \bar{S} = (c/3)\log(\xi/a) \quad \text{for} \quad \ell \gg \xi \gg a \ . \tag{2.88}$$

As the figure shows, the PEPS representation converges to the exact curve (black) for increasing χ — from below (above) for even (odd) χ. Convergence is faster when the gap m is larger. Conversely, $\bar{S}$ (horizontal line in figure) is a better approximation for small m — i.e. closer to the scaling limit $\xi \gg a$ under which Eq. (2.88) was derived.

Before comparing the continuum scaling with Eq. (2.80), a thermodynamic limit result, we make sure that finite size effects are negligible in our numerical results for S. Figure 2.8 (IR) shows this is the case already for $L = 10\xi$ (the figure reports $\chi = \infty$ results, but the same holds for finite χ). Working in this regime, Fig. 2.8 (UV) shows the scaling of $\bar{S}$ with a. The exact result Eq. (2.88) (dashed line, $c = 1$, as expected for a scalar field) is correctly reproduced for $\chi = \infty$ (black line) but not at finite χ:

$$\bar{S} \underset{a\to 0}{\sim} S_{0,\chi} + \begin{cases} (1/3)\log(\xi/a) & \text{for } \chi = \infty \\ \log(\xi/a) & \text{for } \chi \text{ odd} \\ 0 & \text{for } \chi \text{ even} \end{cases} , \qquad S_{0,\infty} = 0 \ . \tag{2.89}$$

Each scaling is symptomatic of a different value of the g_0 coefficient in Eq. (2.80). Even though S is an ill defined divergent quantity in the continuum, g_0 is expected to be universal

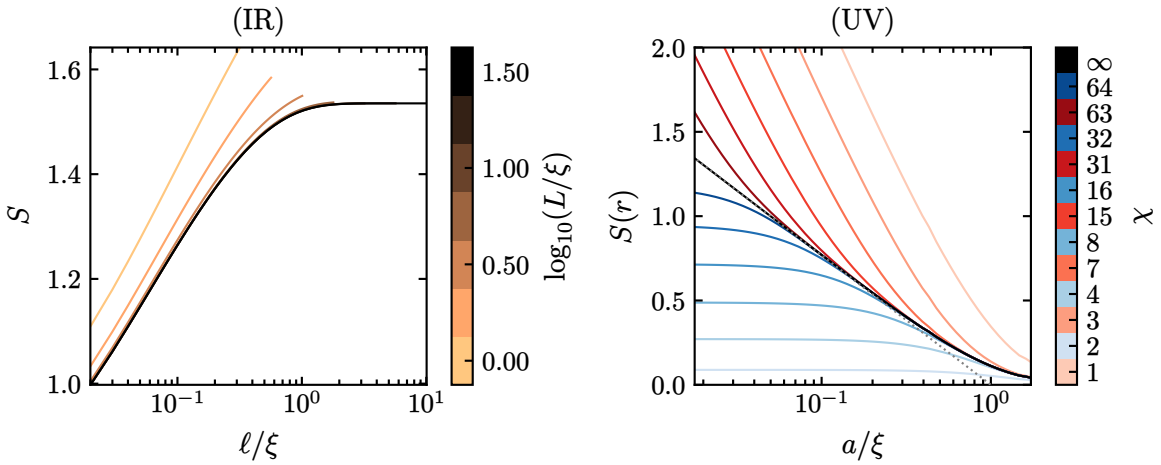

Figure 2.8: Thermodynamic (IR) and continuum (UV) limit behaviour of the GCPEPS entanglement entropy. Specifically: (IR) $L/\xi \to \infty$ convergence of the profiles from Fig. 2.7 — with $a/\xi = 10^{-2}$, $\chi = \infty$; and (UV) $a/\xi \to 0$ scaling of $S(r) \approx \bar{S}$ — with $L/\xi = 100$, $r = \lfloor 10\xi/a \rfloor a \gg \xi$ ($r/\xi \to 10$ for $a \to 0$).

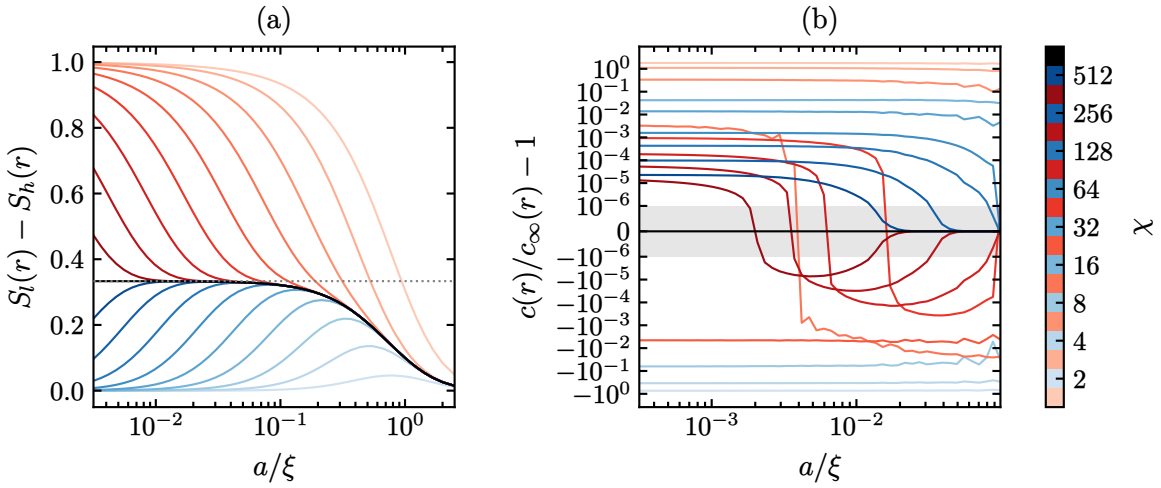

Figure 2.9: Continuum scaling of UV finite entanglement quantities. Specifically: (a) $S(r) \approx \bar{S}$ difference between two fields l, h of different mass with $m_h/m_l = e$, $\xi = 1/m_l$, $r \approx \sqrt{10}\xi$ (up to finite spacing displacements), $L = 10\xi$ — the dashed line marks the expected $\bar{S}_l - \bar{S}_h = (1/3)\log(m_h/m_l) = 1/3$ from Eq. (2.88); (b) entropic c-function $c(r)$ — relative deviation from the $\chi = \infty$ result — for $r \approx \xi/\sqrt{10}$, $L = \sqrt{10}\xi$. The gray shaded area has a linear y-scale. The color code is as in previous plots: red, blue and black lines are obtained for an odd, even, and infinite number of virtual fields, respectively.

[291]. The GCPEPS failure at reproducing its value originates necessarily in the asymptotic behavior Eq. (2.57) of $\omega(k)$ and is thus expected to transcend the specific choice of CTNS coefficients from Eq. (2.55) (see discussion of Fig. 2.6). The mechanism leading to the different scaling is not obvious but it can be safely argued that the high-energy modes do not produce the usual divergence in the even χ case — where the the band becomes flat at large momenta. Indeed, flat bands lead to highly localized eigenstates and have been found to result in weaker entanglement in the Kitaev ladder [292]. An outlook for this study consists in deriving (analytically) the asymptotic scaling of S for $a \to 0$, possibly extending the relativistic result [242, 243] to the non-relativistic finite χ dispersion relations.

In Fig. 2.9 we report the continuum limit scaling of two entanglement related UV finite quantities. Figure 2.9a shows the difference between the entanglement entropy of two Klein-Gordon fields (l and h) with different masses[27], at $r \gg \xi$ ($\xi = \xi_l = 1/m_l$ being the longest correlation length in the system). In agreement with Eq. (2.89), these converge precisely to the "universal" coefficient from Eq. (2.80): $g_0 = 0, 1, 1/3$ for $\chi = \text{even}, \text{odd}, \infty$ respectively — showing once again the failure of the GCPEPS approximation. Figure 2.9b, on the other hand, gives a more optimistic outlook. It shows that increasing χ the GCPEPS estimate of the entropic c-function Eq. (2.81) is converging to its exact (finite) value in the continuum limit. Indeed, their relative deviation from the correct value (i) becomes cutoff independent at small enough a, and (ii) is strictly decreasing with χ.

[27] Contrarily to intuition, this is not just an entirely artificial quantity put together comparing two different models. Indeed, it can be formulated as an entanglement property of a physically realizable system, consisting of the two coexisting, decoupled fields. Then S_l is the Von Neumann entropy of the reduced density matrix $\rho_{\mathrm{A},l}$, obtained tracing out the l degrees of freedom living outside A, plus all those associated with h. Analogously for S_h.

3

Entanglement Generation in Lattice QED_2 Collisions

probing the real-time scattering dynamics

We study numerically entanglement generation during meson-meson collisions in (1+1)*−dimensional quantum electrodynamics* (QED_2)*, by means of tensor networks. In this endeavour, we develop a toolset relevant for a broader class of quantum field theories. The scattering problem for relativistic fields is framed, defining asymptotic states and S-matrix elements. A protocol to extract the latter from real-time lattice simulations is put forward. The theory of staggered lattice fermions is solved exactly. Building upon this solution, we show how to prepare approximate asymptotic* QED_2 *meson wave packets with given momentum and position distributions. We simulate elastic meson-meson collisions, computing some scattering amplitudes and characterizing the entanglement observed during the dynamics. The remnant entanglement between the scattering products is quantified: we find it obeys a scaling relation and identify two regimes of entanglement production.*

Attribution: Most of this chapter reports on original work on the TN simulation of QED_2 scatterings, which has been published in Ref. [115]. The groundwork for this study was laid in Ref. [131], this includes the lattice S-matrix prescription in Section 3.1A, a solution of the staggered fermion Hamiltonian equivalent to that given in Section 3.2, as well as the initial state preparation protocol from Section 3.4B. The introduction to the scattering problem in Section 3.1 is heavily indebted also to Refs. [26, 137].

3.1 The scattering problem

Ever since the pioneering work by Rutherford, Geiger and Marsden, that led to the discovery of the nucleus [293, 294], scattering experiments have been one of the primary strategies by which physicists validate theoretical models and unveil new phenomena across all energy scales. Contemporary applications range from low-energy neutron scatterings in crystallography and material science [295], to high-energy collisions — e.g. those carried out at the large hadron collider (LHC) — probing the interactions of the fundamental building blocks of the universe.

The paradigmatic scattering experiment consists in preparing the system by specifying its content in localized and far-distant regions of space to resemble that of a single particle. This initial state of, typically two, effectively non-interacting particles is then let evolve, the particles approach each other and interact. In this stage, the multi-particle state interpretation is lost; it is recovered when the products of the collision emerge again as well separated excitations with no mutual interaction. Transition amplitudes are measured comparing the appearance of this final state with that of the initial one.

In order to gain physical insights from a scattering process, performing the experiment is often not enough: we also need to extract from theory testable predictions to compare to. To date, on the numerical side, this has been achieved mostly via Monte-Carlo simulation. Here the scattering problem is attacked from a different angle: real-time dynamics simulation via tensor network methods, introduced in Chapter 2. This Section prepares the ground for numerical simulations: we first introduce the theoretical description of a scattering process, and then lay out a prescription for extracting predictions from dynamical lattice simulations. Practically, this means relating the particle content of the initial (infinite past) and final (infinite future) states of a scattering process [137]. Ideally, one would want $\lim_{t\to\infty} e^{-2itH}$, where H is the Hamiltonian of the model. However, this limit involves infinitely oscillating phases and thus does not exist; nor does $\lim_{t\to\pm\infty}|\Psi(t)\rangle$, where $|\Psi(t)\rangle = e^{-itH}|\Psi\rangle$ is the state of a system undergoing a collision. To cure this problem, the *asymptotic evolution* has to be factored out [26, 296]. This procedure results in the definition of the central quantity in scattering theory, namely the scattering matrix or *S-matrix* [137]:

$$S = \Omega_+^\dagger \Omega_- \ , \quad \Omega_\pm = \lim_{t\to\pm\infty} e^{+itH} e^{-itH_0} \ ; \tag{3.1}$$

where H_0 is the Hamiltonian describing the free kinematics of the stable particle states of the theory defined by H. Equation (3.1) is motivated by the assumption[1] that the interaction decays rapidly enough so that, at asymptotic times $t \to \pm\infty$, when particles are far apart, the evolution specified by H coincides with that of H_0, and the scattering solution $|\Psi(t)\rangle$ approaches the trajectories of some freely evolving particle states $|\Phi_\pm\rangle$; i.e. $e^{-itH}|\Psi\rangle \sim e^{-itH_0}|\Phi_\pm\rangle$. We shall now make this picture more precise and concrete.

[1] This assumption is not generally justified but it is known to hold when the theory has a mass gap [26, 296–298], as in the QED$_2$ case [102, 299].

Particles. According to Wigner's classification [300], *particles* are identified with subspaces of the Hilbert space $\mathscr{H}$, which: (i) are orthogonal to the vacuum $|\Omega\rangle$, (ii) correspond to an isolated mass shell, and (iii) carry an *irreducible* (projective, unitary or antiunitary) representation of the symmetry group of the theory. A particle specie, i.e. one irreducible symmetry-invariant subspace, is singled out by some quantum numbers, to be identified. Although the discussion generalizes easily, the focus here is on relativistic theories. Then, besides the mass M, associated with spacetime translations, in $D > 1$ there is a quantum number $J \in \mathbb{Z}^*/2$ associated with the generators of rotations, plus possibly other labels related to the internal symmetry group, which can be analyzed separately[2]. Inside such a subspace, a state can be singled out specifying its spatial momentum $\mathbf{p}$, and possibly a spin projection σ and an internal group irrep index, e.g. a color for $\mathbf{3}$ of SU(3). States specified in this way are called *single-particle states*[3] and denoted $|p\sigma\alpha\rangle$: α collects all the remaining discrete labels, including one identifying the particle specie, and p is the on-shell energy-momentum:

$$p = (p^0, \mathbf{p}) = \{p^\mu\} \,, \quad p^0 = \sqrt{M^2 + \mathbf{p}^2} \,. \tag{3.2}$$

By definition, under Poincaré transformations, single-particle states transform as [137]

$$\mathscr{U}(\Lambda, a)|p\sigma\alpha\rangle = \sqrt{\frac{(\Lambda p)^0}{p^0}} \exp(-ia_\mu p^\mu) \sum_{\sigma'} W^{(\alpha)}_{\sigma'\sigma}(\Lambda, p)|(\Lambda p)\sigma'\alpha\rangle \,. \tag{3.3}$$

Here $\Lambda \in \mathrm{O}(1, D)$ is a Lorentz transformation, $a \in \mathbb{R}^{1,D}$ is a translation, and $W^{(\alpha)}(\Lambda, p)$ is a representative of the little group[4] of particle type α. The coefficient in front of the right hand side makes the normalization of these (improper) momentum eigenstates,

$$\langle q\tau\beta|p\sigma\alpha\rangle = \delta^D(\mathbf{q} - \mathbf{p})\delta_{\tau\sigma}\delta_{\beta\alpha} \,, \tag{3.4}$$

consistent under Poincaré transformations [137].

Importantly, in the above definitions, there is no reference to the particle being "elementary" with respect to the degrees of freedom of the theory. This is crucial in confined theories, such as quantum chromodynamics (QCD). There, at sufficiently low temperatures, the relevant particles are internal group singlets (hadrons) and correspond to *bound states* excited by composite operators rather than by the colour charged quark and gluon fields that appear in the Hamiltonian of the theory [25]. As discussed in more detail in the next Sections, an analogous phenomenon takes place in (1+1)-dimensional quantum electrodynamics.

---

[2] The Coleman-Mandula nogo theorem [301] states that, under reasonable assumptions, continuous external and internal symmetries have to be combined in the "trivial" way, meaning that the overall symmetry group is their direct product. The theorem does not hold in $D = 1$ [118].

[3] The term *bound state* is also used in some literature [302]. Here we reserve it for composite particles. Strictly speaking, any state inside a particle subspace is a single-particle state. The abuse of terminology is due to the nice transformation properties of these (improper) momentum eigenstates, which makes it convenient to single them out. This will be especially true when discussing states of multiple particles.

[4] In one space dimension the little group SO(1) is trivial, thus $W(\Lambda, p) \equiv 1$ for all particle types [131, 136].

Asymptotic scattering states. *Free multi-particle states* are defined as states that transform in a *tensor product* of symmetry irreps, that is, as a product of single-particle states. In particular, for spacetime translations,

$$\mathscr{U}(\mathbf{I}, a)|\{p_k \sigma_k \alpha_k\}\rangle = e^{-ia_\mu \hat{P}^\mu}|\{p_k \sigma_k \alpha_k\}\rangle = \exp\Big(-ia_\mu \sum_k p_k^\mu\Big)|\{p_k \sigma_k \alpha_k\}\rangle \,, \tag{3.5}$$

where k indexes the particles in the state. Free multi-particle states are normalized via a condition analogous to Eq. (3.4) but that also takes into account the indistinguishability of identical particles and their bosonic or fermionic statistics,

$$\langle\{q_k \tau_k \beta_k\}_{k=1}^N|\{p_j \sigma_j \alpha_j\}_{j=1}^M\rangle = \delta_{NM} \sum_{\mathfrak{S}} \operatorname{sgn}\mathfrak{S} \prod_i \delta^D(\mathbf{q}_{\mathfrak{S}i} - \mathbf{p}_i)\delta_{\tau_{\mathfrak{S}i}\sigma_i}\delta_{\beta_{\mathfrak{S}i}\alpha_i} \,, \tag{3.6}$$

where $\mathfrak{S}$ is a permutation of $1, \dots, N$ and $\operatorname{sgn}\mathfrak{S}$ is -1 if an odd number of fermions exchanges is involved, $+1$ otherwise. It follows from Eq. (3.5) that these states are energy and momentum eigenstates belonging to the continuous part of the mass spectrum. Their total energy equates the sum of the energies of their "constituents", whence the "free" attribute. The above transformation law also implies that multi-particle states cannot be localized and are time translation invariant. These states are clearly an idealization and they are not realized in the Hilbert space of interacting theories. On the other hand, superpositions of free multi-particle states can be localized and are realized as asymptotic configurations in nontrivial scattering processes. At least, this happens when the theory has a *mass gap*, namely when in the mass spectrum there is a finite separation between the vacuum and the lowest-lying single-particle state. This guarantees that the interaction decays sufficiently fast [26, 297] and asymptotically particles are effectively non-interacting. In the following we always assume a mass gap.

In the Schrödinger picture[5], the scattering process is described by a *scattering solution* $|\Psi(t)\rangle = e^{-itH}|\Psi\rangle$. Assume that $t = 0$ occurs during the collision. At asymptotic times, $|\Psi(t)\rangle$ approaches the "trajectories" of smooth wave packets of free multi-particle states:

$$|\Psi(t)\rangle \sim \int \mathrm{d}\{\mathbf{p}_k\} \sum_{\{\sigma_k, \alpha_k\}} \phi_\pm(\{p_k, \sigma_k, \alpha_k\}) \, \exp\Big(-it \sum_k p_k^0\Big)|\{p_k \sigma_k \alpha_k\}\rangle \tag{3.7}$$

for $t \to \pm\infty$. Equation (3.7) implicitly defines an Hamiltonian H_0 capturing the asymptotic dynamics of H as the one encoding the free evolution of the multi-particle wave packets[6]. Labelling the latter $|\Phi_\pm\rangle$, we can write Eq. (3.7) more concisely as $e^{-itH}|\Psi\rangle \sim e^{-itH_0}|\Phi_\pm\rangle$.

[5] The Schrödinger picture is not well suited for non-perturbative continuum QFT because it requires sharp time localization [26]. Yet, the aim of this presentation is to prepare the ground for the description of scattering in a lattice theory with a finite and discrete spacetime.

[6] Note that here we are assuming that the past and future asymptotic dynamics is the same or, equivalently, that the initial and final asymptotic Hilbert spaces coincide. This is not necessarily the case [137].

Inverting it,

$$|\Psi\rangle = \lim_{t\to\pm\infty} e^{+itH} e^{-itH_0} |\Phi_\pm\rangle = \Omega_\pm |\Phi_\pm\rangle \ . \tag{3.8}$$

If the (strong) limits exist[7], it defines the Møller operators $\Omega_\pm$, that intertwine states and observables of the asymptotic theory with those of the full interacting theory [26]. Assuming this is the case, scattering solutions are completely determined by their infinite past or infinite future asymptote, and we can use $\phi_\pm$ to label them

$$|\Psi\rangle = \Omega_\pm |\Phi_\pm\rangle = |\phi_-, \text{in}\rangle = |\phi_+, \text{out}\rangle \ . \tag{3.9}$$

That is, $|\phi_-, \text{in}\rangle$ denotes the state that, evolving with H, approaches the free H_0 trajectory of the $t = 0$ wave packet $|\Phi_-\rangle$ for $t \to -\infty$; analogously for $|\phi_+, \text{out}\rangle$. Scattering theory is concerned precisely with the relation between the two "bases" $|\cdot, \text{in}\rangle$ and $|\cdot, \text{out}\rangle$.

S-matrix. If all the probability amplitudes for a state approaching a generic asymptotic configuration in the far past to approach any configuration in the distant future are given, the outcome of any scattering experiment is known. As anticipated at the beginning of this Section, these amplitudes are the S-matrix elements:

$$\langle \{q_k \tau_k \beta_k\}, \text{out} | \{p_k \sigma_k \alpha_k\}, \text{in}\rangle = \langle \{q_k \tau_k \beta_k\} | S | \{p_k \sigma_k \alpha_k\}\rangle \ , \tag{3.10}$$

where limit of narrow momentum space wave packets is implied [137]. Let us stress that S-matrix elements are precisely the coefficients of the expansion of $|\cdot, \text{in}\rangle$ states in terms of $|\cdot, \text{out}\rangle$ states. Transition probabilities are their absolute square. Often spin polarizations are not measured experimentally; then the relevant probability is obtained averaging over the initial polarizations σ_k and summing over final ones τ_k [25].

3.1A *S*-matrix from real-time lattice simulations

The infinite time limits in the above discussion are clearly just a useful idealization [298]: in real world experiments, measurements are carried out at times t_i, t_f that precede and follow the collision by time lapses much larger than the microscopic timescale of the collision itself, but still finite. If the wave packet spreads over a energy range ΔE, then $t \to \pm\infty$ should read $-t_i, t_f \gg 1/\Delta E$ [137]. The measurements should then reveal a state that approximates a free multi-particle wave packet with a degree of precision related to that of the time limit. It follows that the transition amplitudes measured experimentally are

$$\mathcal{A}(\Phi \to \Phi') = \langle \Phi'(t_f) | e^{-i(t_f - t_i)H} | \Phi(t_i)\rangle \ , \tag{3.11}$$

with $|\Phi(t_i)\rangle$ and $|\Phi'(t_f)\rangle$ approximate wave packets of free multi-particle eigenstates.

[7] Besides existence, another important property of $\Omega_\pm$ is their range, which has implications on the isometry/unitarity of the S-matrix in Eq. (3.1). In particular, one speaks of *asymptotic completeness* if every $|\Psi\rangle \in \mathscr{H}$ is either a bound state or a scattering state, namely one that can be written as Eq. (3.8) [303].

The same reasoning applies if the collision takes place in a finite spacetime, such as a lattice. Once the delicate issue of preparing multi-particle wave packets has been addressed (see, e.g., Section 3.4B), evaluating the amplitudes in Eq. (3.11) via tensor network simulations is straightforward. The initial state $|\Phi(t_i)\rangle$ is evolved using standard algorithms (Section 2.2) until some scattering products emerge, after the collision, in the form of well separated particle wave packets. An first clue on how well the evolving state resembles a state of isolated particles is obtained, e.g., comparing local observables to their vacuum expectation value. Once the desired separation is reached, the evolution is terminated and we can compute the overlap of the final state with any $|\Phi'(t_f)\rangle$ we are interested in.

In principle it is also possible to extract the S-matrix elements in Eq. (3.10) from lattice tensor network simulations. In order to bridge from the finite-time amplitudes in Eq. (3.11) to S-matrix elements, the free evolution of the wave packets from t_i, t_f to the collision time $t = 0$ has to be compensated for[8], and appropriate limits have to be taken. Writing,

$$\langle \Phi' | S | \Phi \rangle = \lim_{t_i, t_f \to \mp\infty} \langle \Phi' | e^{+iH_0 t_f} e^{-i(t_f - t_i)H} e^{-iH_0 t_i} | \Phi \rangle = \lim_{t_i, t_f \to \mp\infty} \langle \Phi'(t_f) | e^{-i(t_f - t_i)H} | \Phi(t_i) \rangle \ , \quad (3.12)$$

we see that $\mathcal{A}(\Phi \to \Phi')$ corresponds to an approximate (due to the finite times) and smeared (due to the momentum spread of the wave packets) S-matrix element. To correctly identify which S-matrix element is being computed, $|\Phi(t_i)\rangle, |\Phi'(t_f)\rangle$ and $|\Phi\rangle, |\Phi'\rangle$ have to be related, either simulating the H_0 evolution or, if the masses of the particles in the wave packet are known, transforming the wave packet amplitude as per Eq. (3.7). In order to extrapolate the exact S-matrix element between initial and final states of definite momentum, multiple simulations can be run, increasing $T = |t_i| = |t_f|$ and, simultaneously, shrinking the momentum support $\|\Delta \mathbf{p}\|$ of the reference wave packets $|\Phi\rangle$ and $|\Phi'\rangle$. In doing so, the lattice size L has to be increased to accommodate for the spreading particles. The thermodynamic limit thus reads $L, T, 1/\|\Delta \mathbf{p}\| \to \infty$. Finally, the continuum limit should be taken as well. For an alternative TN approach, based on the Lippmann-Schwinger formalism, see [304].

3.2 Exact solution of staggered fermions

A prerequisite for the description of a scattering process is the identification of the model's particles and their asymptotic-times dynamics [26, 296]. In the absence of bound states or long range interactions, the aforementioned task consists in finding the plane wave solutions of the free part of the Hamiltonian [26].

Here we solve exactly the lattice theory of free staggered fermions in (1+1)-dimensions, defined in Section 1.4A, for periodic boundary conditions. An analogous derivation carries over in the thermodynamic limit, with momentum sums replaced by integrals over the

[8] Recall that the reference wave packet states in Eq. (3.9) are defined at a common time $t = 0$.

Brillouin zone [131]. We compute the energy-momentum spectrum, construct the Fock space, and finally study some features of the infinite mass limit, $m \to \infty$.

Let us recall the Hamiltonian from Eq. (1.95):

$$H = \sum_x \left[\frac{i}{2} \psi^\dagger_{x+1} \psi_x + \text{H.c.} + m(-1)^x \psi^\dagger_x \psi_x \right] . \tag{3.13}$$

In the thermodynamic limit or for periodic boundaries the model is translation invariant. Valid translations, however, are generated by shifts of two lattice steps [186]. It is sometimes convenient to isolate the even and odd sublattices, $\mathrm{E} = \Lambda \cap (2\mathbb{Z})$ and $\mathrm{O} = \Lambda \cap (2\mathbb{Z}+1)$. We define the (complementary) orthogonal projectors

$$\Pi_{xr} = \frac{1 + (-1)^{x+r}}{2} , \quad r \in \mathbb{Z}_2 . \tag{3.14a}$$

Via pointwise product, Π_{x0} (Π_{x1}) projects a field on its even (odd) sublattice component. On top of the usual

$$\Pi_{xs}\Pi_{xt} = \Pi_{xs}\delta_{st} , \quad \textstyle\sum_r \Pi_{xr} = 1 , \tag{3.14b}$$

we have the following useful properties:

$$(-1)^x \Pi_{xr} = (-1)^r \Pi_{xr} , \quad \Pi_{(x+1)r} = \Pi_{x(r+1)} . \tag{3.14c}$$

With these projectors, we introduce the staggered doublet field

$$\zeta_x = (\zeta_{xr})_{r\in\mathbb{Z}_2} , \qquad \zeta_{xr} = \Pi_{xr}\psi_x , \qquad \psi_x = \sum_r \zeta_{xr} ; \tag{3.15}$$

and its Fourier transform ζ_k,

$$\zeta_k = \frac{1}{\sqrt{2\pi}} \sum_x e^{-ikx} \zeta_x , \qquad \zeta_x = \frac{1}{\sqrt{2\pi}} \frac{2\pi}{L} \sum_k e^{+ikx} \zeta_k . \tag{3.16}$$

In momentum space, Π_{xr} becomes

$$\Pi_{kr} = \sqrt{2\pi} \left[\frac{2\pi}{L}\right]^{-1} \frac{\delta_{k0} + (-1)^r \delta_{k\pi}}{2} , \tag{3.17}$$

projecting on the π-periodic and π-antiperiodic parts of a field through convolution:

$$\zeta_{kr} = \frac{1}{\sqrt{2\pi}} \Pi_{kr} * \psi_k , \quad \zeta_{(k+\pi)r} = (-1)^r \zeta_{kr} . \tag{3.18}$$

Often, π periodicities make it convenient to work with the effective momentum space $\Lambda^{*\prime} = \Lambda^* \cap [-\pi/2, \pi/2[$; we denote sums restricted to $\Lambda^{*\prime}$ by $\sum'$.

Spectrum. In terms of the doublet ζ_x, the Hamiltonian reads

$$H = \frac{1}{2}\sum_x \left[\zeta^\dagger_{x+1}\begin{pmatrix} 0 & i \\ i & 0\end{pmatrix}\zeta_x + \zeta^\dagger_x \begin{pmatrix} +m & 0 \\ 0 & -m\end{pmatrix}\zeta_x + \text{H.c.}\right]; \tag{3.19a}$$

Fourier transforming,

$$H = \frac{1}{2}\frac{2\pi}{L}\sum_k \left[\zeta^\dagger_k \begin{pmatrix} +m & ie^{-ik} \\ ie^{-ik} & -m\end{pmatrix}\zeta_k + \text{H.c.}\right] \tag{3.19b}$$

$$= \frac{2\pi}{L}\sum_k \zeta^\dagger_k \begin{pmatrix} +m & \sin k \\ \sin k & -m\end{pmatrix}\zeta_k \ . \tag{3.19c}$$

Equation (3.19c) is a sum of quadratic forms, one for each Fourier mode k, diagonalized by the unitary boost matrices V_k,

$$V_k = \frac{\sqrt{m+\omega_k}}{\sqrt{2\omega_k}}\begin{pmatrix} 1 & +v_k \\ -v_k & 1\end{pmatrix}, \quad V_k V_k^\dagger = 1\,; \tag{3.19d}$$

with,

$$\omega_k = \sqrt{m^2+\sin^2 k}, \quad v_k = \frac{\sin k}{m+\omega_k}\,. \tag{3.19e}$$

Notice that $v_k \to 0$ and $V_k \to \mathbf{1}$ for $m \to \infty$. Introducing

$$(c_k, d^\dagger_{-k}) = \sqrt{2}\, V_k \zeta_k \tag{3.19f}$$

the Hamiltonian becomes

$$H = \frac{2\pi}{L}{\sum_k}' \omega_k \left[c^\dagger_k c_k - d_k d^\dagger_k\right]. \tag{3.19g}$$

In the last step we recognized that the quadratic forms of the k and $k+\pi$ modes are degenerate and restricted the sum to $\Lambda^{*\prime}$.

Explicit expressions for $c^\dagger_k$ and $d^\dagger_k$ in terms of the position space fields, $\psi^\dagger_x$ and ψ_x, are obtained combining the previous results. We report them below for reference:

$$c^\dagger_k = \frac{\sqrt{2}}{\sqrt{2\pi}}\frac{\sqrt{m+\omega_k}}{\sqrt{2\omega_k}}\sum_x e^{ikx}\left[\Pi_{x0} + v_k \Pi_{x1}\right]\psi^\dagger_x\,, \tag{3.20a}$$

$$d^\dagger_k = \frac{\sqrt{2}}{\sqrt{2\pi}}\frac{\sqrt{m+\omega_k}}{\sqrt{2\omega_k}}\sum_x e^{ikx}\left[\Pi_{x1} - v_k \Pi_{x0}\right]\psi_x\,. \tag{3.20b}$$

Moreover, by Eqs. (3.18) and (3.19),

$$c^\dagger_{k+\pi} = +c^\dagger_k\,, \qquad d^\dagger_{k+\pi} = -d^\dagger_k\,. \tag{3.21}$$

To avoid redundancies we take the operators c_k and d_k as defined only for $k \in \Lambda^{*\prime}$. With this caveat, they satisfy the same canonical anticommutation relations of ψ_x,

$$[c_p, c_q^\dagger] = \left[\frac{2\pi}{L}\right]^{-1} \delta_{pq} \ , \quad [d_p, d_q^\dagger] = \left[\frac{2\pi}{L}\right]^{-1} \delta_{pq} \ , \tag{3.22}$$

while other fundamental commutators vanish. Indeed,

$$\begin{aligned} [\zeta_{ps}, \zeta_{qt}^\dagger] &= \frac{1}{2\pi} \sum_{yz} e^{-ipy+iqz} \, [\psi_y, \psi_z^\dagger] \, \Pi_{ys} \Pi_{zt} \\ &= \frac{1}{2\pi} \sum_{yz} e^{-i(p-q)y} \, \delta_{yz} \delta_{st} \, \Pi_{ys} \\ &= \left[\frac{2\pi}{L}\right]^{-1} \delta_{st} \frac{\delta_{pq} + (-1)^s \delta_{p(q+\pi)}}{2} \ . \end{aligned} \tag{3.23}$$

On $\Lambda^{*\prime}$, only the first Kronecker delta contributes and Eq. (3.22) follows by unitarity of V_k.

Using the $d_k, d_k^\dagger$ anticommutator, H can be rewritten as a positive semidefinite operator minus a constant. The constant term, namely $\sum_k' \omega_k$, incorporates both ultraviolet and infrared divergencies when the respective regulators are released, making the continuum limit ill defined. Dropping it by a normal ordering prescription[9], the free staggered fermions energy-momentum operator reads

$$P^\mu = (H, P) = \frac{2\pi}{L} \sum_k{}' k^\mu \left[c_k^\dagger c_k + d_k^\dagger d_k\right] \ , \quad k^\mu = (\omega_k, k) \ . \tag{3.24}$$

Equation (3.24) shows that $c_k^\dagger$ and $d_k^\dagger$ create excitations of energy-momentum k^μ:

$$[P^\mu, c_k^\dagger] = k^\mu c_k^\dagger \ , \quad [P^\mu, d_k^\dagger] = k^\mu d_k^\dagger \ . \tag{3.25}$$

It also identifies ω_k in Eq. (3.19e) as the staggered fermion dispersion relation. Its derivative ω_k' gives the group velocity of fermion and antifermion wave packets on the lattice.

Fock space. The ground state or vacuum $|\Omega\rangle$, is the state with no excitations to destroy:

$$c_k|\Omega\rangle = d_k|\Omega\rangle = 0 \ , \quad P_\mu|\Omega\rangle = 0 \ , \quad \langle\Omega|\Omega\rangle = 1 \ . \tag{3.26}$$

The Fock space of all (normalized and antisymmetrized) single- and multi-particle states of the theory is generated by acting on $|\Omega\rangle$ with strings of creation operators $c_k^\dagger$ and $d_k^\dagger$:

$$|q_N \dots q_1; p_M \dots p_1\rangle = d_{q_N}^\dagger \cdots d_{q_1}^\dagger \, c_{p_M}^\dagger \cdots c_{p_1}^\dagger |\Omega\rangle \ , \tag{3.27}$$

[9] This is, in fact, a basic example of the renormalization procedure mentioned in Section 1.3 [305].

with $p_i, q_j \in \Lambda^{*\prime}$. For instance, by Eqs. (3.22) and (3.26),

$$\langle p|p'\rangle = \left[\frac{2\pi}{L}\right]^{-1} \delta_{pp'} \ , \quad \langle q|q'\rangle = \left[\frac{2\pi}{L}\right]^{-1} \delta_{qq'} \ . \tag{3.28}$$

In terms of c_k and d_k, the global U(1) charge Q reads

$$Q = \sum_x \zeta_x^\dagger \zeta_x = \frac{2\pi}{L} \sum_k \zeta_k^\dagger \zeta_k = \frac{2\pi}{L} {\sum_k}' \left[c_k^\dagger c_k - d_k^\dagger d_k\right] \ , \tag{3.29}$$

an half-filling constant $L/2$ was discarded by normal ordering. Equation (3.29) shows that d-type excitations (antifermions) are the antiparticles of c-type excitations (fermions).

Infinite mass limit. The theory simplifies greatly when $m \gg 1$. For instance, in the non-relativistic $m \to \infty$ limit Hamiltonian is dominated by the mass term and the ground state approaches the "bare vacuum", i.e. the Néel product state $|\Omega\rangle = |0101\ldots\rangle$. Moreover, Eq. (3.20) reduces to

$$c_k^\dagger = \frac{\sqrt{2}}{\sqrt{2\pi}} \sum_{x\in \mathrm{E}} e^{ikx} \psi_x^\dagger \ , \qquad d_k^\dagger = \frac{\sqrt{2}}{\sqrt{2\pi}} \sum_{x\in \mathrm{O}} e^{ikx} \psi_x \ . \tag{3.30}$$

We conclude that, in this limit, fermion and antifermion excitations are supported on the even (E) and odd (O) sublattices, respectively. Indeed, $c_k^\dagger$ and $d_k^\dagger$ become simply the Fourier transforms of $\psi_x^\dagger|_{\mathrm{E}}$ and $\psi_x|_{\mathrm{O}}$. For a fermion wave packet with momentum space probability density function (PDF) $|\phi_k|^2$,

$$\frac{2\pi}{L} {\sum_k}' \phi_k c_k^\dagger = \sum_x \tilde{\phi}_x^C \psi_x^\dagger \ , \tag{3.31}$$

where $\tilde{\phi}_x$ (as a function on E) is the inverse Fourier transform of ϕ_k (as a function on $\Lambda^{*\prime}$):

$$\tilde{\phi}_x^C\Big|_{\mathrm{E}} = \frac{\sqrt{2}}{\sqrt{2\pi}} \frac{2\pi}{L} {\sum_k}' e^{ikx} \phi_k \ . \tag{3.32}$$

It follows from the isometry of the Fourier transform that $|\tilde{\phi}_x|^2$ is also a PDF for $m \to \infty$. An analogous result holds for antifermion wave packets, $\tilde{\phi}_x^D$, on O. Let us stress that $|\tilde{\phi}_x|^2$ is *not* a PDF at finite m. That it becomes one at $m \to \infty$ reflects the fact that, in this limit, $\psi_x^\dagger|_{\mathrm{E}}$ and $\psi_x|_{\mathrm{O}}$ create orthonormal states $|x\rangle$ when acting on $|\Omega\rangle$.

In the continuum limit the distinction between even and odd sites becomes irrelevant and

$$\tilde{\phi}_x = \tilde{\phi}_x^{C,D} = \frac{1}{\sqrt{2\pi}} \int_{-\infty}^{+\infty} \mathrm{d}k \, e^{iky} \phi_k \ . \tag{3.33}$$

3.3 Two reformulations of lattice QED_2

Quantum electrodynamics in 1+1 dimensions (QED_2, a.k.a. *Schwinger model* [113, 114]) is arguably the simplest gauge invariant fermionic quantum field theory that can be written. It thus provides an optimal testbed for new numerical and analytical approaches to the study of gauge theories. The model has been solved exactly in the case of zero bare fermion mass [113, 114]. Despite its simplicity, the model has properties that made it a widespread toy model of chromodynamics — such as *confining behaviour*, *chiral symmetry breaking* and the generation of a *mass gap* [116–118]. Here we always take the fermion to be massive, in which case the lack of an exact solution [306] is partially compensated for by a zoo of lattice studies [299, 307–318], including TN [102, 104, 110, 319–327] and quantum [73, 328–339] simulation ones.

The 1D U(1) Kogut-Susskind Hamiltonian in Eq. (1.118) for one fermion specie reads [185]

$$H = \sum_x \left[\frac{i}{2} \psi^\dagger_{x+1} U_x \psi_x + \text{H.c.} + m(-1)^x \psi^\dagger_x \psi_x + \frac{g^2}{2} (E_x)^2 \right] ; \tag{3.34}$$

it involves a staggered fermion matter field living on the lattice sites, ψ_x, called *electron*; as well as (unitary) gauge parallel transporter U_x and (Hermitian) electric field gE_x operators supported on lattice links. In the U(1) case, the gauge algebra simplifies to

$$[U_y, E_z] = \delta_{yz} U_y \, . \tag{3.35}$$

On each given link, the above is just the commutation relation of angular variables: the electric field generates phase rotations of the parallel transporter, while the latter act as ladder (lowering) operator for the electric field. An irreducible representation of Eq. (3.35) on a given link (left implicit) reads [185, 340]:

$$E|\mathscr{E}\rangle = \mathscr{E}|\mathscr{E}\rangle \, , \quad U|\mathscr{E}\rangle = |\mathscr{E}-1\rangle \, , \quad \mathscr{H}_{\text{link}} = \text{span}(\{|\mathscr{E}\rangle : \mathscr{E} \in \sigma(E) = \mathbb{Z}\}) \, , \tag{3.36}$$

where $\sigma(E)$ denotes the spectrum of the operator E. Gauge operators on different links commute, thus the representation in Eq. (3.36) extends trivially to the whole chain. There exist infinite other unitarily inequivalent representations related to Eq. (3.36) by a shift of the electric field: $E \to E + \delta$, $0 < \delta < 1$ [340]. Here we assume $0 \in \sigma(E)$ on all links. As a side remark, an accidental feature of the (compact) lattice formulation and its discrete E spectrum, quantized in integer units [185], is the solution of the clash between Gauss law and canonical commutation relations, encountered quantizing continuum electromagnetism (Eq. 1.85). Indeed, there cannot exist a generator A of infinitesimal electric field shifts, $[A, gE] = i$, such that we could define $U = U_{\theta=1}$ as an element of a one-parameter family of operators $U_\theta = e^{ig\theta A}$ obeying $[U_\theta, E] = U_\theta$ for all $\theta \in \mathbb{R}$.

Integrating out the electric field. For U(1), the physical state condition in Eq. (1.124) reduces to the lattice version of ordinary Gauss law[10]:

$$\mathcal{G}_x|\Psi_{\text{phys}}\rangle = 0 \ \ \forall x \ , \qquad \mathcal{G}_x = E_x - E_{x-1} - \rho_x \ , \qquad \rho_x = N_x + \frac{1-(-1)^x}{2} \ . \tag{3.37}$$

Given a configuration $|\mathscr{E}\rangle$ of one gauge link, say $(z, z+1)$, and a configuration $|\{\mathscr{N}_x\}\rangle$ of all matter d.o.f., in 1D there is one and only one electric field assignment $\{\mathscr{E}_x\}$ complying with Gauss law. Assuming $x > z$,

$$\mathscr{E}_x = \mathscr{E} + \sum_{z<y\leq x} \left[\mathscr{N}_y + \frac{1-(-1)^y}{2}\right] ; \tag{3.38}$$

similarly for $x < z$. Extending by linearity, $|\mathscr{E}\rangle \otimes |\{\mathscr{N}_x\}\rangle$ vectors provide a basis for $\mathscr{H}_{\text{phys}}$, which is thus unitarily equivalent to $\mathscr{H}_{\text{link}} \otimes \mathscr{H}_{\text{free}}$, where $\mathscr{H}_{\text{free}}$ is the Hilbert space of free staggered fermions. Once Eq. (3.38) has been enforced, there is no longer a propagating gauge field (one d.o.f. per site), reflecting the fact that in one space dimension there are no transverse polarizations available to the massless "photon" field [188]. Another consequence of the lack of transverse directions is that a classical point charge generates a constant electric field, just like a uniform surface charge does in 3D [188]. Therefore, isolated charges correspond to states of infinite energy in the thermodynamic limit and are thus unphysical (confinement). Such states are typically discarded via boundary conditions: by Eq. (3.38), periodic boundaries clearly forbid charged sectors, $Q = \sum_x \rho_x \neq 0$; the same holds for open boundaries, if the electric field is required to vanish at spatial infinity. In the latter case, also the last surviving gauge d.o.f. is eliminated, and $\mathscr{H}_{\text{phys}} \cong \mathscr{H}_{\text{free}}$. Consequently, a free theory operator O is also defined on $\mathscr{H}_{\text{phys}}$ and can be extended to a (gauge invariant) dressed operator $\overline{O}$ on the whole $\mathscr{H}$. Conversely, as far as gauge independent properties of the model are concerned, gauge invariant QED$_2$ operators can be expressed in the $|\{\mathscr{N}_x\}\rangle$ basis. For instance, in this basis, the restriction of the Hamiltonian to the physical subspace reads [308]:

$$H = H_{\text{free}} + \frac{g^2}{2} \sum_x \left[\sum_{y<x} \rho_y\right]^2 , \tag{3.39}$$

where H_{free} is the free staggered fermion Hamiltonian from Eq. (3.13).

In Chapter 1 we stressed how gauge theories are a redundant description of a system. Here, by explicitly solving Gauss law, we successfully removed the gauge redundancy of the model (together with gauge invariance). The above reformulation is convenient for some derivations carried out in this Chapter — however, it comes at a price: the Hamiltonian in Eq. (3.39) contains *non-local* interactions.

[10] The definition of ρ_x used here corresponds to a calibration of the charge density normal ordering on the large mass limit. See Eqs. (2.119) to (2.122) in Ref. [131]. Regardless of the specific calibration, $\sigma(N_x) = \{0, 1\}$ and Eq. (3.37) is thus compatible with a (rescaled) electric field quantized in integer units.

Cyclic electric field truncation. In order to avoid long-range interactions, in numerical simulations we keep the (redundant) link degrees of freedom. Their infinite dimensional local Hilbert space is truncated introducing a cutoff $\mathscr{E}_{\max}$ in the $|E|$ spectrum and imposing $U|-\mathscr{E}_{\max}\rangle = |+\mathscr{E}_{\max}\rangle$; in this way $\sigma(E)$ is identified with $\mathbb{Z}_n$, $n = 2\mathscr{E}_{\max}+1$. This truncation spoils the commutator in Eq. (3.35), explicitly breaking the U(1) gauge invariance of the model down to the $\mathbb{Z}_n$ residual symmetry group of $\exp(-i\sum_x \theta_x \mathcal{G}_x)$ transformations with parameters $\theta_x \in ()\mathbb{Z}$ [208, 209, 311, 341]. The physical state condition in Eq. (3.37) is accordingly weakened and the Gauss law only holds modulo n:

$$\exp\left(-\frac{2\pi i}{n}\mathcal{G}_x\right)|\Psi_{\text{phys}}\rangle = |\Psi_{\text{phys}}\rangle \quad \forall\, x\ . \tag{3.40}$$

It has been shown that the $\mathbb{Z}_3$ model gives already an excellent approximation of the exact QED$_2$ ground state [319, 342], and is also capable of reproducing accurately some dynamical processes of the untruncated theory, the quality of the approximation depends on the value of the model parameters and the specific process under consideration [315, 330].

3.4 Lattice QED$_2$ meson-meson collisions

This Section reports on our simulations of meson-meson collisions in $\mathbb{Z}_n$-truncated QED$_2$. After having outlined the simulation set up (Section 3.4A) we introduce the initial state preparation protocol (Section 3.4B). Its development has been guided by the well understood example of the free fermion theory. For this reason, the free staggered fermion Hamiltonian in Eq. (3.13) have also been simulated. We then discuss the scattering phenomenology and compute some scattering amplitudes (Section 3.4C). Finally, we characterize the entanglement content of the system during the scattering process and estimate the entanglement between the final products generated by the interactions (Section 3.4D).

3.4A Simulation scheme

The `TeNPy` [225] implementation of various tensor Network (TN) methods from Chapter 2 is here employed to tackle the exponential growth of the Hilbert space: we represent states and operators using the MPS and MPO ansatze, in conjunction with (i) the two-site DMRG algorithm (to variationally find ground states) and (ii) the fourth-order TEBD algorithm (for Trotterized time evolution). All simulations are carried out on chains of $L = 200$ sites with open boundaries and, in the QED$_2$ case, vanishing electric field at the boundary links.

Symmetric TN methods are employed to constrain the ground state search and the dynamics in the desired charge sector, thus improving the efficiency and the precision of numerical simulations. Specifically, we impose exactly the conservation of the U(1) global charge Q and, for QED$_2$, also the vanishing of the total $\mathbb{Z}_n$ Gauss charge on even and odd sublattices, i.e., $\sum_{x\in \mathrm{E}} \mathcal{G}_x$ and $\sum_{x\in \mathrm{O}} \mathcal{G}_x$ [343]. The recipe in Section 1.4D can be applied in order to recast Gauss law constraints into link constraints and Eq. (3.34) in a nearest-neighbor Hamiltonian,

as required by TEBD. Alternatively, for $\mathbb{Z}_n$, that procedure can also be pictured as fusing the Hilbert spaces associated with a site $\mathscr{H}_x$ and with the subsequent link $\mathscr{H}_{x,x+1}$ in a single (larger) local computational Hilbert space

$$\tilde{\mathscr{H}}_x = \mathscr{H}_x \otimes \mathscr{H}_{x,x+1} = \text{span}(\{|\mathscr{N}, \mathscr{E}\rangle : \mathscr{N} \in \{0,1\},\ \mathscr{E} \in \mathbb{Z}_n\}) \,. \tag{3.41}$$

The Abelian Gauss law is then enforced directly, as a two site constraint.

Schematically, a simulation goes as follows:

(i) determine the ground state $|\Omega\rangle$ via DMRG;
(ii) prepare initial particle wave packets $|\Psi\rangle$ acting on $|\Omega\rangle$ with MPOs (Section 3.4B);
(iii) determine the time evolution $|\Psi(t)\rangle = e^{-iHt}|\Psi\rangle$, via TEBD.

During the evolution we monitor the expectation values $\langle O\rangle_t = \langle\Psi(t)|O|\Psi(t)\rangle$ of relevant observables O, such as energy $\langle H\rangle_t \equiv \langle H\rangle$, charge density $\langle\psi_x^\dagger\psi_x\rangle_t$, electric field $g\langle E_x\rangle_t$, and various energy densities

$$h_x^{\text{mass}}(t) = m(-1)^x\langle\psi_x^\dagger\psi_x\rangle_t \,, \qquad h_x^{\text{elec}}(t) = \frac{g^2}{2}\langle(E_x)^2\rangle_t \,. \tag{3.42}$$

Moreover, we compute the entanglement entropy $S(x,t)$ associated with every bipartition of the chain in two subsystems, $\mathrm{L} = \{y \in \Lambda \mid y < x\}$ and $\mathrm{R} = \{y \geq x\}$; namely,

$$S(x,t) = -\,\text{tr}\left[\rho(t)\log_2\rho(t)\right] \,, \qquad \rho(t) = \text{tr}_{\mathrm{R}}|\Psi(t)\rangle\langle\Psi(t)| \,. \tag{3.43}$$

Note the base-2 logarithm is used here. Unless otherwise stated, from the next section on, we report the deviation of all the above quantities from the vacuum expectation value.

Finally, we monitor the fraction of configurations affected by truncations of the electric field

$$1 - \mathcal{F}_{\mathrm{U}(1)}(t) = 1 - \langle\Pi_{\mathrm{U}(1)}\rangle_t \,, \tag{3.44}$$

where $\Pi_{\mathrm{U}(1)}$ is the projector on states complying with the U(1) Gauss law $\mathcal{G}_{\mathrm{U}(1)}$ (Eq. 3.37), and can be written as the Kronecker product of on-site operators projecting out the configurations $\mathscr{N}=1$, $\mathscr{E}=-\mathscr{E}_{\max}$ and $\mathscr{N}=0$, $\mathscr{E}=+\mathscr{E}_{\max}$ on even and odd sites respectively.

Convergence. Numerical errors are kept under control. The MPS compression is achieved discarding singular values below $\epsilon = 10^{-6}$, resulting in MPS bond dimensions as high as $\chi = 991$. As a guiding principle[11], we find that the maximum bond dimension χ scales like $\epsilon^{-0.33(1)}$ with the singular value cutoff ϵ, albeit with a g-dependent prefactor (Fig. 3.1). Figures 3.2 and 3.3 show the convergence of the entanglement entropy S with ϵ. We conclude that the truncation amounts to an $\mathcal{O}(10^{-3})$ error on S. The Trotterization with Trotter step $\delta t = 0.05$ is similarly responsible for an overall $\mathcal{O}(10^{-3})$ error on final states. As for the $\mathbb{Z}_n$

[11] χ will eventually saturate — if anything, due to the finite size of the Hilbert space of a finite chain.

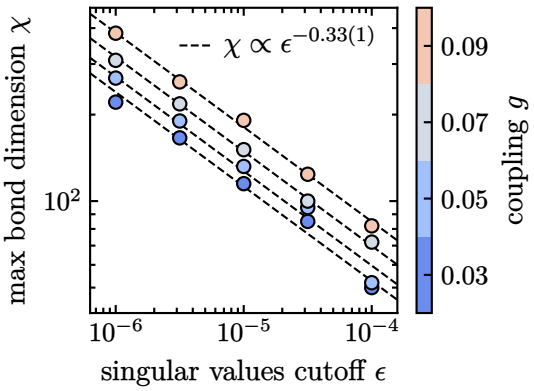

Figure 3.1: Largest MPS bond dimension χ during scattering simulations for $t \in [0, 200]$, as a function of the singular value cutoff ϵ and the coupling g.

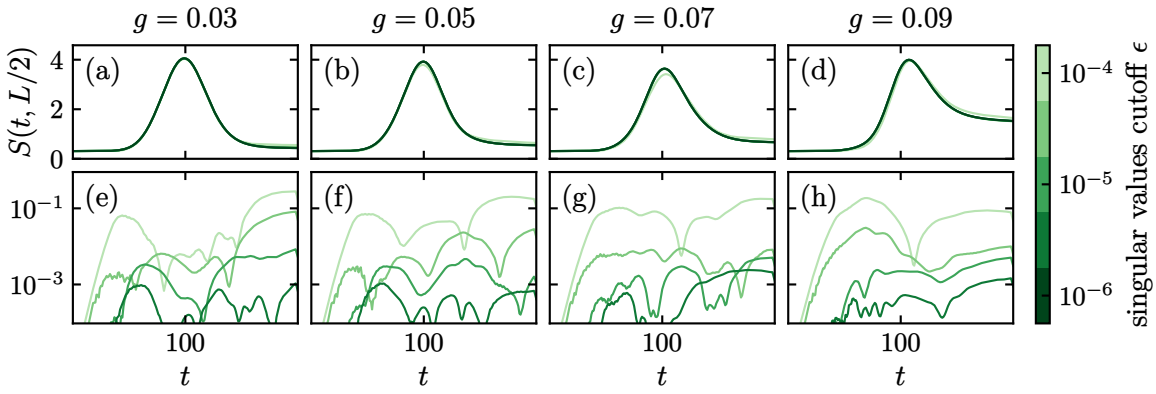

Figure 3.2: Convergence of the mid-chain entanglement entropy $S(t, L/2)$ during scattering events at various couplings g and singular value truncation cutoffs ϵ. *Bottom row:* absolute relative deviation w.r.t. the (smallest) $\epsilon = 10^{-6}$ curve.

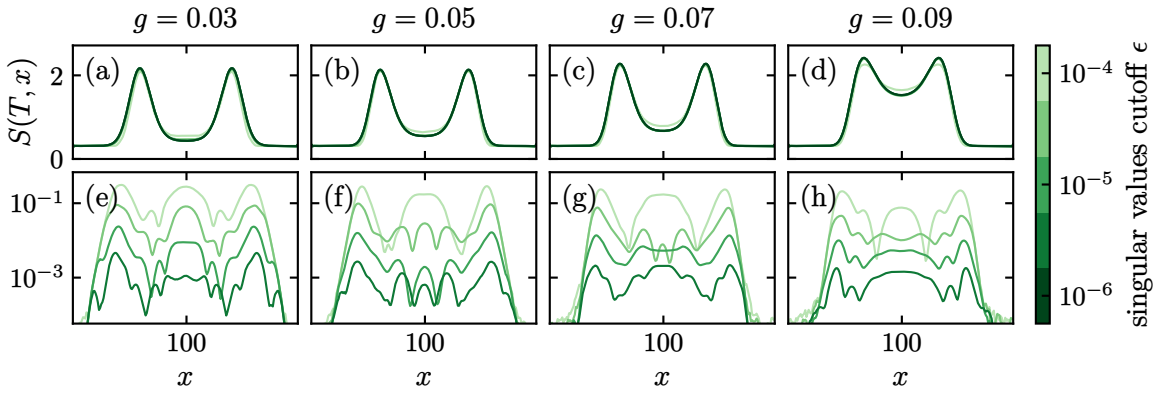

Figure 3.3: Convergence of the final-time $T = 200$ entanglement entropy $S(T, x)$ of some scattering events. Analogous to Fig. 3.2.

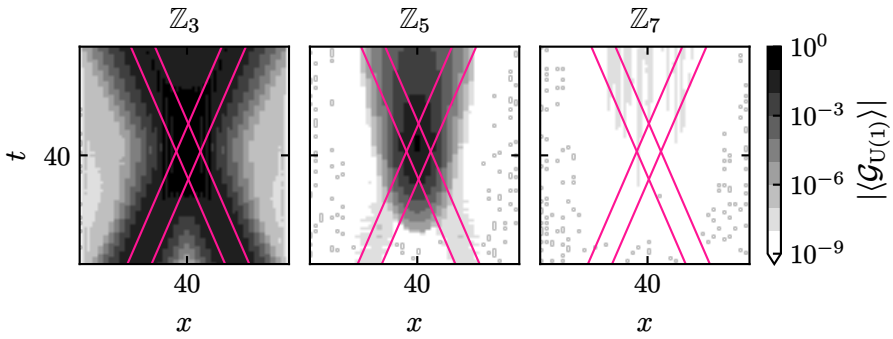

Figure 3.4: Absolute expectation value of the U(1) Gauss law from Eq. (3.37) during test scattering simulations for a few $\mathbb{Z}_n$ link truncations. Parameters: $L = 80$, $m = 0.9$, $g = 0.08$, $\epsilon = 10^{-5}$. Pink lines in overlay mark the free trajectories of the mesons' fermion and antifermion constituents (see Section 3.4B).

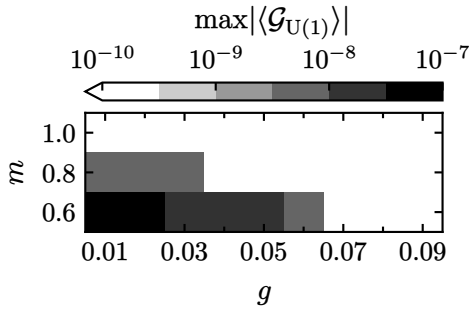

Figure 3.5: Maximum absolute expectation value of the U(1) Gauss law during results-section scattering simulations.

truncation of the electric field: we set $n = 7$, finding a fraction of truncated configurations $1 - \mathcal{F}_{\mathrm{U}(1)} \lesssim \mathcal{O}(10^{-10})$. The effect of the $\mathbb{Z}_n$ truncation can also be quantified in terms of the violation of the U(1) Gauss law, $\mathcal{G}_{\mathrm{U}(1)}$: Figure 3.4 compares $\mathbb{Z}_7$ to stricter truncations for an example scattering taking place on a small $L = 80$ lattice; Fig. 3.5 reports on violations observed in results-section simulations. In all cases, $\mathbb{Z}_7$ electric field truncation effects are negligible compared to other sources of error.

3.4B Initial state preparation

The state of a system undergoing a scattering process long before the collision is populated with wave packets of stable particle excitations localized in far distant space regions [297]. In this Section we present and motivate our protocol for preparing the initial state of a QED$_2$ scattering simulation[12], providing an expression for the wave packet amplitudes and

[12] See Ref. [344] for a similar effort aimed at quantum simulation.

operators involved. We consider initial states of uncorrelated particles — i.e., "separable" wave packet amplitudes in Eq. (3.7):

$$\phi(\{p_k, \sigma_k, \alpha_k\}) = \prod_k \phi_k(p_k, \sigma_k, \alpha_k) \ . \tag{3.45}$$

We start by illustrating how localized particle excitations are prepared in the lattice theory of free staggered fermions, as it provides useful insights into the QED$_2$ case.

The key ingredient of the protocol are a set of wave packet creation MPO, written as

$$O = w_0 W_1 W_2 \cdots W_L w_L \ , \tag{3.46a}$$

where W_x are matrices whose entries are operators acting nontrivially only on the local Hilbert space of site x, while the vectors w_0, w_L are introduced to obtain a uniform bulk and read

$$w_0 = (\ 1 \quad 0 \quad 0 \quad \dots\ ) \ , \qquad w_L = (\ \dots \quad 0 \quad 0 \quad 1\ )^T \ .$$

Free fermions

Once the vacuum $|\Omega\rangle$ of free staggered fermions has been obtained (e.g. by DMRG), preparing free multi-particle states of fermions and antifermions is straightforward. It amounts to acting with $c_k^\dagger$ and $d_k^\dagger$ on $|\Omega\rangle$, as shown in Eq. (3.27). Periodic boundary conditions are assumed in the derivation, here we neglect open boundary effects. Realistic asymptotic states of uncorrelated particles with some degree of position and momentum localization are prepared acting with wave packets of $c_k^\dagger$ and $d_k^\dagger$. Recalling Eq. (3.20), we can write the latter in terms of $\psi_x^\dagger$ and ψ_x:

$$C_\phi^\dagger = \frac{2\pi}{L} {\sum_k}' \phi_k c_k^\dagger = \sum_x \tilde{\phi}_x^C \psi_x^\dagger \ , \qquad D_\phi^\dagger = \frac{2\pi}{L} {\sum_k}' \phi_k d_k^\dagger = \sum_x \tilde{\phi}_x^D \psi_x \ . \tag{3.47}$$

The functions $\tilde{\phi}_x^C$ and $\tilde{\phi}_x^D$ are specified in terms of ϕ_k through Eqs. (3.20a) and (3.20b), respectively. $C_\phi^\dagger$ and $D_\phi^\dagger$ create a fermion and an antifermion respectively, with momentum space probability density $|\phi_k|^2$,

$$\frac{2\pi}{L} {\sum_k}' |\phi_k|^2 = 1 \ . \tag{3.48}$$

Combined with the orthonormality condition in Eq. (3.28), Eq. (3.48) enforces the normalization of the prepared state. The prototypical choice for ϕ_k is

$$\phi_k \propto e^{-ik\mu_x} \, e^{-(k-\mu_k)^2/4\sigma_k^2} \ ; \tag{3.49}$$

where the phase centers the wave packet in μ_x in position space. In the thermodynamic ($\sigma_k \gg 2\pi/L$) and continuum limits, the $|\phi_k|^2$ given in Eq. (3.49) approaches a *Gaussian* probability density with mean μ_k and standard deviation σ_k [345].

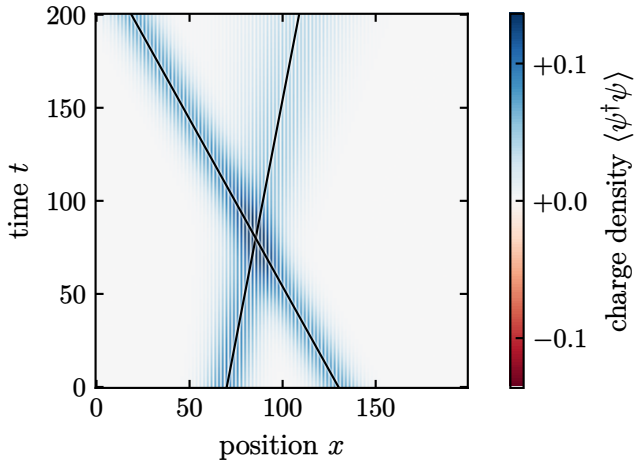

Figure 3.6: Charge density during the free propagation of two different Gaussian fermion wave packets. The black lines in overlay are the trajectories of the wave packet peak predicted by the group velocity ω'_k.

Fermion and antifermion MPO. In terms of the Jordan-Wigner matrix representation of the staggered fermion operators in Eq. (1.99),

$$C_\phi^\dagger = \sum_x \tilde{\phi}_x^C \Big[\prod_{y<x} (-1)^{N_y} \Big] \sigma_x^+ \,. \tag{3.50}$$

Despite the non-local Jordan-Wigner strings, $C_\phi^\dagger$ admits a simple MPO representation with

$$W_x = \begin{pmatrix} (-1)^{N_x} & \tilde{\phi}_x^C \, \sigma_x^+ \\ 0 & 1 \end{pmatrix} \,, \tag{3.51}$$

in Eq. (3.46a) notation. The analogous results for $D_\phi^\dagger$ are obtained via $\sigma^+ \to \sigma^-$.

Sanity check. The time evolution of a state of two Gaussian fermion wave packets with different μ_x, μ_k and σ_k is depicted in Fig. 3.6. The propagation speed of the wave packets matches the lattice group velocity, ω'_k, given by Eq. (3.19e). No surprises here. However, as Fig. 3.6 shows, the free theory has just pure kinematics; in order to observe a nontrivial dynamics, we need to turn to an interacting theory, such as QED$_2$.

QED

As most of gauge models in 1+1 dimensions, QED$_2$ is confining [114, 116, 118] and does not have charged asymptotic states. Its stable particles are neutral *mesons*, i.e., fermion-antifermion bound states. A tentative creation operator for mesons of momentum $k \in \Lambda^*$

reads

$$b_k^\dagger = \frac{2\pi}{L} \sum_{pq}{}' \delta_{(p+q)k}\, \Psi_{pq}\, \bar{c}_p^\dagger \bar{d}_q^\dagger \,, \tag{3.52}$$

for some Ψ_{pq}, to be determined. Here $\bar{c}_k^\dagger, \bar{d}_k^\dagger$ are gauge invariant fermion and antifermion creation operators, obtained writing $c_k^\dagger, d_k^\dagger$ in terms of the position space fields $\psi_x^\dagger, \psi_x$ and dressing the latter with strings of unitary electric field rising or lowering operators acting on their right, to comply with Gauss law:

$$\psi_x^\dagger \to \psi_x^\dagger \prod_{y \geq x} U_y^\dagger \,, \quad \psi_x \to \psi_x \prod_{y \geq x} U_y \,. \tag{3.53}$$

Unless appropriate conditions are imposed on Ψ_{pq}, the operator $b_k^\dagger$ in Eq. (3.52) creates excitations of definite momentum k but not of definite energy. Rather than seeking an approximate solution for QED$_2$ of the (notoriously difficult [137, 346]) bound state problem, here we fix the functional form of Ψ_{pq} with a simple ansatz[13]

$$\Psi_{pq} \equiv \Psi_{p-q} \propto e^{-(q-p)^2/4\sigma_{\Delta k}^2}\, e^{-i(q-p)\mu_{\Delta x}/2} \,. \tag{3.54}$$

Note we switched to center of mass and relative coordinates of the fermion and antifermion constituents and assumed Ψ_{pq} depends only on the latter. Moreover, we require: (i) that the fermion and antifermion are located in close real space positions, y and z, with average separation $\langle z - y \rangle = \mu_{\Delta x}$; (ii) that $(q - p)$ follows a Gaussian probability distribution centered in $\mu_{\Delta k} = 0$ and with standard deviation $\sigma_{\Delta k}$. Using Eq. (3.54) in place of the exact Ψ_{pq} will generally introduce some excitation in the bound state created by $b_k^\dagger$. As a consequence, some internal dynamics is to be expected. We monitor this approximation a posteriori and set the simulation timescale shorter than the lifetime of the mesons.

Meson wave packets are prepared acting on the (interacting) ground state $|\Omega\rangle$ with operators

$$B_\phi^\dagger = \frac{2\pi}{L} \sum_k \phi_k b_k^\dagger = \left[\frac{2\pi}{L}\right]^2 \sum_{pq}{}' \Phi_{pq} \bar{c}_p^\dagger \bar{d}_q^\dagger = \sum_{yz} \tilde{\Phi}_{yz} \psi_y^\dagger \psi_z \left[\prod_{x \geq y} U_x^\dagger\right] \left[\prod_{x \geq z} U_x\right] \,, \tag{3.55}$$

with $\Phi_{pq} = \phi_{p+q} \Psi_{q-p}$. As for the free theory, $\tilde{\Phi}_{yz}$ is defined in terms of Φ_{pq} via Eq. (3.20). Exemplary Φ_{pq} and $\tilde{\Phi}_{yz}$ for a pair of Gaussian meson wave packets, with ϕ_k given by Eq. (3.49), are plotted in Fig. 3.8. The states prepared with $B_\phi^\dagger$ operators are normalized a posteriori because, in our approximation, no exact orthonormality condition analogous to Eq. (3.28) holds a priori for the states created by $b_k^\dagger$, when $g > 0$.

[13] In the end, lattices considered here might not even have enough sites to accurately resolve the internal structure of the bound state.

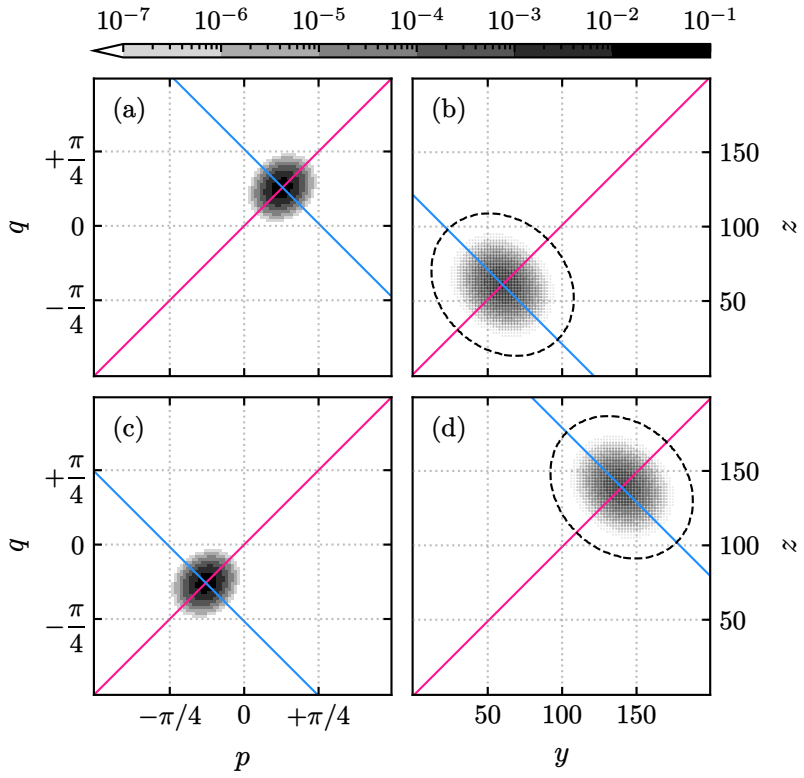

Figure 3.8: $|\Phi_{pq}|^2$ (first column) and $|\tilde{\Phi}_{yz}|^2$ (second) from Eq. (3.55) for two Gaussian meson wave packets (one per row). The wave packet parameters are reported in Table 3.1. The mean values in table are highlighted by straight lines: blue for $\mu_k = \langle p+q \rangle$ and $\mu_x = \langle y+z \rangle$, magenta for $\mu_{\Delta k} = \langle q-p \rangle$ and $\mu_{\Delta x} = \langle z-y \rangle$. The dashed ellipses represent the threshold ($|\tilde{\Phi}_{yz}| = 10^{-6}$) below which we truncate the position space amplitude when constructing the MPO in Eq. (3.56).

	μ_k	σ_k	$\mu_{\Delta k}$	$\sigma_{\Delta k}$	μ_x	$\mu_{\Delta x}$
(a), (b)	$+0.81$	0.11	0	0.09	60.5	$+1$
(c), (d)	-0.81	0.11	0	0.09	139.5	-1

Table 3.1: Parameters in Eqs. (3.49) and (3.54) for the wave packets in Fig. 3.8.

Meson MPO. After the Jordan-Wigner transformation and some algebraic manipulations the meson wave packet creation operator in Eq. (3.55) reads

$$B_\phi^\dagger = \sum_{yz} \tilde{\Phi}_{yz} \begin{cases} \sigma_y^+ U_y^\dagger \left[\prod_{x=y}^{z} (-1)^{N_x} U_x^\dagger \right] \sigma_z^- \,, & y < z \,; \\ N_y \,, & y = z \,; \\ \sigma_z^- U_z \left[\prod_{x=z}^{y} (-1)^{N_x} U_x \right] \sigma_y^+ \,, & y > z \,; \end{cases}$$

the W_x matrices of the associated MPO read (empty entries represent null operators):

$$\left(\begin{array}{c|c|c|c} 1 \;\; \sigma_x^+ U_x & & \tilde{\Phi}_{xL}\, \sigma_x^+ U_x^\dagger \;\cdots\; \tilde{\Phi}_{x(x+1)}\, \sigma_x^+ U_x^\dagger & \tilde{\Phi}_{xx}\, N_x \\ \hline & (-1)^{N_x} U_x & & \tilde{\Phi}_{x(x-1)}\, \sigma_x^- \\ & \ddots & & \vdots \\ & (-1)^{N_x} U_x & & \tilde{\Phi}_{x1}\, \sigma_x^- \\ \hline & & (-1)^{N_x} U_x^\dagger & \\ & & \ddots & \\ & & (-1)^{N_x} U_x^\dagger & \\ \hline & & & \sigma_x^- \\ & & & 1 \end{array}\right) \tag{3.56}$$

These have linear dimension $L+2$, making the contraction with an MPS quite expensive for long chains. However, the MPO can be compressed, numerically [95] or analytically, by discarding the rows and columns related to irrelevant amplitudes, $\tilde{\Phi}_{yz} \ll 1$. As an example, in preparing the mesons depicted in Fig. 3.8 we truncate each meson amplitude $\tilde{\Phi}_{yz}$ outside the dashed ellipses.

Meson stability. Before studying meson-meson scatterings, we simulate the propagation of one meson and test the approximation in Eq. (3.54) in the parameters region explored hereafter. The time evolution of the meson wave packet in Fig. 3.8(a,b) is shown in Fig. 3.9 for mass $m = 0.8$ and couplings up to $g = 0.15$. Similar results are observed for $m = 0.6$ and $m = 1.0$. As anticipated, the meson does not decay during the simulations and, crucially, its entanglement track remains confined in the region where the wave packet is localized. On the other hand, we do observe some meson internal dynamics in the form of periodic inversions of the meson polarization (sign of its electric string). Their frequency increases with g, compatibly with what was observed in Refs. [110, 347]. This behavior is

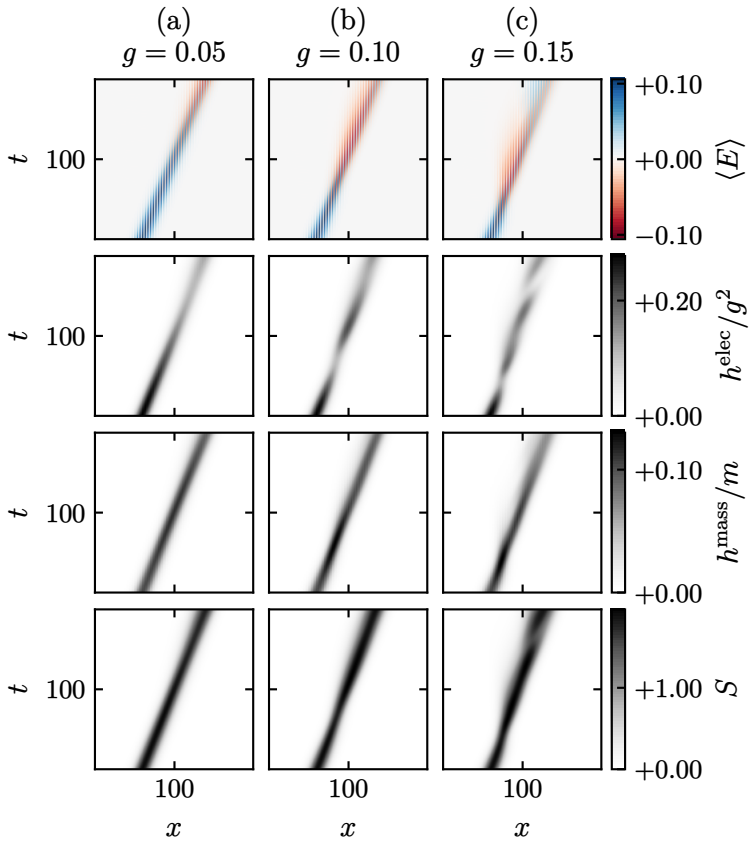

Figure 3.9: Test of the stability of mesons prepared via Eqs. (3.54) and (3.55). Electric field $\langle E_x \rangle$, its energy density h_x^{elec}, mass energy density h_x^{mass} and entanglement entropy S_x (rows) measured during the propagation of a single meson with mass $m = 0.8$, for increasing coupling g (columns).

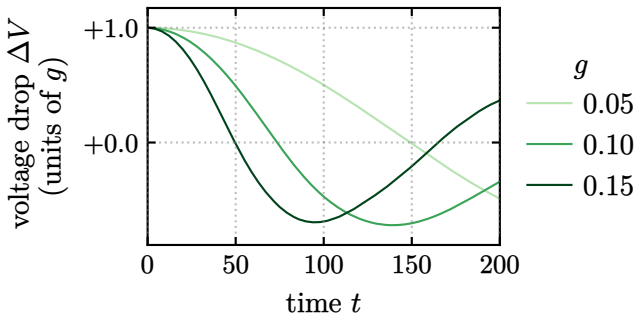

Figure 3.10: Damped oscillation of the voltage drop across the chain ΔV during the propagation of a single meson (simulations in Fig. 3.9) for different values of the coupling g. The oscillation frequency increases with g.

also captured by Fig. 3.10, where the voltage drop across the chain,

$$\Delta V = \sum_x g\langle E_x \rangle \ , \tag{3.57}$$

is plotted as a function of time. The relevant rows of Fig. 3.9 show that the inversions are accompanied by a drop in the electric field energy h^{elec} and a concentration of the mass energy density h^{mass}. We infer that the inversions correspond to damped oscillations of the meson constituents around their center of mass. Hereafter we treat the ansatz for the meson wavefunction in Eq. (3.54) as exact — for instance, in the analysis of Section 3.4D we assume that $b_k^\dagger$ creates monochromatic mesons and neglect the consequences of the internal dynamics on the entanglement.

3.4C Scattering phenomenology

We now turn to simulations of lattice QED$_2$ meson-meson scatterings. We explore a region of model parameters ranging from weak ($g \ll m$) to intermediate ($g/m \approx 1/4$) coupling. All the reported simulations follow the scheme outlined in Section 3.4A and are carried out in the center of mass frame of reference and for parity-symmetric initial configurations. Accordingly, the initial scattering state is prepared by using a pair of uncorrelated meson wave packet creation operators form Eqs. (3.54) and (3.55) with identical σ_k and $\sigma_{\Delta k}$, opposite mean momenta μ_k, and parity symmetric μ_x and $\mu_{\Delta x}$.

An overview of the dynamics is shown in Fig. 3.11. Figures 3.11a to 3.11c show the scattering of two initial mesons for increasing bare mass $m = 0.6,\ 0.8,\ 1.0$ and fixed coupling strength $g = 0.08$. Increasing m clearly affects the kinematics by slowing down the propagation of the mesons before and after the collision but it also results in the generation of a larger entanglement between the scattering products. To quantify the first effect we focus on the initial stage of the evolution ($t \in [20, 50]$), perform a Gaussian fit of the mass energy density profile at each time step, and linearly interpolate the peak trajectories $\mu_x(t)$ via:

$$\mu_x(t) = \omega' t + \mu_x(0) \ . \tag{3.58}$$

The resulting group velocities ω' are plotted in Fig. 3.12, where a slow down at stronger couplings is also noticeable. The second effect, namely the increased entanglement after the scattering, may be interpreted as an indirect consequence of the slow down of the colliding particles, as they effectively interact for a longer time. Figures 3.11d to 3.11f show again the scattering of the initial mesons for fixed bare mass $m = 1.0$ and coupling $g = 0.02,\ 0.08,\ 0.14$. We observe a drastic increase of the post-collision entanglement with the strength g of the interactions. A detailed discussion of this phenomenon is given in Section 3.4D. Furthermore, in Figs. 3.11d and 3.11e the polarizations of the outgoing mesons are inverted, as indicated by the sign of the electric field. The string inversion, however, is not a consequence of the collision. As discussed in Section 3.4B, inversions are an (accidental) internal feature of our meson states and are observed also during the free propagation

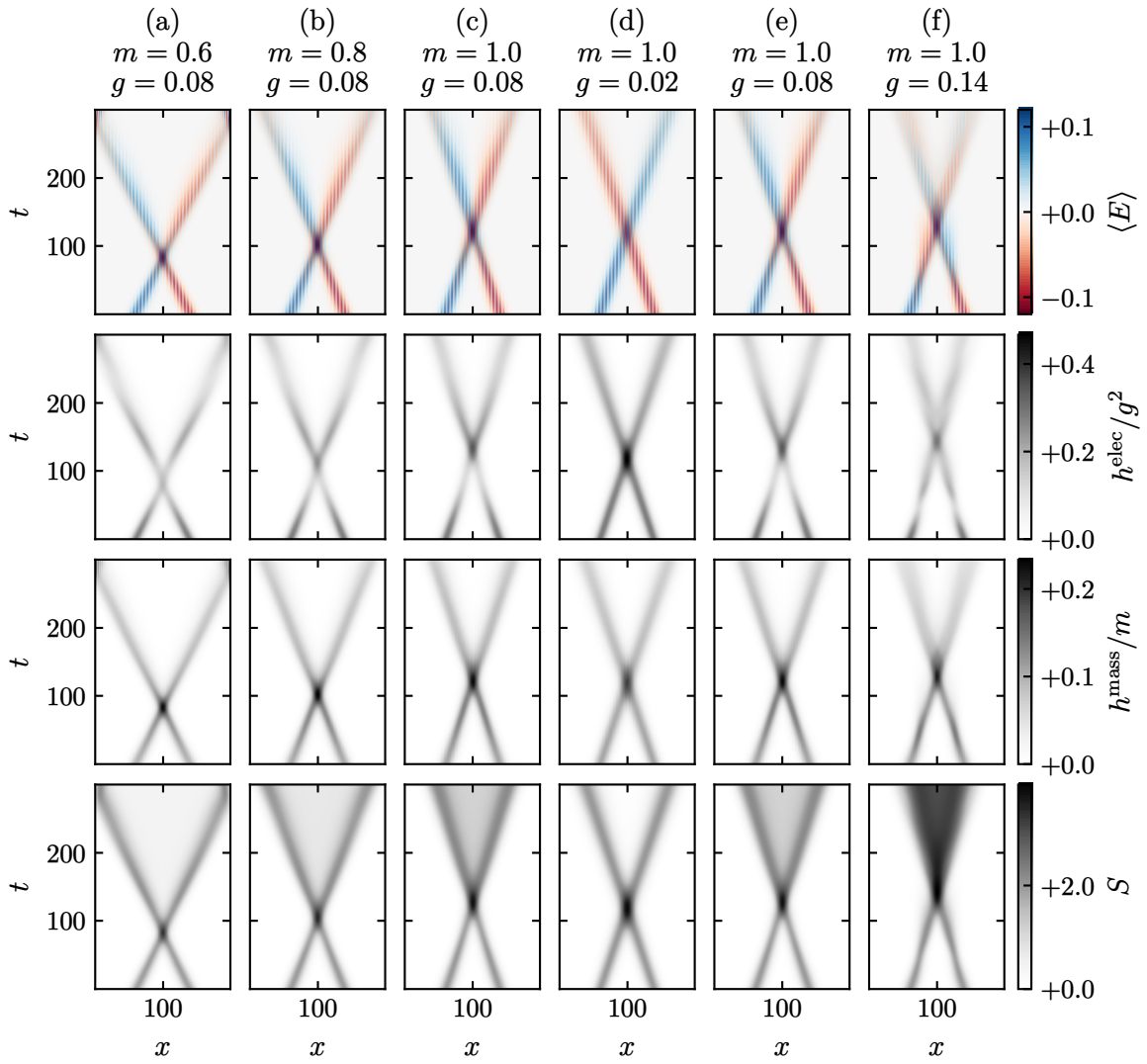

Figure 3.11: Simulations of meson-meson collisions in QED$_2$. Measurements of the electric field $\langle E_x \rangle_t$, its energy density $h_x^{\mathrm{elec}}(t)$, the mass energy density $h_x^{\mathrm{mass}}(t)$ and the entanglement entropy $S(t, x)$ are reported (rows). Various values of the mass m (left block) and coupling g (right block) parameters are considered. The initial meson wave packet distributions are those of Fig. 3.8.

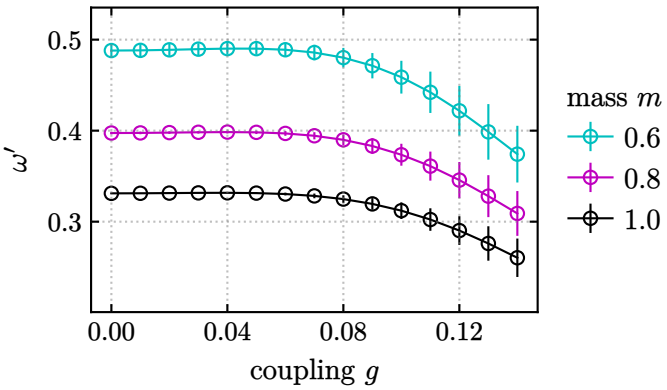

Figure 3.12: Mass m and coupling g dependence of the meson group velocity ω', as defined in Eq. (3.58) and measured during the first (approximately free) stage of the propagation. The fit uncertainty increases with the coupling g because stronger interactions anticipate the deflection of the meson trajectories.

of a single meson in Fig. 3.9.

Energy balance

The total energy $\langle H \rangle$ of a QED$_2$ state can be partitioned in mass, electric and kinetic energy fractions χ^γ, $\gamma \in \{\text{mass}, \text{kin}, \text{elec}\}$. In the simulation frame of reference these are defined as

$$\chi^{\text{mass}} = \frac{\sum_x h_x^{\text{mass}}}{\langle H \rangle} , \quad \chi^{\text{elec}} = \frac{\sum_x h_x^{\text{elec}}}{\langle H \rangle} , \quad \chi^{\text{kin}} = 1 - \chi^{\text{mass}} - \chi^{\text{elec}} . \tag{3.59}$$

We monitor $\chi^\gamma(t)$ during various meson-meson scatterings. The time averages over the whole simulation time span, denoted $\bar{\chi}^\gamma$, are reported in the stacked area plots of Fig. 3.13, together with the standard deviations (time fluctuations) ϵ^γ, $(\epsilon^\gamma)^2 = \overline{(\chi^\gamma(t) - \bar{\chi}^\gamma)^2}$, of the mass and kinetic fractions. The mass and kinetic energies are the dominant contributions in the parameter region we explored, while the electric energy fraction never exceeds 5%, decreasing mildly with the mass and growing as g^2 for large enough couplings ($g \geq 0.05$). The relative weight of the mass and kinetic energies is mostly controlled by the mass parameter. Conversely, energy transfers (namely, amount of fluctuations ϵ^γ) are boosted for larger g, i.e., stronger interactions. Even for the largest simulated couplings, the mass energy is approximately constant during the evolution, with time fluctuations amounting at most to 0.5% of its value. This behavior strongly hints that the simulated processes are elastic collisions. In (1+1)-dimensions, energy-momentum conservation implies that the products of an elastic collision of two particles (of equal mass) have the same momenta of the incoming particles. In the next Section we verify this kinematical constraint by analyzing the momentum content of the initial and final states.

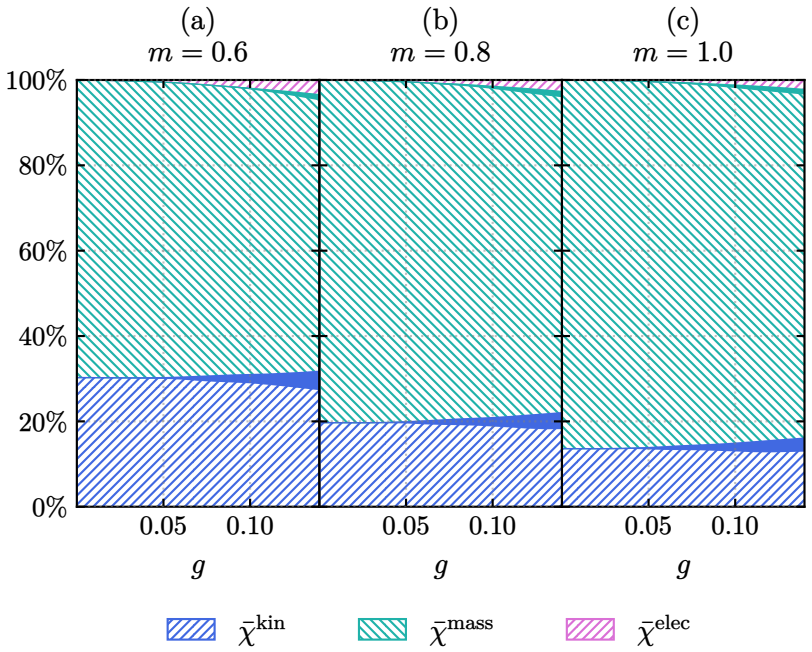

Figure 3.13: Total energy partition in the mass, kinetic and electric energy contributions from Eq. (3.59): time averages (hatched regions) and fluctuations (filled regions) during various meson-meson scatterings. Masses $m = 0.6$ (a), 0.8 (b) and 1.0 (c) and couplings ranging from $g = 0$ to $g = 0.14$ are considered. The thickness of the filled regions reproduce a $\pm 2\epsilon^\gamma$ confidence belt around the mean value χ^γ of the kinetic and mass energy fractions.

Momentum space analysis

Among the most important observables for a scattering process are the species and the momenta of the incoming and outgoing particles involved in the collision. In experiments, the momenta of the incoming particles are tuned by collimating the colliding particle beams. The species and momenta of the scattering products, instead, are inferred from detector data. Our simulations follow a similar procedure: the momenta of the incoming particles are set by the initial state, while those of the scattering products are identified analyzing the final state. The momenta of the excitations contained in a state are reflected by its spatial periodicities. To detect the correlations between pairs of meson excitations in different positions we evaluate the connected 2-point correlation function for the meson composite operator $\Theta_x = \psi_x \psi^\dagger_{x+1}$ (x even), namely $G_{yz} = \langle \Theta_y \Theta^\dagger_z \rangle - \langle \Theta_y \rangle \langle \Theta^\dagger_z \rangle$. Then, we compute the translation invariant momentum space connected 2-point function

$$G_k = \frac{(2)^2}{2\pi} \sum_{yz \in \mathrm{E}} e^{-ik(y-z)} G_{yz} \,. \tag{3.60}$$

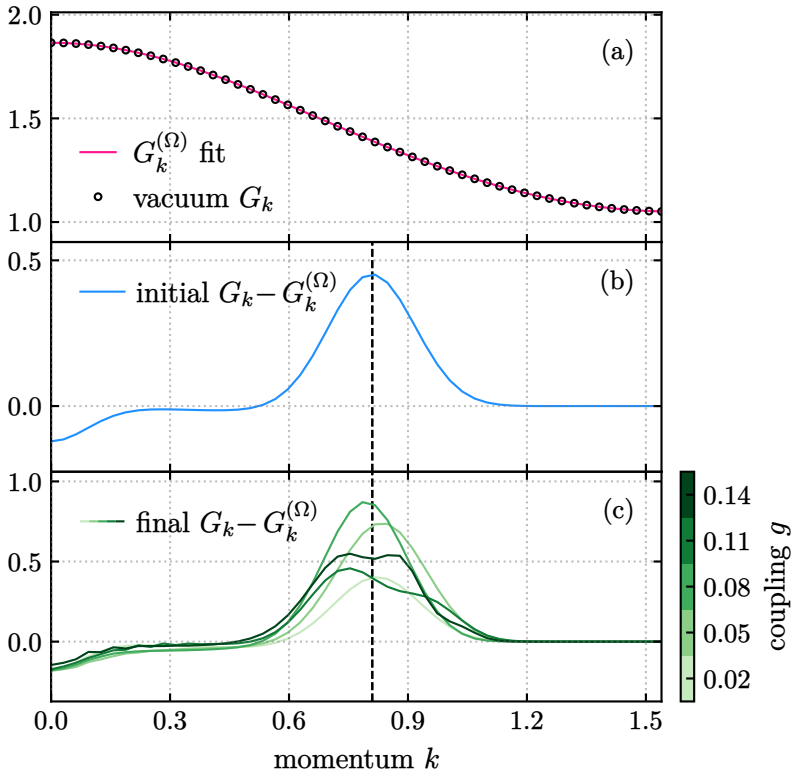

Figure 3.14: Time-independent momentum space connected meson-meson correlation functions, G_k, at $m = 0.6$ and for positive momenta k (the $k < 0$ branch is symmetric). Evaluated: at $g = 0.08$ on the full QED$_2$ vacuum (a) and the initial meson-meson scattering state (b); as well as on final scattering states for various couplings g (see color bar) (c). The vacuum and initial G_k are almost coupling g independent (up to percent order deviations). In (a) the fitted $G_k^{(\Omega)}$ from Eq. (3.61) is also reported, while in (b) and (c) it has been subtracted. The dashed vertical line corresponds to the mean momentum of the (left) initial wave packet.

Before the initial and final scattering states, let us discuss the vacuum correlator. QED$_2$ has a gapped spectrum [102, 299] thus, by Eq. (2.15), G_{yz} is expected to decay exponentially for $|y - z| \gg \xi$ (correlation length):

$$G_{yz}^{(\Omega)} \propto e^{-|y-z|/\xi} \,, \quad G_k^{(\Omega)} \propto \frac{\sinh(2/\xi)}{\cosh(2/\xi) - \cos(2k)} \,. \tag{3.61}$$

Fitting the numerical G_k via Eq. (3.61) we find that this thermodynamic limit result provides an excellent approximation of the numerical data (up to a constant shift, see Fig. 3.14a). Moreover, for all the simulated m and g values we find $\xi/L = \mathcal{O}(10^{-3}) \ll 1$; signaling that we are indeed at the thermodynamic limit and justifying a posteriori the

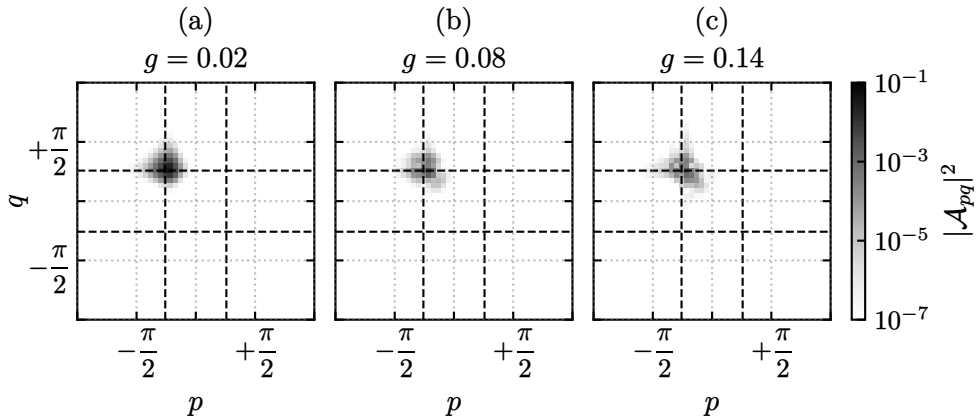

Figure 3.15: Transition probabilities $|\mathcal{A}_{pq}|^2$ to the states defined in Eq. (3.62), for three meson-meson scattering simulations with bare mass $m = 0.8$ and coupling $g = 0.02$ (a), 0.08 (b), and 0.14 (c). Namely, probability of the two mesons in Fig. 3.8 to evolve, after a collision, into pairs of meson wave packets peaked around momenta p and q and located in the left and right side of the chain, respectively. The dashed lines correspond to the initial meson momenta $\mu_k \approx \pm\pi/4$. The resolution of the above images is related to the momentum space standard deviation $\varepsilon \approx 0.14$ of these wave packets and thus, indirectly, to the lattice size. The transition probabilities in Figure are computed projecting on a family of final states with p and q values spaced by $\varepsilon/2$.

usage of the expressions in Eqs. (3.60) and (3.61).

The 2-point function G_k evaluated on initial and final scattering states also presents a background of the type in Eq. (3.61) (up to a shift). On top, we observe peaks detecting the momenta of the incoming and outgoing mesons. The momentum space correlators of some initial and final scattering states are plotted in Figs. 3.14b and 3.14c, with the background removed. All initial and final correlators are peaked around the mean momentum of the initial wave packet, as expected for a $2 \to 2$ elastic scattering in $1 + 1$ dimensions. The distortions appearing in final state correlators are likely caused by the inexact modelling of the meson excitations.

Scattering amplitudes

The standard quantify to compute in order to characterize an elastic or inelastic scattering is the S-matrix in Eq. (3.1). We now compute some finite-time scattering amplitudes of the type in Eq. (3.11) — from these, proper S-matrix elements can in principle be extracted following the prescription outlined in Section 3.1A. Here we focus on transitions amplitudes to final states of two mesons, and we identify the final time t_f, at which the simulation of the scattering dynamics is aborted, with the time at which the mass energy density peaks of the outgoing wave packets are separated by $\Delta x \gtrsim 100$. In order to study the distribution

of their momenta, we consider meson wave packets with amplitudes $\theta_k^{(p,\mathrm{L})}$ and $\theta_k^{(q,\mathrm{R})}$ peaked at momenta p and q and completely delocalized in the left and right half of the chain respectively. That is, we compute the overlap of the final state with states

$$|\Phi'_{pq}(t_f)\rangle = \mathcal{N}_{pq}\left[\frac{2\pi}{L}\right]^2 \sum_{k'k} \theta_{k'}^{(q,\mathrm{R})}\theta_k^{(p,\mathrm{L})} b_{k'}^\dagger b_k^\dagger |\Omega\rangle \,, \tag{3.62}$$

with $\mathcal{N}_{pq}$ enforcing the normalization and

$$\theta_k^{(q,\mathrm{R})} = \frac{1}{\sqrt{2\pi}} \sum_x e^{-i(k-q)x}\,\Theta(x) \,, \tag{3.63}$$

$\Theta(x)$ being the step function. Similarly for $\theta^{(p,\mathrm{L})}$. This choice allows us to have the sharpest possible momentum resolution while still distinguishing the left and right outgoing particles. Furthermore, it allows us to claim that the target multi-particle state Eq. (3.62) is indeed approximately free, since the wave packets are supported on disjoint domains. Exemplary transition probabilities $|\mathcal{A}_{pq}|^2 = |\langle\Phi'_{pq}(t_f)|\Phi(t_f)\rangle|^2$ are plotted in Fig. 3.15. As usual, the initial state consists of the two meson wave packets in Fig. 3.8. As for Fig. 3.14, and as expected for kinematical reasons — the momentum distributions of the initial and final meson wave packets coincide.

As we now show, $\theta^{(p,\mathrm{L})}$ and $\theta^{(q,\mathrm{R})}$ behave as momentum projectors in the continuum and thermodynamic limit.

Half-chain plane waves. Consider a continuum theory in one space dimension and, for simplicity, assume the theory has only one particle specie with single-particle energy-momentum eigenstates $|k\rangle$, $\langle k'|k\rangle = \delta(k'-k)$. The momentum space amplitude of a wave packet $|\theta^q\rangle = \int \mathrm{d}k\,\theta^q(k)|k\rangle$, completely delocalized in the $x>0$ space region and peaked at momentum q, reads

$$\begin{aligned}
\theta^q(k) &= \frac{1}{2\pi}\lim_{\epsilon\to 0^+}\int_{-\infty}^{+\infty}\mathrm{d}x\; e^{-ikx}\,e^{i(q+i\epsilon)x}\,\Theta(x) \\
&= \frac{1}{2\pi i}\lim_{\epsilon\to 0^+}\frac{1}{k-q-i\epsilon} \\
&= \frac{1}{2}\delta(k-q) + \frac{1}{2\pi i}\mathcal{P}\frac{1}{k-q}\,.
\end{aligned} \tag{3.64}$$

Here $\Theta(x)$ is the Heaviside step function and $\mathcal{P}$ denotes the Cauchy principal value, while an $i\epsilon$ prescription has been introduced for formal convergence. This $\theta^q(k)$ should be interpreted in the sense of distributions, it is unnormalizable and the variance of $|\theta^q(k)|^2$ is undefined. Nonetheless, as we now show, $\langle\theta^q|$ projects (sufficiently well behaved) wave packets peaked at $x>0$ in position space, on their component, i.e., wave packet amplitude, of momentum q.

Let $|\phi^y\rangle = \int \mathrm{d}k\, e^{-iky}\phi(k)|k\rangle$ be a wave packet peaked at $x = y$ such that, as a complex function, $\phi(k)$ has no singularities and $|\phi(k)| \to 0$ for $|k| \to \infty$ (these criteria are satisfied, e.g., by a complex Gaussian $e^{-|k|^2}$). We want to compute

$$\langle\theta^q|\phi^y\rangle = -\frac{1}{2\pi i}\lim_{\epsilon\to 0^+}\int_{-\infty}^{+\infty}\mathrm{d}k\,\frac{e^{-iky}\phi(k)}{k-q+i\epsilon}\,. \tag{3.65}$$

For large enough $|k|$,

$$\left|\frac{\phi(k)}{k-q+i\epsilon}\right| \leq \frac{|\phi(k)|}{|k|-|q-i\epsilon|} < |\phi(k)|\,; \tag{3.66}$$

therefore, we can invoke Jordan's lemma closing the contour of integration in the lower half (upper half) of the complex plane for $y > 0$ ($y < 0$). The integrand has a single pole at $k = q - i\epsilon$ with

$$\lim_{\epsilon\to 0^+}\operatorname*{Res}_{k=q-i\epsilon}\frac{e^{-iky}\phi(k)}{k-q+i\epsilon} = e^{-iqy}\phi(q) \tag{3.67}$$

and the residue theorem yields

$$\langle\theta^q|\phi^y\rangle = \Theta(y)e^{-iqy}\phi(q)\,, \tag{3.68}$$

which is exactly the anticipated claim. The analogous result for wave packets delocalized in the $x < 0$ region follows by parity symmetry.

3.4D Entanglement generation

The entanglement entropy S observed in the simulations of Sections 3.4B and 3.4C can be traced back to three major sources: the ground state (S_{grn}, background), the particle wave packets (S_{wps}, intraparticle entanglement) and their interactions (S_{int}, interparticle entanglement). As a first approximation, we treat these contributions as additive.

Both free fermions (with $m > 0$) and QED$_2$ are gapped and — in the thermodynamic limit or for periodic boundaries — translation invariant. Hence, by the entanglement area law, their vacua contribute a uniform (up to boundary effects) background entanglement. In what follows we estimate the wave packet contribution in order to then be able to infer the "interaction entanglement" generated by the dynamics in the QED$_2$ case.

Wavepacket entanglement

Acting on $|\Omega\rangle$ with the wave packet creation operators from Eqs. (3.47) and (3.55), additional entanglement, S_{wps}, appears on top of S_{grn} in the space region where the particles are localized. This entanglement contribution can be easily characterized for freely propagating wave packets in the infinite mass limit.

Fermion and antifermion. Let us start from a single fermion wave packet $|\Psi\rangle = C_\phi^\dagger|\Omega\rangle$; analogous results hold for an antifermion. For $m \to \infty$, the ground state approaches the Néel product state. Consider an LR bipartition obtained cutting the chain Λ at x; we have

$$|\Omega\rangle = |\Omega_{\mathrm{L}}\rangle \otimes |\Omega_{\mathrm{R}}\rangle \,, \tag{3.69}$$

and $|\Psi\rangle$ decomposes as

$$|\Psi\rangle = \left[\sum_{y\in\mathrm{L}} \tilde{\phi}_y^C \psi_y^\dagger |\Omega_{\mathrm{L}}\rangle\right] \otimes |\Omega_{\mathrm{R}}\rangle + |\Omega_{\mathrm{L}}\rangle \otimes \left[\sum_{y\in\mathrm{R}} \tilde{\phi}_y^C \psi_y^\dagger |\Omega_{\mathrm{R}}\rangle\right] . \tag{3.70}$$

Recalling the infinite mass limit results from Section 3.2, $\psi_x^\dagger|\Omega\rangle = |x\rangle$ are orthonormal states $\forall x \in \mathrm{E}$, and $\tilde{\phi}_x$ becomes a probability density function (PDF) for $m \to \infty$. Therefore, the coherent superposition of the overall fermion state in each side of the chain reads

$$|\Psi\rangle = \sqrt{p_{\mathrm{L}}(x)}\, |\Psi_{\mathrm{L}}\rangle \otimes |\Omega_{\mathrm{R}}\rangle + \sqrt{1-p_{\mathrm{L}}(x)}\, |\Omega_{\mathrm{L}}\rangle \otimes |\Psi_{\mathrm{R}}\rangle \,, \quad p_{\mathrm{L}}(x) = \sum_{y<x} \left|\tilde{\phi}_y^C\right|^2 . \tag{3.71}$$

Here p_{L} is the cumulative distribution function (CDF) of $|\tilde{\phi}^C|^2$, while $\{|\Psi_{\mathrm{S}}\rangle, |\Omega_{\mathrm{S}}\rangle\}$ can be completed to orthonormal bases for the subsystems $\mathrm{S} \in \{\mathrm{L},\mathrm{R}\}$. In this basis, the reduced density matrix of the L subsystem reads $\rho_{\mathrm{L}} = \mathrm{diag}(p_{\mathrm{L}}, 1-p_{\mathrm{L}}, 0, 0, \ldots)$, yielding the entanglement entropy profile

$$S(x) = S_{\mathrm{wps}}(x) = -p_{\mathrm{L}} \log_2 p_{\mathrm{L}} - (1-p_{\mathrm{L}}) \log_2 (1-p_{\mathrm{L}}) \,. \tag{3.72}$$

At the median of the wave packet distribution $p_{\mathrm{L}} = 1/2$ and $S = 1$ ("Bell state" [60, 348]).

Specializing to a Gaussian (fermion or antifermion) wave packet in the thermodynamic and continuum limits, by Eq. (3.33), p_{L} becomes the CDF of a normal distribution with mean μ_x and standard deviation $1/2\sigma_k$:

$$p_{\mathrm{L}}(x) = \frac{1}{2}\left[1 + \mathrm{erf}\left(\frac{x-\mu_x}{\sqrt{2}\sigma_x}\right)\right] , \qquad \sigma_x = 1/2\sigma_k \,. \tag{3.73}$$

We denote the associated wave packet entanglement $S_{\mathrm{norm}}(x; \mu_x, \sigma_x)$. As Fig. 3.16 shows, $S_{\mathrm{norm}}(x; \mu_x, \sigma_x)$ closely resembles the PDF $|\phi_x|^2 \propto e^{-(x-\mu_x)^2/2\sigma_x^2}$ (up to the normalization), even though it decays as $x e^{-(x-\mu_x)^2/2\sigma_x^2}$ and thus has heavier tails.

The derivation extends immediately to multiple uncorrelated wave packets. The contributions of different wave packets are additive, up to exclusion principle effects ($\psi_x^\dagger \psi_x^\dagger |\Omega\rangle = 0$), which become irrelevant in the continuum limit or when the spatial support of the wave packet is large enough $\sigma_x \gg$. An explicit check reveals additivity violations of at most a few percent order for two perfectly overlapping wave packets with σ_x of the order of the ones used in the reported simulations. Furthermore, finite mass effects have also been measured

and found to be negligible.

Meson entanglement. The previous results are straightforwardly extended to meson wave packets exploiting the formulation of QED$_2$ with the link degrees of freedom integrated out from Eq. (3.39). In the infinite mass limit the ground state is again the Néel state. Suppose that the meson wave packet creation operator in Eq. (3.55) factorizes as a product of fermion and antifermion creation operators,

$$B_\phi^\dagger = C_{\phi^+}^\dagger D_{\phi^-}^\dagger \ , \tag{3.74}$$

for some amplitudes $\phi^\pm$. Then, by the additivity assumption, the entanglement profile of the meson is the sum of a pair of Eq. (3.72) contributions, $S = S_{\phi^+} + S_{\phi^-}$. Figure 3.8 shows that this is a good approximation for the Gaussian mesons simulated here, which are characterized by $\sigma_k \approx \sigma_{\Delta k}$. In this case, Eq. (3.74) holds up to $\mathcal{O}(\sigma_k^2 - \sigma_{\Delta k}^2)$ terms, with $\phi_k^\pm$ Gaussian amplitudes whose parameters are related to those of the meson wave packet by the substitutions

$$\mu_k \to \frac{\mu_k}{2} \ , \qquad \sigma_k \to \frac{\sqrt{\sigma_k^2 + \sigma_{\Delta k}^2}}{2} \ , \qquad \mu_x \to \mu_x \mp \frac{\mu_{\Delta x}}{2} \ . \tag{3.75}$$

If the fermion and antifermion are almost overlapped $\mu_{\Delta x} \ll 1/\sigma_k$ is negligible, as is the case for the mesons in Fig. 3.8, and the meson entanglement will be simply

$$2S_{\text{norm}}\left(x;\, \mu_x,\, \sigma_x = 1/\sqrt{\sigma_k^2 + \sigma_{\Delta k}^2} \right) , \tag{3.76}$$

where S_{norm} is the result derived for fermions and antifermions.

Entanglement propagation. The evolution of a wave packet of one-particle eigenstates $|k\rangle$ of momentum k and energy ω_k, is given by

$$e^{-iHt} \sum_k \phi_k |k\rangle = \sum_k e^{-i\omega_k t} \phi_k |k\rangle = \sum_k \phi_k(t) |k\rangle \ . \tag{3.77}$$

This holds for fermions and antifermions in the free theory, as well as for (exact) mesons in QED$_2$, even though the dispersion relation ω_k of mesons is not known analytically. For free staggered fermions, expanding the dispersion relation of Eq. (3.19e) in $1/m$ yields

$$\omega_k = m + \frac{\sin^2(k)}{2m} + \mathcal{O}(m^{-3}) \ . \tag{3.78}$$

Disregarding the inconsequential global phase e^{-imt}, the wave packet kinematics comes from subleading terms in the expansion and takes place on timescales $t \sim m$. Accordingly, sending $m \to \infty$ we implicitly assume $t = \tau m$ with τ finite.

Let us focus again on a Gaussian wave packet in the continuum with $\phi_k(t = t_0)$ given by Eq. (3.49). A stationary-phase approximation shows that $|\tilde{\phi}_x(t)|^2$ remains a Gaussian for $t > t_0$, but it moves and spreads according to[14]:

$$\mu_x(t) = \mu_x - \omega'_{\mu_k}(t - t_0) \,, \tag{3.79a}$$

$$\sigma_x^2(t) = \sigma_x^2 + \left[\frac{\omega''_{\mu_k}}{2\sigma_x}\right]^2 (t - t_0)^2 \,. \tag{3.79b}$$

The associated S_{wps} is obtained simply plugging Eq. (3.79) in the Gaussian result, S_{norm}.

For uncorrelated free multi-particle wave packets we again rely on the additivity assumption.

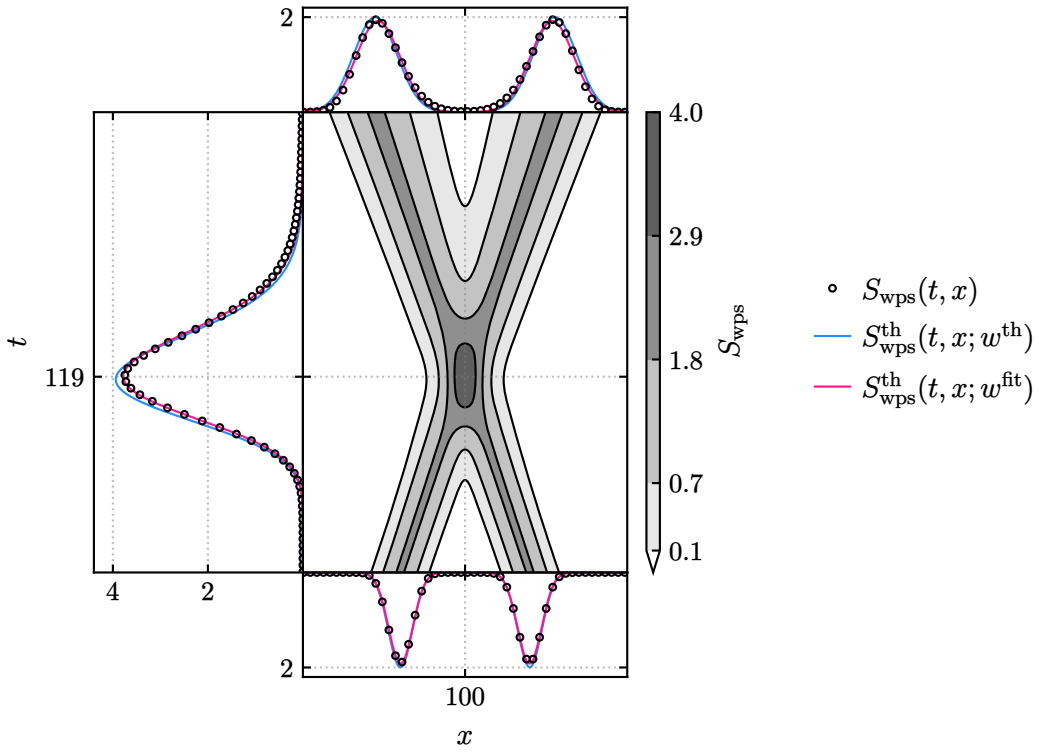

Figure 3.16: Wave packet entanglement entropy during the free propagation of the mesons in Fig. 3.8 for $m = 1$ and $g = 0$. Comparison of the numerical results with the $S^{\text{th}}_{\text{wps}}(t, x; w)$ prediction from Eq. (3.80). The contour plot reproduces the numerical data S_{wps}. The bottom and top panels show the initial and final time entanglement profiles; the left panel shows the mid-chain slice. In each side panel, along with S_{wps} (points), we plot the relevant section of $S^{\text{th}}_{\text{wps}}(t, x; w)$ for $w = w^{\text{th}}$ (blue lines) and $w = w^{\text{fit}}$ (red lines).

[14] Unsurprisingly, if the dispersion is linear there is no spreading.

However that, while free staggered fermions and antifermions always propagate according to Eq. (3.79), for mesons this is true only when they are far apart, so that their mutual interaction can be neglected or, trivially, when $g = 0$. During these "free propagation" stages of the collision, we model the wave packet entanglement due to a pair of parity-symmetric scattered mesons by

$$S^{\mathrm{th}}_{\mathrm{wps}}(t, x; w) = \mathcal{N}\left[S_{\mathrm{norm}}(x; \mu_x(t), \sigma_x(t)) + S_{\mathrm{norm}}(L - 1 - x; \mu_x(t), \sigma_x(t))\right] , \tag{3.80}$$

where $w = (\mathcal{N}{=}2, t_0, \mu_x, \sigma_x, \omega'_{\mu_k}, \omega''_{\mu_k})$ collects all the free parameters. In Fig. 3.16 we compare the numerical wave packet entanglement $S_{\mathrm{wps}}(t, x)$ from a $g = 0$ simulation[15] with the prediction from $S^{\mathrm{th}}_{\mathrm{wps}}(t, x; w)$ — both the expected parameters $w = w^{\mathrm{th}}$ and the values w^{fit} ($t_0 = 0$) that best interpolate the numerical data are shown. The plot confirms that $S^{\mathrm{th}}_{\mathrm{wps}}$ models accurately the numerical entanglement: comparing w^{th} and w^{fit}, the prominent distortion is a slight squashing of the entanglement profiles due to the lack of exact additivity between the various entanglement contributions.

Interaction entanglement

The ground state and the wave packets completely explain the entanglement observed in simulations of the free kinematics. In particular, if the system is cut outside the support of the outgoing wave packets, the entanglement entropy of the bipartition comes from the ground state only. When the interaction is switched on ($g > 0$) this is no longer true, because additional entanglement is generated by the dynamics. In the elastic scattering regime explored with our simulations, the final time entanglement entropy profiles are characterized by a uniform plateau in the region enclosed between the two outgoing wave packets; we thus interpret the dynamically generated entanglement as entanglement between the scattering products. The entanglement plateau is clearly visible in Fig. 3.17a and especially Fig. 3.17b, where we subtract the contribution from the $g = 0$ simulation. For $g > 0$, entanglement is present also in the middle of the chain, where the mass energy density, shown in Fig. 3.17c, vanishes.

The time profile of the mid-chain entanglement in Fig. 3.17d shows that the correlation between the outgoing mesons is produced by the interactions, during the collision. Indeed, in the initial stage of the evolution, when the incoming mesons approach one another, no entanglement is present between them. Once their wave packets overlap, entanglement is detected at the middle of the chain. This process gets delayed as the coupling is increased (see Fig. 3.18a), due to the deflection of the meson trajectories. In Fig. 3.18b we plot the peak mid-chain entanglement $S(t^\star, L/2)$ as a function of $u = m^\alpha k^\beta g$, where $k = 0.81$ is the absolute value of the mean momentum of the initial mesons and the exponents α, β are reported in Fig. 3.19. $S(t^\star, L/2)$ is decreasing at small u, but above the threshold value $u^\star \approx 0.08$ it rapidly increases again. Nevertheless, it is only after the collision that the

[15] The formulation of the model in Eq. (3.39), with link degrees of freedom integrated-out is employed here.

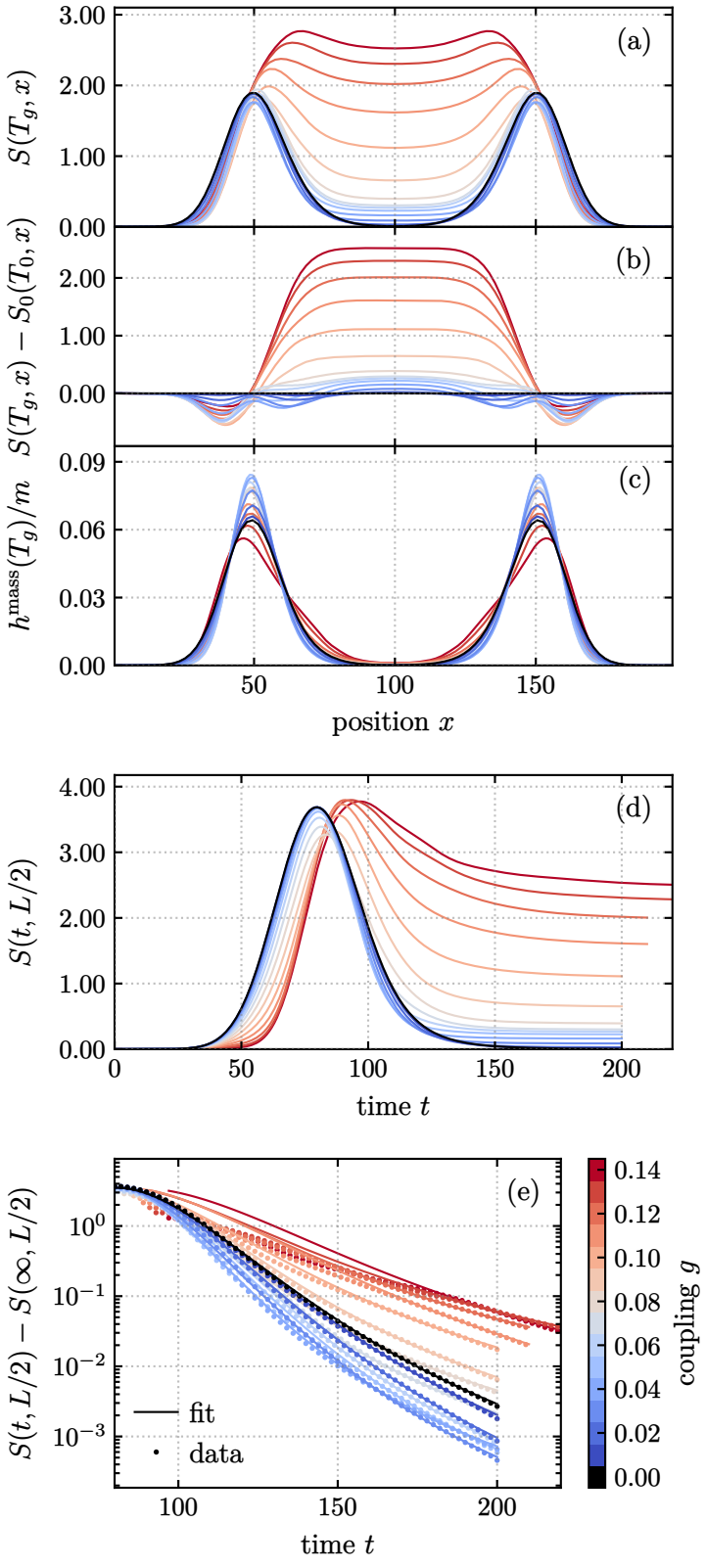

Figure 3.17: Entanglement entropy S and mass energy density h^{mass} space and time sections for elastic meson-meson scatterings with $m = 0.6$ and various g (see color bar in the last row). The vacuum contribution is always subtracted.

Plots (a) to (c) are final time profiles, ($t = T_g$, corresponding to outgoing wave packet peaks separated by $\Delta x \approx 100$); (a) and (b) are entanglement profiles, with the $g = 0$ profile subtracted in (b); (c) shows the mass energy density.

Panel (d) shows the mid-chain entanglement as a function of time, and (e) is an enlargement of its decaying tail, approaching the extrapolated asymptotic value $S(\infty, L/2) = S_{\text{int}} + S_{\text{wps}}(\infty) \approx S_{\text{int}}$.

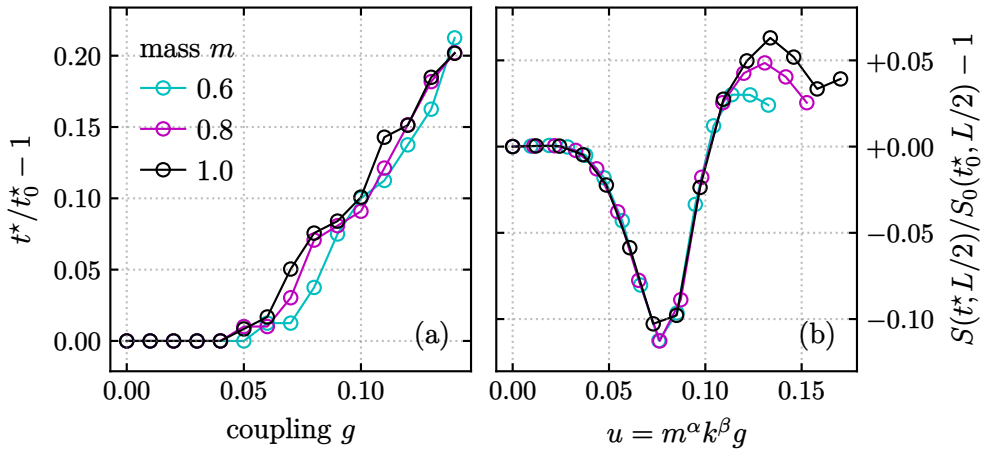

Figure 3.18: Time $t^\star$ (a) and entanglement $S(t^\star_, L/2)$ (b) corresponding to the peak of the mid-chain entanglement profiles, for different masses m and couplings g. The ordinate represents the relative deviation from the values obtained for the free ($g = 0$) simulation, namely $t_0^\star$ and $S_0(t_0^\star, L/2)$.

fundamental distinction between the free and interacting cases — namely, the entanglement of the scattering products — emerges.

Figure 3.19 shows the the coupling dependence of the entanglement between the outgoing mesons generated by the interaction, S_{int}, for different values of the bare fermion mass m and of the mean momenta $\pm k$ of the initial mesons. To quantify S_{int} we assume that all the entanglement due to the interaction is produced during the collision and remains approximately constant afterwards. Thus, in the final stage of the evolution, the mid-chain entanglement can be decomposed as a constant contribution $S_{\text{grn}} + S_{\text{int}}$, due to the ground state and the interaction, plus a decaying component $S_{\text{wps}}(t)$, attributed to the tails of the outgoing meson wave packets. We thus evolve the system until the mesons are spatially separated by $\Delta x \gtrsim 100$ and fit the mid-chain entanglement values sampled in the final $\Delta t = 40$ time interval using the expression provided by Eq. (3.80) for $x = L/2$, plus a constant background. Since we always remove the ground state contribution, the value of the background is precisely the extrapolated S_{int}. The fits are reproduced in Fig. 3.17e. According to Fig. 3.17c, for the highest g values the outgoing wave packets are not Gaussian, as assumed in Eq. (3.80), thus the fits are only partially justified. Yet, especially for stronger couplings, towards the end of the evolution the wave packets give a small relative contribution to the mid-chain entanglement and its final value is already an accurate estimate of S_{int}.

We find that the entanglement produced by the interaction — i.e. the amount of quantum correlations between the outgoing mesons — increases with the coupling, as expected. Moreover, we find that the collapse of the interaction entanglement curves on a unique curve

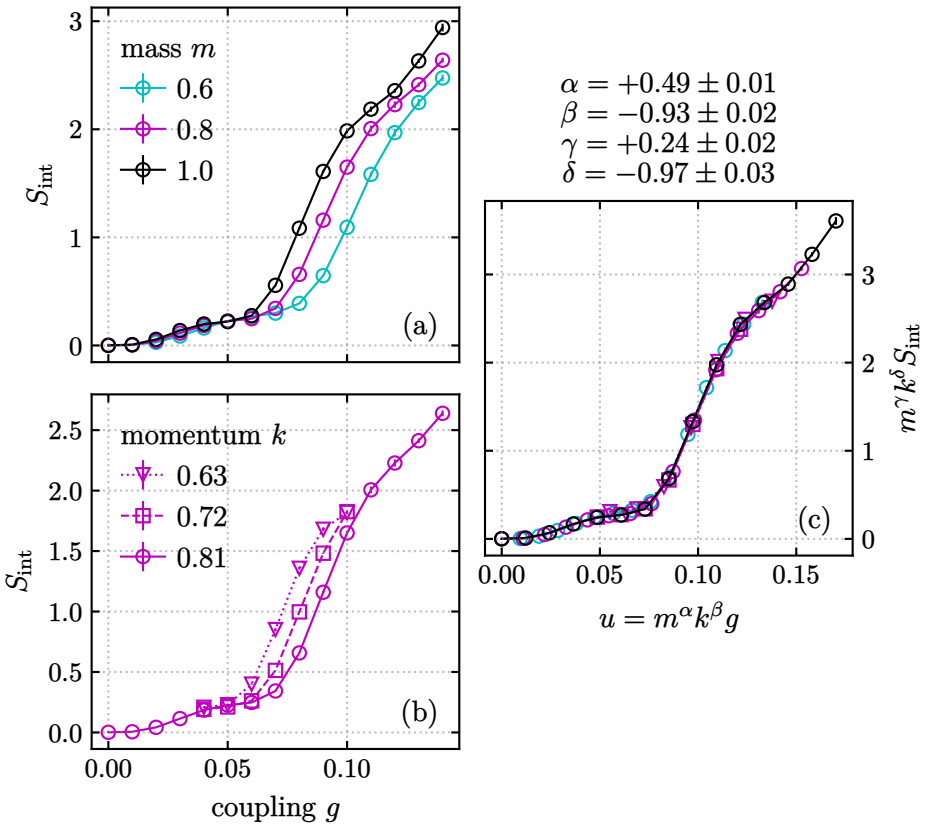

Figure 3.19: Growth of the interaction entanglement S_{int} with the coupling g, for different masses m (a) and mean momenta $\pm k$ of the initial mesons (b). Panel (c) collects all data points from (a)–(b) and shows the universal behavior captured by Eq. (3.81). Error bars represent a $\pm\delta S_{\text{int}}$ uncertainty, δS_{int} being the difference between the extrapolated S_{int} and the final mid-chain entanglement (with ground contribution removed).

$F(u)$ shown in Fig. 3.19c is described by

$$S_{\text{int}}(g, m, k) = m^{-\gamma} k^{-\delta} F(u) \,, \quad u = m^\alpha k^\beta g \,. \tag{3.81}$$

The optimal exponents $\alpha, \beta, \gamma, \delta$ in the least-squares sense are reported in Fig. 3.19c. They are obtained minimizing the residual sum of squares of the rescaled data points from a common interpolating polynomial of degree 10. Equation (3.81) allows us to express our findings in terms of u only: after an initial gentle growth for small u, at $u^\star$ we observe an abrupt increase in the slope of S_{int}, which then stays constant up to $u \approx 0.12$, at which point the slope diminishes again.

4

Hadrons in Hardcore-Gluon QCD_2

a minimal model featuring QCD's pions

After motivating the need for non-perturbative approaches to quantum chromodynamics (QCD)*, we introduce 2-flavor hardcore-gluon* QCD_2*: a truncated* $(1+1)-$*dimensional* $SU(3)$ *lattice gauge theory. We present a formulation of the model where gauge redundancy is absent and study it non-perturbatively by means of tensor networks, at zero and finite density. Criticality is detected in an extended subregion of parameter space and at least two distinct phases are identified, both populated with edge and bulk gapless modes, one embedding the continuum limit. We thereby show that that the model provides a minimal* $SU(3)$ *lattice gauge theory reproducing distinctive properties of real-world* QCD *— most notably, its particle spectrum features charged pions.*

Attribution: This Chapter consist of original research work, which has also been collected in the manuscript in Ref. [126]. The same techniques we use have been developed and employed before, e.g. in Ref. [124], but the model studied here had not been yet investigated and the results are therefore new.

4.1 The quest for non-perturbative QCD

Quantum chromodynamics (QCD) [23, 35, 349] is a Yang-Mills theory with gauge group SU(3)-color, coupled with Dirac fermion matter. It corresponds to the sector of the Standard Model of particle physics responsible for the description of the quark and gluon fields, and their strong interactions. Asymptotic freedom [119, 120] ensures that, at short length scales, these fields manifest as almost free parton particles, thus allowing for a perturbative expansion in a small coupling parameter. Conversely, at wavelengths of the order of the size of a proton, quarks and gluons confine, perturbative techniques become unviable, and a plethora of color-neutral hadron bound states and resonances emerge. Hadrons make up for most of the mass of visible matter [40]. They are also regularly scattered at particle accelerators, such as the Large Hadron Collider (LHC). Understanding QCD at these scales is thus essential to account for collider data, to validate high-energy theories against experimental evidence and, consequently, to our knowledge of the physical universe. Lattice Monte Carlo numerical methods have long been employed in attacking this formidable challenge, producing outstanding predictions for hadron masses and decay rates, and elucidating the mechanisms of color confinement and chiral symmetry breaking, as well as the thermal properties of QCD [39, 350]. Despite this vast array of successes, Monte Carlo methods are plagued with the notorious sign problem in a variety of physically relevant scenarios, such as finite baryon number density and real-time dynamics [39, 42, 351]. Especially in these regimes, there is strong demand for alternative, non-perturbative strategies aiming for a complete characterization of QCD's collective phenomena, such as its phase diagram [111, 352, 353]. In the last decade, quantum simulation and tensor networks have been envisaged as two candidate approaches to fill this gap. Both typically rely on the canonical formulation of the theory and thus share some strengths as well as many challenges. While the idea [57] of quantum simulating QCD is quickly gaining traction [55, 81, 180, 354–365], current day quantum platforms are not yet mature enough to attack directly such a complex theory. It is thus crucial to single out and characterize models of minimal complexity reproducing as many QCD phenomena as possible. Because TN and quantum approaches share a number of implementation steps, the former can provide precious guidance in identifying such simplified models.

In this Chapter we introduce and study a simplified model of (1+1)D 2-flavor QCD. By means of TN, we characterize its phase diagram and spectral properties, summarized in Fig. 4.1. In order to make QCD_2 amenable to TN methods or quantum simulation, we combine the Hamiltonian formulation of LGT by Kogut and Susskind (Section 1.4B) with a gauge field truncation in irrep space (Section 1.4C). In the light of future quantum simulation implementations, we consider only the strictest possible truncation, here labeled *hardcore-gluon* approximation, and do not attempt a finite truncation extrapolation. Our analysis shows that the maximally-truncated model studied here provides a minimal realization of a SU(3) gauge theory reproducing part of the particle spectrum of (1+3)D QCD — namely, charged pions.

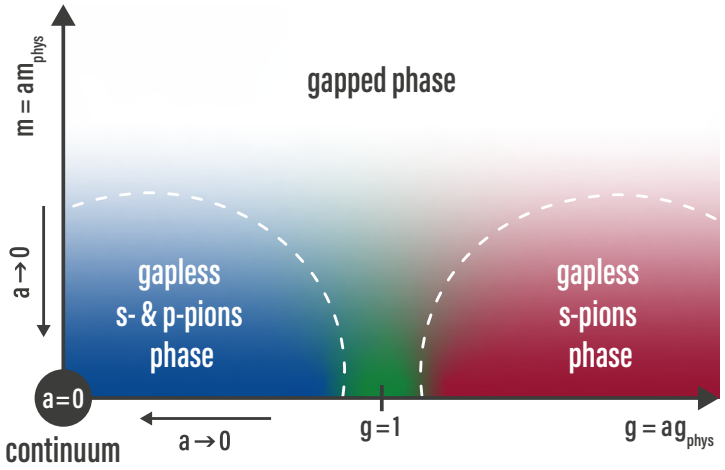

Figure 4.1: Sketch of the phase diagram of hardcore 2-flavor QCD_2 in the (g, m)-plane, $m = m_u = m_d$ (quark masses). The arrows direct towards the continuum, where the lattice correlation length $\xi = \xi_{\text{phys}}/a$ of physical excitations diverges. The model is gapped above a threshold bare quark mass of order $m \sim 10^{-2}$, and gapless below. Within the gapless region, the dashed ellipses highlight the weak ($g \ll 1$, blue) and strong ($g \gg 1$, red) coupling phases, which attracted most of this work's focus. At their interface lays the intermediate coupling regime ($g \approx 1$, green). Both the small and large g phases feature gapless charged pions $\pi^{\pm}$ (s- and p-wave for $g \ll 1$, only s-wave for $g \gg 1$). Circumstantial evidence suggests the neutral pions π^0 are also gapless; protons, neutrons and delta baryons were found to be gapped (at finite g).

4.2 Hardcore-gluon QCD_2 building blocks

At the core of the model is the 1D Kogut-Susskind Hamiltonian from Eq. (1.118)

$$H = \sum_{x,f,c,c'} \left[\frac{i}{2} \psi^{\dagger}_{x,f,c} U_{x;c,c'} \psi_{x+1,f,c'} + \text{H.c.} \right] + \sum_{x,f,c} m_f (-1)^x \psi^{\dagger}_{x,f,c} \psi_{x,f,c} + \sum_x \frac{g^2}{2} E^2_x \,, \tag{4.1}$$

where lattice units have been employed. We remind that the continuum limit is expected to be at vanishing lattice coupling g and bare quark masses m_f.

The staggered fermion field $\psi_{x,f,c}$ acts on *matter quark* degrees of freedom (d.o.f.) living on lattice *sites* x; here it carries a flavor index $f \in \{u, d\}$, plus a color index $c \in \{r, g, b\}$ in the fundamental representation of local SU(3). *Gauge gluon* d.o.f. sit on lattice *links* $(x, x+1)$, where the chromoelectric energy density operator E^2_x and the parallel transporter $U_{x;c,c'}$ act; the latter transforms with the fundamental irrep and its dual at the left and right ends of the link respectively, making the hopping term in Eq. (4.1) gauge invariant. Via the non-Abelian Fourier of Eq. (1.125), the link Hilbert space decomposes as direct sum over SU(3)-color irreps and can be generated acting with $U_{x;c,c'}$ or $U^{\dagger}_{x;c,c'}$ on the singlet state $|\mathbf{1}\rangle$.

Hardcore gluons. We truncate the infinite dimensional link space to a 19-dimensional one following the scheme in Section 1.4C, keeping only the trivial irrep, the fundamental and its dual (Fig. 4.2a):

$$\mathscr{H}_{\text{link}} \cong (\mathbf{1} \otimes \mathbf{1}) \oplus (\mathbf{3} \otimes \overline{\mathbf{3}}) \oplus (\overline{\mathbf{3}} \otimes \mathbf{3}) \ . \tag{4.2}$$

We label this truncation *hardcore-gluon*, in analogy to atomic physics, as the truncated space is spanned acting on the "vacuum" $|\mathbf{1}\rangle$ with (at most) a single application of the parallel transporters $U_{c,c'}$ or $U^\dagger_{c,c'}$. As discussed in Section 1.4C, such a projection preserves exact gauge invariance but spoils the unitarity of parallel transporters.

At strong lattice coupling, $g \gg 1$, the truncation effectively acts as an energy cutoff $g^2\Lambda/2$, with $16/3 \leq \Lambda < 12$ (see Table 1.1). At weak coupling, $g \ll 1$, the truncation cannot be justified on the grounds of a low energy approximation but rather it yields a different model, which we baptize *hardcore 2-flavor QCD$_2$*. Since the continuum limit reads $m_f, g \to 0$, recovering the physics of the original continuum theory requires relaxing the link truncation while sending $a \to 0$ [219, 220]. Here we focus solely on this maximally-truncated model and on the features it shares with (1+3)D QCD, beyond SU(3) gauge invariance and confinement.

Dressed site. We enforce Gauss law following the dressed site approach of Section 1.4D. Under the hardcore-gluon truncation, the rishon semilink spaces read (Fig. 4.2c):

$$\mathscr{H}_{\text{L}} \cong \mathscr{H}_{\text{R}} = \mathbf{1} \oplus \mathbf{3} \oplus \overline{\mathbf{3}} \ . \tag{4.3}$$

Basis labels (grouped by irrep) are $(0), (r, g, b), (c, m, y)$. Within each link enlarged link Hilbert space, $\mathscr{H}_{\text{L}} \otimes \mathscr{H}_{\text{R}}$, the physical link space, $\mathscr{H}_{\text{link}}$, is singled out as the trivial sector of a *local* $\mathbb{Z}_3$ link symmetry generated by

$$\Phi = \left[\mathbf{I}_{\mathbf{1}} \oplus e^{2\pi i/3}\mathbf{I}_{\mathbf{3}} \oplus e^{4\pi i/3}\mathbf{I}_{\overline{\mathbf{3}}}\right]^{\otimes 2} \ . \tag{4.4}$$

Once the link constraint has been enforced, the quadratic Casimir operator $\mathcal{C}_2$ can be defined as single semilink operator, acting on either end of the link. By Table 1.1,

$$\mathcal{C}_2 = \frac{16}{3}(1 - |0\rangle\langle 0|) \ . \tag{4.5}$$

Within the hardcore-gluon truncation, every semilink irrep appears exactly once in a fusion with the fundamental (the comparator irrep, $\mathbf{J} = \mathbf{3}$):

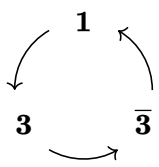

(4.6)

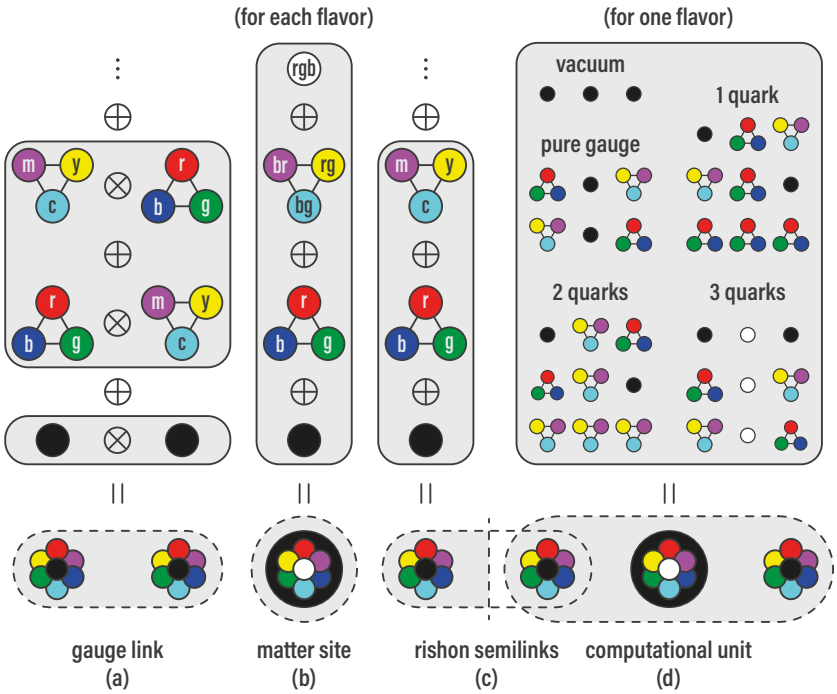

Figure 4.2: Construction of the building blocks for a SU(3) gauge singlet TN or quantum simulator. Cartoon representation of the simplified case of a single quark flavor: (a) color irrep decomposition and truncation of the gauge boson link space (irreps are grouped by their quadratic Casimir eigenvalue); (b) decomposition of the matter fermion site; (c) splitting of the links in rishon semilink spaces; and finally (d) composite rishon-matter-rishon computational unit with its 12 color singlets.

We thus have a single generation of rishon operators[1] (i.e., no degeneracy index α):

$$\zeta_r = |c\rangle\langle 0| + |0\rangle\langle r| - |b\rangle\langle m| + |g\rangle\langle y| \,, \tag{4.7a}$$
$$\zeta_g = |m\rangle\langle 0| + |0\rangle\langle g| - |r\rangle\langle y| + |b\rangle\langle c| \,, \tag{4.7b}$$
$$\zeta_b = |y\rangle\langle 0| + |0\rangle\langle b| - |g\rangle\langle c| + |r\rangle\langle m| \,; \tag{4.7c}$$

and the comparator is simply

$$U_{c,c'} = \zeta_c^\dagger \otimes \zeta_{c'} \,. \tag{4.8}$$

Projection to the physical link space in the is unnecessary because $U_{c,c'}$ already preserves the link symmetry:

$$\Phi U_{c,c'} \Phi^\dagger = 0 \,. \tag{4.9}$$

[1] We renormalized individual irreps to get rid of numerical prefactors. This is not a problem for our purposes because unitarity was already broken by the truncation, which we do not intend to lift.

$3\Lambda/4$	link	rishon	dressed
4	19	7	54
9	83	15	92
10	155	27	166
16	605	57	266
18	805	77	342
24	1534	104	392
25	2686	152	506
28	3136	182	582

Table 4.1: Dimensions of the link, rishon and computational spaces of 2-flavor QCD_2 for truncation cutoffs Λ equal to the few lowest SU(3) quadratic Casimir eigenvalues. The 64-dimensional matter site is unaffected by the truncation.

For N_f quarks in the fundamental irrep $\mathbf{3}$, the matter site decomposes as (Fig. 4.2b):

$$\mathscr{H}_{\text{site}} \cong \left[\bigwedge(\mathbf{3})\right]^{\otimes N_f} = [\,\mathbf{1} \oplus \mathbf{3} \oplus \overline{\mathbf{3}} \oplus \mathbf{1}'\,]^{\otimes N_f} \ . \tag{4.10}$$

Already at $N_f = 1$, the singlet appears twice. At $N_f = 2$, the final decomposition involves also $\mathbf{6}$, $\overline{\mathbf{6}}$ and $\mathbf{8}$, as shown in Table 4.2.

The composite site Hilbert space,

$$\mathscr{H}_{\text{site}} \otimes \mathscr{H}_{\text{L}} \otimes \mathscr{H}_{\text{R}} = [\,\mathbf{1} \oplus \mathbf{3} \oplus \overline{\mathbf{3}} \oplus \mathbf{1}'\,]^{\otimes 2} \otimes [\,\mathbf{1} \oplus \mathbf{3} \oplus \overline{\mathbf{3}}\,]^{\otimes 2} \tag{4.11}$$

contains 54 linearly independent singlets, which form the local computational basis of hard-core 2-flavor QCD_2. They are listed in Table 4.2, organized by various quantum numbers. We thus successfully replaced the non-Abelian Gauss law with a simpler Abelian selection rule on pairs of neighboring dressed sites. As a byproduct, it yields a computational site which embeds both matter and gauge d.o.f. but is still smaller than the original $2^{N_f N_c} = 64$-dimensional matter site alone. The computational matrix elements of any physical local gauge invariant operator can be evaluated from the Clebsch-Gordan expansion of these computational states in the original "physical" matter and rishon bases. The expansion is available online, for reproducibility [366], together with a script for computing matrix elements and with its output for the operators relevant to our numerical simulations. A few local Hilbert spaces dimensions for higher truncation cutoffs Λ are reported in Table 4.1. The first few truncations are within the reach of present-day TN calculations [123].

Inclusion of an electric field A physically motivated extension of the model, which would allow studying electric corrections to QCD_2 in the spontaneously broken electroweak

α	SU(3)-color					$\mathbb{Z}_3$-link		U(1)-flavor(s)		SU(2)-isospin	
	j_{matter}	j_u	j_d	j_R	j_L	ϕ_R	ϕ_L	N_u	N_d	I	I_3
1	$\mathbf{1}$	$\mathbf{1}$	$\mathbf{1}$	$\mathbf{1}$	$\mathbf{1}$	0	0	0	0	0	0
2	$\mathbf{1}$	$\mathbf{1}$	$\mathbf{1}$	$\mathbf{3}$	$\overline{\mathbf{3}}$	-1	$+1$	0	0	0	0
3	$\mathbf{1}$	$\mathbf{1}$	$\mathbf{1}$	$\overline{\mathbf{3}}$	$\mathbf{3}$	$+1$	-1	0	0	0	0
4	$\mathbf{3}$	$\mathbf{1}$	$\mathbf{3}$	$\mathbf{1}$	$\overline{\mathbf{3}}$	0	$+1$	0	1	$1/2$	$-1/2$
5	$\mathbf{3}$	$\mathbf{1}$	$\mathbf{3}$	$\mathbf{3}$	$\mathbf{3}$	-1	-1	0	1	$1/2$	$-1/2$
6	$\mathbf{3}$	$\mathbf{1}$	$\mathbf{3}$	$\overline{\mathbf{3}}$	$\mathbf{1}$	$+1$	0	0	1	$1/2$	$-1/2$
7	$\mathbf{3}$	$\mathbf{3}$	$\mathbf{1}$	$\mathbf{1}$	$\overline{\mathbf{3}}$	0	$+1$	1	0	$1/2$	$+1/2$
8	$\mathbf{3}$	$\mathbf{3}$	$\mathbf{1}$	$\mathbf{3}$	$\mathbf{3}$	-1	-1	1	0	$1/2$	$+1/2$
9	$\mathbf{3}$	$\mathbf{3}$	$\mathbf{1}$	$\overline{\mathbf{3}}$	$\mathbf{1}$	$+1$	0	1	0	$1/2$	$+1/2$
10	$\mathbf{6}$	$\mathbf{3}$	$\mathbf{3}$	$\overline{\mathbf{3}}$	$\overline{\mathbf{3}}$	$+1$	$+1$	1	1	0	0
11	$\overline{\mathbf{3}}$	$\mathbf{1}$	$\overline{\mathbf{3}}$	$\mathbf{1}$	$\mathbf{3}$	0	$+1$	0	2	1	-1
12	$\overline{\mathbf{3}}$	$\mathbf{1}$	$\overline{\mathbf{3}}$	$\mathbf{3}$	$\mathbf{1}$	$+1$	0	0	2	1	-1
13	$\overline{\mathbf{3}}$	$\mathbf{1}$	$\overline{\mathbf{3}}$	$\overline{\mathbf{3}}$	$\overline{\mathbf{3}}$	$+1$	$+1$	0	2	1	-1
14	$\overline{\mathbf{3}}$	$\mathbf{3}$	$\mathbf{3}$	$\mathbf{1}$	$\mathbf{3}$	0	$+1$	1	1	1	0
15	$\overline{\mathbf{3}}$	$\mathbf{3}$	$\mathbf{3}$	$\mathbf{3}$	$\mathbf{1}$	$+1$	0	1	1	1	0
16	$\overline{\mathbf{3}}$	$\mathbf{3}$	$\mathbf{3}$	$\overline{\mathbf{3}}$	$\overline{\mathbf{3}}$	$+1$	$+1$	1	1	1	0
17	$\overline{\mathbf{3}}$	$\overline{\mathbf{3}}$	$\mathbf{1}$	$\mathbf{1}$	$\mathbf{3}$	0	$+1$	2	0	1	$+1$
18	$\overline{\mathbf{3}}$	$\overline{\mathbf{3}}$	$\mathbf{1}$	$\mathbf{3}$	$\mathbf{1}$	$+1$	0	2	0	1	$+1$
19	$\overline{\mathbf{3}}$	$\overline{\mathbf{3}}$	$\mathbf{1}$	$\overline{\mathbf{3}}$	$\overline{\mathbf{3}}$	$+1$	$+1$	2	0	1	$+1$
20	$\mathbf{8}$	$\mathbf{3}$	$\overline{\mathbf{3}}$	$\mathbf{3}$	$\overline{\mathbf{3}}$	-1	$+1$	1	2	$1/2$	$-1/2$
21	$\mathbf{8}$	$\mathbf{3}$	$\overline{\mathbf{3}}$	$\overline{\mathbf{3}}$	$\mathbf{3}$	$+1$	-1	1	2	$1/2$	$-1/2$
22	$\mathbf{8}$	$\overline{\mathbf{3}}$	$\mathbf{3}$	$\mathbf{3}$	$\overline{\mathbf{3}}$	-1	$+1$	2	1	$1/2$	$+1/2$
23	$\mathbf{8}$	$\overline{\mathbf{3}}$	$\mathbf{3}$	$\overline{\mathbf{3}}$	$\mathbf{3}$	$+1$	-1	2	1	$1/2$	$+1/2$
24	$\mathbf{1}$	$\mathbf{1}$	$\mathbf{1}'$	$\mathbf{1}$	$\mathbf{1}$	0	0	0	3	$3/2$	$-3/2$
25	$\mathbf{1}$	$\mathbf{1}$	$\mathbf{1}'$	$\mathbf{3}$	$\overline{\mathbf{3}}$	-1	$+1$	0	3	$3/2$	$-3/2$
26	$\mathbf{1}$	$\mathbf{1}$	$\mathbf{1}'$	$\overline{\mathbf{3}}$	$\mathbf{3}$	$+1$	-1	0	3	$3/2$	$-3/2$
27	$\mathbf{1}$	$\mathbf{3}$	$\overline{\mathbf{3}}$	$\mathbf{1}$	$\mathbf{1}$	0	0	1	2	$3/2$	$-1/2$
28	$\mathbf{1}$	$\mathbf{3}$	$\overline{\mathbf{3}}$	$\mathbf{3}$	$\overline{\mathbf{3}}$	-1	$+1$	1	2	$3/2$	$-1/2$
29	$\mathbf{1}$	$\mathbf{3}$	$\overline{\mathbf{3}}$	$\overline{\mathbf{3}}$	$\mathbf{3}$	$+1$	-1	1	2	$3/2$	$-1/2$
30	$\mathbf{1}$	$\overline{\mathbf{3}}$	$\mathbf{3}$	$\mathbf{1}$	$\mathbf{1}$	0	0	2	1	$3/2$	$+1/2$
31	$\mathbf{1}$	$\overline{\mathbf{3}}$	$\mathbf{3}$	$\mathbf{3}$	$\overline{\mathbf{3}}$	-1	$+1$	2	1	$3/2$	$+1/2$
32	$\mathbf{1}$	$\overline{\mathbf{3}}$	$\mathbf{3}$	$\overline{\mathbf{3}}$	$\mathbf{3}$	$+1$	-1	2	1	$3/2$	$+1/2$
33	$\mathbf{1}$	$\mathbf{1}'$	$\mathbf{1}$	$\mathbf{1}$	$\mathbf{1}$	0	0	3	0	$3/2$	$+3/2$
34	$\mathbf{1}$	$\mathbf{1}'$	$\mathbf{1}$	$\mathbf{3}$	$\overline{\mathbf{3}}$	-1	$+1$	3	0	$3/2$	$+3/2$
35	$\mathbf{1}$	$\mathbf{1}'$	$\mathbf{1}$	$\overline{\mathbf{3}}$	$\mathbf{3}$	$+1$	-1	3	0	$3/2$	$+3/2$
36	$\overline{\mathbf{6}}$	$\overline{\mathbf{3}}$	$\overline{\mathbf{3}}$	$\mathbf{3}$	$\mathbf{3}$	-1	-1	2	2	0	0
37	$\mathbf{3}$	$\mathbf{3}$	$\mathbf{1}'$	$\mathbf{1}$	$\overline{\mathbf{3}}$	0	$+1$	1	3	1	-1
38	$\mathbf{3}$	$\mathbf{3}$	$\mathbf{1}'$	$\mathbf{3}$	$\mathbf{3}$	-1	-1	1	3	1	-1
39	$\mathbf{3}$	$\mathbf{3}$	$\mathbf{1}'$	$\overline{\mathbf{3}}$	$\mathbf{1}$	$+1$	0	1	3	1	-1
40	$\mathbf{3}$	$\overline{\mathbf{3}}$	$\overline{\mathbf{3}}$	$\mathbf{1}$	$\overline{\mathbf{3}}$	0	$+1$	2	2	1	0
41	$\mathbf{3}$	$\overline{\mathbf{3}}$	$\overline{\mathbf{3}}$	$\mathbf{3}$	$\mathbf{3}$	-1	-1	2	2	1	0
42	$\mathbf{3}$	$\overline{\mathbf{3}}$	$\overline{\mathbf{3}}$	$\overline{\mathbf{3}}$	$\mathbf{1}$	$+1$	0	2	2	1	0
43	$\mathbf{3}$	$\mathbf{1}'$	$\mathbf{3}$	$\mathbf{1}$	$\overline{\mathbf{3}}$	0	$+1$	3	1	1	$+1$
44	$\mathbf{3}$	$\mathbf{1}'$	$\mathbf{3}$	$\mathbf{3}$	$\mathbf{3}$	-1	-1	3	1	1	$+1$
45	$\mathbf{3}$	$\mathbf{1}'$	$\mathbf{3}$	$\overline{\mathbf{3}}$	$\mathbf{1}$	$+1$	0	3	1	1	$+1$
46	$\overline{\mathbf{3}}$	$\overline{\mathbf{3}}$	$\mathbf{1}'$	$\mathbf{1}$	$\mathbf{3}$	0	-1	2	3	$1/2$	$-1/2$
47	$\overline{\mathbf{3}}$	$\overline{\mathbf{3}}$	$\mathbf{1}'$	$\mathbf{3}$	$\mathbf{1}$	-1	0	2	3	$1/2$	$-1/2$
48	$\overline{\mathbf{3}}$	$\overline{\mathbf{3}}$	$\mathbf{1}'$	$\overline{\mathbf{3}}$	$\overline{\mathbf{3}}$	$+1$	-1	2	3	$1/2$	$-1/2$
49	$\overline{\mathbf{3}}$	$\mathbf{1}'$	$\overline{\mathbf{3}}$	$\mathbf{1}$	$\mathbf{3}$	0	-1	3	2	$1/2$	$+1/2$
50	$\overline{\mathbf{3}}$	$\mathbf{1}'$	$\overline{\mathbf{3}}$	$\mathbf{3}$	$\mathbf{1}$	-1	0	3	2	$1/2$	$+1/2$
51	$\overline{\mathbf{3}}$	$\mathbf{1}'$	$\overline{\mathbf{3}}$	$\overline{\mathbf{3}}$	$\overline{\mathbf{3}}$	$+1$	-1	3	2	$1/2$	$+1/2$
52	$\mathbf{1}$	$\mathbf{1}'$	$\mathbf{1}'$	$\mathbf{1}$	$\mathbf{1}$	0	0	3	3	0	0
53	$\mathbf{1}$	$\mathbf{1}'$	$\mathbf{1}'$	$\mathbf{3}$	$\overline{\mathbf{3}}$	-1	$+1$	3	3	0	0
54	$\mathbf{1}$	$\mathbf{1}'$	$\mathbf{1}'$	$\overline{\mathbf{3}}$	$\mathbf{3}$	$+1$	-1	3	3	0	0

Table 4.2: Computational basis $|\alpha\rangle$: SU(3)-color irreps of matter, $j_{\text{matter}} \in j_u \otimes j_d$; rishon SU(3)-color irrep $j_{R,L}$ and $\mathbb{Z}_3$-link charge $\phi_{R,L}$; numbers N_u, N_d of up and down quarks; SU(2)-isospin irrep I and projection $I_3 = (N_u - N_d)/2$. Note that $\phi_{R,L}$ contribute to different link charges; SU(2)-isospin provides good quantum numbers only when $m_u = m_d$.

phase [367], consists in adding a U(1)-electromagnetic (em) component to its gauge group [223]. To this aim, new U(1) gauge d.o.f. have to be implanted on each link. All U(1) irreps are one-dimensional and are labeled by $Q \in \mathbb{Z}$. Setting $Q_d = -1$ and $Q_u = +2$, the electric charge of each state in Table 4.2 follows: $Q_\alpha = 2N_u - N_d$. Moreover,

$$U_{\rm em}^Q |Q'\rangle = |Q' + Q\rangle \ , \quad E_{\rm em}|Q\rangle = Q|Q\rangle \ . \tag{4.12}$$

Insisting that the bare vacuum of all d.o.f. is a physical state, at least 5 U(1) irreps have to be kept. We adopt once again the maximal truncation. Then, each row in Table 4.2 is split in $5 - |Q_\alpha|$ entries, with the L rishon in irreps Q_L,

$$-2 - \min(0, Q_\alpha) < Q_L < +2 - \max(0, Q_\alpha) \ , \tag{4.13}$$

and $Q_R = -(Q_L + Q_\alpha)$. The resulting computational basis consists of 150 states. Alternatively, a $\mathbb{Z}_5$ subgroup truncation gives an even more bewildering — albeit still attainable [123] — 270-dimensional computational site.

At the level of the Hamiltonian, the extension amounts to the following formal substitutions:

$$U \to U_{\rm color} U_{\rm em}^{Q_f} \ , \quad gE \to g_{\rm color} E_{\rm color} + g_{\rm em} E_{\rm em} \ . \tag{4.14}$$

4.3 Strong coupling expansion

In this Section we perform a strong coupling expansion (SCE) for hardcore 2-flavor QCD_2. We work in the regime $g \gg 1$, $m_f = 0$, treating the hopping term as a perturbation of the chromoelectric energy term:

$$H_0 = \frac{g^2}{2} \sum_x E_x^2 \ , \qquad H_1 = \sum_{x,f,c,c'} \frac{i}{2} \psi^\dagger_{x,f,c} U^\dagger_{x;c,c'} \psi_{x+1,f,c'} + \text{H.c.} \ ; \tag{4.15}$$

We restrict to the unperturbed ground space $\mathscr{H}_{\rm eff}$ — the null space of H_0 — and use second order, degenerate perturbation theory to define an effective Hamiltonian

$$H_{\rm eff} = g^{-2} \, V^\dagger H_1 (-H_0)^p H_1 V \ , \tag{4.16}$$

which resolves order $O(1/g^2)$ splittings. Here A^p is the Moore-Penrose pseudoinverse of A and V is the isometry from the full Hilbert space to $\mathscr{H}_{\rm eff}$. In the dressed site formulation, V decomposes in a product of local isometries v_x projecting on the gauge-trivial states,

$$v = |ddd\rangle\langle 24| + |udd\rangle\langle 27| + |uud\rangle\langle 30| + |uuu\rangle\langle 33| + |\circ\rangle\langle 1| + |\bullet\rangle\langle 52| \ , \tag{4.17}$$

where we labeled states in $\mathscr{H}_{\rm eff}$ according to their quark content ($\circ$ = empty, $\bullet$ = full). H_0 is a sum of single-body terms and each summand in H_1 changes the gauge state on exactly

one link. It follows that both H_1 factors in Eq. (4.16) must to act on the same link and thus H_{eff} is nearest-neighbor. Up to an additive constant,

$$g^2 H_{\text{eff}} = 3 \sum_x S^z_{\frac{1}{2},x} S^z_{\frac{1}{2},x+1} + \sum_x \vec{S}_{\frac{3}{2},x} \cdot \vec{S}_{\frac{3}{2},x+1} \ , \tag{4.18}$$

where $S^z_{1/2} = (|\circ\rangle\langle\circ| - |\bullet\rangle\langle\bullet|)/2$ and $\vec{S}_{3/2}$ are the spin matrices over $(|ddd\rangle, |udd\rangle, |uud\rangle, |uuu\rangle)$ — the isospin-3/2 quadruplet. Interestingly, the even and odd baryon number subspaces decouple at leading order in the expansion. The dynamics of the former is ruled by an antiferromagnetic Ising model whose $\mathbb{Z}_2$ symmetry represents charge conjugation; the odd baryon number subspace realizes a spin-3/2 antiferromagnetic Heisenberg model with SU(2)-isospin symmetry, which remains unbroken in the massive quarks case, as long as $m_u = m_d$. Numerical evaluation of the single-site reduced density matrix shows that the Heisenberg model dominates the strong coupling physics: at $g = 10$ the populations of the isospin-0 states are suppressed by more than 3 orders of magnitudes with respect to those of the isospin-3/2 quadruplet.

A comparison with the SCE in [180] reveals how the presence of two quarks flavors instead of one greatly enlarges the configuration space of the model, also at the level of the zero chromoelectric energy effective subspace.

4.4 Simulation setup

Symmetric tensor networks. We perform numerical Tensor Network (TN) simulations on a finite chain with open boundary conditions, at zero and finite density. We use DMRG to efficiently obtain MPS representations vacua and excitations of hardcore 2-flavor QCD_2 across the parameter space (m_f, g), gaining insights on the phase diagram of the model. The DMRG implementation we employ protects internal Abelian symmetries [225]. We exploit this feature to: (i) enforce the $\mathbb{Z}_3$ link symmetries; (ii) fix the up-quark number, that is, the number of up-quarks minus the number of up-antiquarks $N_u = \sum_{x,c} (\psi^\dagger_{x,u,c} \psi_{x,u,c} - 1/2)$, (iii) the down-quark number N_d (as above); and (iv) speed-up the numerical simulation [224]. By controlling (N_u, N_d) we can study the model's vacua as well as its flavored excitations. Targeting a given charge sector amounts to starting the variational optimization from an MPS with the desired quantum numbers. Note that, thanks to the locality of DMRG updates, when running ℓ-site DMRG it is sufficient to impose $\ell + 1$ independent link constraints, rather than an extensive number of them [124, 343]. Finally, flavorless particle states (such as a π^0 meson) can also be found by looking for intra-sector excitations [102]; yet, that has a significantly higher computational cost.

In this work we will often target critical phases, which violate the MPS area law entanglement bound. Accordingly, the MPS bond dimension χ, which controls the accuracy and the computational cost of the TN approximation, has to be increased polynomially with the system size [286, 368, 369]. Bond dimensions as high as $\chi = 8192 = 2^{13}$ were used.

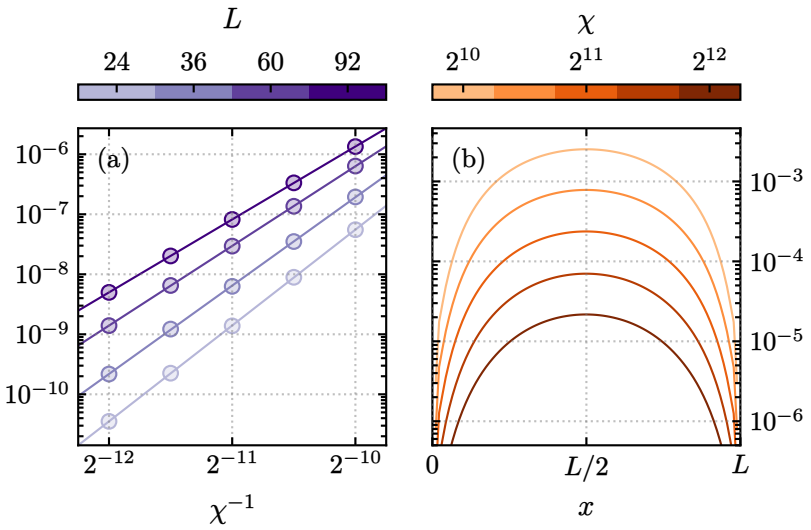

Figure 4.4: Convergence of the energy ε_L (a) and entanglement entropy $S(x)$ (b): relative deviation $|O_\chi/O_{\chi\to\infty} - 1|$ of their value at finite bond dimension χ from the exact one, where $O = \varepsilon_L, S(x)$. The exact value is estimated via a power law interpolation $O_\chi = A\chi^B + O_{\chi\to\infty}$. The precision decreases with the system size, as shown in (a) for the energy. The same holds for the entropy, although only the largest size $L = 92$ is reported in (b).

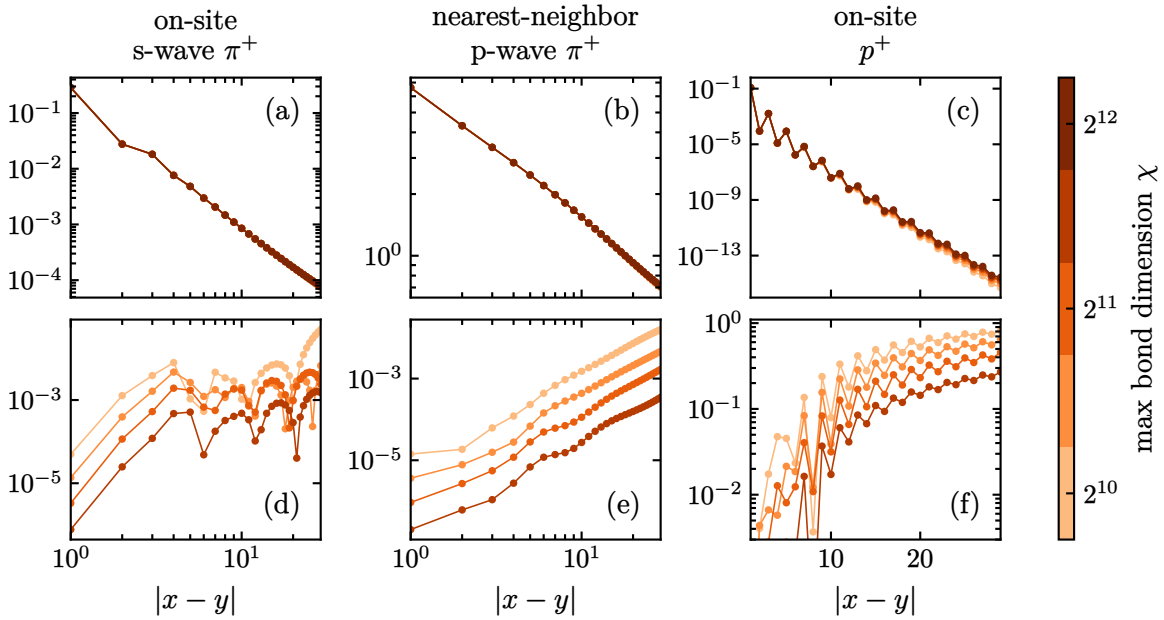

Figure 4.5: Convergence with the maximum bond dimension χ of some $L = 92$ connected 2-point functions as defined in Table 4.4. *Bottom:* relative deviation from the (largest) $\chi = 4096$ curve.

Convergence. The aim of this Chapter consists in characterizing qualitative features of hardcore 2-flavor QCD_2 (mainly, existence of the continuum limit and its particles) rather than extracting quantitative numerical estimates. For this reason, the extrapolation to infinite bond dimension, $\chi \to \infty$, is not performed systematically. We nonetheless verified the numerical convergence in the more computationally demanding weak coupling phase. The results in this Chapter rely on the computation of (i) entanglement entropy profiles (Section 4.5); (ii) energy gaps between ground states in different sectors (Section 4.7A); and (iii) 2-point functions (Section 4.7B). We achieved 6 digits or higher relative precision for vacuum energies (Fig. 4.3a), and expect similar results for other sectors. Consistent with expectations, entanglement entropy and correlators suffer more severely from the TN approximation; truncation effects are nevertheless always below percent order, even in the longest chains (Figs. 4.3b and 4.5); the only exception is the proton correlator which, however, reaches extremely small absolute magnitudes (Figs. 4.4c and 4.4f).

4.5 Criticality and the continuum

The continuum limit of a lattice model is approached when the lattice spacing becomes much smaller than the physical correlation lengths ξ_{phys} of the propagating degrees of freedom: in order for $\xi_{\mathrm{phys}} = a\xi$ to be finite (or ∞) when $a \to 0$, the lattice correlation length ξ has to diverge [370]. We check that hardcore 2-flavor QCD_2 possesses the expected continuum limit in Eq. (1.117) by verifying that $m_f, g \to 0$ is a critical point. The long distance universal properties of a critical phase are encoded by a conformal field theory (CFT). It is a well known CFT result [242, 243] that, for an infinite 1D critical system in its ground state, the entanglement entropy S of a large subregion grows logarithmically with the length of the subregion. Conversely, entanglement area law implies that S is bounded by a constant in a 1D gapped phase [239]. There are finite-size corrections to the critical behaviour: length is replaced by the chord length; moreover, a (possibly oscillating) term decaying as a power law away from the boundary has been observed in Luttinger liquids [371–373]. Ultimately,

$$S(x) \simeq \frac{c}{6} \log \ell + c' + c'' F(\ell/L) \cos(2x\kappa) |\ell|^{-p} \ , \tag{4.19}$$

for a length L open chain cut at x, with $x, L-x \gg 1$. Here $\ell = (L/\pi)\sin(\pi x/L)$ is the chord distance of the cut from the boundary and κ is the Fermi momentum; the central charge c, the critical exponent p and the scaling function F are universal (i.e., they are properties of the CFT alone), while c' and c'' are model-dependent (thus non-universal) constants.

In Fig. 4.6 we fit $S(x)$ to the first two terms in Eq. (4.19) on the whole $m_f = 0$ line subregion of parameter space. We find that the model is always critical in the massless regime and identify two distinct phases with an interface at $g \sim 1$. Although we did not fit the c'' term, we observe that the weak coupling phase — where the continuum physics is expected to lie — is compatible with $\kappa = 0$, while clearly $\kappa = \pi/2$ for $g \gtrsim 1$. Oscillations are particularly pronounced at the phases' interface.

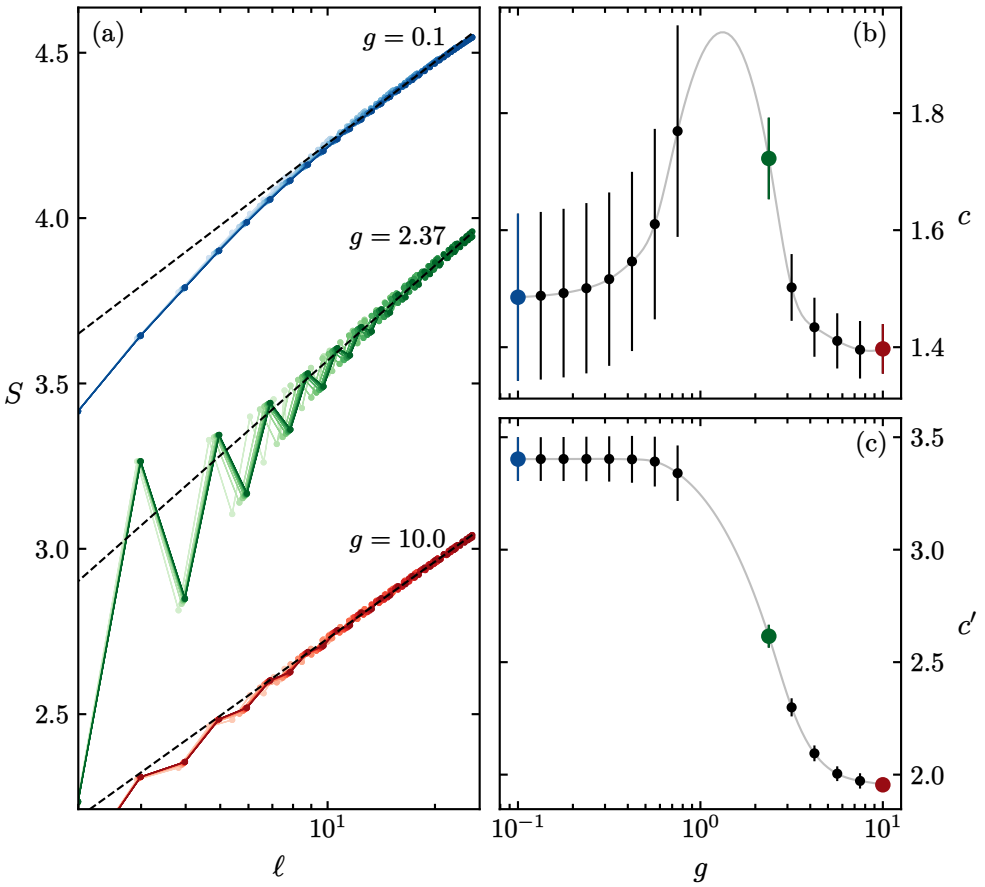

Figure 4.6: Entanglement entropy S of a bipartition as a function of the chord distance of the cut ℓ (a) for: weak, intermediate, and strong coupling g, massless quarks, and many system sizes $L \in [24, 80]$ (darker tones correspond to longer chains). Data points from all L are linearly interpolated to the first two terms in Eq. (4.19), prioritizing large x points via weights ℓ^w. For each $g \in [0.1, 10]$ and $w \in \{0, 1, \dots, 4\}$, a fit is preformed and assigned a weight $(1 - R^2)^{-1}$, R^2 being its coefficient of determination. Estimates of the central charge c (b) and c' (c) as a function of g are obtained averaging over the relevant fits (the gray spline is just for visual aid).

In Fig. 4.7 we study the robustness of criticality to the introduction of bare quark masses. At weak coupling, decreasing m_f the massless phenomenology is eventually recovered, while at strong coupling this happens only for $m_u = m_d$ (in the scanned mass range), when the up and down quarks form a global SU(2)-isospin doublet. That degenerate quark masses favour criticality can be partially understood in the framework of chiral perturbation theory [374], where explicit isospin-breaking is known to induce a correction to the π^0 pion mass. The splitting between the $\pi^\pm$ and π^0 masses implies that they cannot be simultaneously gapless. We expect an analogous phenomenology to arise in the presence electromagnetic

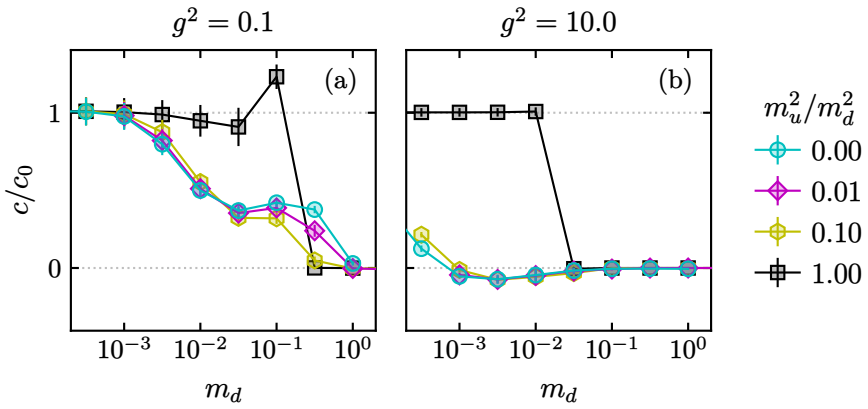

Figure 4.7: Estimated central charge c versus the heavy quark mass m_d, in units of its $m_f = 0$ value c_0; $c \ll 1$ signals a gapped phase. The plots involve $L = 60$ simulations at weak (a) and strong (b) coupling g, and a variety of m_u/m_d each. The computation of c follows the procedure detailed in Fig. 4.6.

interactions, in which case it is the $\pi^{\pm}$ mass that gets a correction [375]. The onset of criticality is abrupt if $m_u = m_d$, while the growth of c is otherwise gradual and mostly controlled by the mass m_d of the heavy quark. Since c roughly "counts" the number of gapless degrees of freedom [376], the above discussion implies that (i) there are multiple massless particles at $m_f = 0$ and (ii) their gaps close at different mass scales when $m_d \neq m_u$. Section 4.7 is devoted precisely to the classification of such gapless particles; pinning the eventual degeneracies of the vacuum sector is a prerequisite.

4.6 Vacuum sector

In this section we inspect the vacuum sector of the model — i.e., the *unflavored* $N_u = N_d = 0$ sector[2]. In particular, we assess whether certain phases undergo spontaneous symmetry breaking (SSB), which is relevant, e.g., when comparing expectation values on excited states with their vacuum (unflavoured ground state) expectation value (VEV). Indeed, certain observables may not admit an unambiguous VEV in the presence of degenerate vacua.

Intra-sector excitations. We compute the 7 lowest energy Hamiltonian eigenstates in the unflavored sector, at $m_f = 0$ and both small and large g. Their gaps are reported in Table 4.3. At large coupling there is no clear hierarchy among them, bolstering the argument in favour of a unique vacuum and rendering the subtraction of VEVs straightforward and unambiguous. The strong coupling vacuum density profiles are **C**, **P**, **F** antisymmetric:

[2] Because of staggered fermions, the zero flavour number charge sector corresponds to half filling of each quark d.o.f., see Eq. (3.29). This also implies that at most $3L/2$ quarks of each specie can be hosted on a chain of length L.

g	$\varepsilon_n - \varepsilon_0 \quad (n = 0, 1, \ldots)$
0.1	0, 1, 19.5, 20.6, 63, 64, 104, ...
10.0	0, 1, 3.9, 7.5, 7.7, 9.9, 10.0, ...

Table 4.3: Gaps of the first few Hamiltonian eigenvalues ε_n in the vacuum sector, at weak and strong coupling. To emphasize the hierarchy of the splittings, we chose units such that $\varepsilon_1 - \varepsilon_0 = 1$, independently for each g value.

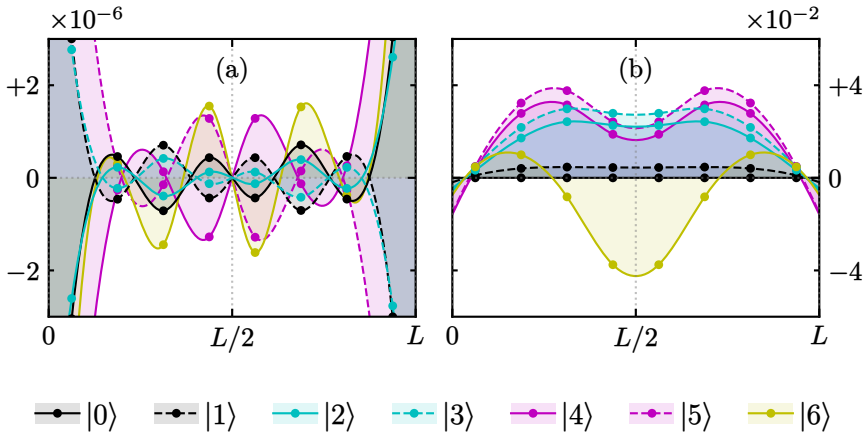

Figure 4.8: Up quark number density $\rho_{x,u}$ (a) and link energy density E_x^2 (b) of the 7 lowest energy eigenstates $|n\rangle$ in the vacuum sector, as found by DMRG, at $g = 0.1$ and $L = 8$. The down flavored profiles $\rho_{x,d}$ are identical. In (b) we subtracted the $|0\rangle$ contribution. Points are spline interpolated; the divergencies at the boundaries are an artifact (Runge's phenomenon [377]).

$\langle \rho_{x,u} \rangle = -\langle \rho_{-x,u} \rangle = -\langle \rho_{x,d} \rangle$. At small coupling, the eigenstates organize in quasi-degenerate doublets with density profiles (see Fig. 4.8a) which are charge **C** and parity **P** conjugate one of the other (each profile is individually **CP** and flavor **F** symmetric). Since the Hamiltonian is **C** and **P** symmetric, it would seem reasonable to treat the two lowest states, $|0\rangle$ and $|1\rangle$, as degenerate vacua. On the other hand, even the finer (inter-doublet) splittings in Table 4.3 are well resolved by DMRG and, as shown by Fig. 4.8b, they originate from a physical effect in the gauge link configuration. We thus rule out SSB and attribute the **C** and **P** violations in the density profiles to the hybridization of the eigenstates found by DMRG with a low-energy flavourless excitation — such as a neutral pion π^0 — whose gap we expect to close in the thermodynamic limit. In order to circumvent problems originating from symmetry violations, we do not subtract number density VEVs in Section 4.7.

Structure factors. If the symmetry σ suspected of being broken is known, SSB can also be detected testing for long-range order via some associated order parameter. Figure 4.9

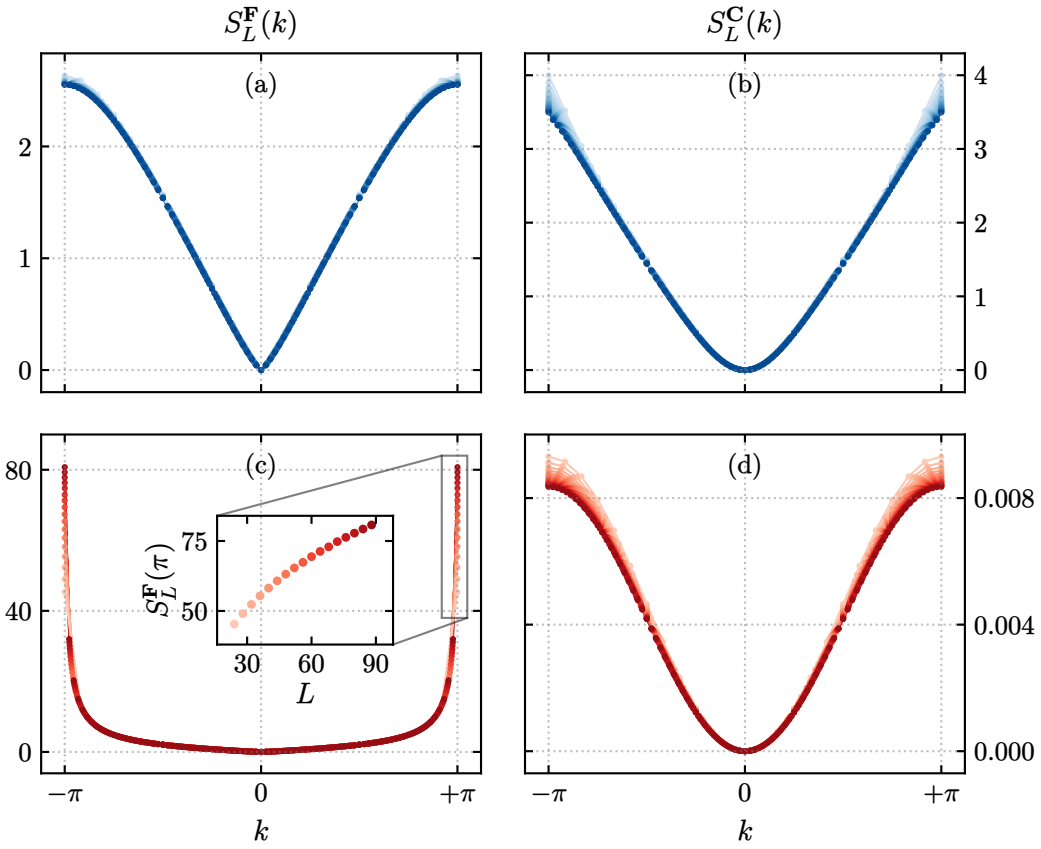

Figure 4.9: Structure factors from Eq. (4.20) detecting **F** (left) and **C** (right) long-range order at $g = 0.1$ (top, blue) and $g = 10.0$ (bottom, red). Finite size scaling with $L \in [24, 88]$ (darker tones correspond to longer chains).

shows the finite size scaling of the structure factors,

$$S_L^{\sigma}(k) = \frac{1}{L} \sum_{y,z} e^{-ik(y-z)} \langle O_y^{\sigma} O_z^{\sigma} \rangle \ , \tag{4.20}$$

for $\sigma \in \{\mathbf{F}, \mathbf{C}\}$, with $O_x^{\mathbf{F},\mathbf{C}} = \rho_{x,u} \mp \rho_{x,d}$. A peak $S_L^{\sigma}(k) \sim L$ would reveal long-range order in σ with $2\pi/k$-periodicity. The peak at $k = \pi$ in Fig. 4.9c shows the emergence of antiferromagnetic flavor order at strong coupling. Still, $S_L^{\mathbf{F}}(\pi)$ grows sub-linearly with L (inset plot), suggesting that the order is quasi-long-range. This result is compatible with the Mermin-Wagner theorem [378–380], forbidding spontaneous breaking of continuos symmetries in 1D quantum models with short range interactions (**F** corresponds to a $\mathbb{Z}_2$ subgroup of U(2)-isospin). The fact (see Section 4.3) that the isospin-3/2 quadruplet dominates the strong coupling physics while $|\circ\rangle$ and $|\bullet\rangle$ are highly suppressed, explains both the quasi-long-range **F** order (arising from the antiferromagnetic $\mathrm{XXX}_{3/2}$ model) and the lack of **C** breaking (which would be expected for an antiferromagnetic Ising model).

4.7 Particle spectrum

We now turn to characterizing some of the particle excitations of hardcore 2-flavor QCD_2, focusing on modes which survive in the continuum — i.e. those whose mass gap $M = 1/\xi$ measured in lattice units closes when approaching the continuum limit [370]. The argument is dual to the one for the correlation length: if a gap does not close, $M_{\text{phys}} = M/a$ diverges when $a \to 0$ and the particle is effectively pushed out of the spectrum. Gauge theories are known to generally confine in one space dimension [37, 118], we thus look for color-neutral excitations. Among these, working at $m_f = 0$, we investigate the fate of the gap of charged pions $\pi^+ = u\bar{d}$, protons $p^+ = uud$, and Delta baryons $\Delta^{++} = uuu$. The extension to $\pi^- = d\bar{u}$, $n^0 = udd$, and $\Delta^- = ddd$ follows by flavor parity symmetry. More exotic hadrons, such as tetra- and pentaquarks [381–383], could also be studied with the same techniques, provided enough flavors are included in the Hamiltonian.

Gapless modes are identified by either [384] (i) computing directly particles' rest states (ground states in the appropriate symmetry sectors) and their gaps; or (ii) studying the vacuum 2-point function of fields with the desired quantum numbers. An advantage of the former approach is that, in TN calculations, energies are much less sensitive than correlators to the MPS bond dimension. On the other hand, via correlation functions, information about many different particle types can be efficiently extracted from a single vacuum MPS. Additionally, correlation functions always probe the bulk physics while eventual edge modes have to be detected and discarded by hand when computing inter-sector gaps.

4.7A Inter-sector excitations

We obtain finite density states with N particles of type $\Sigma \in \{\pi^+, p^+, \Delta^{++}\}$ by constraining DMRG to the flavor symmetry sector $Q_f = NQ_f^\Sigma$, where $Q_f^\Sigma = (Q_u^\Sigma, Q_d^\Sigma)$ is the flavor charge of Σ, e.g. $Q_f^{\pi^+} = (+1, -1)$. For each specie, we start from the vacuum ($N = 0$) and increase N until the chain is completely filled. All the results in this subsection regard the weak coupling phase, $g = 0.1$.

Figure 4.10 shows link energy densities E_x^2 and particle number densities

$$\rho_x^\Sigma = \textstyle\sum_f Q_f^\Sigma \rho_{x,f} \left(\sum_f |Q_f^\Sigma|\right)^{-1} , \tag{4.21}$$

with[3]

$$\rho_{x,f} = \sum_c (\psi_{x,f,c}^\dagger \psi_{x,f,c} - 1/2) , \tag{4.22}$$

for fillings up to $N = 11$, taking $N = 1$ as a reference state. For all species Σ, the $N = 1$ densities decay away from the boundaries, a strong signature of a low-energy edge excitation — an edge zero mode. Conversely, $N > 1$ states are manifestly bulk excitations of $N-1$

[3] The subtraction of $1/2$ from number densities is due to staggered fermions. See also Footnote 10 (Page 80).

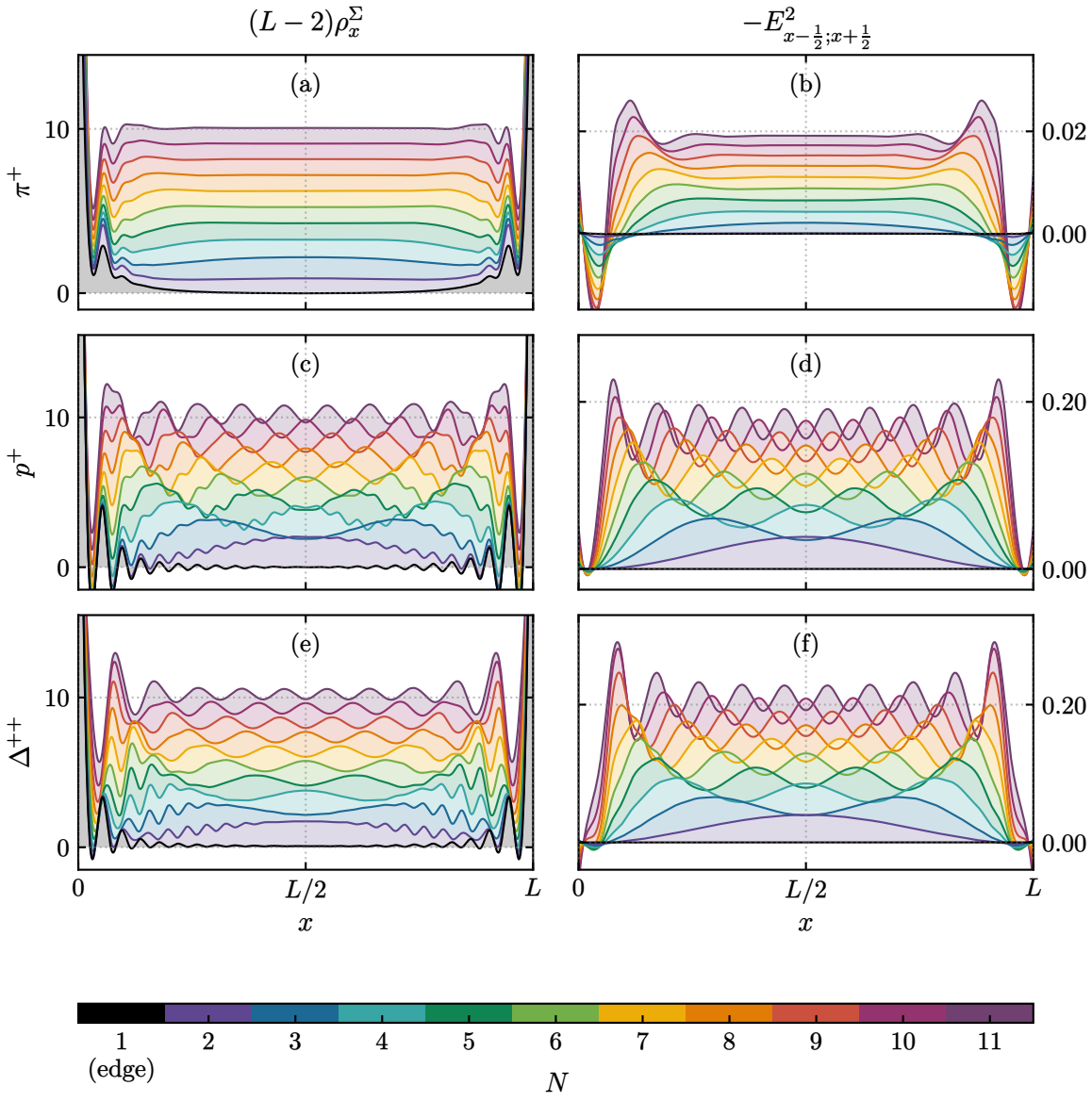

Figure 4.10: Local observables evaluated on states of up to $N = 11$ excitations of specie $\Sigma \in \pi^+,\ p^+,\ \Delta^{++}$ (rows). Specifically: particle number density ρ_x^Σ rescaled by the bulk size $L-2$ (left), and gauge field energy density in units of g^2, E_x^2 (right). The $N = 0$ (vacuum) contribution is subtracted in E_x^2 plots. Points are spline interpolated to make the plots more readable. Fixed parameters: $L = 48$, $g = 0.1$, $m_f = 0$.

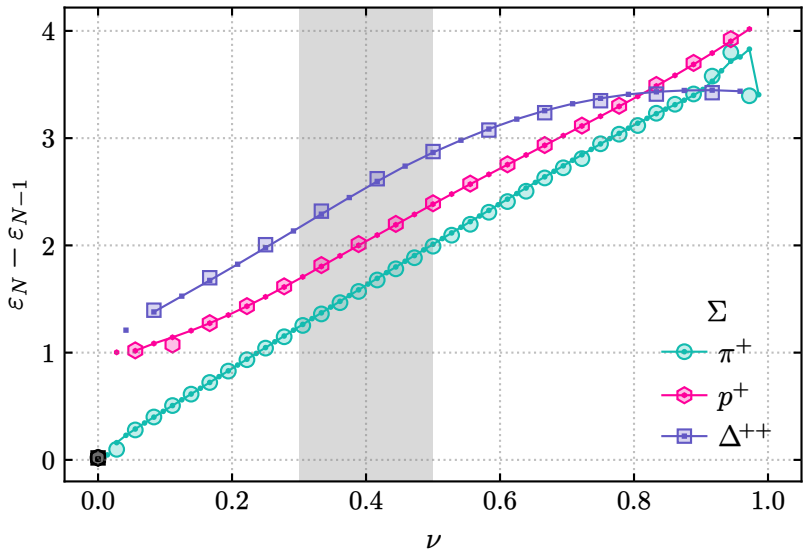

Figure 4.11: Energy gaps between states at different π^+, p^+ and Δ^{++} filling ν. At $g = 0.1$, $m_f = 0$. Bigger points are obtained at $L = 24$, while lines and smaller markers come from $L = 48$. Black points at the origin refer to the edge mode ($N = 1$) gaps with respect to the vacuum. The shading emphasizes the alignment of all species' slopes at intermediate ν.

hardcore particles (see first column). For p^+ and Δ^{++}, the N-th profile is approximatively reproduced stacking the first $N - 1$ free particle-in-a-box probability density functions, suggesting that p^+ and Δ^{++} are almost free. Friedel oscillations are also present in density profiles of fermionic modes (p^+, Δ^{++}) but absent in bosonic ones (π^+) [385].

The energy gaps $\varepsilon_N - \varepsilon_{N-1}$ between subsequent states are plotted in Fig. 4.11 as a function of the up quark filling fraction, adjusted by discarding the edge modes' contribution:

$$\nu = (Q_u - Q_u^{\Sigma})/(3L/2) \tag{4.23}$$

This ensures that, for each specie Σ, the first nonzero ν corresponds to the first bulk mode; in the thermodynamic limit, the associated gap is the mass gap M of Σ. Subsequent gaps measure the energy cost of adding one particle to the system at finite density, and thus can be interpreted as a finite-size chemical potential. On the other hand, in a weakly interacting picture, adding particles means progressively exciting higher wavenumber modes. Then, ν is the highest occupied wavenumber and — neglecting the interaction energy — each curve in Fig. 4.11 mimics the dispersion relation of the corresponding specie. Corroborating a weakly interacting explanation are (i) the collapse of data from different system sizes $L = 24, 48$; (ii) the linearity of the π^+ case, compatible with a vanishing mass gap (Fig. 4.12); and (iii) the common slope of curves from different species at intermediate momenta. The latter suggests the emergence of a "speed of light", hinting at the restoration of Lorentz invariance

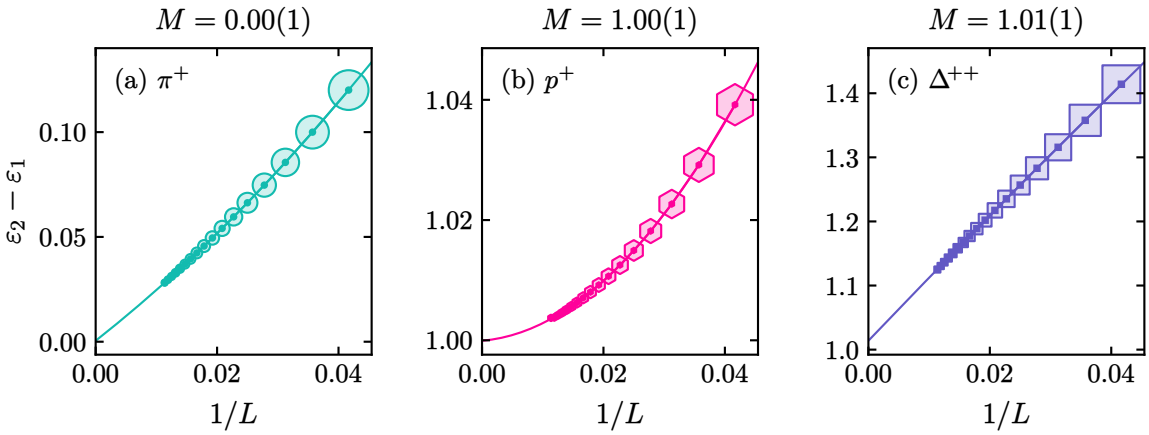

Figure 4.12: Finite size scaling of the gap $\varepsilon_2 - \varepsilon_1$ of the first π^+, p^+ and Δ^{++} bulk modes; $L \in [24, 88]$. The lines show the interpolation with a degree 2 polynomial, the extrapolated mass M is reported above each plot. The error estimate corresponds to the difference with respect to a linear interpolation. Fixed parameters: $g = 0.1$, $m_f = 0$.

— at least away from cutoff effects (infrared and ultraviolet) and eventual interactions with the edge mode at low ν.

We compute the lattice mass M of π^+, p^+, Δ^{++} particles by means of a finite-size scaling analysis of the respective first bulk gaps. Indeed, we expect $(\varepsilon_2 - \varepsilon_1) \to (\varepsilon_2 - \varepsilon_0) \to M$ in the large L limit, provided the edge mode gap and the bulk-boundary interaction vanish quickly enough (the former is expected to fall exponentially [386]). The results are shown in Fig. 4.12. Protons p^+, neutrons n^0, Δ^{++} and Δ^- baryons have an gap $M \approx 1$ in lattice units at $g = 0.1$. While we cannot exclude that their gaps will close in the $g \to 0$ limit, we can safely conclude that is the case for charged pions $\pi^\pm$, which are gapless already at finite coupling ($g = 0.1$).

4.7B Correlators

As discussed in Section 2.1A, asymptotically, connected correlators $G_{yz} = \langle \Phi_y \Phi_z^\dagger \rangle - \langle \Phi_y \rangle \langle \Phi_z^\dagger \rangle$ of massive (massless) fields Φ_x are expected to decay exponentially (algebraically) with space separation. More precisely, $G_{yz} \simeq C e^{-M|y-z|}$ and $G_{yz} \simeq C|y-z|^{-2\Delta}$ respectively; where M is the physical mass (inverse correlation length), Δ is the CFT scaling dimension of the field operator, and C can be reabsorbed in the field normalization.

We evaluate the vacuum 2-point function[4] G_{yz} for the field operators in Table 4.4. The $m_f = 0$ phase is found to be a liquid of pions with gapped protons and Delta baryons, in agreement with the energy gaps results from the previous section. Here we show that this

[4] All considered operators violate flavour number conservation, hence the disconnected component vanishes.

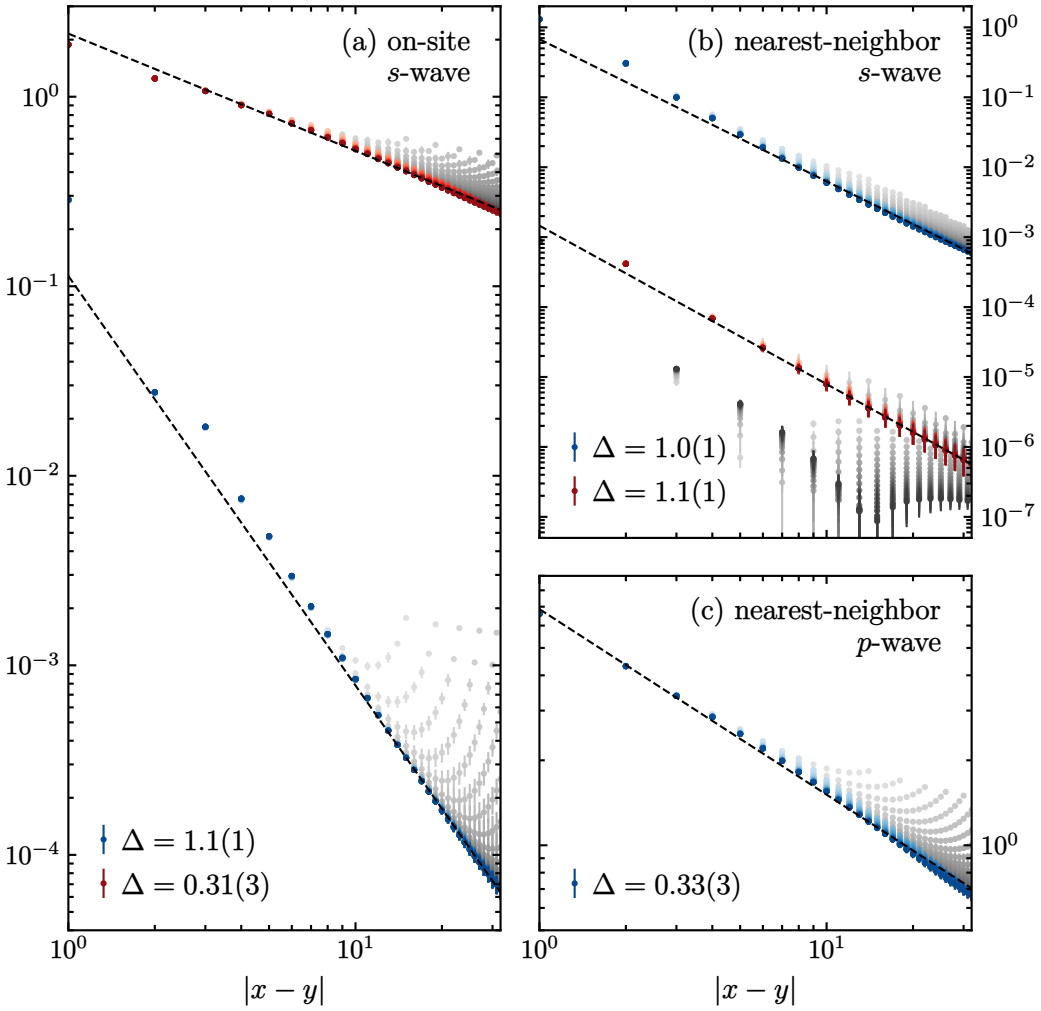

Figure 4.13: Log-log scale power law decay of π^+ correlators from Table 4.4; at $g = 0.1$ (blue) and $g = 10$ (red); $L \in [24, 100]$ (darker tones for longer chains). The correlation strength and its uncertainty are obtained averaging over equidistant (x, y) pairs. The scaling dimensions Δ of the associated operators are extrapolated via linear regression. Data points $1 \leq |x - y| \leq L/3$ from all system sizes L are included and given a weight proportional to $|x - y|$ (to enhance the asymptotic behaviour); points close to the boundary have been excluded and are shown in greyscale. The strong coupling s-wave pion correlator exhibits an even-odd distance oscillatory pattern, therefore only even distances are fitted. The 10% error estimates come from the comparison with unweighted fits.

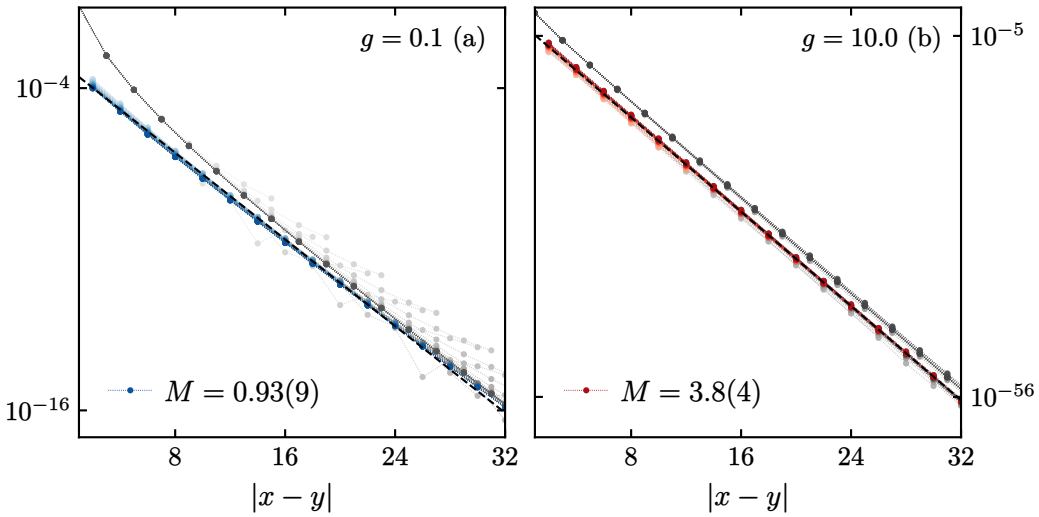

Figure 4.14: Log scale exponential decay of p^+ correlator from Table 4.4; at $g = 0.1$ (blue, a) and $g = 10$ (red, b); $L \in [24, 100]$ (darker tones for longer chains). Methodology as per Fig. 4.13. The fit slopes provide the particle's mass $M = 1/\xi$. Only even distances are interpolated due to a clear even-odd distance staggering; fitting odd distances yields similar results. Up to normalization, Δ^{++} correlators are close to p^+ ones.

characterization applies to the strong coupling phase as well. However, correlators allow to distinguish between at least two kind (s- and p-wave) of π^+ excitations. As we now show, different pions realize superfluid order in the weak and strong coupling regimes. All small-g pion correlators in Fig. 4.13 decay as power laws with ($\Delta \approx 1/3$ or $\Delta \approx 1$); while at large g the p-wave π^+ is gapped. As anticipated, p^+ (Fig. 4.14) and Δ^{++} are gapped; they have similar correlation lengths, compatible with the mass estimates from Fig. 4.12.

excitation	operator Φ_x
on-site s-wave π^+	$\sum_c \psi_{x,u,c}\psi^\dagger_{x,d,c}$
nearest-neighbor s-wave π^+	$\sum_{c,c'}(\psi_{x,u,c}U_{x;c,c'}\psi^\dagger_{x+1,d,c'} + \psi_{x+1,u,c}U^\dagger_{x;c,c'}\psi^\dagger_{x,d,c'})$
nearest-neighbor p-wave π^+	$\sum_{c,c'}(\psi_{x,u,c}U_{x;c,c'}\psi^\dagger_{x+1,d,c'} - \psi_{x+1,u,c}U^\dagger_{x;c,c'}\psi^\dagger_{x,d,c'})$
on-site p^+	$\psi_{x,u,r}\psi_{x,u,g}\psi_{x,d,b} + \psi_{x,u,g}\psi_{x,u,b}\psi_{x,d,r} + \psi_{x,u,b}\psi_{x,u,r}\psi_{x,d,g}$
on-site Δ^{++}	$\psi_{x,u,r}\psi_{x,u,g}\psi_{x,u,b}$

Table 4.4: Operators Φ_x exciting some of the simplest color-neutral candidate particles of the model; p- and s-wave labels are assigned according to their parity transformation properties, by analogy with the (1+3)D case.

4.8 A minimal model of QCD

In obtaining the results form the previous section, a series of methods and properties of the model have been derived. We now summarize them, providing additional context, discussing their implications and giving an outlook on future directions.

We truncated the infinite-dimensional SU(3) link space of QCD by means of a cutoff in color irrep space [132]. Although we considered only the strictest possibility, the truncation can be controlled by tuning the number of included irreps. We expect equilibrium TN simulations of less severe truncations to be feasible. These could shed light on the effects of the truncation and on the untruncated limit, which is key in recovering the continuum physics of true QCD. Two other extensions within the reach of present-day simulations are the inclusion of more quark flavors, which would allow to study tetra- or pentaquarks, or the inclusion of a U(1) electric field, for which we sketched an implementation plan.

A more long-term goal which is worth pursuing is higher spacetime dimensions [123, 129, 130, 387–392]. There, the existence of a transverse polarization makes the gluon a dynamical field, thus giving access to a richer spectrum containing glueballs [393] and possibly other exotic excitations from the QCD folklore. A first TN study of a non-Abelian Yang-Mills theory in (2+1)D has just appeared [130]. Finally, improved Hamiltonians [179, 180] and high performance computing will become essential in the strive for precision results.

Showing that the model has the expected continuum limit is equivalent to proving that it has a critical point at $g, m_u, m_d \to 0$. This was carried out in Section 4.5, by inspecting the vacuum entanglement [394]. Incidentally, we found that criticality persists in a whole cylinder around the $m_u = m_d = 0$ line in (g, m_u, m_d)-space, elongated along the $m_u = m_d$ plane and spanning a weak and a strong coupling phase. In Section 4.7 we identified some of the respective gapless bulk modes. See Fig. 4.1 for a summary. At finite lattice spacing, the weak coupling phase is dominated by a (gapless) superfluid of p-wave, charged pions $\pi^{\pm}$. We supported this claim with two independent analyses: finite-size scaling of inter-sector gaps and decay of π^+ liquid order parameters. These observations are strong signatures that $\pi^{\pm}$ mesons belong to the physical particle spectrum in the continuum limit [370], inspiring future works devoted to the TN simulation of $\pi^+\pi^-$ collisions [115, 326, 336] in hardcore 2-flavor QCD_2.

Let us conclude by suggesting that the studied model is in some sense "minimal". Compared to other truncation schemes [395], the one adopted here provides the smallest non-trivial link space dimension while preserving exactly the local SU(3) symmetry. Moreover, in the QLM approach, D-theory [204, 212] mandates that the untruncated theory is obtained by dimensional reduction from a QLM in one more space dimension. Despite its elegance, increasing the space dimension makes the approach somewhat demanding for TN methods. Conversely, within the chosen truncation scheme our model is the simplest having pions in the continuum spectrum. Discarding additional irreps completely freezes the gauge field and thus the dynamics. Restricting to a single quark flavor clearly prevents $\pi^{\pm}$ from existing;

furthermore, the model was studied numerically and no signature of gapless neutral pion π^0 was found [124]. Finally, the splitting of links into rishons and the gluing of the latter in a composite site can be skipped with no consequences on the physics, but then the computational Hilbert space is larger ($64^L 19^{L-1}$ vs 54^L). On the other hand, giving up on exact SU(3) gauge invariance, a number of finite SU(3) subgroups have been explored in literature [396–400], some of which of lower order than the link space used here. Inspiring results were recently obtained from the MC simulation of $S(1080)$ [210]; yet, the associated link space is much larger than the one constructed here. Finally, a promising proposal which achieves controllable truncation by deforming the gauge symmetry algebra to a quantum group has been recently put forward [125, 205–207].

Conclusion and Outlook

This Thesis aims at contributing to the tensor network simulation of high-energy physics. Although still in its infancy, this program has recently started to bear results that challenge more traditional non-perturbative numerical approaches — especially in real-time dynamics and finite chemical potential regimes, where Monte Carlo is hampered by the sign problem. The present conjuncture offers a unique opportunity for substantial progress, building upon a solid conceptual framework (lattice QFT) and an established numerical toolset (TN) while facing new challenges posed by the complexity of the models encoding nature's fundamental interactions. Our results demonstrate that TN algorithms can address efficiently and accurately low-dimensional LGT problems and our hope is that, ultimately, they will help bring the field a little bit closer to the end goal of simulating realistic high-energy physics (HEP). Such a formidable task can be attacked from multiple angles and the original achievements presented in this Thesis may be organized along three main directions.

Phenomenological: mimicking prototypical HEP phenomenology in toy models for which TN have long proven to be viable techniques. The definition of a recipe for the TN simulation of scattering events and its application to lattice QED_2 is part of this effort.

Model building: identifying and characterizing new testbed LGT amenable to TN that reproduce selected features of prominent HEP models. This is one of our motivations for introducing hardcore 2-flavor QCD_2 and studying its particle spectrum.

Methodological: improving, extending, or complementing TN methods targeted at QFT applications. The development of the dressed site formalism for LGT and the scrutiny of the CPEPS approximation of relativistic field theories can be ascribed to this goal.

In the following we recap our results in more detail and discuss their implications, providing an outlook on promising future research paths.

TN-LGT building block: the dressed site. Gauge theories exhibit a high degree of symmetry which translates into an extensive number of local Gauss-law type constraints [143]. Protecting gauge symmetries can be a challenge for TN methods as well as quantum computation [401–403], but it is pivotal for the correctness and accuracy of the simulation. Enforcing Gauss laws at the operator level leads to a non local operator algebra [26]; while imposing it in the weaker form, at the level of the states, leads to a redundant description which could impact adversely on the computational cost of simulations. The dressed site construction represent a compromise solution which trades the generally non-Abelian Gauss

law for simpler Abelian local constraints, and provides a significant computational speed-up by eliminating a large amount of redundancy while preserving locality [105]. At the end of the first Chapter we gave a systematic framing to this idea, showing how to implement it for a general gauge and matter content. The dressed site formalism works in any space dimension and is agnostic to the specific TN ansatz on which the simulations are run. In fact, it could provide a valuable building block also for analog and digital quantum computation. The computation of the dressed site basis and operators can be a burdensome task, especially for non-Abelian LGT. The development of software automating the process and thus expediting the preparatory work for Hamiltonian LGT simulation is underway.

Probing the real-time scattering dynamics. In the third Chapter we discussed how to implement real-time TN simulations of scattering process, and proposed a recipe to extract S-matrix elements. We applied it to lattice QED_2, also known as Schwinger model, studying meson-meson collisions. We elaborated a protocol providing an MPS representation of the initial scattering state. The protocol is based on the solution of the free theory of staggered fermions, it is thus limited to weak lattice coupling values but can be easily extended to higher space dimensions or non-Abelian LGT (i.e., multiple families of fermions).

We studied the scattering phenomenology, showing that the simulated collisions are elastic and verifying that the momenta of the scattering products fulfill the expected kinematic constraints. To this aim, we showcased two analyses of the final scattering state, namely computation of meson correlators and projection on an appropriate family of wave-packets. Exploiting specific strengths of TN methods, we characterized the entanglement content of the system during the scattering process. We identified three, approximately additive, contributions: (i) *vacuum entanglement*: a uniform background due to the correlations in the ground state; (ii) *intra-particle entanglement*: bumps localized where particle wave-packets are supported, which we model analytically; and finally (iii) *inter-particle entanglement*: a dynamically-generated entanglement string correlating the products of the collision, which we isolate and estimate numerically. In the explored parameters region, we found a phenomenological scaling relation describing the interplay of the mass, the coupling, the meson momenta, and the inter-particle entanglement generated by the interactions.

With this study we have shown that TN methods are capable of numerically simulating the real-time scattering dynamics of (1+1)-dimensional lattice QFT efficiently and accurately. In this regard, we stress that it is only our approximation of the initial meson states that prevented us from studying the dynamics of QED_2 at stronger couplings — rather than the breakdown of the numerical tools employed. In the outlook of Ref. [131] we suggested that tangent space MPS methods [404–409], in particular Ref. [410], could allow to overcome this obstacle and provide an alternative, non-perturbative, initial state preparation protocol. The idea was later implemented in Ref. [326], where the authors successfully simulated non-elastic meson-meson collisions at strong coupling using a bosonized formulation of the model and the MPS quasiparticle ansatz. While QED_2 provides an ideal testbed, we expect also the dynamics of more complex one-dimensional LGT to be accessible to TN simulation.

A minimal SU(3) LGT featuring QCD's hadrons. Hadron-hadron collisions are the most important outlook of the kind of study that we just presented. Accomplishing it requires identifying a simple enough SU(3) LGT featuring QCD-like hadrons, and devising techniques that make it amenable to TN methods. In the fourth Chapter we combined a Hamiltonian lattice regularization with a gauge field truncation in irrep space to introduce hardcore 2-flavor QCD_2: a maximally-truncated SU(3)-color LGT with up and down quark fields. By TN simulation we proved that (i) the continuum limit of the model is well defined and (ii) it has charged pions in the particle spectrum — in analogy with (1+3)D QCD. We stress that both results are expected for any proper discretization of ordinary QCD, but they were far from obvious with the truncation in place. Rather, we argued that our model is a minimal realization of a SU(3) gauge theory displaying such features; it thus qualifies as an ideal QCD testbed in settings where computational resources are still a bottleneck, such as quantum computation and real-time TN simulation [411–414].

We constructed the model's gauge invariant dressed site and relied on it to find MPS representations of vacua, single particle and finite density states for a wide range of bare quark masses and couplings parameters. The existence of the continuum limit, namely of a critical point of the lattice model [370], was elucidated inspecting the vacuum entanglement. The associated lattice gapless modes where identified studying the finite-size scaling of inter-sector gaps and the decay of correlators (liquid order parameters). A superfluid phase of charged pions is a strong signature that $\pi^{\pm}$ mesons belong to the physical particle spectrum in the continuum limit. Within the chosen truncation scheme, further restricting the gauge field configurations completely freezes the dynamics, while no gapless lattice hadrons where found in a previous study involving a single quark flavor [124].

Our primary goal was paving the way for real-time TN simulations of pion-pion scattering, but we believe that hardcore 2-flavor QCD_2 could also attract near-term implementations on qudit platforms [62]. A possible extension that we touched upon is the inclusion of electric corrections. Finally, a preliminary resource estimation suggests equilibrium TN simulations of less severe truncations to be feasible; these could help clarify how much the continuum limit of hardcore-gluon QCD_2 differs from that of true QCD_2.

Working directly in the continuum. All the accomplishments presented above rely on the paradigm of Hamiltonian lattice QFT to "convert" continuum quantum field theories into many-body quantum systems and make them amenable to TN simulation. While our results hopefully served as yet another convincing proof of the effectiveness of the lattice framework, the difficulty of studying continuos systems is partially deferred to the delicate issue of extrapolating the continuum limit. The versatility of TN states as non-perturbative variational ansatze makes it tempting to extend TN methods to handle directly quantum degrees of freedom in continuous space [275, 276]. In the second Chapter we explored this possibility studying the CPEPS ansatz [230]. We elucidated how, for ground CPEPS obtained via imaginary time evolution, the auxiliary fields can be interpreted as snapshots of past (imaginary) times. We then focused on Gaussian CPEPS and on their ability to

capture the entanglement entropy of relativistic QFT vacua. Although we found that this class can indeed encode a UV divergent entanglement entropy, the scaling does not match the one expected for relativistic QFT. We attribute this failure to the fact that parent Hamiltonians of Gaussian CPEPS have dispersion relations that, unlike relativistic ones, are rational functions of the squared momentum.

Outlook. Implementing realistic and competitive TN simulations unraveling the intricate fabric of interactions among the fundamental constituents of the universe is a formidable and exciting task. As such, it bears plenty of room for advances along manifold directions. A number of potential avenues for future research has been mentioned already. Of course, a critical requirement for simulating realistic HEP is being able to address problems in 1+3 spacetime dimensions. This undertaking will surely require hard work but the outcome can be highly rewarding and, indeed, works tackling higher-dimensional LGT have started to appear in the last few years [123, 129, 130, 387–392]. Nevertheless, technical progress (algorithmic improvements and optimizations) and, possibly, also conceptual breakthroughs (defying area law entanglement bounds) are still needed — and a paradigm shift towards a community effort for the development of highly parallelizable TN routines [415, 416] that take advantage of high-performance computing clusters could be greatly beneficial. Finally, similar challenges are being faced by the quantum simulation and computation community. At these thrilling times, foreshadowing the advent of fault-tolerant quantum computers [64], there is careful optimism that the latter will one day contribute to enhancing our understanding of fundamental physics. In virtue of this symbiosis between classical TN and quantum approaches, we hope that some of the accomplishments of this Thesis will guide the preliminary implementation steps of similar quantum computations of HEP, and contribute to benchmark early stage quantum devices.

Bibliography

[1] A. Shomer. A pedagogical explanation for the non-renormalizability of gravity. Technical report, December 2007. arXiv:0709.3555 [gr-qc, physics:hep-ph, physics:hep-th] type: article.

[2] S. Weinberg. *Dreams of a Final Theory: The Scientist's Search for the Ultimate Laws of Nature*. Knopf Doubleday Publishing Group, February 1994.

[3] S. Weinberg. The making of the Standard Model. *The European Physical Journal C: Particles and Fields*, 34(1):5–13, May 2004.

[4] J. Fröhlich and P.-A. Marchetti. Quantum field theory of anyons. *Letters in Mathematical Physics*, 16(4):347–358, November 1988.

[5] H. Kleinert. *Gauge Fields in Condensed Matter*. WORLD SCIENTIFIC, 1989.

[6] E. Fradkin. *Field Theories of Condensed Matter Physics*. Cambridge University Press, February 2013.

[7] J. Fröhlich. Gauge invariance and anomalies in condensed matter physics. *Journal of Mathematical Physics*, 64(3):031903, March 2023.

[8] P. W. Anderson. Coherent Excited States in the Theory of Superconductivity: Gauge Invariance and the Meissner Effect. *Physical Review*, 110(4):827–835, May 1958.

[9] A. Mann. High-temperature superconductivity at 25: Still in suspense. *Nature*, 475(7356):280–282, July 2011.

[10] P. A. M. Dirac. The Quantum Theory of the Emission and Absorption of Radiation. *Proceedings of the Royal Society of London. Series A, Containing Papers of a Mathematical and Physical Character*, 114(767):243–265, January 1927.

[11] J. Schwinger. On Quantum-Electrodynamics and the Magnetic Moment of the Electron. *Physical Review*, 73(4):416–417, February 1948.

[12] S. Laporta and E. Remiddi. The analytical value of the electron $(g-2)$ at order α^3 in QED. *Physics Letters B*, 379(1):283–291, June 1996.

[13] X. Fan, T. Myers, B. Sukra, and G. Gabrielse. Measurement of the Electron Magnetic Moment. *Physical Review Letters*, 130(7):071801, February 2023.

[14] S.-I. Tomonaga, J. Schwinger, and R. P. Feynman. The Nobel Prize in Physics 1965, 1965.

[15] S. Weinberg. A Model of Leptons. *Physical Review Letters*, 19(21):1264–1266, November 1967.

[16] The Nobel Prizes in Physics 1979, 1984, 1999, 2013.

[17] M. E. Peskin. Theory of precision electroweak measurements. In *17th SLAC Summer Institute on Particle Physics: Physics at the 100-GeV Mass Scale (Topical Conference last 3 days) (SSI 89)*, pages 71–126, March 1990.

[18] J. Erler and M. Schott. Electroweak precision tests of the Standard Model after the discovery of the Higgs boson. *Progress in Particle and Nuclear Physics*, 106:68–119, May 2019.

[19] M. Gell-Mann. A schematic model of baryons and mesons. *Physics Letters*, 8(3):214–215, February 1964.

[20] G. Zweig. An SU_3 model for strong interaction symmetry and its breaking; Version 2. 1964.

[21] E. D. Bloom, D. H. Coward, H. DeStaebler, J. Drees, G. Miller, L. W. Mo, R. E. Taylor, M. Breidenbach, J. I. Friedman, G. C. Hartmann, and H. W. Kendall. High-Energy Inelastic $e-p$ Scattering at 6° and 10°. *Physical Review Letters*, 23(16):930–934, October 1969.

[22] J. D. Bjorken. Asymptotic Sum Rules at Infinite Momentum. *Physical Review*, 179(5):1547–1553, March 1969.

[23] H. Fritzsch, M. Gell-Mann, and H. Leutwyler. Advantages of the color octet gluon picture. *Physics Letters B*, 47(4):365–368, November 1973.

[24] The Nobel Prizes in Physics 1969, 1990, 2004.

[25] M. E. Peskin and D. V. Schroeder. *An Introduction To Quantum Field Theory*. Avalon Publishing, October 1995.

[26] F. Strocchi. *An Introduction to Non-Perturbative Foundations of Quantum Field Theory*. International Series of Monographs on Physics. Oxford University Press, Oxford, New York, February 2013.

[27] F. J. Dyson. Divergence of Perturbation Theory in Quantum Electrodynamics. *Physical Review*, 85(4):631–632, February 1952.

[28] G. V. Dunne. Perturbative–nonperturbative connection in quantum mechanics and field theory. In *Continuous Advances in QCD 2002*, pages 478–505, December 2002. arXiv:hep-th/0207046.

[29] K. G. Wilson. Renormalization Group and Critical Phenomena. I. Renormalization Group and the Kadanoff Scaling Picture. *Physical Review B*, 4(9):3174–3183, November 1971.

[30] K. G. Wilson. Renormalization Group and Critical Phenomena. II. Phase-Space Cell Analysis of Critical Behavior. *Physical Review B*, 4(9):3184–3205, November 1971.

[31] K. G. Wilson. The Nobel Prize in Physics 1982, 1982.

[32] S. Ferrara, A. F. Grillo, and R. Gatto. Tensor representations of conformal algebra and conformally covariant operator product expansion. *Annals of Physics*, 76(1):161–188, March 1973.

[33] D. Poland and D. Simmons-Duffin. The conformal bootstrap. *Nature Physics*, 12(6):535–539, June 2016.

[34] J. Maldacena. The large N limit of superconformal field theories and supergravity. *Advances in Theoretical and Mathematical Physics*, 2(2):231–252, March 1998.

[35] K. G. Wilson. Confinement of quarks. *Physical Review D*, 10(8):2445–2459, October 1974.

[36] U.-J. Wiese. An introduction to lattice field theory. August 2009.

[37] M. Creutz. Monte Carlo study of quantized SU(2) gauge theory. *Physical Review D*, 21(8):2308–2315, April 1980.

[38] H. J. Rothe. *Lattice Gauge Theories.* WORLD SCIENTIFIC, March 2012.

[39] C. Detar and S. Gottlieb. Lattice quantum chromodynamics comes of age. *Physics Today*, 57(2):45–51, February 2004.

[40] S. Dürr, Z. Fodor, J. Frison, C. Hoelbling, R. Hoffmann, S. D. Katz, S. Krieg, T. Kurth, L. Lellouch, T. Lippert, K. K. Szabo, and G. Vulvert. Ab Initio Determination of Light Hadron Masses. *Science*, 322(5905):1224–1227, November 2008.

[41] F. Gross, E. Klempt, S. J. Brodsky, A. J. Buras, V. D. Burkert, G. Heinrich, K. Jakobs, C. A. Meyer, K. Orginos, M. Strickland, J. Stachel, G. Zanderighi, N. Brambilla, P. Braun-Munzinger, D. Britzger, S. Capstick, T. Cohen, V. Crede, M. Constantinou, C. Davies, L. Del Debbio, A. Denig, C. DeTar, A. Deur, Y. Dokshitzer, H. G. Dosch, J. Dudek, M. Dunford, E. Epelbaum, M. A. Escobedo, H. Fritzsch, K. Fukushima, P. Gambino, D. Gillberg, S. Gottlieb, P. Grafstrom, M. Grazzini, B. Grube, A. Guskov, T. Iijima, X. Ji, F. Karsch, S. Kluth, J. B. Kogut, F. Krauss, S. Kumano, D. Leinweber, H. Leutwyler, H.-B. Li, Y. Li, B. Malaescu, C. Mariotti, P. Maris, S. Marzani, W. Melnitchouk, J. Messchendorp, H. Meyer, R. E. Mitchell, C. Mondal, F. Nerling, S. Neubert, M. Pappagallo, S. Pastore, J. R. Peláez, A. Puckett, J. Qiu, K. Rabbertz, A. Ramos, P. Rossi, A. Rustamov, A. Schäfer, S. Scherer, M. Schindler, S. Schramm, M. Shifman, E. Shuryak, T. Sjöstrand, G. Sterman, I. W.

Stewart, J. Stroth, E. Swanson, G. F. de Téramond, U. Thoma, A. Vairo, D. van Dyk, J. Vary, J. Virto, M. Vos, C. Weiss, M. Wobisch, S. L. Wu, C. Young, F. Yuan, X. Zhao, and X. Zhou. 50 Years of Quantum Chromodynamics. Technical report, December 2022.

[42] K. Nagata. Finite-density lattice QCD and sign problem: Current status and open problems. *Progress in Particle and Nuclear Physics*, 127:103991, November 2022.

[43] P. Coleman. *Introduction to Many-Body Physics*. Cambridge University Press, November 2015.

[44] A. Maas. *Lattice quantum field theory, Lecture in SS 2020 at the KFU Graz*. 2020.

[45] G. C. Wick. Properties of Bethe-Salpeter Wave Functions. *Physical Review*, 96(4):1124–1134, November 1954.

[46] D. Schlingemann. From euclidean field theory to quantum field theory. *Reviews in Mathematical Physics*, 11(09):1151–1178, October 1999.

[47] M. Troyer and U.-J. Wiese. Computational Complexity and Fundamental Limitations to Fermionic Quantum Monte Carlo Simulations. *Physical Review Letters*, 94(17):170201, May 2005.

[48] T. D. Kieu and C. J. Griffin. Monte Carlo simulations with indefinite and complex-valued measures. *Physical Review E*, 49(5):3855–3859, May 1994.

[49] S. Chandrasekharan and U.-J. Wiese. Meron-Cluster Solution of Fermion Sign Problems. *Physical Review Letters*, 83(16):3116–3119, October 1999.

[50] G. Aarts. Can Stochastic Quantization Evade the Sign Problem? The Relativistic Bose Gas at Finite Chemical Potential. *Physical Review Letters*, 102(13):131601, April 2009.

[51] L. Wang, Y.-H. Liu, M. Iazzi, M. Troyer, and G. Harcos. Split orthogonal group: A guiding principle for sign-problem-free fermionic simulations. *Physical Review Letters*, 115(25):250601, December 2015. arXiv:1506.05349 [cond-mat, physics:physics, physics:quant-ph].

[52] Z.-X. Li and H. Yao. Sign-Problem-Free Fermionic Quantum Monte Carlo: Developments and Applications. *Annual Review of Condensed Matter Physics*, 10(1):337–356, March 2019. arXiv:1805.08219 [cond-mat].

[53] A. Alexandru, G. Başar, P. F. Bedaque, and N. C. Warrington. Complex paths around the sign problem. *Reviews of Modern Physics*, 94(1):015006, March 2022.

[54] G. Aarts, J. Aichelin, C. Allton, A. Athenodorou, D. Bachtis, C. Bonanno, N. Brambilla, E. Bratkovskaya, M. Bruno, M. Caselle, C. Conti, R. Contino, L. Cosmai, F. Cuteri, L. Del Debbio, M. D'Elia, P. Dimopoulos, F. Di Renzo, T. Galatyuk, J. N. Guenther, R. Houtz, F. Karsch, A. Y. Kotov, M. P. Lombardo, B. Lucini,

L. Maio, M. Panero, J. M. Pawlowski, A. Pelissetto, O. Philipsen, A. Rago, C. Ratti, S. M. Ryan, F. Sannino, C. Sasaki, P. Schicho, C. Schmidt, S. Sharma, O. Soloveva, M. Sorba, and U.-J. Wiese. Phase Transitions in Particle Physics: Results and Perspectives from Lattice Quantum Chromo-Dynamics. *Progress in Particle and Nuclear Physics*, 133:104070, November 2023.

[55] U.-J. Wiese. Towards quantum simulating QCD. *Nuclear Physics A*, 931:246–256, November 2014.

[56] M. C. Bañuls, K. Cichy, J. I. Cirac, K. Jansen, S. Kühn, and H. Saito. Towards overcoming the Monte Carlo sign problem with tensor networks. *EPJ Web of Conferences*, 137:04001, 2017. arXiv: 1611.04791.

[57] R. P. Feynman. Simulating physics with computers. *International Journal of Theoretical Physics*, 21(6):467–488, June 1982.

[58] J. Eisert. Entanglement and tensor network states. Technical report, September 2013.

[59] T. Farrelly and J. Streich. Discretizing quantum field theories for quantum simulation. Technical report, July 2020.

[60] M. A. Nielsen and I. L. Chuang. Quantum Computation and Quantum Information: 10th Anniversary Edition, December 2010.

[61] J. I. Cirac and P. Zoller. Quantum Computations with Cold Trapped Ions. *Physical Review Letters*, 74(20):4091–4094, May 1995.

[62] M. Ringbauer, M. Meth, L. Postler, R. Stricker, R. Blatt, P. Schindler, and T. Monz. A universal qudit quantum processor with trapped ions. *Nature Physics*, 18(9):1053–1057, September 2022.

[63] C. S. Adams, J. D. Pritchard, and J. P. Shaffer. Rydberg atom quantum technologies. *Journal of Physics B: Atomic, Molecular and Optical Physics*, 53(1):012002, December 2019.

[64] D. Bluvstein, S. J. Evered, A. A. Geim, S. H. Li, H. Zhou, T. Manovitz, S. Ebadi, M. Cain, M. Kalinowski, D. Hangleiter, J. P. B. Ataides, N. Maskara, I. Cong, X. Gao, P. S. Rodriguez, T. Karolyshyn, G. Semeghini, M. J. Gullans, M. Greiner, V. Vuletic, and M. D. Lukin. Logical quantum processor based on reconfigurable atom arrays. *Nature*, December 2023. arXiv:2312.03982 [cond-mat, physics:physics, physics:quant-ph].

[65] F. Arute, K. Arya, R. Babbush, D. Bacon, J. C. Bardin, R. Barends, R. Biswas, S. Boixo, F. G. S. L. Brandao, D. A. Buell, B. Burkett, Y. Chen, Z. Chen, B. Chiaro, R. Collins, W. Courtney, A. Dunsworth, E. Farhi, B. Foxen, A. Fowler, C. Gidney, M. Giustina, R. Graff, K. Guerin, S. Habegger, M. P. Harrigan, M. J. Hartmann, A. Ho, M. Hoffmann, T. Huang, T. S. Humble, S. V. Isakov, E. Jeffrey, Z. Jiang, D. Kafri, K. Kechedzhi, J. Kelly, P. V. Klimov, S. Knysh, A. Korotkov,

F. Kostritsa, D. Landhuis, M. Lindmark, E. Lucero, D. Lyakh, S. Mandrà, J. R. McClean, M. McEwen, A. Megrant, X. Mi, K. Michielsen, M. Mohseni, J. Mutus, O. Naaman, M. Neeley, C. Neill, M. Y. Niu, E. Ostby, A. Petukhov, J. C. Platt, C. Quintana, E. G. Rieffel, P. Roushan, N. C. Rubin, D. Sank, K. J. Satzinger, V. Smelyanskiy, K. J. Sung, M. D. Trevithick, A. Vainsencher, B. Villalonga, T. White, Z. J. Yao, P. Yeh, A. Zalcman, H. Neven, and J. M. Martinis. Quantum supremacy using a programmable superconducting processor. *Nature*, 574(7779):505–510, October 2019.

[66] J. Preskill. Simulating quantum field theory with a quantum computer. In *Proceedings of The 36th Annual International Symposium on Lattice Field Theory — PoS(LATTICE2018)*, volume 334, page 024. SISSA Medialab, May 2019.

[67] T. Hey. *Feynman Lectures on Computation: Anniversary Edition.* Frontiers in Physics Ser. CRC Press, Milton, 2nd edition, May 2023. Description based on publisher supplied metadata and other sources.

[68] Y. Wang, Z. Hu, B. C. Sanders, and S. Kais. Qudits and High-Dimensional Quantum Computing. *Frontiers in Physics*, 8, 2020.

[69] R. P. Feynman. Quantum mechanical computers. *Foundations of Physics*, 16(6):507–531, June 1986.

[70] S. P. Jordan. *Quantum Computation Beyond the Circuit Model.* PhD thesis, arXiv, September 2008. arXiv:0809.2307 [quant-ph] type: article.

[71] D. Banerjee, M. Dalmonte, M. Müller, E. Rico, P. Stebler, U.-J. Wiese, and P. Zoller. Atomic Quantum Simulation of Dynamical Gauge Fields Coupled to Fermionic Matter: From String Breaking to Evolution after a Quench. *Physical Review Letters*, 109(17):175302, October 2012.

[72] D. Banerjee, M. Bögli, M. Dalmonte, E. Rico, P. Stebler, U.-J. Wiese, and P. Zoller. Atomic Quantum Simulation of U(N) and SU(N) Non-Abelian Lattice Gauge Theories. *Physical Review Letters*, 110(12):125303, March 2013.

[73] P. Hauke, D. Marcos, M. Dalmonte, and P. Zoller. Quantum Simulation of a Lattice Schwinger Model in a Chain of Trapped Ions. *Physical Review X*, 3(4):041018, November 2013.

[74] E. Zohar. Quantum simulation of fundamental physics. *Nature*, 534(7608):480–481, June 2016.

[75] M. Dalmonte and S. Montangero. Lattice gauge theory simulations in the quantum information era. *Contemp. Phys.*, 57(3):388–412, July 2016.

[76] E. Zohar, J. I. Cirac, and B. Reznik. Quantum Simulations of Lattice Gauge Theories using Ultracold Atoms in Optical Lattices. *Rep. Prog. Phys.*, 79(1):014401, January 2016. arXiv: 1503.02312.

[77] M. C. Bañuls, R. Blatt, J. Catani, A. Celi, J. I. Cirac, M. Dalmonte, L. Fallani, K. Jansen, M. Lewenstein, S. Montangero, C. A. Muschik, B. Reznik, E. Rico, L. Tagliacozzo, K. Van Acoleyen, F. Verstraete, U.-J. Wiese, M. Wingate, J. Zakrzewski, and P. Zoller. Simulating lattice gauge theories within quantum technologies. *arXiv:1911.00003*, 74(8):165, October 2020.

[78] M. Aidelsburger, L. Barbiero, A. Bermudez, T. Chanda, A. Dauphin, D. González-Cuadra, P. R. Grzybowski, S. Hands, F. Jendrzejewski, J. Jünemann, G. Juzeli unas, V. Kasper, A. Piga, S.-J. Ran, M. Rizzi, G. Sierra, L. Tagliacozzo, E. Tirrito, T. V. Zache, J. Zakrzewski, E. Zohar, and M. Lewenstein. Cold atoms meet lattice gauge theory. *Philosophical Transactions of the Royal Society A: Mathematical, Physical and Engineering Sciences*, 380(2216):20210064, December 2021.

[79] C. W. Bauer, Z. Davoudi, A. B. Balantekin, T. Bhattacharya, M. Carena, W. A. de Jong, P. Draper, A. El-Khadra, N. Gemelke, M. Hanada, D. Kharzeev, H. Lamm, Y.-Y. Li, J. Liu, M. Lukin, Y. Meurice, C. Monroe, B. Nachman, G. Pagano, J. Preskill, E. Rinaldi, A. Roggero, D. I. Santiago, M. J. Savage, I. Siddiqi, G. Siopsis, D. Van Zanten, N. Wiebe, Y. Yamauchi, K. Yeter-Aydeniz, and S. Zorzetti. Quantum Simulation for High-Energy Physics. *PRX Quantum*, 4(2):027001, Apr 2023. PRX Quantum 4, 027001, 2023.

[80] A. Di Meglio, K. Jansen, I. Tavernelli, C. Alexandrou, S. Arunachalam, C. W. Bauer, K. Borras, S. Carrazza, A. Crippa, V. Croft, R. de Putter, A. Delgado, V. Dunjko, D. J. Egger, E. Fernandez-Combarro, E. Fuchs, L. Funcke, D. Gonzalez-Cuadra, M. Grossi, J. C. Halimeh, Z. Holmes, S. Kuhn, D. Lacroix, R. Lewis, D. Lucchesi, M. L. Martinez, F. Meloni, A. Mezzacapo, S. Montangero, L. Nagano, V. Radescu, E. R. Ortega, A. Roggero, J. Schuhmacher, J. Seixas, P. Silvi, P. Spentzouris, F. Tacchino, K. Temme, K. Terashi, J. Tura, C. Tuysuz, S. Vallecorsa, U.-J. Wiese, S. Yoo, and J. Zhang. Quantum Computing for High-Energy Physics: State of the Art and Challenges. Summary of the QC4HEP Working Group. Technical report, July 2023.

[81] L. Funcke, T. Hartung, K. Jansen, and S. Kühn. Review on Quantum Computing for Lattice Field Theory. Technical report, February 2023.

[82] B. Villalonga, S. Boixo, B. Nelson, C. Henze, E. Rieffel, R. Biswas, and S. Mandrà. A flexible high-performance simulator for verifying and benchmarking quantum circuits implemented on real hardware. *npj Quantum Information*, 5(1):1–16, October 2019.

[83] A. Smith, M. S. Kim, F. Pollmann, and J. Knolle. Simulating quantum many-body dynamics on a current digital quantum computer. *npj Quantum Information*, 5(1):1–13, November 2019. arXiv: 1906.06343.

[84] S. V. Mathis, G. Mazzola, and I. Tavernelli. Toward scalable simulations of Lattice

Gauge Theories on quantum computers. *arXiv:2005.10271 [cond-mat, physics:hep-lat, physics:quant-ph]*, May 2020. arXiv: 2005.10271.

[85] A. Kan and Y. Nam. Lattice quantum chromodynamics and electrodynamics on a universal quantum computer. July 2021.

[86] R. Orús. A practical introduction to tensor networks: Matrix product states and projected entangled pair states. *Annals of Physics*, 349:117–158, October 2014.

[87] S. Montangero. *Introduction to Tensor Network Methods: Numerical simulations of low-dimensional many-body quantum systems.* Springer International Publishing, 2018.

[88] J. Eisert, M. Cramer, and M. B. Plenio. Colloquium: Area laws for the entanglement entropy. *Reviews of Modern Physics*, 82(1):277–306, February 2010.

[89] M. Fannes, B. Nachtergaele, and R. F. Werner. Exact Antiferromagnetic Ground States of Quantum Spin Chains. *Europhysics Letters*, 10(7):633, December 1989.

[90] M. Fannes, B. Nachtergaele, and R. F. Werner. Finitely correlated states on quantum spin chains. *Communications in Mathematical Physics*, 144(3):443–490, March 1992.

[91] S. R. White. Density Matrix Formulation for Quantum Renormalization Groups. *Physical Review Letters*, 69(19):2863–2866, November 1992.

[92] S. Östlund and S. Rommer. Thermodynamic Limit of Density Matrix Renormalization. *Physical Review Letters*, 75(19):3537–3540, November 1995.

[93] S. Rommer and S. Östlund. Class of ansatz wave functions for one-dimensional spin systems and their relation to the density matrix renormalization group. *Physical Review B*, 55(4):2164–2181, January 1997.

[94] J. Dukelsky, M. A. Martín-Delgado, T. Nishino, and G. Sierra. Equivalence of the variational matrix product method and the density matrix renormalization group applied to spin chains. *Europhysics Letters*, 43(4):457, August 1998.

[95] U. Schollwöck. The density-matrix renormalization group in the age of matrix product states. *Annals of Physics*, 326(1):96–192, January 2011.

[96] F. Verstraete, V. Murg, and J. I. Cirac. Matrix product states, projected entangled pair states, and variational renormalization group methods for quantum spin systems. *Advances in Physics*, 57(2):143–224, March 2008.

[97] M. Levin and C. P. Nave. Tensor Renormalization Group Approach to Two-Dimensional Classical Lattice Models. *Physical Review Letters*, 99(12):120601, September 2007.

[98] K. Boguslawski, K. H. Marti, Ö. Legeza, and M. Reiher. Accurate ab Initio Spin Densities. *Journal of Chemical Theory and Computation*, 8(6):1970–1982, June 2012.

[99] N. Nakatani and G. K.-L. Chan. Efficient tree tensor network states (TTNS) for quantum chemistry: Generalizations of the density matrix renormalization group algorithm. *The Journal of Chemical Physics*, 138(13):134113, April 2013.

[100] E. Stoudenmire and D. J. Schwab. Supervised Learning with Tensor Networks. In *Advances in Neural Information Processing Systems*, volume 29. Curran Associates, Inc., 2016.

[101] T. Felser, M. Trenti, L. Sestini, A. Gianelle, D. Zuliani, D. Lucchesi, and S. Montangero. Quantum-inspired machine learning on high-energy physics data. *npj Quantum Information*, 7(1):1–8, July 2021.

[102] M. C. Bañuls, K. Cichy, J. I. Cirac, and K. Jansen. The mass spectrum of the Schwinger model with matrix product states. *Journal of High Energy Physics*, 2013(11):158, November 2013.

[103] B. Buyens, J. Haegeman, K. Van Acoleyen, H. Verschelde, and F. Verstraete. Matrix Product States for Gauge Field Theories. *Physical Review Letters*, 113(9):091601, August 2014.

[104] E. Rico, T. Pichler, M. Dalmonte, P. Zoller, and S. Montangero. Tensor Networks for Lattice Gauge Theories and Atomic Quantum Simulation. *Physical Review Letters*, 112(20):201601, May 2014.

[105] P. Silvi, E. Rico, T. Calarco, and S. Montangero. Lattice gauge tensor networks. *New Journal of Physics*, 16(10):103015, October 2014.

[106] L. Tagliacozzo, A. Celi, and M. Lewenstein. Tensor Networks for Lattice Gauge Theories with Continuous Groups. *Physical Review X*, 4(4):041024, November 2014.

[107] M. C. Bañuls, K. Cichy, J. I. Cirac, K. Jansen, and H. Saito. Matrix Product States for Lattice Field Theories. Technical report, April 2014. arXiv:1310.4118 [cond-mat, physics:hep-lat, physics:quant-ph] type: article.

[108] E. Zohar, M. Burrello, T. B. Wahl, and J. I. Cirac. Fermionic projected entangled pair states and local U(1) gauge theories. *Annals of Physics*, 363:385–439, 2015.

[109] S. Kühn, E. Zohar, J. I. Cirac, and M. C. Bañuls. Non-Abelian string breaking phenomena with matrix product states. *Journal of High Energy Physics*, 2015(7):130, July 2015.

[110] T. Pichler, M. Dalmonte, E. Rico, P. Zoller, and S. Montangero. Real-Time Dynamics in U(1) Lattice Gauge Theories with Tensor Networks. *Physical Review X*, 6(1):011023, March 2016.

[111] M. C. Bañuls and K. Cichy. Tensors cast their nets for quarks. *Nature Physics*, 17(7):762–763, July 2021.

[112] S. Montangero, E. Rico, and P. Silvi. Loop-free tensor networks for high-energy physics. *Philosophical Transactions of the Royal Society A*, February 2022.

[113] J. Schwinger. Gauge Invariance and Mass. II. *Physical Review*, 128(5):2425–2429, December 1962.

[114] J. H. Lowenstein and J. A. Swieca. Quantum electrodynamics in two dimensions. *Annals of Physics*, 68(1):172–195, November 1971.

[115] M. Rigobello, S. Notarnicola, G. Magnifico, and S. Montangero. Entanglement generation in $(1 + 1)$D QED scattering processes. *Physical Review D*, 104(11):114501, December 2021.

[116] S. Coleman, R. Jackiw, and L. Susskind. Charge shielding and quark confinement in the massive schwinger model. *Annals of Physics*, 93(1):267–275, September 1975.

[117] N. Nakanishi. Asymptotic Completeness and Confinement in the Massive Schwinger Model. *Progress of Theoretical Physics*, 59(2):607–618, February 1978.

[118] E. Abdalla, M. C. B. Abdalla, and K. D. Rothe. *Non-Perturbative Methods in 2 Dimensional Quantum Field Theory*. WORLD SCIENTIFIC, 2nd edition, July 2001.

[119] D. J. Gross and F. Wilczek. Ultraviolet Behavior of Non-Abelian Gauge Theories. *Physical Review Letters*, 30(26):1343–1346, June 1973.

[120] H. D. Politzer. Reliable Perturbative Results for Strong Interactions? *Physical Review Letters*, 30(26):1346–1349, June 1973.

[121] C. Alabiso and G. Schierholz. Infrared slavery and quark confinement. *Nuclear Physics B*, 110(1):81–92, July 1976.

[122] H. Wittig. QCD on the Lattice. pages 137–262. Springer International Publishing, Cham, 2020.

[123] G. Magnifico, T. Felser, P. Silvi, and S. Montangero. Lattice quantum electrodynamics in $(3+1)$-dimensions at finite density with tensor networks. *Nature Communications*, 12(1):3600, November 2021.

[124] P. Silvi, Y. Sauer, F. Tschirsich, and S. Montangero. Tensor network simulation of an SU(3) lattice gauge theory in 1D. *Physical Review D*, 100(7):074512, October 2019.

[125] T. Hayata and Y. Hidaka. Breaking new ground for quantum and classical simulations of SU(3) Yang-Mills theory. Technical report, June 2023.

[126] M. Rigobello, G. Magnifico, P. Silvi, and S. Montangero. Hadrons in (1+1)D Hamiltonian hardcore lattice QCD. Technical report, August 2023.

[127] T. Hayata, Y. Hidaka, and K. Nishimura. Dense QCD_2 with matrix product states. Technical report, November 2023. arXiv:2311.11643 [hep-lat, physics:hep-th, physics:nucl-th, physics:quant-ph] type: article.

[128] P. Silvi, E. Rico, M. Dalmonte, F. Tschirsich, and S. Montangero. Finite-density phase diagram of a (1+1)-d non-abelian lattice gauge theory with tensor networks. *Quantum*, 1:9, April 2017. arXiv:1606.05510 [cond-mat, physics:hep-lat, physics:quant-ph].

[129] T. Felser, P. Silvi, M. Collura, and S. Montangero. Two-Dimensional Quantum-Link Lattice Quantum Electrodynamics at Finite Density. *Physical Review X*, 10:041040, November 2020.

[130] G. Cataldi, G. Magnifico, P. Silvi, and S. Montangero. (2+1)D SU(2) Yang-Mills Lattice Gauge Theory at finite density via tensor networks. Technical report, July 2023.

[131] M. Rigobello. Scattering Processes via Tensor Network Simulations. Master's thesis, University of Padova, 2020.

[132] E. Zohar and M. Burrello. Formulation of lattice gauge theories for quantum simulations. *Physical Review D*, 91(5):054506, March 2015.

[133] A. Milsted and T. J. Osborne. Quantum Yang-Mills theory: An overview of a program. *Physical Review D*, 98(1):014505, July 2018.

[134] C. N. Yang and R. L. Mills. Conservation of Isotopic Spin and Isotopic Gauge Invariance. *Physical Review*, 96(1):191–195, October 1954.

[135] S. Weinberg. What is Quantum Field Theory, and What Did We Think It Is? In *Conceptual foundations of quantum field theory. Proceedings, Symposium and Workshop, Boston, USA, March 1-3, 1996*, pages 241–251, 3 1996. arXiv: hep-th/9702027 version: 1.

[136] P. Yip. Spinors in two dimensions. *J. Math. Phys.*, 24(5):1206–1212, May 1983.

[137] S. Weinberg. *The Quantum Theory of Fields*, volume 1. Cambridge University Press, Cambridge, 1995.

[138] C. Itzykson and J. B. Zuber. *Quantum Field Theory.* International Series In Pure and Applied Physics. McGraw-Hill, New York, 1980.

[139] B. S. DeWitt and B. S. DeWitt. *The Global Approach to Quantum Field Theory.* Oxford University Press, 2003.

[140] A. O. Barut and G. H. Mullen. Quantization of two-component higher order spinor equations. *Annals of Physics*, 20(2):184–202, November 1962.

[141] R. F. Streater and A. S. Wightman. *PCT, Spin and Statistics, and All That.* W. A. Benjamin, 1964.

[142] M. B. Green, J. H. Schwarz, and E. Witten. Superstring Theory: Volume 1, Introduction: 25th Anniversary Edition, 2012.

[143] M. Henneaux and C. Teitelboim. *Quantization of Gauge Systems*. Princeton University Press, August 1992.

[144] A. Mariani. *Finite-group Yang-Mills lattice gauge theories in the Hamiltonian formalism*. PhD thesis, November 2020.

[145] A. Mariani, S. Pradhan, and E. Ercolessi. Hamiltonians and gauge-invariant Hilbert space for lattice Yang-Mills-like theories with finite gauge group. *Physical Review D*, 107(11):114513, June 2023.

[146] D. Bleecker. *Gauge Theory and Variational Principles*. Courier Corporation, January 2013.

[147] N. E. Bralic. Exact computation of loop averages in two-dimensional Yang-Mills theory. *Phys. Rev. D*, 22(12):3090–3103, December 1980.

[148] A. A. Belavin, A. M. Polyakov, A. S. Schwartz, and Y. S. Tyupkin. Pseudoparticle solutions of the Yang-Mills equations. *Phys. Lett. B*, 59(1):85–87, October 1975.

[149] C. G. Callan, R. F. Dashen, and D. J. Gross. The structure of the gauge theory vacuum. *Phys. Lett. B*, 63(3):334–340, August 1976.

[150] N. Bourbaki. *Lie Groups and Lie Algebras: Chapters 1-3*. Springer Science & Business Media, 1989.

[151] P. G. Bergmann. Non-Linear Field Theories. *Physical Review*, 75(4):680–685, February 1949.

[152] P. A. M. Dirac. Generalized Hamiltonian Dynamics. *Can. J. Math.*, 2:129–148, 1950.

[153] V. N. Gribov. Quantization of non-Abelian gauge theories. *Nuclear Physics B*, 139(1):1–19, June 1978.

[154] L. Castellani. Symmetries in constrained hamiltonian systems. *Ann. Phys.*, 143(2):357 – 371, 1982.

[155] A. Wipf. Hamilton's formalism for systems with constraints. In J. Ehlers and H. Friedrich, editors, *Canonical Gravity: From Classical to Quantum*, Lecture Notes in Physics, pages 22–58, Berlin, Heidelberg, 1994. Springer.

[156] P. A. M. Dirac. *The Principles of Quantum Mechanics*. Clarendon Press, 1930.

[157] H. J. Groenewold. On the principles of elementary quantum mechanics. *Physica*, 12(7):405–460, October 1946.

[158] N. H. McCoy. On the Function in Quantum Mechanics which Corresponds to a Given Function in Classical Mechanics. *Proceedings of the National Academy of Sciences of the United States of America*, 18(11):674–676, 1932.

[159] R. Ferrari, L. E. Picasso, and F. Strocchi. Some remarks on local operators in quantum electrodynamics. *Communications in Mathematical Physics*, 35(1):25–38, March 1974.

[160] M. Creutz. Quantum electrodynamics in the temporal gauge. *Ann. Phys.*, 117(2):471–483, February 1979.

[161] R. Jackiw. Topological investigations of quantized gauge theories. pages 211–359. WORLD SCIENTIFIC, Netherlands, December 1985. INIS Reference Number: 16043172.

[162] S. Weinberg. *The Quantum Theory of Fields: Volume 2: Modern Applications*, volume 2. Cambridge University Press, Cambridge, 1996.

[163] P. Gorantla, H. T. Lam, N. Seiberg, and S.-H. Shao. Low-energy limit of some exotic lattice theories and UV/IR mixing. *Physical Review B*, 104(23):235116, December 2021.

[164] M. E. Fisher and M. N. Barber. Scaling Theory for Finite-Size Effects in the Critical Region. *Phys. Rev. Lett.*, 28(23):1516–1519, June 1972.

[165] A. Pelissetto and E. Vicari. Scaling behaviors at quantum and classical first-order transitions. Technical report, February 2023.

[166] M. Lüscher. Volume dependence of the energy spectrum in massive quantum field theories. *Communications in Mathematical Physics*, 105(2):153–188, June 1986.

[167] M. Lüscher. Signatures of unstable particles in finite volume. *Nuclear Physics B*, 364(1):237–251, October 1991.

[168] R. Batterman, editor. *The Oxford Handbook of Philosophy of Physics*, chapter 6 Effective Field Theories. Oxford Handbooks. Oxford University Press, Oxford, New York, March 2013.

[169] J. B. Kogut. An introduction to lattice gauge theory and spin systems. *Rev. Mod. Phys.*, 51(4):659–713, October 1979.

[170] J. B. Kogut and M. A. Stephanov. *The Phases of Quantum Chromodynamics: From Confinement to Extreme Environments*, chapter 6 The Hamiltonian version of lattice gauge theory. Cambridge University Press, December 2003.

[171] W. L. Briggs and V. E. Henson. *The DFT: An Owners' Manual for the Discrete Fourier Transform.* SIAM, January 1995.

[172] S. Chandrasekharan and U.-J. Wiese. An Introduction to Chiral Symmetry on the Lattice. *Prog. Part. Nucl. Phys. 53 (2004) 373-418*, May 2004.

[173] K. Symanzik. Cutoff Dependence in Lattice ø44Theory. NATO Advanced Study Institutes Series, pages 313–330. Springer US, Boston, MA, 1980.

[174] P. Weisz. Continuum limit improved lattice action for pure Yang-Mills theory (I). *Nuclear Physics B*, 212(1):1–17, February 1983.

[175] P. Weisz and R. Wohlert. Continuum limit improved lattice action for pure Yang-Mills theory (II). *Nuclear Physics B*, 236(2):397–422, April 1984.

[176] G. Parisi. Symanzik's improvement program. *Nuclear Physics B*, 254:58–70, January 1985.

[177] G. D. Moore. Improved Hamiltonian for Minkowski Yang-Mills theory. *Nuclear Physics B*, 480(3):689–726, December 1996.

[178] X.-Q. Luo, S.-H. Guo, H. Kröger, and D. Schütte. Improving the lattice QCD hamiltonian. *Nuclear Physics B - Proceedings Supplements*, 63(1):931–933, April 1998.

[179] M. Carena, H. Lamm, Y.-Y. Li, and W. Liu. Improved Hamiltonians for Quantum Simulations of Gauge Theories. *Physical Review Letters*, 129(5):051601, July 2022.

[180] A. N. Ciavarella. Quantum Simulation of Lattice QCD with Improved Hamiltonians. Technical report, July 2023. arXiv:2307.05593 [hep-lat, physics:nucl-th, physics:quant-ph] type: article.

[181] M. Troyer. Computational quantum physics, 2010.

[182] U. Wolff. Basics of lattice quantum field theory. 2010.

[183] M. Lüscher. Advanced Lattice QCD. Technical report, February 1998.

[184] J. Kogut and L. Susskind. Hamiltonian formulation of Wilson's lattice gauge theories. *Physical Review D*, 11(2):395–408, January 1975.

[185] T. Banks, L. Susskind, and J. Kogut. Strong-coupling calculations of lattice gauge theories: $(1 + 1)$-dimensional exercises. *Physical Review D*, 13(4):1043–1053, February 1976.

[186] L. Susskind. Lattice fermions. *Physical Review D*, 16(10):3031–3039, November 1977.

[187] R. Gupta. Introduction to Lattice QCD. July 1998.

[188] D. Tong. *Gauge theory.* 2018.

[189] H. B. Nielsen and M. Ninomiya. A no-go theorem for regularizing chiral fermions. *Phys. Lett. B*, 105(2):219–223, October 1981.

[190] H. B. Nielsen and M. Ninomiya. Absence of neutrinos on a lattice: (I). Proof by homotopy theory. *Nuclear Physics B*, 185(1):20–40, July 1981.

[191] H. B. Nielsen and M. Ninomiya. Absence of neutrinos on a lattice: (II). Intuitive topological proof. *Nuclear Physics B*, 193(1):173–194, December 1981.

[192] D. Friedan. A proof of the Nielsen-Ninomiya theorem. *Commun. Math. Phys.*, 85(4):481–490, December 1982.

[193] S. L. Adler. Axial-Vector Vertex in Spinor Electrodynamics. *Phys. Rev.*, 177(5):2426–2438, January 1969.

[194] J. S. Bell and R. Jackiw. A PCAC puzzle: $\pi 0 \to \gamma\gamma$ in the σ-model. *Il Nuovo Cimento A (1965-1970)*, 60(1):47–61, March 1969.

[195] S. B. Treiman, R. Jackiw, B. Zumino, and E. Witten. *Current Algebra and Anomalies.* WORLD SCIENTIFIC, 1985.

[196] L. H. Karsten and J. Smith. Lattice fermions: Species doubling, chiral invariance and the triangle anomaly. *Nucl. Phys. B*, 183(1):103–140, May 1981.

[197] D. B. Kaplan. Chiral Symmetry and Lattice Fermions. January 2012.

[198] P. Jordan and E. Wigner. Über das Paulische Äquivalenzverbot. *Zeitschrift für Physik*, 47(9):631–651, September 1928.

[199] E. Lieb, T. Schultz, and D. Mattis. Two soluble models of an antiferromagnetic chain. *Annals of Physics*, 16(3):407–466, December 1961.

[200] A. M. Polyakov. *Gauge Fields and Strings.* Harwood Academic Publishers, 1987.

[201] S. Coleman. More about the massive Schwinger model. *Annals of Physics*, 101(1):239–267, September 1976.

[202] D. Horn. Finite matrix models with continuous local gauge invariance. *Physics Letters B*, 100(2):149–151, March 1981.

[203] S. Chandrasekharan and U. J. Wiese. Quantum link models: A discrete approach to gauge theories. *Nuclear Physics B*, 492(1):455–471, May 1997.

[204] U.-J. Wiese. From quantum link models to D-theory: a resource efficient framework for the quantum simulation and computation of gauge theories. *Philosophical Transactions of the Royal Society A: Mathematical, Physical and Engineering Sciences*, 380(2216), December 2021.

[205] G. Bimonte, A. Stern, and P. Vitale. $\mathrm{SU}_q(2)$ lattice gauge theory. *Physical Review D*, 54(1):1054–1062, July 1996.

[206] T. V. Zache, D. González-Cuadra, and P. Zoller. Quantum and classical spin network algorithms for q-deformed Kogut-Susskind gauge theories. *Physical Review Letters*, 131(17):171902, October 2023. arXiv:2304.02527 [cond-mat, physics:hep-lat, physics:quant-ph].

[207] T. Hayata and Y. Hidaka. String-net formulation of Hamiltonian lattice Yang-Mills theories and quantum many-body scars in a nonabelian gauge theory. Technical report, May 2023.

[208] D. Horn, M. Weinstein, and S. Yankielowicz. Hamiltonian approach to $Z(N)$ lattice gauge theories. *Physical Review D: Particles and Fields*, 19:3715–3731, June 1979.

[209] S. Notarnicola, E. Ercolessi, P. Facchi, G. Marmo, S. Pascazio, and F. V. Pepe. Discrete Abelian gauge theories for quantum simulations of QED. *Journal of Physics. A. Mathematical and Theoretical*, 48(30):30FT01, July 2015. arXiv: 1503.04340.

[210] A. Alexandru, P. F. Bedaque, R. Brett, and H. Lamm. Spectrum of digitized QCD: Glueballs in a $S(1080)$ gauge theory. *Physical Review D*, 105(11):114508, June 2022.

[211] C. W. Bauer, I. D'Andrea, M. Freytsis, and D. M. Grabowska. A new basis for Hamiltonian SU(2) simulations. Technical report, July 2023.

[212] B. B. Beard, R. C. Brower, S. Chandrasekharan, D. Chen, A. Tsapalis, and U.-J. Wiese. D-Theory: Field Theory via Dimensional Reduction of Discrete Variables. *Nucl. Phys. B: Proc. Suppl.*, 63(1):775–789, April 1998.

[213] Y. Tong, V. V. Albert, J. R. McClean, J. Preskill, and Y. Su. Provably accurate simulation of gauge theories and bosonic systems. *Quantum*, 6:816, September 2022.

[214] F. Peter and H. Weyl. Die Vollständigkeit der primitiven Darstellungen einer geschlossenen kontinuierlichen Gruppe. *Mathematische Annalen*, 97(1):737–755, December 1927.

[215] G. Burgio, R. De Pietri, H. A. Morales-Técotl, L. F. Urrutia, and J. D. Vergara. The basis of the physical Hilbert space of lattice gauge theories. *Nuclear Physics B*, 566(3):547–561, February 2000.

[216] J. F. Cornwell. Chapter 4 - Representations of Groups – Principal Ideas. volume 1 of *Techniques of Physics*, pages 47–63. Academic Press, San Diego, January 1997.

[217] T. Bröcker and T. t. Dieck. *Representations of Compact Lie Groups*. Springer Science & Business Media, June 2003.

[218] R. Slansky. Group theory for unified model building. *Physics Reports*, 79(1):1–128, December 1981.

[219] P. Orland and D. Rohrlich. Lattice gauge magnets: Local isospin from spin. *Nuclear Physics B*, 338(3):647–672, July 1990.

[220] M. C. Bañuls, K. Cichy, J. I. Cirac, K. Jansen, and S. Kühn. Efficient Basis Formulation for $(1+1)$-Dimensional SU(2) Lattice Gauge Theory: Spectral Calculations with Matrix Product States. *Physical Review X*, 7(4):041046, November 2017.

[221] E. Zohar and J. I. Cirac. Removing staggered fermionic matter in $U(N)$ and $SU(N)$ lattice gauge theories. *Physical Review D*, 99(11):114511, June 2019.

[222] M. Ballarin, G. Cataldi, G. Magnifico, D. Jaschke, M. Di Liberto, I. Siloi, S. Montangero, and P. Silvi. Scalable digital quantum simulation of lattice fermion theories

with local encoding. Technical report, December 2023. arXiv:2310.15091 [cond-mat, physics:quant-ph] type: article.

[223] F. M. Surace, P. Fromholz, F. Scazza, and M. Dalmonte. Scalable, ab initio protocol for quantum simulating SU(N)×U(1) Lattice Gauge Theories. Technical report, November 2023. arXiv:2310.08643 [cond-mat, physics:hep-lat, physics:quant-ph] type: article.

[224] P. Silvi, F. Tschirsich, M. Gerster, J. Jünemann, D. Jaschke, M. Rizzi, and S. Montangero. The Tensor Networks Anthology: Simulation techniques for many-body quantum lattice systems. *SciPost Physics Lecture Notes*, 8:8, March 2019.

[225] J. Hauschild and F. Pollmann. Efficient numerical simulations with Tensor Networks: Tensor Network Python (TeNPy). *SciPost Physics Lecture Notes*, 5, April 2018.

[226] tensornetwork.org. Tensor renormalization group algorithm. https://tensornetwork.org/trg/.

[227] K.-I. Aoki, T. Kobayashi, and H. Tomita. Domain Wall Renormalization Group Analysis of 2-dimensional Ising Model. *International Journal of Modern Physics B*, 23(18):3739–3751, July 2009.

[228] tensors.net. Example codes: Trg. https://www.tensors.net/trg.

[229] C. Q. Cook. The Tensor Renormalization Group, 2015.

[230] T. Shachar and E. Zohar. Approximating relativistic quantum field theories with continuous tensor networks. *Physical Review D*, 105(4):045016, February 2022.

[231] M. Lindsey. *The Quantum Many-Body Problem: Methods and Analysis*. PhD thesis, 2019.

[232] TOP500, November 2023. Page Version ID: 1185271853.

[233] C. Eckart and G. Young. The approximation of one matrix by another of lower rank. *Psychometrika*, 1(3):211–218, September 1936.

[234] R. M. Johnson. On a theorem stated by eckart and young. *Psychometrika*, 28(3):259–263, September 1963.

[235] I. Bengtsson and K. Życzkowski. *Geometry of Quantum States: An Introduction to Quantum Entanglement*. Cambridge University Press, Cambridge, 2 edition, 2017.

[236] U. Fano. Description of States in Quantum Mechanics by Density Matrix and Operator Techniques. *Reviews of Modern Physics*, 29(1):74–93, January 1957.

[237] C. H. Bennett, H. J. Bernstein, S. Popescu, and B. Schumacher. Concentrating partial entanglement by local operations. *Physical Review A*, 53(4):2046–2052, April 1996.

[238] M. B. Hastings and T. Koma. Spectral Gap and Exponential Decay of Correlations. *Communications in Mathematical Physics*, 265(3):781–804, August 2006.

[239] M. Srednicki. Entropy and Area. *Physical Review Letters*, 71(5):666–669, August 1993.

[240] M. B. Hastings. An area law for one-dimensional quantum systems. *J. Stat. Mech: Theory Exp.*, 2007(08):P08024–P08024, August 2007.

[241] F. G. S. L. Brandão and M. Horodecki. Exponential Decay of Correlations Implies Area Law. *Communications in Mathematical Physics*, 333(2):761–798, January 2015.

[242] C. Holzhey, F. Larsen, and F. Wilczek. Geometric and Renormalized Entropy in Conformal Field Theory. *Nuclear Physics B*, 424(3):443–467, August 1994.

[243] P. Calabrese and J. Cardy. Entanglement Entropy and Quantum Field Theory. *Journal of Statistical Mechanics: Theory and Experiment*, 2004(06):P06002, June 2004.

[244] G. Vidal, J. I. Latorre, E. Rico, and A. Kitaev. Entanglement in Quantum Critical Phenomena. *Physical Review Letters*, 90(22):227902, June 2003.

[245] D. Poulin, A. Qarry, R. Somma, and F. Verstraete. Quantum Simulation of Time-Dependent Hamiltonians and the Convenient Illusion of Hilbert Space. *Physical Review Letters*, 106(17):170501, April 2011. arXiv:1102.1360 [quant-ph].

[246] G. Vidal. Efficient Simulation of One-Dimensional Quantum Many-Body Systems. *Physical Review Letters*, 93(4):040502, July 2004.

[247] F. Verstraete and J. I. Cirac. Renormalization algorithms for Quantum-Many Body Systems in two and higher dimensions. Technical report, July 2004. arXiv:cond-mat/0407066 type: article.

[248] M. Bañuls, K. Cichy, J. Cirac, K. Jansen, and S. Kühn. Tensor networks and their use for lattice gauge theories. In *Proceedings of The 36th Annual International Symposium on Lattice Field Theory — PoS(LATTICE2018)*. Sissa Medialab, May 2019.

[249] L. Tagliacozzo, A. Celi, A. Zamora, and M. Lewenstein. Optical Abelian lattice gauge theories. *Annals of Physics*, 330:160–191, March 2013.

[250] B. Buyens, K. Van Acoleyen, J. Haegeman, and F. Verstraete. Matrix product states for Hamiltonian lattice gauge theories. Technical report, October 2014. arXiv:1411.0020 [cond-mat, physics:hep-lat] type: article.

[251] B. Buyens, J. Haegeman, F. Verstraete, and K. Van Acoleyen. Tensor networks for gauge field theories. Technical report, November 2015. arXiv:1511.04288 [cond-mat, physics:hep-lat, physics:hep-th, physics:quant-ph] type: article.

[252] E. Zohar and M. Burrello. Building projected entangled pair states with a local gauge symmetry. *New Journal of Physics*, 18(4):043008, April 2016.

[253] J. Biamonte and V. Bergholm. Tensor Networks in a Nutshell, July 2017.

[254] J. Biamonte. Lectures on Quantum Tensor Networks, December 2019.

[255] T. Felser. *Tree tensor networks for high-dimensional quantum systems and beyond.* PhD thesis, Saarländische Universitäts- und Landesbibliothek, 2021.

[256] F. Verstraete, M. M. Wolf, D. Perez-Garcia, and J. I. Cirac. Criticality, the Area Law, and the Computational Power of Projected Entangled Pair States. *Physical Review Letters*, 96:220601, June 2006.

[257] L. Accardi. Topics in quantum probability. *Physics Reports*, 77(3):169–192, November 1981.

[258] A. Klümper, A. Schadschneider, and J. Zittartz. Matrix Product Ground States for One-Dimensional Spin-1 Quantum Antiferromagnets. *Europhysics Letters (EPL)*, 24(4):293–297, November 1993. arXiv:cond-mat/9307028.

[259] B. Pirvu, V. Murg, J. I. Cirac, and F. Verstraete. Matrix product operator representations. *New Journal of Physics*, 12(2):025012, February 2010.

[260] S. R. White. Density-matrix algorithms for quantum renormalization groups. *Physical Review B*, 48(14):10345–10356, October 1993.

[261] U. Schollwöck. The density-matrix renormalization group. *Reviews of Modern Physics*, 77(1):259–315, April 2005.

[262] K. G. Wilson. The renormalization group: Critical phenomena and the Kondo problem. *Reviews of Modern Physics*, 47(4):773–840, October 1975.

[263] *Density-Matrix Renormalization.* Springer Berlin Heidelberg, 1999.

[264] Y.-Y. Shi, L.-M. Duan, and G. Vidal. Classical simulation of quantum many-body systems with a tree tensor network. *Physical Review A*, 74(2):022320, August 2006.

[265] L. Tagliacozzo, G. Evenbly, and G. Vidal. Simulation of two-dimensional quantum systems using a tree tensor network that exploits the entropic area law. *Physical Review B*, 80(23):235127, December 2009.

[266] P. Silvi, V. Giovannetti, S. Montangero, M. Rizzi, J. I. Cirac, and R. Fazio. Homogeneous binary trees as ground states of quantum critical Hamiltonians. *Physical Review A*, 81(6):062335, June 2010.

[267] V. Murg, F. Verstraete, Ö. Legeza, and R. M. Noack. Simulating strongly correlated quantum systems with tree tensor networks. *Physical Review B*, 82(20):205105, November 2010.

[268] F. Verstraete, J. J. García-Ripoll, and J. I. Cirac. Matrix Product Density Operators: Simulation of Finite-Temperature and Dissipative Systems. *Physical Review Letters*, 93(20):207204, November 2004.

[269] M. Suzuki. General theory of fractal path integrals with applications to many-body theories and statistical physics. *Journal of Mathematical Physics*, 32(2):400–407, 1991.

[270] H. H. Zhao, Z. Y. Xie, Q. N. Chen, Z. C. Wei, J. W. Cai, and T. Xiang. Renormalization of tensor-network states. *Physical Review B*, 81(17):174411, May 2010. arXiv:1002.1405 [cond-mat, physics:physics, physics:quant-ph].

[271] R. J. Baxter. *Exactly Solved Models in Statistical Mechanics*. Academic Press, 1982.

[272] T. Hsieh. From d-dimensional Quantum to $d+1$-dimensional Classical Systems, 2012.

[273] L. Onsager. Crystal Statistics. I. A Two-Dimensional Model with an Order-Disorder Transition. *Physical Review*, 65(3-4):117–149, February 1944.

[274] S. M. Bhattacharjee and A. Khare. Fifty Years of the Exact Solution of the Two-Dimensional Ising Model by Onsager. *Curr. Sci.*, 69:816–820, November 1995.

[275] F. Verstraete and J. I. Cirac. Continuous Matrix Product States for Quantum Fields. *Physical Review Letters*, 104(19):190405, May 2010.

[276] A. Tilloy and J. I. Cirac. Continuous tensor network states for quantum fields. *Physical Review X*, 9, 2019.

[277] R. P. Feynman. Difficulties in Applying the Variational Principle to Quantum Field Theories. pages 28–40. WORLD SCIENTIFIC, July 1988.

[278] A. Tilloy. Variational method in relativistic quantum field theory without cutoff. *Physical Review D*, 104(9):L091904, November 2021.

[279] S. Bravyi, D. P. DiVincenzo, and D. Loss. Schrieffer–Wolff transformation for quantum many-body systems. *Annals of Physics*, 326(10):2793–2826, October 2011.

[280] G. Y. Hu and R. F. O'Connell. Analytical inversion of symmetric tridiagonal matrices. *Journal of Physics A: Mathematical and General*, 29(7):1511, April 1996.

[281] Y. Huang and W. F. McColl. Analytical inversion of general tridiagonal matrices. *Journal of Physics A: Mathematical and General*, 30(22):7919, November 1997.

[282] E. Kılıç. Explicit formula for the inverse of a tridiagonal matrix by backward continued fractions. *Applied Mathematics and Computation*, 197(1):345–357, March 2008.

[283] R. Zwicky. A brief Introduction to Dispersion Relations and Analyticity. Technical report, October 2016. arXiv:1610.06090 [hep-ph, physics:hep-th] type: article.

[284] A. Tilloy. Relativistic continuous matrix product states for quantum fields without cutoff. *Physical Review D*, 104(9):096007, November 2021.

[285] J. Haegeman, J. I. Cirac, T. J. Osborne, H. Verschelde, and F. Verstraete. Applying the Variational Principle to $(1 + 1)$-Dimensional Quantum Field Theories. *Physical Review Letters*, 105(25):251601, December 2010.

[286] V. Stojevic, J. Haegeman, I. P. McCulloch, L. Tagliacozzo, and F. Verstraete. Conformal data from finite entanglement scaling. *Physical Review B*, 91(3):035120, January 2015.

[287] C. Boudreault, C. Berthiere, and W. Witczak-Krempa. Entanglement and separability in continuum Rokhsar-Kivelson states. *Physical Review Research*, 4(3):033251, September 2022.

[288] M. R. M. Mozaffar and A. Mollabashi. Time scaling of entanglement in integrable scale-invariant theories. *Physical Review Research*, 4(2):L022010, April 2022.

[289] P. W. Anderson. Infrared Catastrophe in Fermi Gases with Local Scattering Potentials. *Physical Review Letters*, 18(24):1049–1051, June 1967.

[290] C. Callan and F. Wilczek. On geometric entropy. *Physics Letters B*, 333(1):55–61, July 1994.

[291] H. Casini and M. Huerta. Entanglement entropy in free quantum field theory. *Journal of Physics A: Mathematical and Theoretical*, 42(50):504007, December 2009.

[292] R. Nehra, D. S. Bhakuni, A. Ramachandran, and A. Sharma. Flat bands and entanglement in the Kitaev ladder. *Physical Review Research*, 2(1):013175, February 2020.

[293] H. Gegier, E. Marsden, and E. Rutherford. On a diffuse reflection of the α-particles. *Proceedings of the Royal Society of London. Series A, Containing Papers of a Mathematical and Physical Character*, 82(557):495–500, July 1909.

[294] E. Rutherford. LXXIX. The scattering of α and β particles by matter and the structure of the atom. *The London, Edinburgh, and Dublin Philosophical Magazine and Journal of Science*, 21(125):669–688, May 1911.

[295] W. Langel. Introduction to neutron scattering. *ChemTexts*, 9(4):12, October 2023.

[296] H. Hannesdottir and M. D. Schwartz. S-Matrix for massless particles. *Physical Review D: Particles and Fields*, 101(10):105001, August 2020.

[297] R. Haag. *Local Quantum Physics: Fields, Particles, Algebras*. Theoretical and Mathematical Physics. Springer Berlin Heidelberg, 1996.

[298] D. Buchholz and S. J. Summers. Scattering in Relativistic Quantum Field Theory: Fundamental Concepts and Tools, September 2005.

[299] K. Cichy, A. Kujawa-Cichy, and M. Szyniszewski. Lattice Hamiltonian approach to the massless Schwinger model: Precise extraction of the mass gap. *Computer Physics Communications*, 184(7):1666–1672, July 2013.

[300] E. Wigner. On Unitary Representations of the Inhomogeneous Lorentz Group. *Ann. of Math.*, 40(1):149–204, 1939.

[301] S. Coleman and J. Mandula. All Possible Symmetries of the S Matrix. *Phys. Rev.*, 159(5):1251–1256, July 1967.

[302] D. Ruelle. A remark on bound states in potential-scattering theory. *Il Nuovo Cimento A (1965-1970)*, 61(4):655–662, June 1969.

[303] V. Bach. Schrödinger Operators. pages 487–494. Academic Press, Oxford, January 2006.

[304] L. Vanderstraeten, F. Verstraete, and J. Haegeman. Scattering particles in quantum spin chains. *Physical Review B*, 92(12):125136, September 2015.

[305] D. Tong. *Quantum Field Theory.* 2007.

[306] C. Adam. Massive Schwinger Model within Mass Perturbation Theory. *Annals of Physics*, 259(1):1–63, September 1997.

[307] C. J. Hamer, J. Kogut, D. P. Crewther, and M. M. Mazzolini. The massive Schwinger model on a lattice: Background field, chiral symmetry and the string tension. *Nuclear Physics B*, 208(3):413–438, December 1982.

[308] C. J. Hamer, Z. Weihong, and J. Oitmaa. Series Expansions for the Massive Schwinger Model in Hamiltonian lattice theory. *Physical Review D*, 56(1):55–67, July 1997.

[309] P. Sriganesh, C. J. Hamer, and R. J. Bursill. New finite-lattice study of the massive Schwinger model. *Physical Review D*, 62(3):034508, July 2000.

[310] T. M. R. Byrnes, P. Sriganesh, R. J. Bursill, and C. J. Hamer. Density matrix renormalization group approach to the massive Schwinger model. *Physical Review D*, 66(1):013002, July 2002.

[311] E. Ercolessi, P. Facchi, G. Magnifico, S. Pascazio, and F. V. Pepe. Phase transitions in Z_n gauge models: Towards quantum simulations of the Schwinger-Weyl QED. *Physical Review D: Particles and Fields*, 98(7):074503, October 2018.

[312] G. Magnifico, D. Vodola, E. Ercolessi, S. P. Kumar, M. Müller, and A. Bermudez. Symmetry-protected topological phases in lattice gauge theories: Topological QED_2. *Physical Review D*, 99(1):014503, January 2019.

[313] G. Magnifico, D. Vodola, E. Ercolessi, S. P. Kumar, M. Müller, and A. Bermudez. $\mathbb{Z}_N$ gauge theories coupled to topological fermions: QED_2 with a quantum mechanical θ angle. *Physical Review B*, 100:115152, September 2019.

[314] C. Nagele, J. E. Cejudo, T. Byrnes, and M. Kleban. Flux unwinding in the lattice Schwinger model. *Phys. Rev. D*, 99(9):094501, May 2019.

[315] G. Magnifico, M. Dalmonte, P. Facchi, S. Pascazio, F. V. Pepe, and E. Ercolessi. Real Time Dynamics and Confinement in the $\mathbb{Z}_n$ Schwinger-Weyl lattice model for

1+1 QED. *Quantum*, 4:281, June 2020. arXiv:1909.04821 [cond-mat, physics:hep-lat, physics:hep-th, physics:quant-ph].

[316] R. Dempsey, I. R. Klebanov, S. S. Pufu, B. T. Søgaard, and B. Zan. Phase Diagram of the Two-Flavor Schwinger Model at Zero Temperature. Technical report, June 2023.

[317] J.-Y. Desaules, D. Banerjee, A. Hudomal, Z. Papić, A. Sen, and J. C. Halimeh. Weak ergodicity breaking in the Schwinger model. *Physical Review B*, 107(20):L201105, May 2023.

[318] H. Ohata. Monte Carlo study of Schwinger model without the sign problem. Technical report, March 2023.

[319] S. Kühn, J. I. Cirac, and M.-C. Bañuls. Quantum simulation of the Schwinger model: A study of feasibility. *Physical Review A*, 90(4):042305, October 2014. arXiv: 1407.4995 version: 2.

[320] B. Buyens, F. Verstraete, and K. Van Acoleyen. Hamiltonian simulation of the Schwinger model at finite temperature. *Physical Review D*, 94(8):085018, October 2016.

[321] M. C. Bañuls, K. Cichy, J. I. Cirac, K. Jansen, and S. Kühn. Density Induced Phase Transitions in the Schwinger Model: A Study with Matrix Product States. *Physical Review Letters*, 118(7):071601, February 2017.

[322] B. Buyens, J. Haegeman, F. Hebenstreit, F. Verstraete, and K. Van Acoleyen. Real-time simulation of the Schwinger effect with matrix product states. *Physical Review D: Particles and Fields*, 96(11):114501, December 2017.

[323] L. Funcke, K. Jansen, and S. Kühn. Topological vacuum structure of the Schwinger model with matrix product states. *Physical Review D: Particles and Fields*, 101:054507, March 2020.

[324] T. V. Zache, M. Van Damme, J. C. Halimeh, P. Hauke, and D. Banerjee. Towards the continuum limit of a $(1+1)$d quantum link Schwinger model. *Physical Review D*, 106(9):L091502, November 2022.

[325] T. Angelides, L. Funcke, K. Jansen, and S. Kühn. Computing the Mass Shift of Wilson and Staggered Fermions in the Lattice Schwinger Model with Matrix Product States. *Physical Review D*, 108(1):014516, March 2023.

[326] R. Belyansky, S. Whitsitt, N. Mueller, A. Fahimniya, E. R. Bennewitz, Z. Davoudi, and A. V. Gorshkov. High-Energy Collision of Quarks and Hadrons in the Schwinger Model: From Tensor Networks to Circuit QED. Technical report, July 2023.

[327] L. Funcke, K. Jansen, and S. Kühn. Exploring the cp-violating dashen phase in the schwinger model with tensor networks. Technical report, March 2023.

[328] E. A. Martinez, C. A. Muschik, P. Schindler, D. Nigg, A. Erhard, M. Heyl, P. Hauke, M. Dalmonte, T. Monz, P. Zoller, and R. Blatt. Real-time dynamics of lattice gauge theories with a few-qubit quantum computer. *Nature*, 534(7608):516–519, June 2016.

[329] P. Arrighi, C. Bény, and T. Farrelly. A quantum cellular automaton for one-dimensional QED. March 2019.

[330] S. Notarnicola, M. Collura, and S. Montangero. Real-time-dynamics quantum simulation of $(1 + 1)$-dimensional lattice QED with Rydberg atoms. *Physical Review Research*, 2(1):013288, March 2020.

[331] L. Funcke, T. Hartung, K. Jansen, S. Kühn, M.-O. Pleinert, S. Schuster, and J. von Zanthier. Exploring the phase structure of the multi-flavor schwinger model with quantum computing. November 2022.

[332] N. H. Nguyen, M. C. Tran, Y. Zhu, A. M. Green, C. H. Alderete, Z. Davoudi, and N. M. Linke. Digital Quantum Simulation of the Schwinger Model and Symmetry Protection with Trapped Ions. *PRX Quantum*, 3(2):020324, May 2022.

[333] X.-D. Xie, X. Guo, H. Xing, Z.-Y. Xue, D.-B. Zhang, and S.-L. Zhu. Variational thermal quantum simulation of the lattice Schwinger model. *Physical Review D*, 106(5):054509, September 2022.

[334] J.-Y. Desaules, A. Hudomal, D. Banerjee, A. Sen, Z. Papić, and J. C. Halimeh. Prominent quantum many-body scars in a truncated Schwinger model. *Physical Review B*, 107(20):205112, May 2023.

[335] R. C. Farrell, M. Illa, A. N. Ciavarella, and M. J. Savage. Scalable Circuits for Preparing Ground States on Digital Quantum Computers: The Schwinger Model Vacuum on 100 Qubits. Technical report, August 2023.

[336] A. Florio, D. Frenklakh, K. Ikeda, D. Kharzeev, V. Korepin, S. Shi, and K. Yu. Real-time non-perturbative dynamics of jet production: quantum entanglement and vacuum modification. *Physical Review Letters*, 131(2):021902, July 2023.

[337] L. Nagano, A. Bapat, and C. W. Bauer. Quench dynamics of the Schwinger model via variational quantum algorithms. Technical report, February 2023.

[338] J. W. Pedersen, E. Itou, R.-Y. Sun, and S. Yunoki. Quantum Simulation of Finite Temperature Schwinger Model via Quantum Imaginary Time Evolution. Technical report, November 2023. arXiv:2311.11616 [hep-lat, physics:hep-th, physics:quant-ph] type: article.

[339] D. Pomarico, L. Cosmai, P. Facchi, C. Lupo, S. Pascazio, and F. V. Pepe. Dynamical quantum phase transitions of the Schwinger model: real-time dynamics on IBM Quantum. *Entropy*, 25(4):608, April 2023.

[340] K. Konishi and G. Paffuti. *Quantum Mechanics: A New Introduction*. Oxford University Press, Oxford, New York, March 2009.

[341] S. Elitzur, R. B. Pearson, and J. Shigemitsu. Phase structure of discrete Abelian spin and gauge systems. *Physical Review D: Particles and Fields*, 19(12):3698–3714, June 1979.

[342] B. Buyens, S. Montangero, J. Haegeman, F. Verstraete, and K. Van Acoleyen. Finite-representation approximation of lattice gauge theories at the continuum limit with tensor networks. *Physical Review D: Particles and Fields*, 95:094509, May 2017.

[343] F. Tschirsich, S. Montangero, and M. Dalmonte. Phase diagram and conformal string excitations of square ice using gauge invariant matrix product states. *SciPost Physics*, 6(3):028, March 2019.

[344] M. Turco, G. M. Quinta, J. Seixas, and Y. Omar. Towards Quantum Simulation of Bound States Scattering. Technical report, May 2023.

[345] P. J. Szablowski. Discrete Normal distribution and its relationship with Jacobi Theta functions. *Statistics & Probability Letters*, 52(3):289–299, April 2001.

[346] M. M. Broido. Green functions in particle physics. *Rep. Progr. Phys.*, 32(2):493–545, July 1969.

[347] F. M. Surace, P. P. Mazza, G. Giudici, A. Lerose, A. Gambassi, and M. Dalmonte. Lattice Gauge Theories and String Dynamics in Rydberg Atom Quantum Simulators. *Physical Review X*, 10(2):021041, September 2020.

[348] J. S. Bell. On the Einstein Podolsky Rosen paradox. *Physics Physique Fizika*, 1(3):195–200, November 1964.

[349] N. Brambilla, S. Eidelman, P. Foka, S. Gardner, A. S. Kronfeld, M. G. Alford, R. Alkofer, M. Butenschoen, T. D. Cohen, J. Erdmenger, L. Fabbietti, M. Faber, J. L. Goity, B. Ketzer, H. W. Lin, F. J. Llanes-Estrada, H. B. Meyer, P. Pakhlov, E. Pallante, M. I. Polikarpov, H. Sazdjian, A. Schmitt, W. M. Snow, A. Vairo, R. Vogt, A. Vuorinen, H. Wittig, P. Arnold, P. Christakoglou, P. Di Nezza, Z. Fodor, X. Garcia i Tormo, R. Höllwieser, M. A. Janik, A. Kalweit, D. Keane, E. Kiritsis, A. Mischke, R. Mizuk, G. Odyniec, K. Papadodimas, A. Pich, R. Pittau, J.-W. Qiu, G. Ricciardi, C. A. Salgado, K. Schwenzer, N. G. Stefanis, G. M. von Hippel, and V. I. Zakharov. QCD and strongly coupled gauge theories: challenges and perspectives. *The European Physical Journal C*, 74(10):2981, October 2014.

[350] H.-W. Lin. Hadron Spectroscopy and Structure from Lattice QCD. *Few-Body Systems*, 63(4):65, September 2022.

[351] D. Grabowska, D. B. Kaplan, and A. N. Nicholson. Sign problems, noise, and chiral symmetry breaking in a QCD-like theory. *Physical Review D*, 87(1):014504, January 2013.

[352] J. B. Kogut and M. A. Stephanov. *The Phases of Quantum Chromodynamics: From Confinement to Extreme Environments.* Cambridge Monographs on Particle Physics, Nuclear Physics and Cosmology. Cambridge University Press, Cambridge, 2003.

[353] S. Borsanyi, Z. Fodor, J. N. Guenther, R. Kara, S. D. Katz, P. Parotto, A. Pasztor, C. Ratti, and K. K. Szabó. QCD Crossover at Finite Chemical Potential from Lattice Simulations. *Physical Review Letters*, 125(5):052001, July 2020.

[354] R. C. Farrell, I. A. Chernyshev, S. J. M. Powell, N. A. Zemlevskiy, M. Illa, and M. J. Savage. Preparations for quantum simulations of quantum chromodynamics in $1+1$ dimensions. I. Axial gauge. *Physical Review D*, 107(5):054512, July 2023.

[355] R. C. Farrell, I. A. Chernyshev, S. J. M. Powell, N. A. Zemlevskiy, M. Illa, and M. J. Savage. Preparations for quantum simulations of quantum chromodynamics in $1+1$ dimensions. II. Single-baryon β-decay in real time. *Physical Review D*, 107(5):054513, March 2023.

[356] H. A. Chawdhry and M. Pellen. Quantum simulation of colour in perturbative quantum chromodynamics. Technical report, March 2023.

[357] C. W. Bauer, Z. Davoudi, N. Klco, and M. J. Savage. Quantum simulation of fundamental particles and forces. *Nature Reviews Physics*, 5(7):420–432, July 2023.

[358] S. V. Kadam, I. Raychowdhury, and J. R. Stryker. Loop-string-hadron formulation of an SU(3) gauge theory with dynamical quarks. *Physical Review D*, 107(9):094513, May 2023.

[359] Z. Wang, F. Wang, J. Vovrosh, J. Knolle, F. Mintert, and R. Mukherjee. Quantum simulation of hadronic states with Rydberg-dressed atoms. Technical report, April 2023.

[360] W. Qian, R. Basili, S. Pal, G. Luecke, and J. P. Vary. Solving hadron structures using the basis light-front quantization approach on quantum computers. *Physical Review Research*, 4(4):043193, December 2022.

[361] X. Yao. Quantum Simulation of Light-Front QCD for Jet Quenching in Nuclear Environments. Technical report, December 2022.

[362] J. Barata, X. Du, M. Li, W. Qian, and C. A. Salgado. Medium induced jet broadening in a quantum computer. *Physical Review D*, 106(7):074013, October 2022.

[363] J. Barata and C. A. Salgado. A quantum strategy to compute the jet quenching parameter $\hat{q}$. Technical report, April 2021.

[364] J. Berges, M. P. Heller, A. Mazeliauskas, and R. Venugopalan. QCD thermalization: *Ab initio* approaches and interdisciplinary connections. *Reviews of Modern Physics*, 93(3):035003, August 2021.

[365] N. Collaboration, H. Lamm, S. Lawrence, and Y. Yamauchi. Parton physics on a quantum computer. *Physical Review Research*, 2(1):013272, March 2020.

[366] M. Rigobello. QHLGT-models, August 2023.

[367] Z. R. Kordov, R. Horsley, W. Kamleh, Y. Nakamura, H. Perlt, P. E. L. Rakow, G. Schierholz, H. Stüben, R. D. Young, and J. M. Zanotti. Weak decay constants of the pseudoscalar mesons from lattice QCD+QED. Technical report, April 2023.

[368] F. Pollmann, S. Mukerjee, A. M. Turner, and J. E. Moore. Theory of Finite-Entanglement Scaling at One-Dimensional Quantum Critical Points. *Physical Review Letters*, 102(25):255701, June 2009.

[369] B. Pirvu, G. Vidal, F. Verstraete, and L. Tagliacozzo. Matrix product states for critical spin chains: Finite-size versus finite-entanglement scaling. *Physical Review B*, 86(7):075117, August 2012.

[370] M. P. Hernández. 1 Lattice field theory fundamentals. page 20. Oxford University Press, August 2011.

[371] N. Laflorencie, E. S. Sørensen, M.-S. Chang, and I. Affleck. Boundary Effects in the Critical Scaling of Entanglement Entropy in 1D Systems. *Physical Review Letters*, 96(10):100603, March 2006.

[372] P. Calabrese, M. Campostrini, F. Essler, and B. Nienhuis. Parity Effects in the Scaling of Block Entanglement in Gapless Spin Chains. *Physical Review Letters*, 104(9):095701, March 2010.

[373] J. C. Xavier and F. C. Alcaraz. Finite-size corrections of the entanglement entropy of critical quantum chains. *Physical Review B*, 85(2):024418, January 2012.

[374] G. Ecker. Chiral perturbation theory. *Progress in Particle and Nuclear Physics*, 35:1–80, January 1995.

[375] T. Das, G. S. Guralnik, V. S. Mathur, F. E. Low, and J. E. Young. Electromagnetic Mass Difference of Pions. *Physical Review Letters*, 18(18):759–761, May 1967.

[376] A. B. Zamolodchikov. Irreversibility of the Flux of the Renormalization Group in a 2D Field Theory. *JETP lett*, 43(12):730–732, 1986.

[377] E. W. Cheney and W. A. Light. *A Course in Approximation Theory*. American Mathematical Soc., January 2009.

[378] N. D. Mermin and H. Wagner. Absence of Ferromagnetism or Antiferromagnetism in One- or Two-Dimensional Isotropic Heisenberg Models. *Physical Review Letters*, 17(22):1133–1136, November 1966.

[379] P. C. Hohenberg. Existence of Long-Range Order in One and Two Dimensions. *Physical Review*, 158(2):383–386, June 1967.

[380] S. Sachdev. *Quantum Phase Transitions*. Cambridge University Press, Cambridge, 2 edition, 2011.

[381] R. J. Jaffe. Multi-Quark Hadrons. 1. The Phenomenology of (2 Quark 2 anti-Quark) Mesons. *Phys. Rev. D*, 15(1):267–280, January 1977.

[382] P. Bicudo. Tetraquarks and pentaquarks in lattice QCD with light and heavy quarks. Technical report, December 2022.

[383] Y. Y. Atas, J. F. Haase, J. Zhang, V. Wei, S. M.-L. Pfaendler, R. Lewis, and C. A. Muschik. Simulating one-dimensional quantum chromodynamics on a quantum computer: Real-time evolutions of tetra- and pentaquarks. Technical report, February 2023.

[384] E. Itou, A. Matsumoto, and Y. Tanizaki. Calculating composite-particle spectra in Hamiltonian formalism and demonstration in 2-flavor $\mathrm{QED}_{1+1\mathrm{d}}$. Technical report, July 2023.

[385] E. G. Dalla Torre, D. Benjamin, Y. He, D. Dentelski, and E. Demler. Friedel oscillations as a probe of fermionic quasiparticles. *Physical Review B*, 93(20):205117, May 2016.

[386] D. Vodola, L. Lepori, E. Ercolessi, and G. Pupillo. Long-range Ising and Kitaev models: phases, correlations and edge modes. *New Journal of Physics*, 18(1):015001, December 2015.

[387] T. Felser, S. Notarnicola, and S. Montangero. Efficient Tensor Network Ansatz for High-Dimensional Quantum Many-Body Problems. *Physical Review Letters*, 126(17):170603, April 2021.

[388] M. S. J. Tepaske and D. J. Luitz. Three-dimensional isometric tensor networks. *Physical Review Research*, 3(2):023236, May 2021.

[389] J. Osborne, I. P. McCulloch, B. Yang, P. Hauke, and J. C. Halimeh. Large-Scale 2+1D U(1) Gauge Theory with Dynamical Matter in a Cold-Atom Quantum Simulator. Technical report, November 2022.

[390] P. Emonts and E. Zohar. Fermionic Gaussian PEPS in $3 + 1d$: Rotations and Relativistic Limits. *Physical Review D*, 108(1):014514, April 2023.

[391] P. Emonts, A. Kelman, U. Borla, S. Moroz, S. Gazit, and E. Zohar. Finding the ground state of a lattice gauge theory with fermionic tensor networks: a $2 + 1d$ $\mathbb{Z}_2$ demonstration. *Physical Review D*, 107(1):014505, January 2023.

[392] J. Osborne, I. P. McCulloch, and J. C. Halimeh. Disorder-Free Localization in $2+1$D Lattice Gauge Theories with Dynamical Matter. Technical report, January 2023.

[393] D. Vadacchino. A review on Glueball hunting. Technical report, May 2023.

[394] K. Ikeda, D. E. Kharzeev, R. Meyer, and S. Shi. Detecting the critical point through entanglement in Schwinger model. Technical report, May 2023.

[395] R. Brower, S. Chandrasekharan, and U.-J. Wiese. QCD as a quantum link model. *Physical Review D*, 60(9):094502, September 1999.

[396] P. O. Ludl. Systematic analysis of finite family symmetry groups and their application to the lepton sector. Technical report, July 2010.

[397] H. Flyvbjerg. Group space decimation: A way to simulate QCD by the 1080 element subgroup of SU(3)? *Nuclear Physics B*, 243(2):350–364, September 1984.

[398] R. Zwicky and T. Fischbacher. Discrete minimal flavor violation. *Physical Review D*, 80(7):076009, October 2009.

[399] A. Merle and R. Zwicky. Explicit and spontaneous breaking of SU(3) into its finite subgroups. *Journal of High Energy Physics*, 2012(2):128, February 2012.

[400] J. Bloch, R. Lohmayer, S. Schweiss, and J. Unmuth-Yockey. Effective $\mathbb{Z}_3$ model for finite-density QCD with tensor networks. In *Proceedings of The 38th International Symposium on Lattice Field Theory — PoS(LATTICE2021)*, volume 396, page 062, October 2022.

[401] J. C. Halimeh, H. Lang, and P. Hauke. Gauge protection in non-abelian lattice gauge theories. *New Journal of Physics*, 24(3):033015, March 2022.

[402] I. Raychowdhury and J. R. Stryker. Solving Gauss's law on digital quantum computers with loop-string-hadron digitization. *Physical Review Research*, 2(3):033039, July 2020.

[403] E. Mathew and I. Raychowdhury. Protecting local and global symmetries in simulating 1+1-D non-abelian gauge theories. *Physical Review D*, 106(5):054510, September 2022.

[404] L. Vanderstraeten, J. Haegeman, and F. Verstraete. Tangent-space methods for uniform matrix product states. *SciPost Physics Lecture Notes*, 7, January 2019.

[405] J. Haegeman, C. Lubich, I. Oseledets, B. Vandereycken, and F. Verstraete. Unifying time evolution and optimization with matrix product states. *Physical Review B*, 94(16):165116, October 2016.

[406] J. Haegeman, M. Mariën, T. J. Osborne, and F. Verstraete. Geometry of matrix product states: Metric, parallel transport, and curvature. *Journal of Mathematical Physics*, 55(2):021902, February 2014.

[407] J. Haegeman, T. J. Osborne, and F. Verstraete. Post-matrix product state methods: To tangent space and beyond. *Physical Review B*, 88(7):075133, August 2013.

[408] J. Haegeman, S. Michalakis, B. Nachtergaele, T. J. Osborne, N. Schuch, and F. Verstraete. Elementary Excitations in Gapped Quantum Spin Systems. *Physical Review Letters*, 111(8):080401, August 2013.

[409] L. Vanderstraeten, J. Haegeman, T. J. Osborne, and F. Verstraete. S Matrix from Matrix Product States. *Physical Review Letters*, 112(25):257202, June 2014.

[410] M. Van Damme, L. Vanderstraeten, J. De Nardis, J. Haegeman, and F. Verstraete. Real-time scattering of interacting quasiparticles in quantum spin chains. *Physical Review Research*, 3(1):013078, January 2021.

[411] S. Scopa, P. Calabrese, and A. Bastianello. Entanglement dynamics in confining spin chains. *Physical Review B*, 105(12):125413, March 2022.

[412] J. Vovrosh, H. Zhao, J. Knolle, and A. Bastianello. Confinement induced impurity states in spin chains. *Physical Review B*, 105(10):L100301, March 2022.

[413] M. C. Bañuls, M. P. Heller, K. Jansen, J. Knaute, and V. Svensson. A quantum information perspective on meson melting. Technical report, June 2022.

[414] J. Knaute. Meson content of entanglement spectra after integrable and nonintegrable quantum quenches. *Physical Review B*, 107(10):L100303, March 2023.

[415] C. Huang, F. Zhang, M. Newman, X. Ni, D. Ding, J. Cai, X. Gao, T. Wang, F. Wu, G. Zhang, H.-S. Ku, Z. Tian, J. Wu, H. Xu, H. Yu, B. Yuan, M. Szegedy, Y. Shi, H.-H. Zhao, C. Deng, and J. Chen. Efficient parallelization of tensor network contraction for simulating quantum computation. *Nature Computational Science*, 1(9):578–587, September 2021.

[416] M. Ballarin, G. Cataldi, A. Costantini, M. Gerster, T. Felser, D. Jaschke, L. Kohn, G. Magnifico, S. Montangero, S. Notarnicola, A. Pagano, N. Reinić, M. Rigobello, M. Rizzi, P. Silvi, M. Trenti, F. Tschirsich, and L. Zangrando. Quantum Tea – The Quantum Tensor network Emulator Applications, 2023.